SAPIENZA
UNIVERSITÀ DI ROMA

Through the looking glass and what ATLAS found there: a Dark Sector search for light Dark Matter

Scuola di dottorato Vito Volterra

Dottorato di Ricerca in Fisica – XXXII Ciclo

Candidate

Cristiano Sebastiani
ID number 1382044

Thesis Advisor

Prof. Stefano Giagu

Co-Advisors

Dr. Carl Gwilliam
Dr. Vincenzo Vagnoni

A thesis submitted in partial fulfillment of the requirements
for the degree of Doctor of Philosophy in Physics

31 October 2019

Thesis defended on 7 February 2019
in front of a Board of Examiners composed by:

Prof. Vincenzo Canale (chairman)

Prof. Fedele Lizzi

Prof. Paolo De Bernardis

Through the looking glass and what ATLAS found there: a Dark Sector search for light Dark Matter

Ph.D. thesis. Sapienza – University of Rome

This thesis has been typeset by LaTeX and the Sapthesis class.

Version: January 10, 2020

Author's email: cristiano.sebastiani@cern.ch

Dedicated to
Zorro I

Abstract

Latest theories beyond the Standard Model predict a new 'dark force' mediated by a light neutral particle called a dark photon, which opens a window to a complex Dark Sector. Through kinetic mixing a dark photon produced from the decay of a Higgs boson can decay back to SM particles with a sizeable lifetime, giving rise to striking signatures at hadron colliders. This work presents the results of a search for long-lived dark photons decaying into displaced collimated jet-like structures of leptons and light hadrons, referred to as 'dark-photon jets'. The search uses data corresponding to an integrated luminosity of 36.1 fb^{-1} collected in proton–proton collisions at $\sqrt{s} = 13$ TeV recorded in 2015–2016 of Run-2 data taking with the ATLAS detector at the Large Hadron Collider. The observed number of events is consistent with the expected background, and limits on the production cross section times branching fraction as a function of the proper decay length of the dark photon are reported. The enormous amount of data that will be collected by ATLAS during the Run-3 (300 fb^{-1}) and High-Luminosity (3000 fb^{-1}) 14 TeV LHC phase, and the updated ATLAS detector setup, will offer a unique opportunity to probe unexplored regions of phase space in the context of this search. Sensitivity prospects for Run-3 and High-Luminosity LHC are discussed and two new muon trigger algorithms are studied to improve the selection efficiency of displaced muon pairs. The current dark-photon jet analysis reach will continue to expand in parameter space and signature topologies proving to be a powerful tool for probing the Dark Sector at the LHC.

Contents

Chapter 1

Introduction

The particle nature of Dark Matter (DM) is amongst the urgent question in fundamental physics. After completing the Standard Model (SM) theory of particle physics with the discovery of the Higgs boson in 2012, the experiments situated at the Large Hadron Collider [1] (LHC) in Geneva are shifting their focus to addressing the DM mystery. The LHC collides bunches of protons at a centre-of-mass energy of $\sqrt{s} = 13$ TeV and delivers data to six experiments, among which there is ATLAS [2].

Irrefutable astrophysical and cosmological measurements based on gravitational interactions reveal the existence of DM, which makes up for a quarter of our Universe [3]. Several extensions of the SM propose a solution to the DM puzzle predicting new particles that could be observed at hadron colliders. The leading class of candidates searched for at the LHC are Weakly Interacting Massive Particles (WIMP), which are predicted to couple to SM particles through a generic weak interaction. A rich worldwide program explored the energy frontier probing DM interactions with the SM at different energy scales, ranging from a few GeV to several TeV. However, no DM signal has been observed yet. ATLAS Run-1 and early Run-2 searches have ruled out wide areas of WIMP parameter space, urging the necessity of a new paradigm.

One interesting alternative scenario is the Dark Sector (DS), where DM particles are only a piece of a new extended sector. The new hidden sector with its own complex structure can include new particles and new 'dark forces' such as a dark photon, mediator of a electromagnetic-like force. The presence of new forces may have gone easily undetected by all experiments so far due the weakness of the coupling between the DS and the SM. Dark sector searches target the portal mediator rather the DM itself, assuming only the existence of a non-gravitational coupling between the two sectors and without any hypothesis on the DM structure. The new hypothetical interactions are tightly linked to the structure of the SM and can be mediated by vector, Higgs, and neutrino portals. Of specific interest for this thesis are models which include both vector and Higgs portals, where a massive dark photon kinetically mixes with the SM photon. Such models provide an incredibly rich phenomenology that can give rise to striking signatures in the detectors at the LHC. These can be detected through numerous unconventional signatures: long time-of-flight, late calorimetric energy deposits or displaced vertices.

One of the most interesting signature is the 'dark-photon jet' (or 'lepton-jet),

where a neutral particle with macroscopic life-time decays to pairs of light leptons and hadrons with a jet-like structure. Dark-photon jet searches are a great challenge for the ATLAS experiment, requiring dedicated trigger algorithms and non-standard object reconstruction. This thesis documents ATLAS current and future efforts in the search for displaced dark-photon jets. The latest ATLAS Run-2 search using 36.1 $fb^{-1}$of collected data results are presented, and ATLAS plans for the legacy analysis with the full Run-2 dataset composed of 139 $fb^{-1}$are introduced. Starting from these results, the prospects and improvements expected for the High Luminosity LHC Run are discussed. Presented in this thesis are the only LHC Run-2 [4] dark-photon jet results and HL-LHC prospects [5] published to date, significantly expanding the Dark Sector program at LHC.

An overview of the SM theory and its extension to the Dark Sectors with its phenomenology are discussed in Chapters 2 and 3. Chapter 4 summarise the main characteristics of the ATLAS detector and the reconstruction of physics objects. The Run-2 search for dark-photon jets in the 2015-2016 dataset is described in detail in Chapter 5, and its future extensions are discussed in Chapter 6. Finally, Chapter 7 show the HL-LHC prospects of the ATLAS dark-photon jets searches.

Chapter 2

Standard Model and beyond

The Standard Model (SM) theory of particle physics describes the behaviour of all elementary particles under three of the four known fundamental forces: electromagnetic, weak and strong interactions. These are explained in terms of relativistic quantum field theory, which is not able to describe the gravitational interaction. However the gravitational interaction can be considered negligible at the collider energy scale. The model was first introduced in the late 60s and it has been able to explain and predict an incredible wide array of phenomena of elementary particle physics. 50 years of experimental evidence have tested the model with great precision but have also shown few hints of a new physics beyond the SM (BSM).

This Chapter introduces the basics of SM theory and possible extensions to overcome its limitations.

2.1 The Standard Model

The SM is formulated in the relativistic quantum field theory framework, which represents each particle as a field and its dynamic by a Lagrangian. The model is postulated under a defined set of symmetries under which it must be invariant. The SM is symmetric under translation, rotation and boost transformations. It is also gauge invariant under the local $SU(3)_C \times SU(2)_L \times U(1)_Y$ gauge symmetry. Each of these gauge symmetries can be roughly related to a fundamental interaction: the $U(3)_C$ non-abelian group is related to the strong force, and the $SU(2)_L \times U(1)Y$ is related to the electroweak force.

Elementary particles can be divided in two categories according to their spin values: integer spin particles which follow Bose-Einstein statistics (bosons), and half-integer spin particles which follow Fermi-Dirac statistics and Pauli exclusion principle (fermions). Fermions are interacting particles described by quantum numbers and categorised in leptons and quarks. Spin-1 boson particles, also known as gauge bosons, act as force mediators and govern interactions of fermions. The Higgs boson is the only spin-0 particle in the model and its mechanism is crucial to provide a mass to other particles of the Standard Model. Figure 2.1 show all known SM fundamental particles.

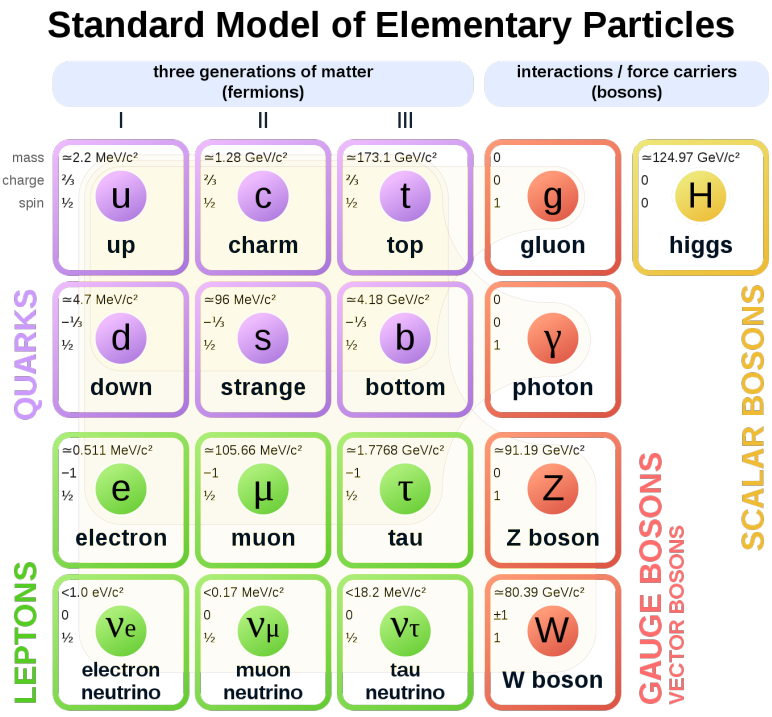

Figure 2.1. Know Standard Model particles.

2.1.1 Particles

Leptons

Leptons are grouped in three different families, one for each lepton flavour: electron (e), muon (μ), and tau (τ). The three families are ordered by mass and each comprises a positively charged lepton and a neutral charged lepton called a neutrino. Charged leptons interact under the electromagnetic and weak forces, whereas the neutrinos interact only under the weak force. A distinctive neutrino characteristic is that the flavour eigenstate does not correspond to the mass eigenstate, giving rise to neutrino flavour oscillation. Leptons are present also as anti-particles.

Quarks

Quarks are grouped in three families of quark pairs, one up-type and one down-type. Up-type quarks have an electric charge of $Q = \frac{2}{3}e$, down-type quarks have an electric charge of $Q = -\frac{1}{3}e$. Each of the six quarks has its own flavour: up (u), down (d), strange (s), charm (c), bottom (b), and top (t). Finally, each quark is also color charged and interacts via the strong force. The same as for leptons, quarks have their respective anti-particles called anti-quarks. Quarks exists in nature only as color-free composite particles, usually made of a quark-anti-quark pair (mesons) or of three quarks (barions).

Gauge bosons
Gauge bosons act as force mediators on fermions particles which are charged under the corresponding force quantum number. Gluons are the massless and electrically neutral mediators of the strong interaction acting on color charged particles. There are a total of 8 gluons, one for each generator of the $SU(3)_C$ gauge symmetry. The electro-weak $W^{\pm}/Z$ bosons are mediators of the weak interaction. The $W^{\pm}$ interact only with left-handed fermions and right-handed anti-fermions, while the Z boson interacts with all fermion and anti-fermions. The electro-weak bosons gain mass through spontaneous symmetry breaking, making the weak interaction a short-range force. The photon γ is the massless mediator of the electromagnetic force, which interacts with all electrically charged particles.

Scalar boson
The Higgs boson is the only spin-0 particle in the SM and gives mass to all elementary particles, with the exception of photons and gluons. Gauge boson gain mass through the process of electro-weak symmetry breaking, while the leptons and quarks via Yukawa coupling.

2.1.2 Quantum Electro-Dynamics

Quantum Electro-Dynamics [6] (QED) describes electromagnetic interactions of particles in terms of relativistic quantum field theory. A formulation of Maxwell's theory can be obtained starting from the Lorentz-invariant Lagrangian describing the free propagation of a free fermionic field ψ, and the kinetic term of an electromagnetic field $A_\mu(x)$:

$$\mathscr{L}_{QED} = \bar{\psi}(i\gamma^\mu\partial_\mu - m)\psi - \frac{1}{4}F^{\mu\nu}F_{\mu\nu}, \tag{2.1}$$

where the γ_μ are the Dirac matrices [7] and $F^{\mu\nu}$ is the electromagnetic tensor $F^{\mu\nu} = \partial^\mu A^\nu - \partial^\nu A^\mu$.

This Lagrangian needs to be invariant under local transformation of the $U(1)$ symmetry group, described by:

$$\psi(x) \to \psi'(x) = e^{if(x)}\psi(x), \tag{2.2}$$

where $f(x)$ defines the transformation for each point of the space-time coordinate x. The invariance of the Lagrangian under $U(1)$ symmetry is achieved by introducing the covariant derivative, defined as

$$D_\mu = \partial_\mu + ieA_\mu, \tag{2.3}$$

in the place of the partial derivative operator ∂_μ. The final QED Lagrangian is therefore:

$$\mathscr{L}_{QED} = \bar{\psi}(i\gamma^\mu\partial_\mu - m)\psi - \frac{1}{4}F^{\mu\nu}F_{\mu\nu} - e\bar{\psi}\gamma^\mu A_\mu\psi. \tag{2.4}$$

The new interaction term describes the coupling between charged fermions and the potential of the electromagnetic field.

2.1.3 Quantum Chromo-Dynamics

Quantum Chromo-Dynamics [8,9] (QCD) describes the strong interactions of quarks and gluons. In this $SU(3)$ non-abelian theory there are 8 massless gauge fields $G^a_{\mu\nu}$, one for each generator λ^a of the symmetry group. Quarks need to transform under the $SU(3)$ symmetry group and are represented as three component spinors ψ. Each element of the group can also be expressed as a 3×3 matrix defined as $U = qe^{i\alpha_a Ta}$. Unlike QED, the gauge bosons are charged under the group and therefore interact with each other.

Defining the covariant derivative for $SU(3)$ as:

$$D_\mu = \partial_\mu + i\alpha_s A_{\mu a} T^a, \tag{2.5}$$

where α_s is the QCD coupling constant. We can then define the QCD tensor field $G^a_{\mu\nu}$ as follow:

$$G^a_{\mu\nu} = \partial_\mu A^a_\nu - \partial_\nu A^a_\mu + \alpha_s f^{abc} A^b_\mu A^c_\nu, \tag{2.6}$$

where f^{abc} are the structure constants of the group built from the non-commutative QCD generators, $[T_a, T_b] = i f_{abc} T^c$.

Finally, the QCD Lagrangian is:

$$\mathscr{L}_{QCD} = \bar{q}(i\gamma^\mu \partial_\mu - m)q + \bar{q}(i\alpha_s T^a G^a_\mu - m)q - \frac{1}{4} G^a_{\mu\nu} G^{\mu\nu}_a. \tag{2.7}$$

An important feature of QCD, known as color confinement, is that free quarks cannot be observed as it is impossible to separate them from a combined state. This is due to the running coupling α_s of QCD theory which becomes larger at higher distances. Instead at small distances the coupling gets weak and quarks inside hadrons can be assumed to behave as free particles. This assumption, called asymptotic freedom, is crucial to be able to perform perturbative QCD calculation and provide quantitative predictions for hadronic interactions.

2.1.4 Electroweak model

First proposed in the late 60's by Weinberg [10] and Salam [11], the electroweak theory describes the unification of the electromagnetic and weak interactions under the $SU(2)_L \times U(1)_Y$ symmetry group. The weak interactions, which in analogy to QED are mediated by vector gauge bosons, are experienced by left-handed chiral particles, and right-handed chiral anti-particles, and its characterised by a smaller relative intensity compared to the electromagnetic and strong interactions. Under weak interactions left-handed and right-handed components transform differently under gauge transformations. These distinctive features of the weak interactions are responsible of radioactive decays and parity violation. The generators of the $SU(2)$ group are the weak isospin $\vec{\tau} = \frac{1}{2}\vec{\sigma}$ described by the Pauli matrices, and of the $U(1)$ group is the hypercharge Y. The group's local gauge transformations for left-handed fermions $\psi(x)_L$ and right-handed fermions $\psi(x)_R$ are

$$\psi(x)_L \to \chi'(x)_L = e^{i\vec{\alpha}(x)\vec{\tau} + i\beta(x)Y} \psi(x)_L, \tag{2.8}$$

$$\psi(x)_R \rightarrow \psi'(x)_R = e^{i\beta(x)Y}\psi(x)_R. \tag{2.9}$$

$\alpha(x)$ and $\beta(x)$ are the phases, χ_L is the weak isospin doublet that describes left-handed fermions.

The covariant derivative for electroweak interaction is then introduced as:

$$D_\mu = \partial_\mu + ig'\frac{Y}{2}B_\mu(x) + ig\frac{\tau^a}{2}W^a_\mu(x) \tag{2.10}$$

where g' and g are the coupling constants, $B_\mu(x)$ is the $U(1)_Y$ group field, and $W^a_\mu(x)$ is the $SU(2)_L$ group field. Finally the electroweak lagrangian is formulated:

$$\mathscr{L}_{EW} = \sum_{j=1}^{3} i\bar{\psi}_j(x)\gamma^\mu D_\mu\psi_j(x) - \frac{1}{4}B_{\mu\nu}B^{\mu\nu} - \frac{1}{4}W^a_{\mu\nu}W^{\mu\nu}_a. \tag{2.11}$$

The observable vector fields are obtained by the following combination of the gauge group fields:

$$A_\mu = W^3_\mu sin\theta_W + B_\mu cos\theta_W, \tag{2.12}$$

$$Z_\mu = W^3_\mu cos\theta_W + B_\mu sin\theta_W, \tag{2.13}$$

$$W^\pm_\mu = \frac{1}{\sqrt{2}}(W^1_\mu \mp W^2_\mu), \tag{2.14}$$

where θ_W is the Weinberg angle. The electric charge e is then described in terms of the coupling constants and the Weinberg angle:

$$e = gsin\theta_W = g'cos\theta_W. \tag{2.15}$$

This theory appears to be in contrast with experimental results as all SM gauge bosons appear to be massless, any mass term introduced by hand would spoil the theory renormalizability. This discrepancy is resolved by the Higgs mechanism that naturally introduces mass terms in the SM lagrangian.

2.1.5 Higgs mechanism

The Higgs mechanism [12,13] was first introduced in 1964 by Higgs, Brout and Englert, to solve the mass generation in the SM. The model introduces the spontaneous breaking of the $SU(2)_L \times U(1)_Y$ symmetry group into the $U(1)_{EM}$ group, giving rise to a new scalar boson called the Higgs boson. In a lagrangian system which presents a degenerate ground eigenstate, the spontaneous symmetry breaking is obtained by choosing one of these eigenstates as the state of minimum energy. As a result, three massless Goldstone bosons appear giving mass to the vector bosons and keeping the photon massless. The electroweak symmetry breaking is performed by assuming a new $SU(2)$ isospin doublet complex scalar field:

$$\phi = \begin{pmatrix}\phi_\alpha \\ \phi_\beta\end{pmatrix} = \sqrt{\frac{1}{2}}\begin{pmatrix}\phi_1 + i\phi_2 \\ \phi_3 + i\phi_4\end{pmatrix}. \tag{2.16}$$

This new field is invariant under local $SU(2)$ transformation, defining the new covariant derivative:

$$D_\mu = \partial_\mu + ig\frac{\tau_a}{2}W_\mu^a. \tag{2.17}$$

Therefore, the new electroweak lagrangian is:

$$\mathscr{L} = \left(\partial_\mu\phi + ig\frac{\tau}{2}W_\mu\phi\right)^\dagger \left(\partial_\mu\phi + ig\frac{\tau}{2}W^\mu\phi\right) - \frac{1}{4}W_{\mu\nu}W^{\mu\nu} - V(\phi), \tag{2.18}$$

where the Higgs potential $V(\phi)$ is defined as:

$$V(\phi) = \mu^2\phi^\dagger\phi + \lambda(\phi^\dagger\phi)^2, \tag{2.19}$$

with μ and λ free parameters. For values $\lambda > 0$ the potential is inferiorly bounded and the theory is stable. Additionally, for values $\mu^2 < 0$ the minimum is degenerate along a circumference, as shown in Figure 2.2.

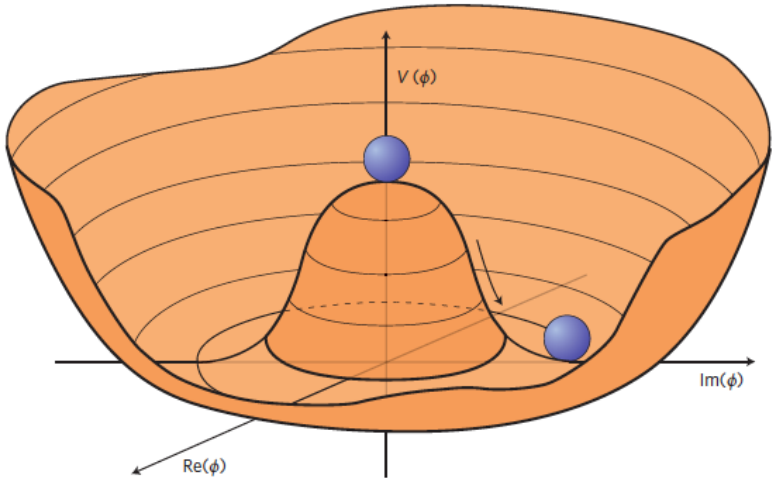

Figure 2.2. An illustration of the Higgs potential in the case that $\mu^2 < 0$, in which case the minimum is at $|\phi|^2 = \frac{-\mu^2}{2\lambda}$. Choosing any of the points at the bottom of the potential breaks spontaneously the rotational U(1) symmetry.

The symmetry breaking is obtained choosing the ground state to be $\phi_1 = \phi_2 = \phi_4 = 0$ and $\phi_3 = \sqrt{\frac{-\mu^2}{\lambda}} = v$:

$$\phi(x) = \sqrt{\frac{1}{2}}\begin{pmatrix}0\\v\end{pmatrix}. \tag{2.20}$$

To perform perturbative calculations, the ground state $\phi(x)$ can be expanded by perturbation parametrized by four scalar fields θ_1, θ_2, θ_3, and $h(x)$, as follow:

$$\phi(x) = \sqrt{\frac{1}{2}}\begin{pmatrix}\theta_1 + i\theta_2\\v + h - i\theta_3\end{pmatrix}. \tag{2.21}$$

Three of these scalar fields, θ_1, θ_2, θ_3, are the massless Goldstone bosons which can be removed by a SU(2) gauge transformation. The field can thus be expressed by the remaining the Higgs scalar field $h(x)$:

$$\phi(x) = \sqrt{\frac{1}{2}} \begin{pmatrix} 0 \\ v + h(x) \end{pmatrix}. \tag{2.22}$$

The Higgs lagrangian in terms of this field is formulated as:

$$\mathscr{L}_{Higgs} = \frac{1}{2}\partial_\mu h \partial^\mu h + (v+h)^2 \left(\frac{g^2}{4} W_\mu^\dagger W^\mu + \frac{g^2}{8cos^2\theta_W} Z_\mu Z^\mu \right) - \lambda^2 h^2 - \lambda v h^3 - \frac{\lambda}{4} h^4. \tag{2.23}$$

As a result from the spontaneous symmetry breaking the $W^\pm$ and Z vector gauge bosons have gained a mass, while leaving the photon massless, and a new scalar boson h is included. Nevertheless the model has introduced several new parameters to the theory. For instance the vacuum expectation value of the Higgs field v, which is connected to the Fermi constant:

$$v^2 = \frac{1}{\sqrt{2} G_F} \simeq 246 \text{ GeV}^2. \tag{2.24}$$

Other parameters remain free, such as λ and the Higgs boson mass m_H.

Last, mass terms for leptons and fermions are added in this framework via Yukawa couplings, by adding the following local gauge invariant mass terms to the lagrangian:

$$\mathscr{L}_{Yukawa}^{leptons} = -G_l \left(\left(\bar{\nu}_l, \bar{l} \right)_L \begin{pmatrix} \phi_\alpha \\ \phi_\beta \end{pmatrix} l_R + \bar{l}_R \left(\bar{\phi}_\alpha, \bar{\phi}_\beta \right) \begin{pmatrix} \nu_l \\ l \end{pmatrix}_L \right), \tag{2.25}$$

$$\mathscr{L}_{Yukawa}^{quark} = -\lambda_d^{ij} \left(\bar{u}_i, \bar{d}'_j \right)_L \begin{pmatrix} \phi_\alpha \\ \phi_\beta \end{pmatrix} d_{jR} - \lambda_u^{ij} \left(\bar{u}_i, \bar{d}'_j \right)_L \begin{pmatrix} \bar{\phi}_{alpha} \\ \bar{\phi}_\beta \end{pmatrix} u_{jR} + h.c. \tag{2.26}$$

where $d'_i = V_{CKM} d_i$, are the eigenstates for the d, s, b quarks rotated by the Cabibbo-Kobayashi-Maskawa (CKM) matrix. After the spontaneous symmetry breaking the lagrangian is formulated as:

$$\mathscr{L}_{Yukawa}^{leptons} = -\lambda_l \left(\left(\bar{\nu}, \bar{l} \right)_L \begin{pmatrix} \phi_\alpha \\ \phi_\beta \end{pmatrix} l_R + h.c. \right), \tag{2.27}$$

$$\mathscr{L}_{Yukawa}^{quarks} = -m_d^i \bar{d}_i d_i \left(1 + \frac{h}{v} \right) - m_u^i \bar{u}_i u_i \left(1 + \frac{h}{v} \right). \tag{2.28}$$

Fermion masses are proportional to the Higgs coupling to leptons and quarks, and are a free parameter of the theory not predicted by the SM.

2.2 SM limitations

Despite its incredible success the Standard Model is not able to solve several observed anomalies in particle physics. Some of the hints from Nature for a more fundamental theory are presented in this section along with the most popular alternative models.

2.2.1 Beyond the standard model

The main argument in support of an incomplete SM is the hierarchy problem, which highlights the discrepancy between the weak and gravitational energy scale. The relatively small Higgs boson mass presents a hint of fine tuning in the model, not explaining why the model prevents huge high order corrections due to Higgs couplings to SM particles. First order corrections to the Higgs mass can be written as:

$$\delta m_H = -\frac{\lambda_f^2}{16\pi^2}\left[2\Lambda^2 + \mathscr{O}\left(m_f^2 ln\frac{\Lambda}{m_f}\right)\right], \tag{2.29}$$

where λ_f is the Yukawa coupling and Λ is the cut-off energy scale at which the model ceases to be valid. The mass correction is quadratically divergent in Λ, thus problematic if the SM is assumed to be valid up to the Plank scale. This divergence does not represent an issue in the model when the mass correction δm_H is of the same order of the mass itself, leading to a unnatural fine tuned cancellation of terms. The hierarchy problem would require new physics at a TeV scale, assuming a cut-off at $\Lambda \sim \mathscr{O}(1\text{TeV})$, or an extended theory to solve the divergence problem.

An additional irrefutable hint of new physics comes from the astrophysical evidence of Dark Matter (DM), inferred by gravitational means in several different scenarios. The DM is estimated to compose up to $\sim 25\%$ of the universe, however its composition and interactions with SM particles remains an unveiled mystery. These are just a few of the motivations for a search of new physics and the composition of a new complete theory of the universe.

2.2.2 Dark Matter genesis

The observed DM abundance in the early Universe can arise from different production mechanisms [14] depending on the DM coupling to the SM. In the case where the DM reached a thermal equilibrium with the SM, the production can be explained by a *freeze-out* mechanism where the particle density freezes when the interaction rate between DM and SM becomes smaller than the Hubble rate. However, if the DM was never in thermal equilibrium with the SM due to a small coupling the abundance can be explained by a *freeze-in* mechanism. In this alternative scenario the DM particle density freezes when the production rate becomes negligible due to Boltzmann suppression.

freeze-out

In the *freeze-out* mechanism, the DM decouples from the SM sector when its interactions cannot compensate anymore for the rapid expansion of the Universe. Thus the DM number density freezes to a constant value. This scenario requires a coupling of the same strength of the weak scale ($y \sim (0.1)$), for the majority of the models. The simplest case includes stable DM particles χ and considers only annihilation processes $\chi\ \chi \leftrightarrow SM$ to solve the abundance, neglecting possible asymmetries in the DM spectrum and large self-interactions.

Starting from the Boltzmann equation, used to determine the number density of a non-relativistic particle class, the relic density can be calculated as follow [15]:

$$\frac{dn}{dt} + 3H_0 n = -\langle \sigma v \rangle (n^2 - n_{eq}^2), \tag{2.30}$$

where n is the particle number density, H_0 is the Hubble constant measured by the Planck experiment to be $H_0 = 67.8 \pm 0.9$ kms^{-1}Mpc^{-1} [3], n_{eq} the particle density at the thermal equilibrium and $\langle \sigma v \rangle$ the thermal average of the annihilation rate.

The standard approximate solution to this equation in the freeze-out regime, yields the present DM relic density Ω_χ:

$$\Omega_\chi h^2 \sim \frac{3 \cdot 10^{-27} \text{ cm}^3\text{s}^{-1}}{\langle \sigma v \rangle}, \tag{2.31}$$

where the Hubble parameter is defined as $h = H_0/100$ kms^{-1}Mpc^{-1}.

The relic density is inversely proportional to the annihilation rate at the freeze-out time. When the annihilation rate becomes small enough the freeze out is reached and the number density remains constant. This dependence is shown in Figure 2.3. The

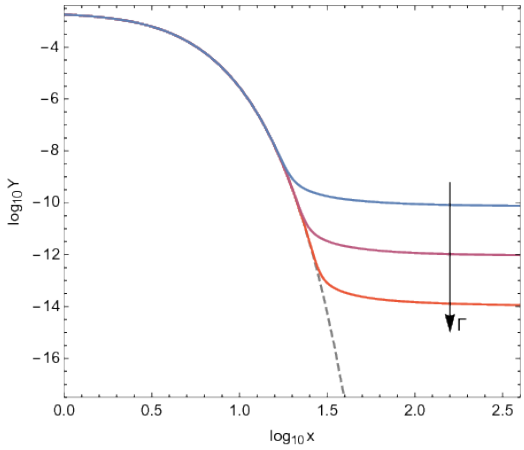

Figure 2.3. DM freeze-out production mechanism for three different values of the interaction rate between the SM and DM particles χ. The arrows indicate the effect of increasing the annihilation rate Γ and the gray dashed line shows the equilibrium density of DM particles.

freeze-out is the main mechanism for dark matter genesis in the Weakly Interactive Massive Particle (WIMP) models.

freeze-in

In the *freeze-in* mechanism, the DM never reached thermal equilibrium with the SM due to a very small coupling between these two sectors, of the order of $y \lesssim O(10^{-7})$, and interactions are not strong enough for the *freeze-out* to happen. In this case the DM particles number density in the early Universe slowly increases in $SM \rightarrow \chi\,\chi$ processes until it becomes Boltzmann-suppressed, $n_{SM} \propto exp(-m_{SM}/T)$. At this point the number density becomes constant and the DM abundance freezes in. Solving the Boltzmann equation with the *freeze-in* assumptions, the standard approximate solution for the simplest case yields the following DM relic density:

$$\Omega_\chi h^2 \sim \frac{1 \cdot 10^{24} n_\chi \langle \sigma v \rangle}{m_\chi}. \tag{2.32}$$

The increase of the interaction rate between the DM and SM implies a larger final DM abundance, an opposite effect to that of the *freeze-out* case. This is visible in Figure 2.4, where the particle density evolution with time is shown for different assumptions of interaction rate.

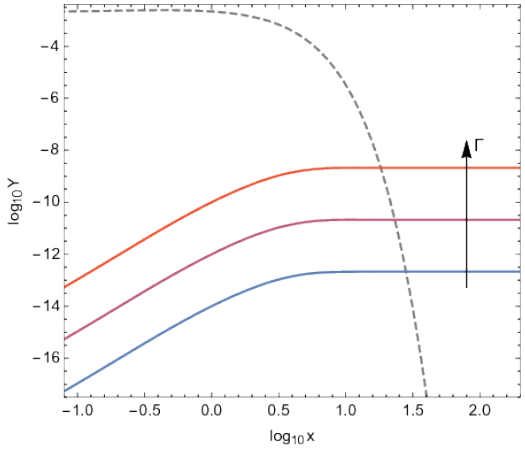

Figure 2.4. DM freeze-in production mechanism for three different values of the interaction rate between the SM and DM particles χ. The arrows indicate the effect of increasing the interaction rate Γ and the gray dashed line shows the equilibrium density of DM particles.

A schematic representation of the evolution of DM relic density as a function of the coupling between the DM and the SM that show the transition of the two mechanism is depicted in Figure 2.5. The *freeze-in* is the main dark matter genesis mechanism for the Feebly Interactive Massive Particles (FIMP) models, in opposition of the WIMP framework.

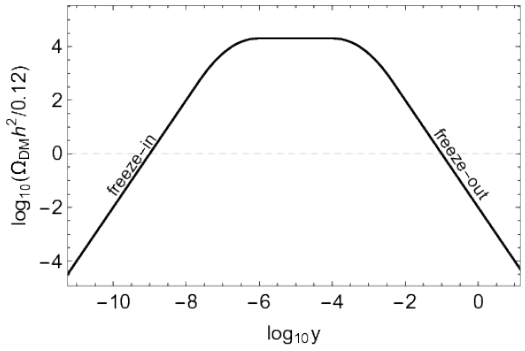

Figure 2.5. A schematic representation of the DM relic density as a function of the coupling between DM and the SM [14].

2.2.3 Weakly Interactive Massive Particles

The principal Dark Matter paradigm, commonly assumed in particle physics searches, is that of the WIMP. This paradigm assumes a DM composed of an elementary particle with small couplings to SM, of the same strength of weak interactions. Moreover, these are considered to move non-relativistically in order to be compatible with the *freeze-out* mechanism. WIMP particle searches are categorised by specific experimental signatures: direct, indirect, and collider searches. Direct detection experiments search for nuclear recoils due to WIMP-nuclei scattering in a large volume of active material. A WIMP flux of about $10^5 \mathrm{cm}^{-2}\mathrm{s}^{-1}$ is expected to flow through the Earth, as a consequence of the Earth movement inside the DM halo that permeates the galaxy, for a reference WIMP candidate with a mass of 100 GeV. The collision rate is thus very small and these processes are extremely rare. These experiments are usually placed in deep underground laboratories to suppress the cosmic-ray background, trying to reach a zero background search. Indirect detection experiments search for WIMP pair annihilations to SM particles, such as neutrinos and positrons, in the sky. In this scenario, gravitational induced accumulation of WIMP particles in heavy objects reach the necessary density for annihilation processes. Instead, collider experiments search for WIMP production in high-energy collisions. All possible dark matter detection channels are schematically shown in Figure 2.6.

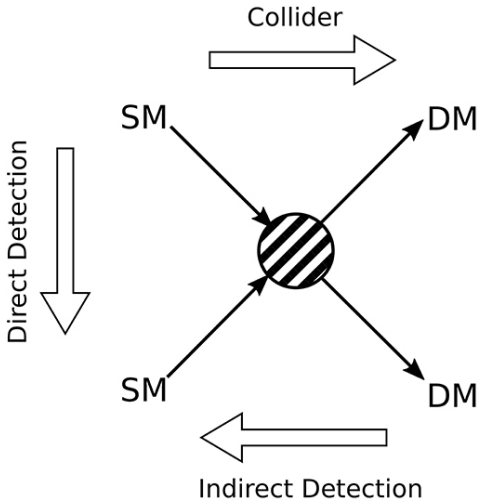

Figure 2.6. Schematic showing the possible dark matter detection channels.

These searches are complementary to one another, each probing different mass ranges and energy scales. The LHC program has put a great effort on WIMP searches, probing a wide spread of WIMP simplified model parameter space ranging from the electroweak scale up to many TeV. Instead, direct and indirect searches explore more minimal models which assume only the DM density and a WIMP-nucleon interaction. A summary of important results of the many direct searches experiment is shown in Figure 2.7, where the WIMP-nucleon cross section is plotted versus the WIMP mass for a spin independent interaction.

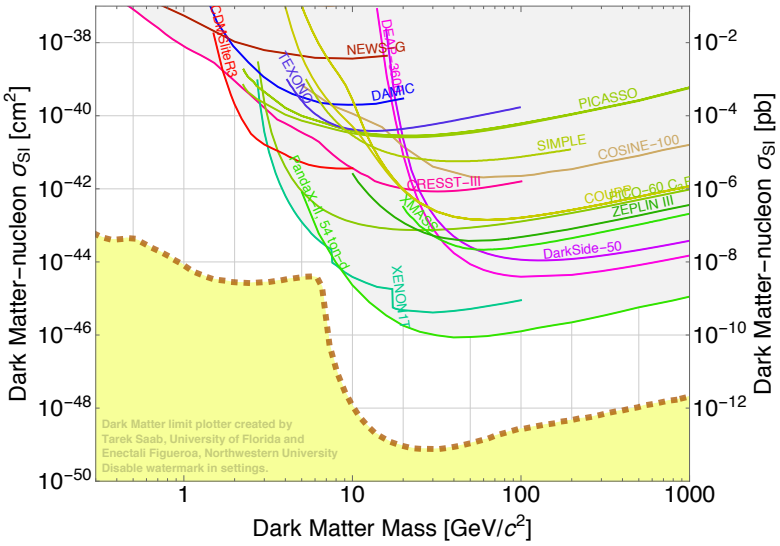

Figure 2.7. Spin-independent WIMP-nucleon scattering results.

The strongest limits on WIMP-nucleon interaction come from PANDAX-II [16] and XENON-1T [17] experiments, based on double-phase technology that allow to exploit both the ionization and scintillation information. These limits are in contradiction with the claimed WIMP observation from DAMA-LIBRA of an observed annual modulation of the event rate at 8.9σ [18]. Although a definitive WIMP discovery has yet to be made, these measurements have motivated an extended search of DM models outside the WIMP paradigm. LHC experimental efforts have been devoted to the energy frontier, exploring new particles masses above the EW scale with significant couplings. The intensity frontier is largely unexplored, where one could search for new particles below the EW scale not yet detected due to their small coupling with the SM particles. In this region, one of the most promising theories are the Dark Sector models, which assume a new hidden structure of forces and particles, of which DM could be composed, and feebly connected to the SM via portals. These models shift the searches from the detection of DM candidates to the portal itself, a necessary link between DM and SM. Portal searches are restricted by the SM symmetries and limited to: Higgs, vector, and neutrino portals. Vector and Higgs portals are especially relevant for LHC searches, providing a rich unconventional phenomenology inaccessible to direct and indirect experiments. These new weak long-range interactions may have easily gone undetected in experiments so far and a renovated effort is now ongoing towards hidden portal searches. The most popular portal models of interest for this thesis is introduced in the next chapter.

Chapter 3

Dark Sector models

This chapter will provide an overview of the Dark Sector models and their theoretical motivation, with a specific regard to the rich unconventional phenomenology relevant for the LHC searches. The model used in the dark-photon jet analysis will be discussed together with a broader class of vector and Higgs portal frameworks. Finally, the current theoretical and experimental constraints on dark photon models parameter space and the reach of this analysis will be described.

3.1 Motivations

So far the DM LHC programme has mainly focused on WIMP searches targeting SM objects recoiling against missing transverse energy. Limits have become more stringent and the quest more complicated, evolving to either trickier models or raising the cut-off energy. Therefore, a new complementary approach is needed to fully explore all possibilities, investigating a new model-independent perspective. The only basic assumption to be made is a DM interaction through some non-gravitational coupling with SM particles. In this scenario, the focus will shift from the unknown DM sector composition and its mass hierarchy to the new mediator itself. Dark portal models remove any assumption on the DM composition and thus provide a large model independence with a huge discovery potential. The minimal dark portal assumption introduces a new vector boson A', which is the best candidate for LHC searches. A window into a dark sector may also be found in Exotics Higgs decays, due to its extremely narrow width $\Gamma \sim 4$ MeV even the smallest coupling could lead to a sizeable decay cross-section. ATLAS latest constraints [19] on the SM Higgs branching fraction to BSM constrains it to be less than 20 %, thus favoring the search for Higgs boson exotic decay modes. Vector portal models offer a unique indirect probe of most DM formulations and can help explain the DM genesis. In thermal WIMP models, the dark photon can enhance the DM annihilation cross-section without affecting the relic abundance, allowing for WIMP particles to have delayed decays to the SM. These models are referred to as 'secluded DM' [20]. In non-thermal FIMP models [14], annihilation through a vector portal mediator with its very weak coupling can be the main process to contributing to the *freeze-in* mechanism. Due to the small production cross-section implied in these models, the vector portal offers one of the very few frameworks that can test frozen-in DM. The LHC experimental

programme is now drawing more and more attention to the rich phenomenology of non-standard Higgs decays and unconventional signatures.

3.2 Minimal model

The simplest Dark Sector framework extends the SM by adding a new hidden sector with an extra $U(1)'$ gauge group with a vector boson as mediator, hereafter called a dark photon (A', γ_{d}). SM particles are not charged under the new group and the only renormalizable interaction is through kinetic mixing with the SM photon, thus gaining a small effective charge. In addition, the new $U(1)'$ gauge group may be considered spontaneously broken by a dark Higgs mechanism, generating a mass. This would prevent a new long-range force appearing in the model. The dark Higgs boson can play a leading role also due to its possible coupling to the SM Higgs, resulting in a mixing between the two scalars. The interaction can therefore be through a vector portal, via the kinetic mixing coupling (ϵ), or through a Higgs portal, via Higgs mixing (κ). The dark photon mass ($m_{A'}$) may range from zero to heavier than the Z boson mass. It is convention to distinguish a light mass regime below 10 GeV and a high mass regime above 10 GeV, where the dark photon is also referred to as dark Z (Z_d).

3.2.1 Gauge sector

In this chapter a light massive dark photon is assumed by adding the following new gauge terms in the Lagrangian [21]:

$$\mathscr{L} = -\frac{1}{4}\hat{B}_{\mu\nu}\hat{B}^{\mu\nu} - \frac{1}{4}\hat{A}'_{\mu\nu}\hat{A}'^{\mu\nu} + \frac{1}{2}\frac{\epsilon}{cos\theta_W}\hat{A}'_{\mu\nu}\hat{B}^{\mu\nu} + \frac{1}{2}m^2_{A',0}A'^{\mu}\hat{A}'_{\mu}. \tag{3.1}$$

The new interaction is driven by the parameter ϵ which can assume any value. Considering this new gauge sector the fields can be redefined by diagonalising the kinetic mixing term as follow:

$$\begin{pmatrix} A' \\ B \end{pmatrix} = \begin{pmatrix} \sqrt{1-\frac{\epsilon^2}{cos^2\theta_W}} & 0 \\ -\frac{\epsilon}{cos\theta_W} & 1 \end{pmatrix} \begin{pmatrix} \hat{A}' \\ \hat{B} \end{pmatrix}. \tag{3.2}$$

When including all three neutral vectors, the full mass matrix can be written as follow:

$$\mathscr{M}^2_V = m^2_Z \begin{pmatrix} 0 & 0 & 0 \\ 0 & 1 & -\eta sin\theta_W \\ 0 & -\eta sin\theta_W & \eta^2 sin^2\theta_W + \delta^2 \end{pmatrix}, \tag{3.3}$$

where, in terms of θ_W and the Z mass before the mixing ($m_{Z,0}$):

$$\eta = \frac{\epsilon}{cos\theta_W\sqrt{1-\frac{\epsilon^2}{cos^2\theta_W}}}, \tag{3.4}$$

$$\delta = \frac{m^2_{A'}}{m^2_{Z,0}}. \tag{3.5}$$

Electromagnetism remains unbroken and the SM photon massless, however the Z and A' field mix with each other. The mass eigenstates are derived by diagonalising the sub-matrix, obtaining:

$$\begin{pmatrix} Z \\ A' \end{pmatrix} = \begin{pmatrix} cos\alpha & sin\alpha \\ -sin\alpha & cos\alpha \end{pmatrix} \begin{pmatrix} Z_0 & A'_0 \end{pmatrix}, \tag{3.6}$$

where the mixing angle α is defined as:

$$tan\alpha = \frac{1 - \eta^2 sin^2\theta_W - \delta^2 - Sign(1-\delta^2)\sqrt{4\eta^2 sin^2\theta_W + (1 - \eta^2 sin^2\theta_W - \delta^2)^2}}{2\eta sin\theta_W}. \tag{3.7}$$

For $\alpha \ll 1$ and $\epsilon \ll 1$, the masses are:

$$m^2_{A'} \simeq \delta^2 m^2_{Z,0}(1 - \epsilon^2 tan^2\theta_W) \tag{3.8}$$

$$m^2_Z \simeq m^2_{Z,0}(1 + \epsilon^2 tan^2\theta_W). \tag{3.9}$$

For small ϵ coupling, the dark photon interference with the SM Z boson is strongly suppressed and it will be produced almost entirely on-shell.

Under the assumption that no dark state particles exist below the dark photon mass, the dark photon exclusively decays to SM particles via kinetic mixing. In the mass range $m_{A'} \geq 2m_e \sim 1$MeV, the dark photon can decay to SM fermions with a dominant branching ratio to leptons. The partial decay width of the dark photon [22] to SM leptons is:

$$\Gamma_{A' \to \bar{l}l} = \frac{4}{3}\epsilon^2 \alpha m_{A'} \sqrt{1 - \frac{4m_l^2}{m^2_{A'}}} \left(1 + \frac{2m_l^2}{m^2_{A'}}\right). \tag{3.10}$$

For masses $m_{A'} > 2m_\pi$ hadronic decays are also to be considered, with a resulting partial decay width:

$$\Gamma_{A' \to hadrons} = \frac{4}{3}\epsilon^2 \alpha m_{A'} \sqrt{1 - \frac{4m_\mu^2}{m^2_{A'}}} \left(1 + \frac{2m_\mu^2}{m^2_{A'}}\right) R(s = m^2_{A'}), \tag{3.11}$$

where $R(s = m^2_{A'}) = \sigma_{e^+e^- \to hadrons}/\sigma_{e^+e^- \to \mu^+\mu^-}$.

Figure 3.1 shows the dark photon total decay width and branching fractions for $\epsilon = 10^{-2}$. The dark photon has a sizeable branching fraction to leptons except in the mass range of hadronic resonances.

Neutrino decays are neglected since they are heavily suppressed by a factor $\frac{m^4_{A'}}{m^4_Z} \sim 10^{-8}$.

The resulting dark photon proper lifetime τ, expressed in seconds, is related to both ϵ and mass. A good approximation of the relation [22] can be written as:

$$\tau \propto \left(\frac{10^{-4}}{\epsilon}\right)^2 \left(\frac{100 \text{ MeV}}{m_{\gamma_d}}\right). \tag{3.12}$$

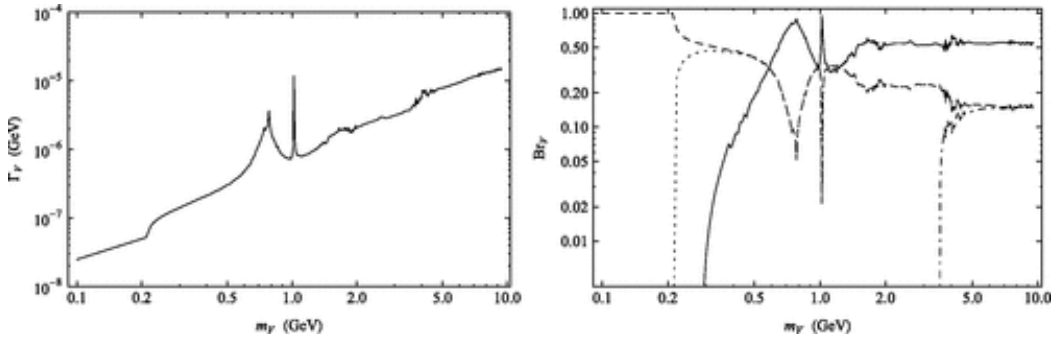

Figure 3.1. Dark photon total width (left) and branching fractions (right) for $A' \to e^+e^-$ (dashed), $A' \to \mu^+\mu^-$ (dotted), $A' \to \tau^+\tau^-$ (dot-dashed), and $A' \to hadrons$ (solid) [22]. The kinetic mixing is fixed at $\epsilon = 10^{-2}$.

3.2.2 Higgs sector

The extension of the SM Higgs potential to the dark Higgs field (S) can be written as:

$$V_0(H,S) = -\mu^2|H|^2 + \lambda|H|^4 - 2\mu_S^2|S|^2 + \lambda_S|S|^4 + \kappa|S|^2|H|^2, \tag{3.13}$$

where μ_S and λ_S are free parameters, and κ is the Higgs mixing parameter. After the electroweak symmetry breaking, the new dark Higgs singlet state acquires a vacuum expectation value v_S which generates the dark photon mass. The new Higgs mass matrix, obtained by expanding in small fluctuation h_0 and s_0 around the vacuum, is [21]:

$$\mathscr{M} = \begin{pmatrix} 2v^2\lambda & vv_S\kappa \\ vv_S\kappa & 2v_S^2\lambda_S \end{pmatrix}. \tag{3.14}$$

Thus the mass eigenstates are defined as:

$$\begin{pmatrix} h \\ s \end{pmatrix} = \begin{pmatrix} cos\theta_h & -sin\theta_h \\ sin\theta_h & cos\theta_h \end{pmatrix} \begin{pmatrix} h_0 \\ s_0 \end{pmatrix}, \tag{3.15}$$

where θ_h is defined as:

$$tan\theta_h = \frac{v^2\lambda - v_S^2\lambda_S - Sign(v^2\lambda - v_S^2\lambda_S)\sqrt{v^4\lambda^2 + v_S^4\lambda_S^2 + v^2v_S^2(\kappa^2 - 2\lambda\lambda_S)}}{vv_S\kappa}. \tag{3.16}$$

For small mixing angles θ_h, S is dominantly SM-singlet Higgs like and the masses are:

$$m_h^2 = 2\lambda v^2 + 2s_h^2(\lambda v^2 - \lambda_S v_S^2) + \mathscr{O}(\kappa^4) \tag{3.17}$$

$$m_s^2 = 2\lambda_S v_S^2 - 2s_h^2(\lambda v^2 - \lambda_S v_S^2) + \mathscr{O}(\kappa^4). \tag{3.18}$$

The mixing between H and S generates a non-zero coupling to dark photons, allowing for the process $h \to A'A'$ in the case of $m_h \geq 2m_{A'}$. The resulting decay width [22] is:

$$\Gamma_{h\to A'A'} = \frac{\alpha m_h^3}{8m_{A'}^2}\sqrt{1-\frac{4m_{A'}^2}{m_h^2}}\left(1-\frac{4m_{A'}^2}{m_h^2}+\frac{12m_{A'}^4}{m_h^4}\right). \tag{3.19}$$

The Higgs boson is also allowed to decay directly into dark scalars in a $h \to ss$ process. In this thesis we assume that s is heavy enough that this decay is kinetically forbidden.

3.3 Phenomenology and signatures

The wide range of phenomena observable at colliders that arise from a Dark Sector scenario such as the one described in the previous section can be classified depending on the mixing parameters regimes.

- Gauge mixing dominates ($\epsilon \gg \kappa$): dominant decay is $h \to ZZ_d \to ff + Z$, where f denotes a SM fermion.
- Higgs mixing dominates ($\kappa \gg \epsilon$): dominant decay is $h \to Z_dZ_d \to 4f$. If $m_S \leq \frac{m_h}{2}, m_{Zd} \leq \frac{m_S}{2}$, the decay $h \to ss \to 4Z_d$ is also relevant.
- intermediate regime ($\kappa \sim \epsilon$): all exotic Higgs decays are accessible.

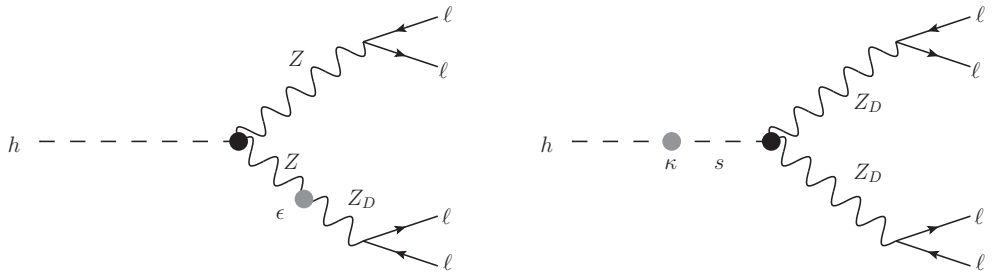

Figure 3.2. Diagrams for dark photon (Z_D) production via vector portal (left), and via Higgs portal (right). [21].

These production modes, shown in Figure 3.2, can be the building blocks of a more complex scenario like hidden valley models [23], where the Higgs boson decays directly into dark sector particles. In this scenario, if the dark photon cannot decay into the lightest stable hidden particle, it will decay to SM particles via kinetic mixing. Such processes can lead to a high dark photon multiplicity together with missing transverse energy coming from the non-interacting dark sector particles. Moreover, a high coupling can lead to a strong emission of dark photons from dark state particles [24] generating multiple A' along the same flight direction. An example of a hidden valley process $h \to DarkStates \to nA' + X$, where n is a natural number, is depicted in Figure 3.3.

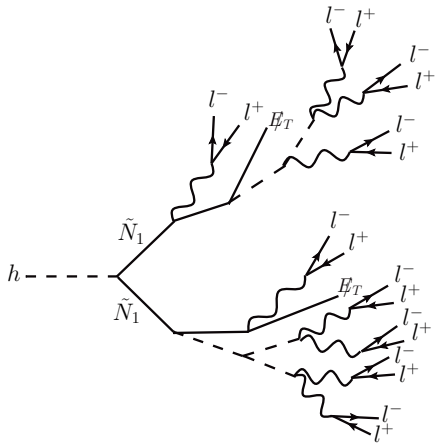

Figure 3.3. An example of a hidden valley decay chain. The hidden sector cascades can lead to many leptons per Higgs decay [25].

If only the vector portal is assumed, without a Higgs portal, the dominant discovery process would be Drell-Yan production. This channel can be probed in dilepton searches looking for bumps in the $e^+e^-/\mu^+\mu-$ spectrum, although not competitive due to the suppression given by the needed double mixing ϵ^2, one for production and one for decay. This thesis will focus on scenarios where the Higgs portal is present to exploit the huge boost in sensitivity from exotic Higgs decays.

ATLAS dark photon searches are divided in many different analyses depending on the mass range and lifetime. In case of light dark photons, final-state decay products are highly boosted and thus very collimated. In this kinematic regime, the ATLAS reconstruction system is not able to resolve the decay products which will be considered collectively as a single object, referred to as dark-photon jet or lepton-jet. Instead in the heavy dark photon regime, the decay products are considered to be non-collimated and with enough separation to be reconstructed as single objects by ATLAS. The dark photon lifetime also plays a crucial role in final state signatures, since direct decays inside each sub-detectors will generate a unique mark. If the lifetime is long enough it may also be considered as collider-stable giving rise to missing transverse energy signatures.

3.4 Current bounds

Dark photon results are usually mapped into a two dimensional plane ϵ versus $m_{A'}$, assuming only a vector portal. Constraints have been set by several experiments covering wide regions of parameter space from the sub-GeV to the multi-TeV mass range. A summary of the most recent constraints [26] on A' searches are shown in Figure 3.4.

The high-ϵ range down to $\sim 10^{-3}$ is dominated by B-factories in the high-mass region and by muon magnetic moment measurements in the low-mass region. In this region the most stringent limits are set by: the LHCb collaboration in inclusive

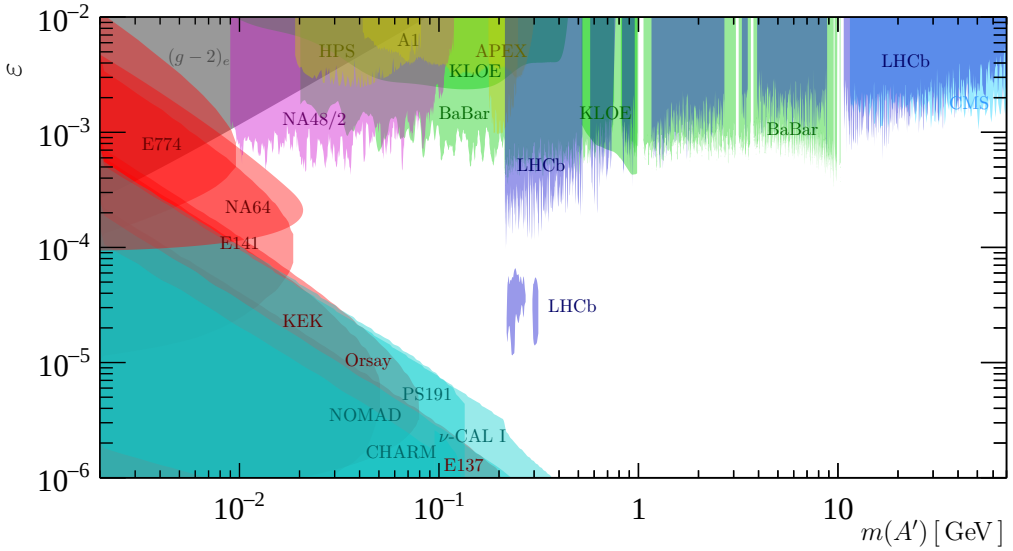

Figure 3.4. Constraints on visible A' decays [26] in the parameter space ϵ versus $m_{A'}$ for: electron beam dump (red), proton beam dump (cyan), e^+e^- colliders (green), pp collisions (blue), meson deacys (magenta), electron on fixed target experiments (yellow), and muon magnetic moment (grey).

di-muon production from pp collisions [27], the BaBar collaboration in electron and muon final states from e^+e^- annihilation [28], and the NA48/2 experiment in the $\pi^0 \to A'\gamma$ process [29] in meson decays. Instead the low-mass and low-ϵ region down to $\sim 10^{-7}$ is excluded by fixed-target and beam-dump experiments. The most tight limits are set by the E141, E137, E774, KEK and Orsay electron beam dump experiments [30–34], and ν-CAL I, CHARM proton beam-dump experiments [35–37].

The whole intermediate region with a dark photon mass between 100 MeV and 90 GeV for ϵ smaller than 10^{-3} has not yet been excluded and is soon to be probed by high energy collider experiments. The displaced dark-photon jet analysis will target this specific region of phase space.

3.5 FRVZ benchmark model

The displaced dark-photon jet search is designed to have a model-independent approach, aiming to exploit only the experimental features of the dark-photon jet signature. The analysis will then produce all the necessary acceptance and efficiency tables for the main kinematic variables necessary to interpret the results in specific models. For example, the DPJ definition has to be broad enough to select a wide variety of dark photon scenario. A single DPJ must be able to include high multiplicity of close-by dark photons and consider a different variety of shapes. The number of radiated dark photons [23] is proportional to the size of the dark gauge coupling α_d [38].

To define and optimise the analysis cuts, the Falkowsky-Ruderman-Volansky-Zupan [25, 39] (FRVZ) benchmark model is considered. FRVZ is a hidden valley

model that is able to reproduce the key aspects of the DPJ signature and most importantly is representative of a broad class of models. It features a Higgs boson decaying to a pair of dark fermions f_{d_2} which can produce either two or four dark photons. In the first case, shown in Figure 3.5 (left), each f_{d_2} decays into a lighter dark fermion f_{d_1} assumed to be the hidden lightest stable particle (HLSP) and a dark photon. In the second case, shown in Figure 3.5 (right), each f_{d_2} decays into a f_{d_1} particle and a dark scalar s_{d} which decays into a pair of dark photons. Possible radiation of dark photon is neglected in this model, which corresponds to an assumed dark coupling $\alpha_{\mathrm{d}} \lesssim 0.01$.

The Higgs boson may be assumed to be SM-like with a mass $m_H = 125$ GeV or a heavier BSM scalar. Finally, only the gluon-gluon fusion (ggF) is assumed as a production process.

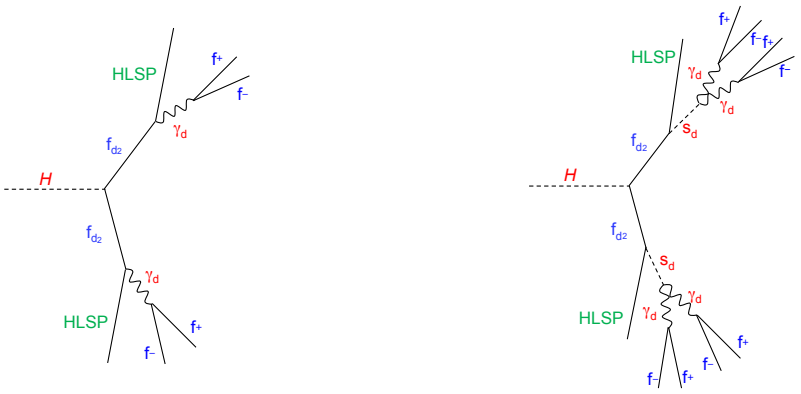

Figure 3.5. The two processes of the FRVZ model used as benchmarks in the analysis. The first process (left), present two dark fermion f_{d_2} decays into a γ_{d} and an HLSP. The second process (right), present two dark fermion f_{d_2} decays into an HLSP and a dark scalar s_{d} , that in turn decays into a pair of dark photons. The γ_{d} decays into SM fermions, denoted by f^+ and f^-.

The model presents a great flexibility in reproducing many different kinematic scenarios controlling the dark sector mass spectrum and the couplings. The HLSP mass determines the amount of missing transverse momentum in the final state, and in the limit of a negligible mass the baseline $h \to \gamma_{\mathrm{d}}\gamma_{\mathrm{d}}$ process is reproduced. The f_{d_2} and f_{d_1} masses determine the boost and the opening angle of the dark photon in the final state. Usually, these are chosen to be light relative to the Higgs boson mass, and far from the kinematic threshold at $m_{f_{\mathrm{d}_1}} + m_{\gamma_{\mathrm{d}}} = m_{f_{\mathrm{d}_2}}$. The Higgs mixing parameter κ controls the Higgs branching fraction into the dark sector. Instead the kinetic mixing parameter ϵ determines the lifetime of the dark photon.

Chapter 4

LHC and the ATLAS detector

In this chapter the Large Hadron Collider (LHC) [1], the world's largest and most powerful particle accelerator, is introduced and the ATLAS detector's structure and functionalities are described.

4.1 The Large Hadron Collider

The LHC hadron accelerator was built by the (Conseil Européen pour la Recherche Nucléaire) between 1998 and 2008. It replaced the Large Electron-Positron collider inside the 27 km long tunnel situated 100 m underground on the border between Switzerland and France.

The LHC is a circular proton-proton accelerator able to operate at an unprecedented center-of-mass energy of 14 TeV and an instantaneous luminosity of the order of 10^{34} cm^{-2} s^{-1}. At the time of writing the LHC has been in maintenance shutdown since Nov 2018, after having operated for a three year period at 7 TeV in 2010–2011 and at 8 TeV in 2012, called Run-1, and for a four year period at 13 TeV in 2015–2018, called Run-2.

4.1.1 CERN accelerator complex

The CERN laboratory hosts a complex of several accelerators. There the proton beams are created and accelerated by a sequence of sub-accelerators to the final center-of-mass energy and finally collided at different interaction points of the main accelerator, the LHC. A schematic of the CERN accelerator complex [40] is shown in Figure 4.1.

Protons are first created from a source of ionized hydrogen atoms and then injected into the first linear accelerator (LINAC2), where they are accelerated up to an energy of 50 MeV before passing through a sequence of circular accelerators. The beam accelerates subsequently through the first circular accelerator, the Proton Synchroton Booster (PSB), reaching an energy of 1.4 GeV, the Proton Synchrotron (PS), arriving at an energy of 25 GeV, and finally the Super Proton Synchrotorn (SPS), reaching the target energy of 450 GeV. The last acceleration step happens in the LHC where the proton beam reaches the nominal energy.

The ring hosts two separate parallel beams running in opposite directions, which are diverted at the collision point by quadrupole magnets.

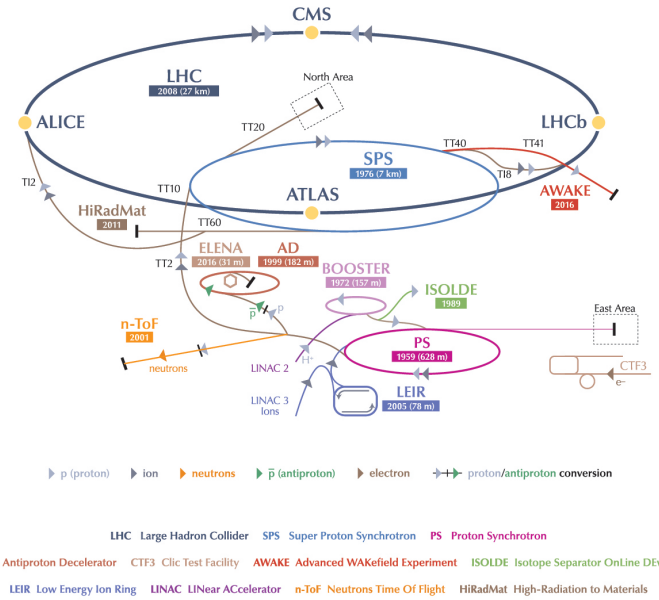

Figure 4.1. Scheme of the CERN accelerator complex, from the first linear accelerator to the LHC and a subset of the many experiments supported by these accelerators [41].

The collision points host four experiments: ATLAS [2] (A Toroidal LHC ApparatuS) and CMS [42] (Compact Muon Solenoid), two multi-purpose experiment, ALICE [43] (A Large Ion Colliding Experiment), designed to study heavy nuclei interactions, and LHCb [44], focused on the study of b-physics.

4.1.2 Run-2 LHC performance

The proton beams enter the LHC divided in bunches at a frequency of 40 MHz, hence separated in time by 25 ns. The bunch fill pattern is designed to maximise the rate of the collisions for a total of 2556 proton filled bunches in Run-2, out of a maximum allowed of 2808. The number of collisions that can be produced in a particle collider per cm^2 and per second is defined by the instantaneous luminosity, computed as

$$L = \frac{N_{\mathrm{b}}^2 n_{\mathrm{b}} f_{\mathrm{rev}} \gamma}{4\pi\sigma_x\sigma_y} F. \tag{4.1}$$

The instantaneous luminosity depends only on the machine characteristics and not on specific physics processes, thus it is a useful parameter when comparing the performance of different accelerator machines. It is proportional to the bunch revolution frequency f_{rev}, the Lorentz boost factor γ and the number of colliding

particles contained in each bunch, N_b, times the number of bunches, n_b. It is inversely proportional to the root mean square of the beam width in the x and y directions, σ_x and σ_y. Finally the instantaneous luminosity is corrected by a geometrical factor F which takes into account the crossing angle with which the beams are made to collide. The total luminosity delivered over a time period is called integrated luminosity, and is computed as

$$L_\mathrm{int} = \int L dt. \tag{4.2}$$

This is used to quantify the amount of data delivered by the LHC and recorded by the experiment. In Figure 4.2 the integrated luminosity recorded by the ATLAS experiment during Run-2 is shown. In 2015–2018 data taking the LHC delivered 156 fb^{-1} of pp collisions of which ATLAS recorded 147 fb^{-1}. This analysis makes use of 36.1 fb^{-1} of data collected between 2015 and 2016.

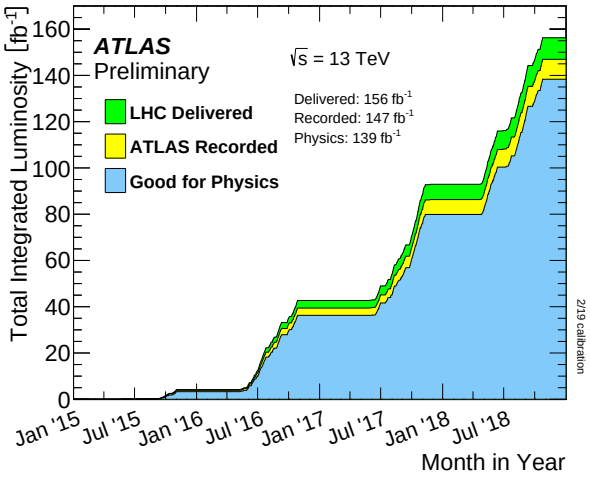

Figure 4.2. Cumulative luminosity versus time delivered to ATLAS (green), recorded by ATLAS (yellow) and certified to be good quality data (blue) during stable beams for pp collisions at 13 TeV centre-of-mass energy in LHC Run 2 [45].

A high luminosity environment can be extremely challenging for the detector and the trigger systems, having to cope with an extremely high particle multiplicity in the collisions. This is the case for the in-time pile-up effect, when multiple collisions occur during the same bunch crossing, and for the out-of-time pile-up, when the system reads out for a time span longer than the time between two bunch crossings. A parameter used to describe this effect is the average number of interactions per bunch crossings, $\langle\mu\rangle$, computed as follows

$$\langle\mu\rangle = \frac{L \cdot \sigma_\mathrm{inelastic}}{n_b \cdot f_\mathrm{rev}}. \tag{4.3}$$

The luminosity-weighted distribution of the mean number of interactions per bunch crossing for the Run-2 data taking is presented in Figure 4.3. The mean $\langle\mu\rangle$ was found to be 13.4 for the 2015 data taking and 25.1 for 2016 data taking.

A summary of LHC machine performance during Run-2 is presented in Figure 4.4.

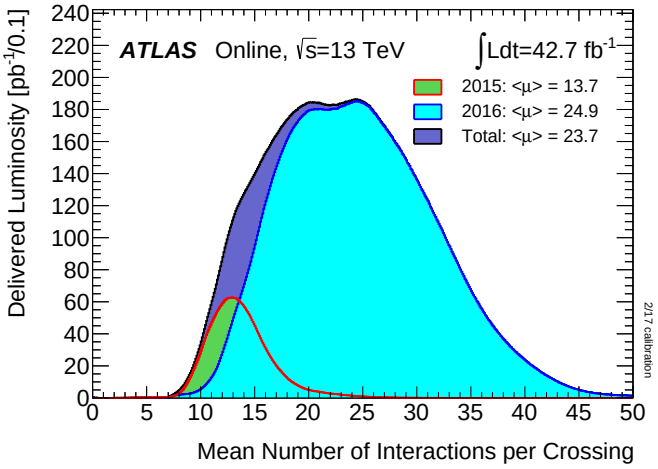

Figure 4.3. Shown is the luminosity-weighted distribution of the mean number of interactions per crossing for the 2015-2016 Run-2 *pp* collision data at 13 TeV centre-of-mass energy [45].

Parameter	2015	2016	2017	2018
Maximum number of colliding bunch pairs (n_b)	2232	2208	2544/1909	2544
Bunch spacing (ns)	25	25	25/8b4e	25
Typical bunch population (10^{11} protons)	1.1	1.1	1.1/1.2	1.1
β^* (m)	0.8	0.4	0.3	0.3–0.25
Peak luminosity $\mathcal{L}_{\text{peak}}$ ($10^{33}\,\text{cm}^{-2}\text{s}^{-1}$)	5	13	16	19
Peak number of inelastic interactions/crossing ($\langle\mu\rangle$)	~ 16	~ 41	$\sim 45/60$	~ 55
Luminosity-weighted mean inelastic interactions/crossing	13	25	38	36
Total delivered integrated luminosity (fb^{-1})	4.0	38.5	50.2	63.4

Figure 4.4. Selected LHC parameters for pp collisions at $\sqrt{s} = 13$ TeV in 2015–2018. The values shown are representative of the best accelerator performance during normal physics operation [46]. The value of the beta function [47], which describes the transverse size of the particle beam along the nominal beam trajectory, at the interaction point is referred to as β^*.

4.2 ATLAS detector

The ATLAS experiment is a general purpose detector designed to study LHC *pp* interactions at $\sqrt{s} = 14$ TeV. ATLAS extends for 44 m in length with a diameter of 25 m for a total mass of 7000 tons. A schematic picture of the detector is shown in Figure 4.5. It is structured in three concentric cylindrical sub-detectors which surround the *pp* interaction point. The innermost part is the inner detector (ID) followed by the calorimeter and the Muon Spectrometer (MS).

The ID is capable of tracking with high precision all charged particles produced in collisions and reconstructs the vertices of interaction. The calorimeter system comprises an electromagnetic sub-system (ECAL), designed for the identification of electromagnetic showers, and an hadronic sub-system (HCAL), designed to perform an accurate energy measurement of jets and missing transverse momentum. Finally, the MS is dedicated to the identification and high precision measurement of muons and their momentum. These detectors are usually separated into barrel and end-cap

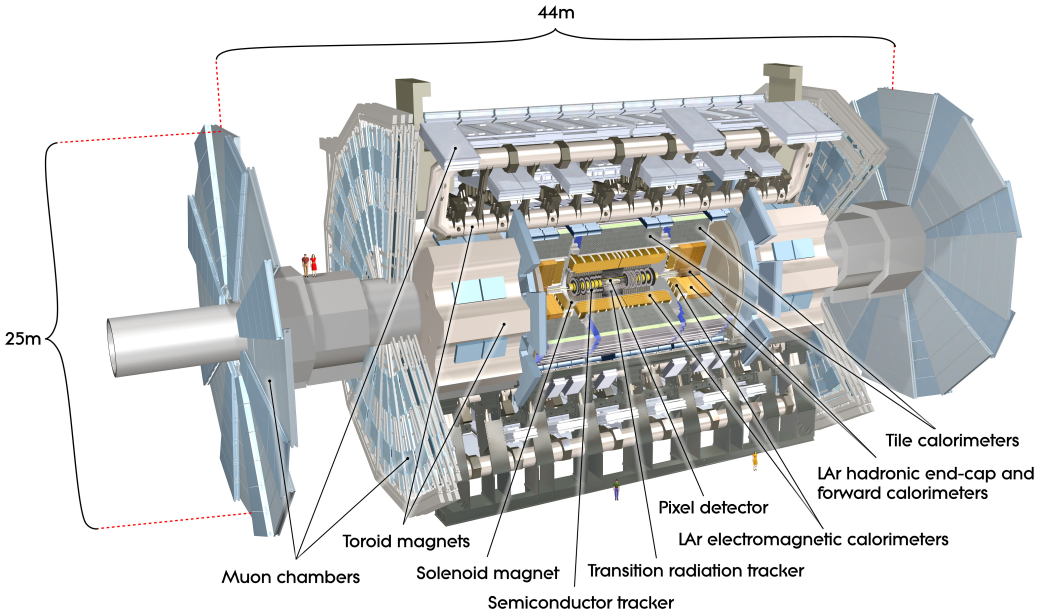

Figure 4.5. The four major components of the ATLAS detector are the Inner Detector, the Calorimeter, the Muon Spectrometer and the Magnet System [2].

regions, and present a nearly 4π steradians coverage in solid angle.

4.2.1 Coordinate system

The interaction point identifies the origin of the ATLAS reference system defined by a z-axis, oriented along the direction of the beams, and the perpendicular $x - y$ plane, where the positive x-semi-axis points towards the center of the ring and the positive y-semi-axis points upwards. A reference in cylindrical coordinates, as shown in Figure 4.6, is also considered, defined by the azimuthal angle ϕ, measured around the beam, and the polar angle θ, measured with respect to the beam axis. The radial distance measured from the origin in the $x - y$ plane is denoted as R, and the longitudinal as z.

Useful kinematic variables can then be defined in this coordinate system to be invariant for Lorentz boost along the longitudinal axis, as in hadron colliders the momentum along the z-axis of the initial system is unknown. An example is the rapidity, which is defined as

$$y = \frac{1}{2} \log \frac{E + p_z}{E - p_z}, \tag{4.4}$$

where E is the energy of the particle and p_z is the momentum along the z-axis. In the limit where the particle is travelling close to the speed of light, or equivalently in the approximation that the mass of the particle is negligible, the pseudorapidity can be used, defined as

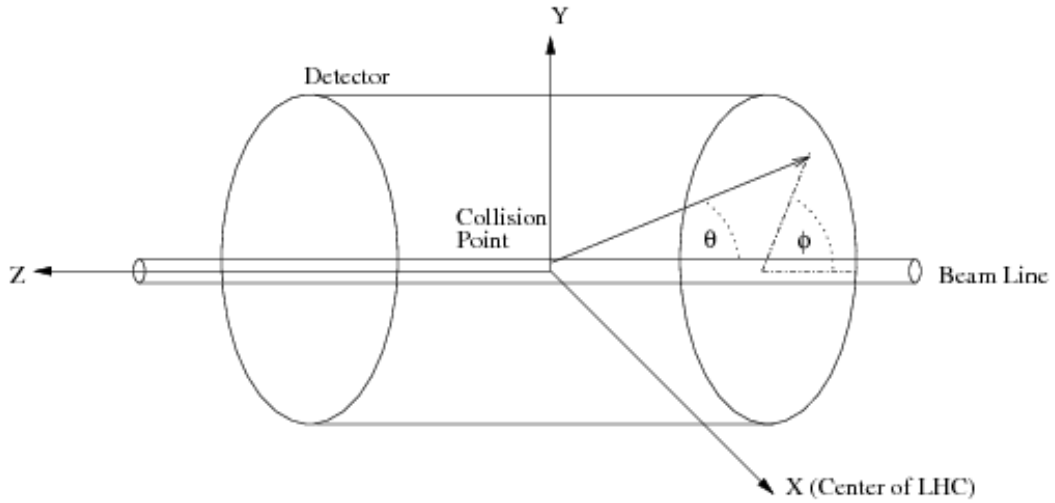

Figure 4.6. Illustration of ATLAS coordinate system.

$$\eta = -\log \tan \frac{\theta}{2}. \tag{4.5}$$

The distance between objects can thus be defined in the $\eta - \phi$ space, and denoted as $\Delta R = \sqrt{\Delta\eta^2 + \Delta\phi^2}$.

4.2.2 Magnet

The ATLAS detector contains the world's largest superconducting magnet system [48], a crucial item for the momentum measurement of charged particles produced in the interactions. Following the Lorentz force, the momentum of a charged particle entering perpendicularly a magnetic field can be measured by the radius of curvature. An intense magnetic field is thus necessary to measure high-p_{T} particles. The system, shown schematically in Figure 4.7, is composed of the following superconducting magnets:

- Central Solenoid: provides a 2 T axial magnetic field for the inner tracker;
- Barrel Toroid: air-core system that provides a 0.5 T magnetic field in the barrel region of the muon spectrometer. The field integral is $2 - 6$ T $\cdot$ m.
- End-cap Toroid: air-core system that provides a 1.0 T magnetic field in the end-cap region of the muon spectrometer. The field integral is $4 - 8$ T $\cdot$ m.

The ATLAS air-core toroid system was designed to reduce to a minimum all possible particle interactions with the system material along the flight-path, allowing a precise measurement of the track.

4.2.3 Tracking system

The inner detector [49] (ID), as shown in Figure 4.8, is the closest system to the beam pipe and is responsible for the reconstruction of charged particle tracks and

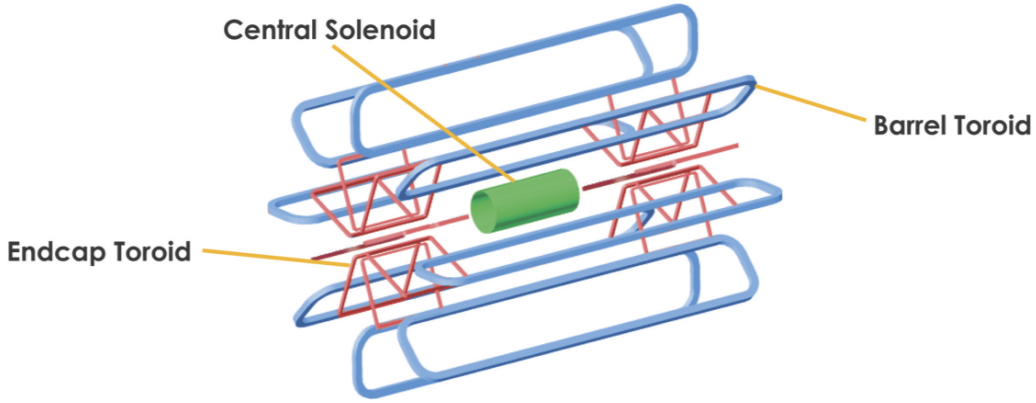

Figure 4.7. Schematic view of the ATLAS magnet system: central solenoid, 8 barrel toroid coils and 2×8 coils of the end-cap toroids [48].

their production vertex. It extends from 33 mm to 1082 mm in radius and covers the pseudorapidity region of $|\eta| \leq 2.5$. It is composed of three different sub-systems: the pixel detector (PD), the semiconductor tracker (SCT), and the transition radiation tracker (TRT). These sub-systems have to cope with a very large track occupancy and therefore are designed with a very fine granularity in order to be able to make high precision measurements.

Pixel detector

The silicon pixel detector [50, 51] is composed of three layers in the barrel region situated at radial distances of 50.5, 88.5 and 122.5 mm, and three layers in the end-cap region situated at longitudinal distances of 49.5, 58.0 and 65.0 mm. A silicon pixel of dimension 400×50 μm^2 presents a resolution of 10 μm in the $R - \phi$ direction and of 115 μm in the z direction. The whole systems contains 1744 sensors with 46080 read-out pixels each, for a total of 80 millions read-out channels.

During the 2013–2015 shut-down the pixel detector was extended with a fourth layer, the Instertable B-Layer (IBL), installed at a radius of 33.3 mm. The IBL improved significantly the ID performance recorded in Run-1, enhancing the good vertex reconstruction and secondary vertex identification. These features significantly improved the capability of identifying jets coming from b-quarks. Moreover, it ensured a full ϕ coverage for high-p_{T} tracks.

Semiconductor tracking

The SCT [52] is designed to provide in the intermediate radial range of the ID a high precision measurement of the impact parameter and transverse momentum. It is composed of four layers of silicon microstrip modules, placed axially with respect to the beam pipe at radial distances of 300, 373, 447 and 520 mm. Each SCT module contains 768 readout strips of 80 μm pitch, arranged in two layers in a stereo configuration, for a total dimension of 6.36×6.40 cm^2. The stereo configuration provides a precision measurement in the principal coordinate $R - \phi$ of 17 μm, and in the second coordinate z of 580 μm. The two end-caps have the same configuration and are composed of nine disks placed in the forward region $1.4 \leq |\eta| \leq 2.5$ up to

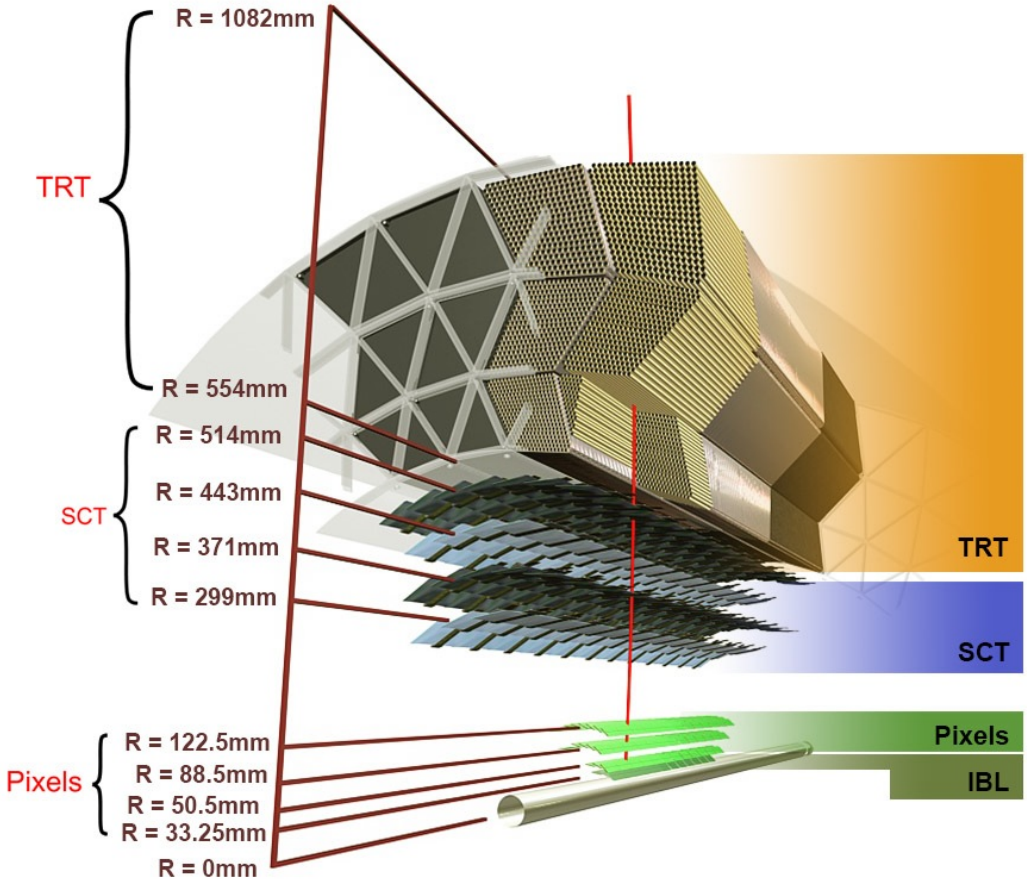

Figure 4.8. Sketch of the ATLAS inner detector showing all its components, including the new insertable B-layer (IBL). The distances to the interaction point are also shown [49].

radii of 560 mm. The entire system is mapped to more than 6 million read-out channels.

Transition radiation tracker

The external part of the ID is the transition radiation tracker, crucial for track reconstruction and particle identification. It is composed of 4 mm diameter tubes, arranged in 36 layers, filled with a gaseous mixture of 70% Xe, 27% CO_2 and 3% O. The ionization signal from a charged particle passing through the straw is collected by a gold-plated 30 μm tungsten wire, placed at the center. The Xe gas mixture is crucial for the particle identification capabilities of this sub-detector based on transition radiation photon detection. A significant discrimination power is achieved between electrons and charged pions with energy in the range 1 GeV $\leq E \leq$ 100 GeV. The TRT radial extension goes from 56 to 107 cm, providing a measurement only in the $R-\phi$ ($z-\phi$ in the end-cap) coordinate with a resolution of 130μm.

The overall ID system resolution for charged particles' momentum is

$$\frac{\sigma_{p_T}}{p_T} = 0.05\% p_T[\text{GeV}] \oplus 1\%. \tag{4.6}$$

4.2.4 Calorimeters

The ATLAS calorimeter system is used to measure the energy of photons, electrons, hadrons and the missing transverse momentum. It is composed of two sub-systems of sampling calorimeters: the internal Electromagnetic calorimeter (ECAL) and the external Hadronic Calorimeter (HCAL). The sampling calorimeter technique alternates active material layers, where the energy is read out, with passive material layers with high interaction cross-section, used as an absorber. The ECAL high granularity is well suited for photon and electron reconstruction, and has a total depth of 22 radiation lengths in the barrel and 24 in the end-caps. The HCAL is designed to contain almost completely hadronic showers in its 9.7 interaction lengths in the barrel and 10 in end-caps.

ECAL

For the ECAL [53] calorimeter, lead is used as the passive material and Liquid Argon (LAr) as the active material. This choice of materials has shown a great radiation hardness, preserving high performance for the whole data taking. The material layers are folded in an accordion geometry, as shown in Figure 4.9, to maximise particle interactions with the different layers and to avoid the presence of possible dead zones. To provide a high granularity, the ECAL is segmented into three longitudinal sections and an additional pre-shower (pre-sampler) section with narrow cells. The ECAL barrel starts at a radius of 1.41 m and ends at 1.96 m with a z extension of ± 3.21 m, covering the $|\eta| \leq 1.475$ interval. In the $1.37 \leq |\eta| \leq 3.2$ region, the ECAL endacap starts at $z \pm 3.70$ m and ends at $z \pm 4.25$ m. In the region $|\eta| < 1.8$ an additional calorimeter finely segmented layer of LAr and lead is located in the innermost position close to the beam-pipe. The transition region between barrel and end-cap, in the pseudorapidity range $1.375 \leq |\eta| \leq 1.52$, contains a large amount of inactive material providing necessary services to the ID. Significant energy loss is recorded in this region, resulting in a low precision measurement, which is often removed in analyses selection.

The whole system is placed inside three independent cryostats to maintain the very low temperature of 89 K, needed for correct functioning.

The energy resolution of the ECAL is

$$\frac{\Delta E}{E} = \frac{10\%}{\sqrt{E}} \oplus 0.7\%, \tag{4.7}$$

where E is expressed in GeV.

HCAL

The HCAL is designed to measure the energy deposits and direction of hadronic showers produced by strongly interacting particles. Hadronic showers are the result of hadronic interactions which produce secondary hadrons with energy in the GeV to MeV scale. The system provides significant containment of hadronic showers to

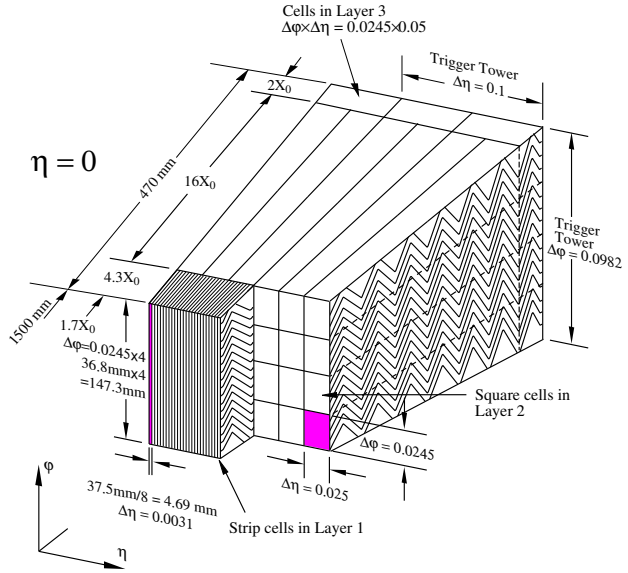

Figure 4.9. Sketch of a ECAL barrel module where the different layers are clearly visible. The granularity in eta and phi of the cells of each of the three layers is shown.

prevent leakage to the muon spectrometer and guarantees a good missing transverse momentum measurement. The HCAL barrels surround the ECAL starting at a radius of 2.28 m and end at 4.25 m with a z extension of ± 4.10 m, covering the $|\eta| \leq 1.0$ interval. In the endcap regions $|\eta| \leq 4.9$, the HCAL starts at $z \pm 4.3$ m and ends at $z \pm 6.05$ m. Different sampling techniques are chosen depending on the high radiation environment.

Tile Cal

The hadronic tile calorimeter [54] is located in the barrel covering the region $|\eta| \leq 1.0$, and in two extension regions $0.8 \leq |\eta| \leq 1.7$. Steel is used as passive material and scintillating tiles as active materials, which produce a signal proportional to the number of secondary particles produced in the interaction. The detector yields an energy resolution of:

$$\frac{\Delta E}{E} = \frac{50\%}{\sqrt{E}} \oplus 3\%. \tag{4.8}$$

Hadronic end-cap calorimeter

The Hadronic End-Cap Calorimeter [55] (HEC) is composed of two independent wheels of radius 2.03 m and covers the range $1.5 \leq |\eta| \leq 3.2$. It uses LAr as active medium and copper plates as absorbers, as the amount of radiation in the end-caps is greater than in the barrel. The HEC has an energy resolution of:

$$\frac{\Delta E}{E} = \frac{50\%}{\sqrt{E}} \oplus 3\%. \tag{4.9}$$

Forward hadronic calorimeter
The Forward Calorimeter (FCAL) is placed in the high-eta region very close to the beam pipe where the particle density is extremely high, covering the region $3.1 \leq |\eta| \leq 4.9$. It is composed of three layers using LAr as active material and copper, for the innermost layer, and tungsten, for the external layers, as abosrbers. FCAL has a resolution of:

$$\frac{\Delta E}{E} = \frac{100\%}{\sqrt{E}} \oplus 10\%. \tag{4.10}$$

4.2.5 Muon spectrometer

The muon spectrometer [56] (MS) is located in the outermost part of the ATLAS detector and is designed to track muon particles that escape the HCAL. Muons pass through the calorimeter materials losing a small fraction of their energy, of some MeV/mm. The MS is composed of very fast momentum measurement chambers and high precision tracking chambers immersed in a toroidal magnetic field, which allow an independent muon transverse momentum measurement. In the barrel region, $|\eta| \leq 1.05$, three cylindrical layers are situated around the beam axis at radial distances of ∼5 m (barrel inner, BI), ∼7.5 m (barrel middle, BM) and ∼10 m (barrel outer, BO). In the two end-cap regions, $1.05 \leq |\eta| \leq 2.7$, three muon wheels are placed perpendicular to the z-axis at longitudinal distances from the IP of 7.5 m, 13 m and 22 m. The layout of the stations and muon chambers are presented in Figures 4.10 and 4.11.

The overall momentum resolution for low-p_{T} muons is $\sigma(p_{\mathrm{T}})/p_{\mathrm{T}} \sim 2-3\%$, while for high-$p_{\mathrm{T}}$ is $\sigma(p_{\mathrm{T}})/p_{\mathrm{T}} \sim 10\%$.

MS trigger chambers
The barrel region muon trigger system relies on Resistive Plate Chambers (RPC). The RPC is a gaseous detector consisting of two bakelite plates separated by a 2 mm gap filled with a gas mixture of 97% tetrafluoroethane ($C_2H_2F_4$) and 3% isobutane (C_4H_{10}). A high electric field of 4.5 kV/mm is maintained between the two plates to amplify the primary ionization of charged particles crossing the detector. The charged induced on metallic strips in the outer sides of the bakelite plates is collected as signal. Two RPC units are placed in each layer orthogonal to one another, providing information on both η and ϕ coordinates. Two layers are installed in the middle station, for the low-p_{T} trigger, and a third layer is installed in the outer station, for the high-p_{T} trigger.

In the end-cap region, muons are triggered by very thin multi-wire chambers (TGC). TGCs are designed to have the anode-cathode spacing smaller than the anode-anode spacing for a very short drift time of 20 ns. The chambers are filled with a highly quenching gas mixture of 55% CO_2 and 45% n-pentane ($n-C_5H_{12}$) operating in saturation mode.

Both RPC and TGC are also used to improve the measurement along the second coordinate in the non-bending plane ϕ.

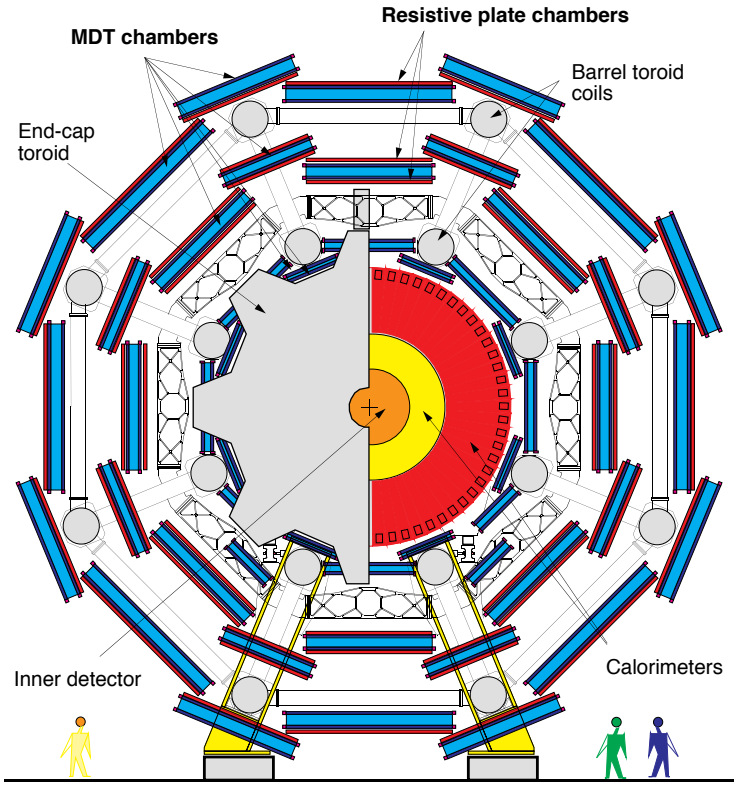

Figure 4.10. Schematic view of the transversal projection of the muon spectrometer [56].

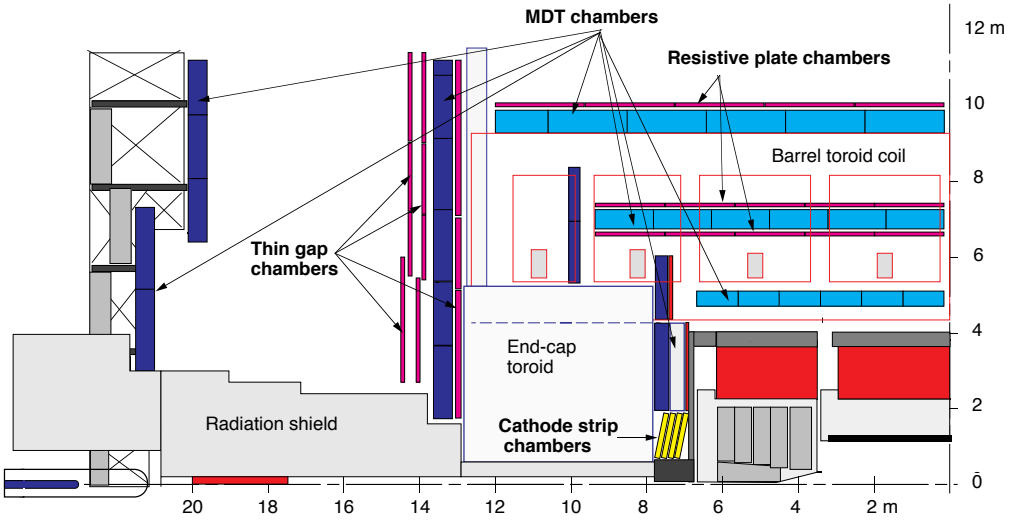

Figure 4.11. Schematic view of the longitudinal projection of the muon spectrometer [56].

MS high precision chambers
The Monitored Drift Tubes (MDT) chambers are used for high precision track measurement in the barrel region and in the end-cap up to $|\eta| \leq 2$. Each side of the chambers is composed of two multi-layers of aluminum drift tubes, with diameter of 30 mm and thickness of 400 μm, filled with a gas mixture of Ar and CO_2 at a pressure of 3 bar. The drift time in each tube is measured by a Tungsten-Rhenium wire placed in the center, yielding a resolution of 80 μm. The total chamber resolution is 35 μm. In the high occupancy forward region $2 \leq |\eta| \leq 2.7$, where rates greater than 150 Hz/cm^2 are found, the more robust multi-wire strip cathodes chambers (CSC) are adopted. CSC cathodes are segmented in orthogonal strip wires to allow a measurement in both coordinates with a resolution of 60 μm in R and 5 mm in the ϕ direction. These chambers present also a good time resolution of about 7 ns.

4.2.6 Trigger

The trigger and data acquisition (TDAQ) has the crucial task of performing an online event selection to cope with the impressive event rate of the Run-2 LHC system of 40 MHz. Due to limitation in data storage, computing and transfer rates, it is unthinkable to read out and store all LHC events. Moreover, most of the data are not of interest for the ATLAS physics program, as the rate is dominated by low-p_{T} inelastic and diffractive collisions. A balance between the data acquisition rates and high efficiency for selecting interesting physics data has to be found, keeping in mind that an event not triggered is lost forever. The ATLAS Run-2 TDAQ system [57] is built on two levels of online selection, as shown in Figure 4.12: a first hardware level-1 (L1), that significantly reduces the event rate, and a second software level (HLT), where the final decision is made.

L1
The hardware L1 exploits quickly accessible coarse data from the calorimeters and MS in dedicated regions of interest (RoI). Calorimeters provide information about clusters of energy deposits, missing transverse energy and raw shape dimensions, while the muon spectrometer provides information from trigger chambers about transverse momentum and track position. At L1 the event rate of 40 MHz is reduced to 100 kHz with a 2.5 μs latency.

HLT
The software level integrates the RoI data with the full detector information and runs complex trigger algorithms to select the events. A fast reconstruction step is first used for the trigger selection, followed by a more precise refinement similar to the offline reconstruction. The HLT is the first step in which ID information is incorporated in the trigger, only track information inside identified RoI at L1 are used due processing time constraint. The muon fast reconstruction integrates each L1 muon candidate with MDT data preforming a track fit extrapolated to the ID. The ID fast tracking consists in trigger specific pattern algorithms, designed to identify compatible track segments and hit points. Raw calorimetric informations are reconstructed by fast algorithms into cluster and cell objects, which will later

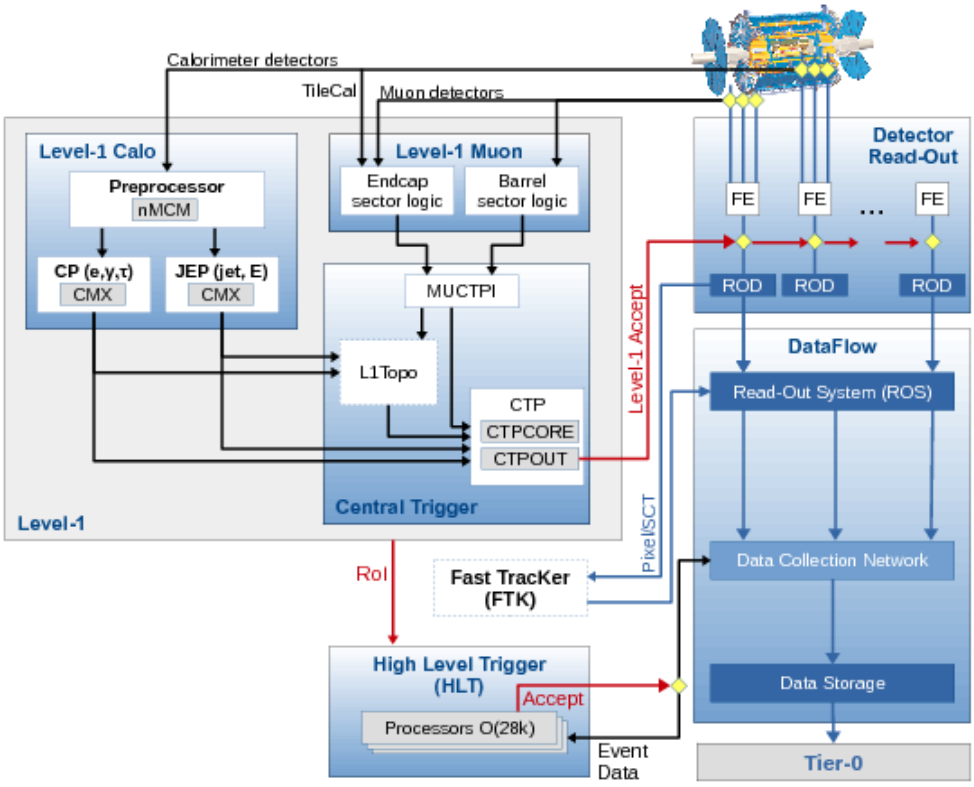

Figure 4.12. Schematic view of ATLAS TDAQ system in Run-2 [58].

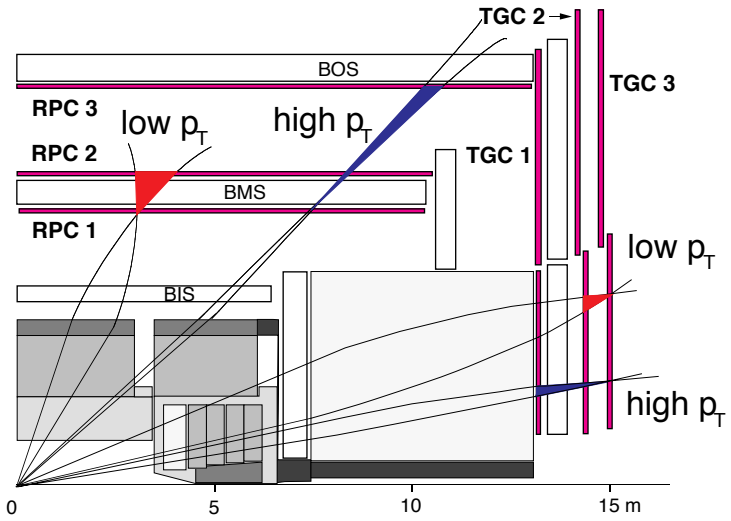

Figure 4.13. L1 muon low-p_{T} and high-p_{T} triggers in the Muon Spectrometer barrel and end-cap.

be reconstructed in jet, electron, and photon candidates. The final event rate is reduced to 1kHz with a latency of 0.2 μs.

4.2.7 L1 Muon trigger

Many hypothetical new physics processes include several decay modes into muons, which are a perfect probe for discovering dark sectors. The L1 muon trigger processes information from the MS in a dedicated region of interest (RoI) of dimension 0.4×0.4 in $\Delta\eta \times \Delta\phi$ in the barrel, and 0.2×0.2 in the end-caps, matching coincident hits in space and time. The trigger has to operate in a high rate environment with high efficiency and low transverse momentum threshold. Hits collected from the RPC or TGC trigger chambers are used to build hit patterns. If the pattern is contained inside a fixed window pointing to the IP, whose width defines the p_{T} threshold, the trigger match is done. A hit pattern of a muon with infinite momentum would result in a straight line, therefore a high-p_{T} muon would fire also low-p_{T} triggers, which requires fewer coincidences within a trigger window. Instead, a low-p_{T} muon would fall outside a high-p_{T} trigger window. Figure 4.13 show a schematic picture of the low-p_{T} and high-p_{T} triggers.

4.3 Reconstruction - Physics objects

This section will describe the identification and reconstruction techniques of the different physical objects in ATLAS. A particular focus will be put on muons and jets, the main components of the dark-photon jet analysis. Standard object definitions are usually recommended by the ATLAS collaboration, but further optimisation can be done at analysis level to improve the selection and maximise the sensitivity. The reconstruction is a multi-stage process designed to find particle-like signatures starting from tracks and clusters, built using the detector signals. The reconstructed

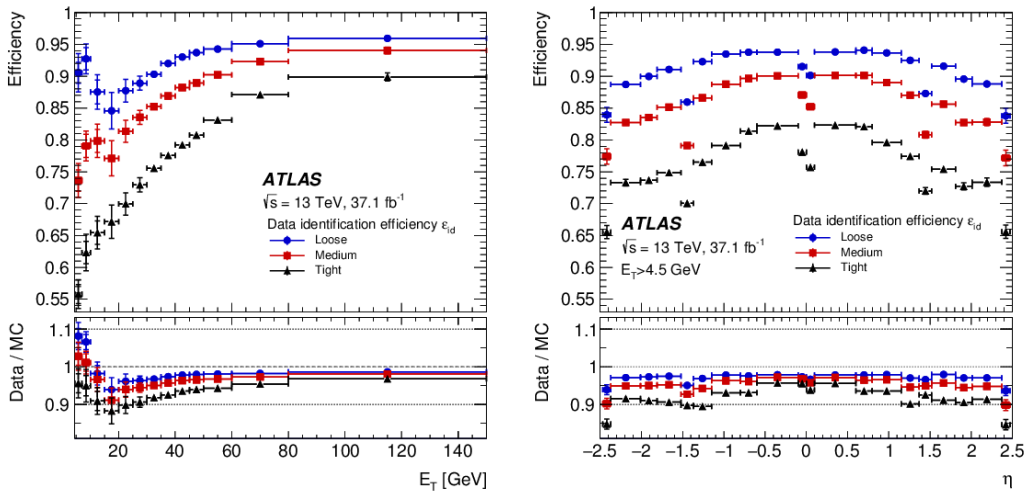

Figure 4.14. Measured electron-identification efficiencies in $Z \to ee$ events for the loose (blue circle), medium (red square), and tight (black triangle) operating points as a function of E_{T} (left) and η (right) [59].

objects are then combined and classified into high-level physics objects, e.g electrons or jets, with all the measured physical properties, such as their momenta, energy or charge.

4.3.1 Electrons

Electrons are reconstructed with combined information from energy deposits in the ECAL and associated tracks in the ID. The electron candidates are discriminated from background by a likelihood-based identification algorithm, which exploits several properties from track information to calorimeter shower shapes. Correctly identified electrons are then classified in three quality categories: loose, medium, and tight. Electrons selected by a tighter working point are also contained in the looser selections. The electron identification algorithms' performance are presented in Figure 4.14 for muons from $Z \to ee$ events as a function of the transverse energy and η.

High energy electrons tend to deposit more energy in the last ECAL layers or in the early HCAL layers, presenting narrower cascade shapes. To take into account this effect the loose and medium selections are constructed to be robust against E_{T} dependence. Additional cuts on electron discriminating variables are included in the tight selection to maintain a good efficiency for electron candidates with high E_{T}.

Isolation requirements are added to the electron selection to further suppress background from non-prompt electrons, such as electrons originating from converted photons. Analyses using low energy electrons usually choose a tight isolation requirement for high background rejection, while those using high energy electrons may prefer a loose isolation for a high signal efficiency. The isolation selection evaluates track and energy clusters found within a cone around the electron candidate. The most relevant variables are:

- topo-$E_{\mathrm{T}}^{cone,20}$: calorimeter isolation energy defined as the sum of transverse energies of topological clusters [60] found within a cone of $\Delta R = 0.2$ around the electron candidate, excluding the clusters of the electron itself.
- $p_{\mathrm{T}}^{varcone,20}$: track isolation defined as the sum of transverse momenta of all tracks found within a cone of $\Delta R = 0.2$ around the electron candidate track, excluding the track of the electron itself.

These are used to build the isolation working points presented in Table 4.1.

	efficiency		
Operating point	calorimeter isolation	track isolation	total efficiency
LooseTrackOnly	-	99 %	99 %
Loose	99 %	99 %	∼98 %
Tight	96 %	99 %	∼95 %
Gradient	0.1143 % $\times E_{\mathrm{T}}$+ 92.14 %	0.1143 % $\times E_{\mathrm{T}}$+ 92.14 %	90/99 % at 25/60 GeV
GradientLoose	0.057 % $\times E_{\mathrm{T}}$+ 95.57 %	0.057 % $\times E_{\mathrm{T}}$+ 95.57 %	95/99 % at 25/60 GeV

Table 4.1. Electron isolation working points efficiencies information.

The electron information is not used to obtain the first dark-photon jet results of Run-2 with the 2015–2016 data, but their use in the Run-2 legacy analysis is discussed in Chapter 7.

4.3.2 Muons

ATLAS muon reconstruction [61] exploits the information provided by the ID and the MS sub-detectors leading to four muon types being defined:

- Combined (CB): combination of the independent tracks reconstructed in the ID and MS. Provides the best purity and best momentum resolution;
- Segmented-tagged (ST): ID track associated with at least one local track in the MDT or CSC chambers. The ST selection is used for low-p_{T} muons or muons falling outside the MS acceptance regions;
- Calorimeter-tagged (CT): combination of ID tracks and matched energy deposits in the calorimeter compatible with a minimum ionizing particle. This identification criteria is optimised to recover acceptance in the region ($|\eta| \leq 0.1$) where the ATLAS muon spectrometer is only partially instrumented to allow for cabling and services.
- Stand-alone (SA, msonly): reconstruction using only the information provided by the MS. The muon track is required to have hits in at least three layers in the barrel, or three in the end-caps, and to be compatible with a muon originating from the IP. In standard analyses SA muons are used in the pseudorapidity outside the ID range $2.5 \leq |\eta| \leq 2.7$;

The dark-photon jet analysis uses SA muons in the whole pseudorapidity range to select displaced decays that would not leave any track in the ID. Additionally,

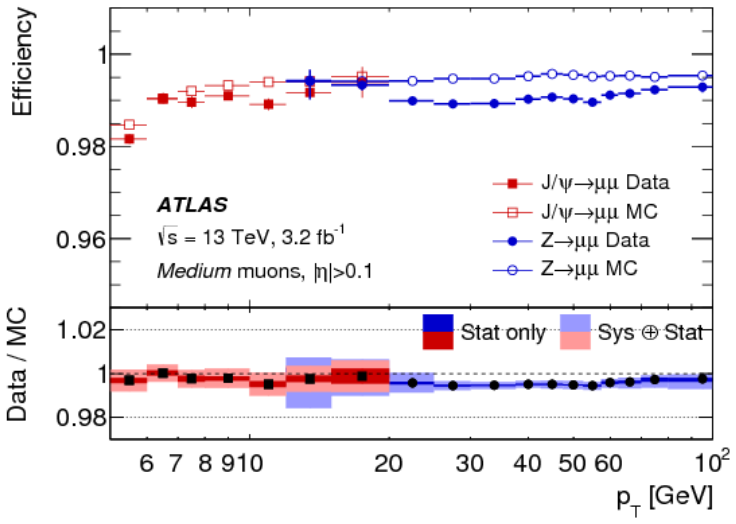

Figure 4.15. Reconstruction efficiency for the medium muon selection as a function of the p_{T} of the muon, in the region $0.1 < |\eta| < 2.5$ as obtained with $Z \to \mu\mu$ and $J/\psi \to \mu\mu$ events [61].

the analysis extends the standard SA criteria requiring to have at least two hit in the barrel, instead of three, to be able to reconstruct dark photon decays that occur after of the innermost MDT layer.

Muon identification algorithms, similar to the ones used for electrons, are also used to suppress the background coming primarily from pion and kaon decays. Four working points are defined in order of purity: loose, medium, tight, and high-p_{T}. The DPJ analysis adopts the medium selection to maximise the reconstruction efficiency while retaining good quality muons. The medium quality efficiency for prompt muons as a function of the p_{T} is presented in Figure 4.15, obtained with $Z \to \mu\mu$ and $J/\psi \to \mu\mu$ samples.

ATLAS standard muon isolation, defined from the same variables of electron isolation, is not adopted in the analysis as no tracks are expected in the ID. Only a custom dark-photon jet isolation is applied in the analysis, explained in detail in Section 5. In this search, muons with pseudorapidity in the range $1.0 \leq |\eta| \leq 1.1$ are rejected to avoid the transition region of the MS between barrel and end-cap. Moreover, only muons in the pseudorapidity interval $|\eta| < 2.5$, corresponding to the ID coverage, are selected to ensure isolation from ID tracks.

4.3.3 Jets

In the DPJ search, jets are expected from displaced γ_{d} decays into electron or hadron pairs in the hadronic calorimeter. These are expected to be isolated in the ID with most of the energy deposits in the HCAL, appearing narrower than ordinary jets. ATLAS jets are reconstructed from topological clusters of energy deposits in the calorimeters using the anti-k_t clustering algorithm [62, 63] with a distance parameter $R = 0.4$. Anti-k_t is a sequential clustering algorithm based on the evaluation of the distance d_{ij} between two clusters (i,j) and the distance d_{iB} between the pseudo-jet

and the beam (B), defined as:

$$d_{ij} = min(p_{\mathrm{T},i}^{2p}, p_{\mathrm{T},j}^{2p}) \frac{\Delta R_{ij}^2}{R^2}, d_{iB} = p_{\mathrm{T},i}^{2p}, \tag{4.11}$$

where $p_{\mathrm{T},i}^{2p}$ is the transverse momentum of the i-th object and p is the algorithm parameter $p = -1$. The clustering begins with the hardest constituent i as seed. For each iteration all distances d_{ij} between the i-th constituent and all other constituents j are computed. If the minimum value of the d_{ij} set is smaller than d_{iB}, then the i-th and the j-th constituent are combined into a single pseudo-jet summing the four-momenta. In the following iteration the pseudo-jet will be used as seed and the i-th and j-th constituents will no longer be considered. Instead, if $d_{ij} \geq d_{iB}$, the pseudo-jet is considered as a jet. Clustering ends when only jets are left in the event.

This algorithm tends to cluster soft particles with hard objects before clustering between themselves. For example, an isolated hard particle will cluster all soft particles within a $2R$ distance in a size R cone, resulting in a conical-shape jet. The algorithm is therefore sensitive only to hard particles proximity at disadvantage of soft radiation. Jet objects are then calibrated in energy to correct for calorimeter response non-linearities, leakage, mis-reconstruction, weighting the energy deposits arising in the ECAL and HCAL differently. An additional correction due to pile-up may be also applied.

Jet Vertex Tagger (JVT)

The Jet Vertex Tagger [64] (JVT) is a technique used in ATLAS for pile-up suppression. JVT uses a multivariate combination of the following pile-up sensitive track information:

- Jet Vertex Fraction (JVF): defined as the ratio of the scalar sum of the transverse momentum of the associated tracks that originate from the PV to the scalar sum of the transverse momentum of all associated tracks corrected with the average scalar sum of pileup associated tracks. It is used to select jets originating from the PV.
- $R_{p_{\mathrm{T}}}$: defined as the ratio of the scalar sum of the transverse momentum of the associated tracks that originate from the PV to the fully calibrated jet transverse momentum, which includes pileup subtraction.

Figure 4.16 presents the distribution of JVF and $R_{p_{\mathrm{T}}}$ for pile-up (PU) and hard-scatter (HS) jets with $20 \leq p_{\mathrm{T}} \leq 30$ GeV.

JVT uses a k-nearest neighbour (kNN) algorithm [66] trained on these two variables to differentiate between pile-up jets and jets originating from the PV. The tagger output is shown in Figure 4.17 (left) for light-quark and gluon initiated hard-scatter jets. As result, the JVT signal efficiency is independent of the number of PV in the event, as shown in Figure 4.17 (right), therefore optimal for pile-up suppression and robust against its increase.

Since dark-photon jets produced in the hadronic calorimeter have a JVT output distribution similar to that of pile-up jets, in this search the JVT output is used oppositely to the typical ATLAS implementation.

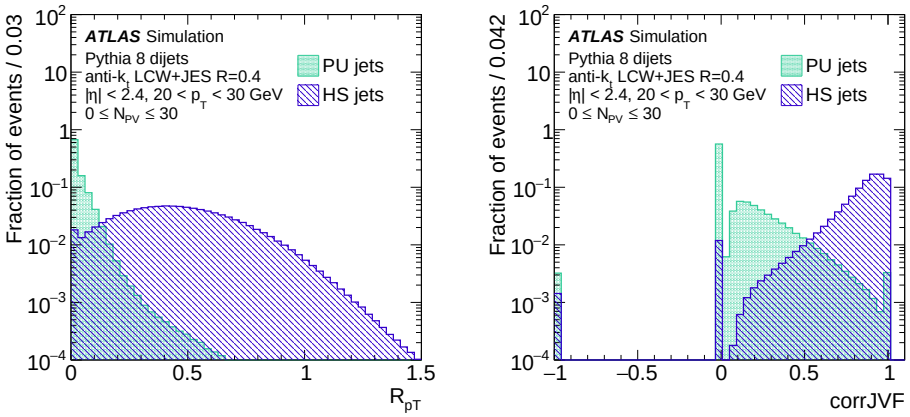

Figure 4.16. JVT input variables distribution, $R_{p_{\mathrm{T}}}$ (left) and JVF (right) for pile-up (PU) and hard-scatter (HS) jets with $20 \leq p_{\mathrm{T}} \leq 30$GeV [65].

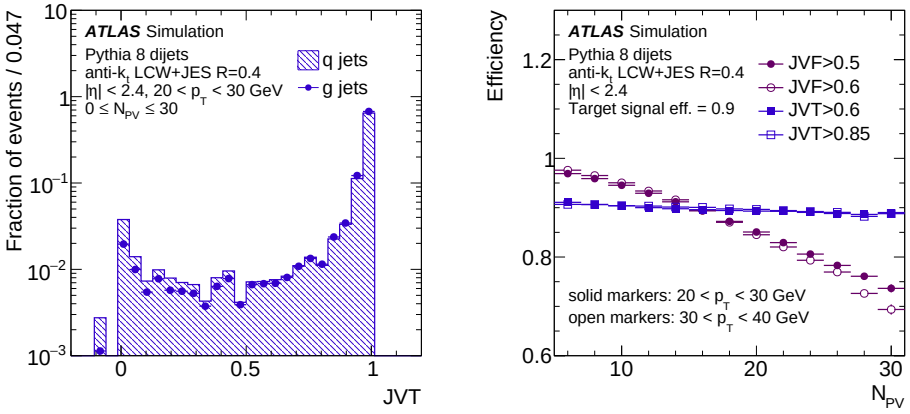

Figure 4.17. JVT output distribution for light-quark and gluon initiated hard-scatter jets (left). Primary-vertex dependence of the hard-scatter jet efficiency for $20 \leq p_{\mathrm{T}} \leq 30$ GeV (solid markers) and $30 \leq p_{\mathrm{T}} \leq 40$GeV (open markers) jets for fixed cuts of JVT (blue square) and JVF (violet circle) such that the inclusive efficiency is 90 %

Jet energy scale and resolution

The jet energy calibration is needed to compensate for all possible calorimeter "loss effects", e.g. presence of dead detection material or simply reconstruction inefficiencies. The goal is to correct the jet energy to the true process, this operation is referred to as Jet Energy Scale (JES). JES calibration starts with pile-up subtraction and origin correction, to make the jet point back to the hard-scatter vertex. The topo-cluster kinematic properties are then recomputed leaving the energy unchanged. Finally the jet response is corrected by applying energy corrections in p_{T} and η bins from the truth-level MC jet response (E_{reco}/E_{truth}). The whole calibration is analysed in detail in Ref. [67].

The systematic uncertainties associated to the calibration procedure must be taken into account. The JES uncertainty is well described by the variation applied by the calibration to the mean value of the jet response distribution. An additional source of systematic uncertainty arises from the Jet Energy Resolution (JER), which quantifies the width of the Gaussian jet response distribution. The JER uncertainty takes into account many different effects from the stochastic nature of hadronic showers to electronic noise.

ATLAS standard jet-cleaning criteria [68] applied in most analyses to reject fake jets are not applied in the displaced dark-photon jet search. These criteria discard jets with high values of $E_{\mathrm{HCAL}}/E_{\mathrm{ECAL}}$, a typical discriminant of a signal displaced jet. Therefore a dedicated cleaning algorithm for displaced jet in the HCAL is applied instead, with no requirements on the ratio $E_{\mathrm{HCAL}}/E_{\mathrm{ECAL}}$. Jets are required to have transverse momentum $p_{\mathrm{T}} \geq 20$ GeV and $|\eta| < 2.5$. In addition, the weighted mean time difference between $t = 0$ (bunch-crossing time) and the time of the energy deposit in the calorimeter cells is required to be in the range [-4 ns, 4 ns] to reduce cosmic-ray background and beam-induced background (BIB) jets.

4.3.4 Missing transverse momentum

E_{T}^{miss} measures a momentum imbalance in the transverse plane in the event. If a particle produced in a *pp* collision escapes ATLAS undetected, as for neutrinos or other neutral weakly interacting particles predicted by several BSM theories, it will cause a momentum imbalance in the transverse plane. Secondary effects that may contribute to the E_{T}^{miss} are caused by erroneous object reconstruction or particles escaping a not completely hermetic detector. It is characterised by a hard term, which includes all the fully reconstructed objects, and a soft term, which includes contributions from detector signal objects not associated with any specific reconstructed object. It is defined as the negative vector sum of the momenta of the respective calibrated objects and computed as follow:

$$\vec{E}_{\mathrm{T}}^{miss} = -\left(\sum_{i \in hardterm} \vec{p}_{\mathrm{T},i} + \sum_{i \in softterm} \vec{p}_{\mathrm{T},i} \right). \tag{4.12}$$

The measurement of missing energy is a key ingredient for many BSM searches for the identification of new predicted particles which do not interact with the detector material. The missing transverse energy (E_{T}^{miss}) is not used in the Run-2 2015–2016

dark-photon jet search, but its use in the Run-2 legacy analysis is discussed in Chapter 7.

Chapter 5

Search for dark-photon jets in the 2015–2016 dataset

The dark-photon jet search for long-lived decay of light dark photons, probes small values of the kinetic mixing term, $\epsilon < 10^{-5}$, and a dark photon mass range between twice the muon mass and twice the tau mass. For these kinetic mixing values, the γ_{d} has a macroscopic lifetime and it decays far from its production point. Moreover, due to its small mass, the γ_{d} is expected to be produced with large boost, resulting in collimated groups of leptons and light hadrons in a jet-like structure, here referred to as a dark-photon jet.

The DPJ signature represents a challenge for both the trigger and the reconstruction capabilities of the ATLAS detector, which is optimised for prompt decays. Collimated charged particles in the final state can be difficult to reconstruct, due to the detector granularity. In the case of particles which decay away from the interaction point, past the inner tracking system, only the information from the calorimeters and the Muon Spectrometer is available for the reconstruction of the decay products. The ID can then be used to define track isolation criteria to reduce the dominant SM backgrounds. The unknown structure of the dark sector and its coupling to the SM particles define the signature properties of the DPJ, such as the jet shape and particle multiplicity. A model independent search strategy is adopted, focusing only on the experimental topology of the DPJ. The results can then be interpreted in specific models with different parameter assumptions.

The analysis relies on dedicated triggers, designed to select displaced decays not associated to the IP. Events are categorised into different channels based on the DPJ constituent particles. The selection exploits multivariate techniques in order to suppress the multi-jet and cosmic-ray backgrounds in a way which is optimised for the various DPJ channels. This technique allows the exploitation of the fully hadronic signature for the first time in ATLAS DPJ searches, resulting in increased sensitivity compared to the previous ATLAS results using the data collected in 2011 and 2012 at the centre-of-mass energy of 7 and 8 TeV respectively [69, 70].
The search for displaced DPJs presented in this chapter employs the full dataset collected by ATLAS during 2015–2016 data taking at $\sqrt{s} = 13$ TeV.

The data and simulation samples used in this search are detailed in Section 5.1. Section 5.3 describes the experimental signatures and the reconstruction of the DPJs

in the detector. Trigger and event selection are detailed in Sections 5.2 and 5.4. Sections 5.5 and 5.6, define the background estimation and systematic uncertainties. Finally the search results and interpretation are presented in Section 5.7.

5.1 Data and simulation samples

5.1.1 2015–2016 dataset

Data were collected during 2015–2016 in pp collisions at a center-of-mass energy of 13 TeV. Recorded events were selected using a set of dedicated triggers, described in Section 5.2. Only runs in which all the ATLAS sub-detectors were operating at nominal conditions are selected, as defined in the Good Run List (GRL) provided by the Collaboration. The total integrated luminosity corresponds to 36.1 fb^{-1} with a 2.1% uncertainty [46]. The instantaneous luminosity delivered to the ATLAS detector had a peak value of 5×10^{33} cm^{-2} s^{-1} in 2015 and of 13.8×10^{33} cm^{-2} s^{-1} in 2016, with an average number of interactions per bunch crossing $\langle\mu\rangle = 23.7$.

5.1.2 Zero-bias dataset

Zero-bias is a beam bunch-crossing time trigger which uses random physics triggers in coincidence with the colliding bunches. It is designed to collect unbiased events with a 100% efficiency. Only active beam bunch crossings have to be read out to maximise the probability of obtaining events with valid collisions. Data collected with the zero-bias trigger are used to estimate background contamination from underlying event structure, such as pile-up events. The zero-bias trigger used in this analysis collected events during the same periods of time as the trigger used to select signal events. Thus, this dataset contains background events with the correct run conditions and proportion to the collision dataset.

5.1.3 Di-jet dataset

A di-jet dataset is recorded in collision data with a single jet trigger "HLT_j60" with a transverse momentum threshold of $p_{\text{T}} = 60$ GeV and requiring a di-jet event. A di-jet event requires two hard jet in the pseudorapidity region $|\eta| < 2.5$ with a transverse momentum $p_{\text{T}} \geq 20$ GeV, with a minimum angular separation to one another of $\Delta\phi \geq 2.5$. This dataset is used as a control sample for systematic uncertainty studies and cross-checks.

5.1.4 Cosmic and Beam induced background datasets

The nominal LHC configuration for pp collisions contains 3564 bunch crossings per revolution, and not all bunch slots are actually filled with protons. Bunch crossing where one or both beams are not filled with protons are ideal for studies on non-collision backgrounds.

A cosmic-ray background enriched dataset is collected during empty bunch crossings (cosmic dataset) and used for the background estimation. An empty bunch crossing takes place when neither beam is filled with protons and each empty bunch is separated from filled bunches by at least five empty bunches on each side.

A beam induced background (BIB) [71] enriched dataset is collected during unpaired isolated bunch crossings (BIB dataset). In unpaired bunch crossings only one of the two beams is filled with protons and separated from filled bunches by at least three unfilled bunches on each side. This dataset is used to identify characteristic features of BIB and to estimate the residual contamination in the collision dataset.

The same triggers used to select the collision dataset (see Section 5.2) were operating during the 2015 and 2016 data taking in the empty and unpaired bunch crossings. The ratio of the number of filled to empty bunch crossings, F_{CR}, is used to scale the number of events in the cosmic dataset to that in the *pp* collision data. It is computed with the following formula:

$$\begin{aligned} F_{\mathrm{CR}} &= \frac{\sum_{2015+2016} \mathrm{Time}_{\mathrm{paired}}}{\sum_{2016} \mathrm{Time}_{\mathrm{empty}}} \\ \mathrm{N}_{2015+2016}^{\mathrm{expected,paired}} &= \mathrm{F}_{\mathrm{CR}} \times \mathrm{N}_{2016}^{\mathrm{observed,empty}}, \end{aligned} \tag{5.1}$$

and found to be 2.1. Finally, cosmic and BIB datasets are subject to the same GRL used for selecting the collision dataset.

5.1.5 Simulated samples

Recorded data are compared to simulated samples to compute the detector reconstruction efficiencies and acceptance, and to estimate the systematic uncertainties. Simulated samples are also used to evaluate the final contribution of the signal processes. The simulation of a process usually starts by defining the energy of the colliding particles, estimated by the Parton Distribution Function (PDF) set. At this point a generator models the hard process, based on the matrix element (ME) computations, estimating the contributions due to the leading physics processes. The hadronization effects and gluon radiation are included into the event by the parton showering (PS), generating the final state hadrons. Additional collisions may be overlaid to the event to simulate pile-up events. Finally, the generated events are processed through a full simulation of the ATLAS detector geometry and response.

Signal Processes

The FRVZ model [25, 39] MC samples are generated at leading order using MadGraph 5_aMC@NLO 2.2.3 [72] interfaced to Pythia 8.210 [73] for parton shower generation. The A14 set of tuned parameters (tune) for parton showering and hadronisation [74] are used together with the NNPDF2.3LO PDF set [75].

Six different signal samples are generated to explore different phase-space regions of the FRVZ model. A SM Higgs boson with a mass of 125 GeV and a beyond-the-SM (BSM) heavy scalar boson with a mass of 800 GeV are considered. The ggF Higgs boson production cross-section in *pp* collisions at $\sqrt{s} = 13$ TeV, estimated at next-to-next-to-leading order (NNLO) [76], is $\sigma_{\mathrm{SM}} = 43.87$ pb for $m_H = 125$ GeV and $\sigma = 5$ pb for $m_H = 800$ GeV. To produce event with back-to-back DPJs in the $H \to 2\gamma_{\mathrm{d}} + X$ process, the mass of the hidden fermion f_{d_2} is chosen to be low

relative to the Higgs boson mass and far from the kinematic threshold. In the case of $H \to 4\gamma_d + X$ process, the mass of the hidden scalar s_d is also chosen to be low relative to the Higgs boson mass, so that two back-to-back DPJs are expected, each consisting of two collimated dark photons. The dark-photon mass is chosen to be 0.4 GeV, above the pion pair mass threshold, and the γ_d decay branching fractions ($\mathcal{B}$) are expected to be $\mathcal{B}(\gamma_d \to ee) = 45\%$, $\mathcal{B}(\gamma_d \to \mu\mu) = 45\%$, $\mathcal{B}(\gamma_d \to \pi\pi) = 10\%$ [25]. The γ_d proper decay length $c\tau$ is chosen in order to have $\sim 80\%$ of the decays that occur before the muon trigger chambers, at 7 m in radius and 13 m along the z-axis. For the SM 125 GeV $H \to 2\gamma_d + X$ mass point two additional samples are generated with different proper decay lengths, one with a $c\tau$ of 4.9 mm and one with a $c\tau$ of 492 mm, to validate the procedure for extrapolating limits to different proper decay length. This procedure is detailed in Section 5.7.3. All the simulated samples produced for the model and all the generation parameters are summarised in Table 5.1.

Sample	m_H [GeV]	$m_{f_{d_2}}$ [GeV]	m_{HLSP} [GeV]	m_{s_d} [GeV]	m_{γ_d} [GeV]	$c\tau$ [mm]
$H \to 2\gamma_d + X$	125	5.0	2.0	–	0.4	4.9
$H \to 2\gamma_d + X$	125	5.0	2.0	–	0.4	49
$H \to 2\gamma_d + X$	125	5.0	2.0	–	0.4	492
$H \to 4\gamma_d + X$	125	5.0	2.0	2.0	0.4	82
$H \to 2\gamma_d + X$	800	5.0	2.0	–	0.4	12
$H \to 4\gamma_d + X$	800	5.0	2.0	2.0	0.4	21

Table 5.1. Parameters used for the MC simulations of the benchmark model.

Background processes

The main source of background in this analysis comes from QCD multi-jet events. Simulation samples are generated to study this background and to estimate systematic uncertainties. The MC samples were generated with Pythia 8.210 using the same tune and PDF as for the signal samples.

Subdominant SM processes that could lead to potential sources of background include W+jets, Z+jets, $t\bar{t}$, single-top-quark, WW, WZ, and ZZ production events. Simulation of the W+jets, Z+jets , WW, WZ, and ZZ events are generated using Sherpa 2.2.2 [77] with the NNPDF 3.0 NNLO [78] PDF set. Single top and $t\bar{t}$ MC samples were generated using Powheg-BOX 1.2856 [79] and Pythia 6.428 [80] with the Perugia2012 [81] tune for parton showering and hadronisation, and CT10/CTEQ6L1 [82, 83] PDF sets.

Finally, MC samples of $J/\psi \to \mu\mu$ events are generated to evaluate systematic uncertainties for muon trigger and reconstruction efficiencies. The MC samples are generated using Pythia8+Photos++ [84] with the A14 tune for parton showering and hadronisation, and the CTEQ6L1 PDF set.

All generated MC events were processed through a full simulation of the ATLAS detector geometry and response [85] using the Geant4 [86] toolkit. The simulation

includes multiple pp interactions per bunch crossing (pile-up), as well as the detector response to interactions in bunch crossings before and after the one producing the hard interaction. In order to model the effect of pile-up, simulated inclusive pp events are overlaid on each generated event and reweighted to match the conditions of the 2015-2016 data sample. The multiple interactions were simulated with PYTHIA 8.210 using the A2 tune [87] and the MSTW2008LO PDF set [88].

5.2 Triggers for event selection

The data sample is selected by the logical OR of three dedicated triggers designed to specifically target displaced decays. The standard ATLAS triggers [89] are optimised for prompt objects and show several limitations for the selection of displaced collimated decays.

5.2.1 Narrow-scan Trigger

The narrow-scan algorithm is designed to trigger events with highly collimated muons with low activity in the ID. A single muon with $p_{\mathrm{T}} \geq 20$ GeV is selected at L1 and matched to a muon at HLT. The collimated muons would fall in the same RoI, and therefore would not be selected by a multi-muon trigger at L1. A second muon is scanned for at HLT using only information from the MS, without an explicit match to a L1 muon object, in a cone of $\Delta R = 0.5$ around the muon seed, with $p_{\mathrm{T}} \geq 6$ GeV. The scanned muon threshold has been increased during the 2016 data taking, first to 10 GeV and then 15 GeV (see Table 5.2), to reduce the trigger rate. The scanned muon is explicitly required to be unmatched to any ID track.

Period	Integrated Luminosity [fb^{-1}]	Leading muon threshold [GeV]	"scanned" muon threshold [GeV]
2015 - all periods	3.2	20	6
2016 - period A - F	14.9	20	10
2016 - period G - END	18.0	20	15

Table 5.2. p_{T} thresholds of the narrow-scan in the 2015-2016 data taking periods.

The narrow-scan trigger efficiency is evaluated for the $H \rightarrow 2\gamma_{\mathrm{d}} + X$ process signal models. At truth level, dark photons decaying into muons in the acceptance region of the ID ($|\eta| \leq 2.4$) are selected with a p_{T} requirement of 20 GeV for the leading muon, and of 6 GeV for the sub-leading muon. The selection efficiency as a function of the transverse and longitudinal decay position of the dark photon is shown in Figure 5.1.

A drop in efficiency is expected for a transverse decay length L_{xy} around 7 m, where the MS pivot triggering planes, which correspond to the top layers of the RPC middle stations, are located. At least a hit in the pivot plane is necessary for the MS trigger system to select a muon. Efficiencies as a function of the leading muon transverse momentum in the barrel region, with $L_{xy} \leq 7$ m and $|\eta| \leq 0.9$ of the γ_{d}, and in the end-cap region, with $L_z \leq 7$ m and $|\eta| \geq 1.1$ of the γ_{d}, are shown in Figure 5.2.

A higher efficiency is expected for the $m_{\mathrm{H}} = 800$ GeV signal sample, where the highly boosted muons are more likely to pass the p_{T} trigger thresholds.

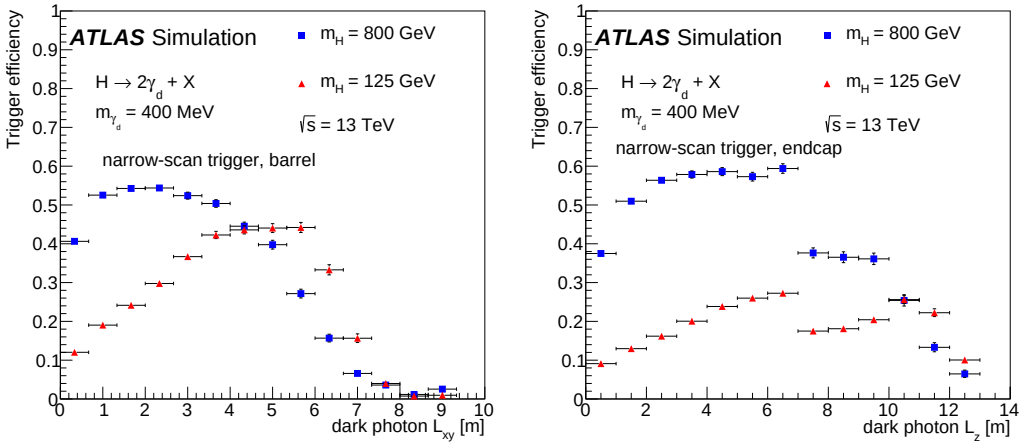

Figure 5.1. Narrow-Scan trigger efficiency as a function of the transverse (left) and longitudinal (right) decay position of the γ_{d} for $\gamma_{\mathrm{d}} \to \mu\mu$. A 6 GeV threshold on the second muon is required. The uncertainties are statistical only.

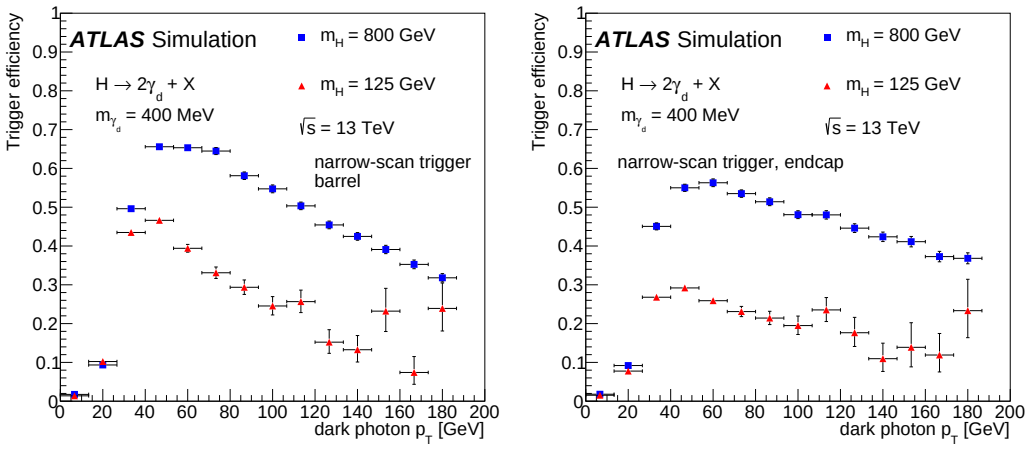

Figure 5.2. Narrow-Scan trigger efficiency as a function of the transverse momentum of the γ_{d} in the barrel (left) and in the endcap (right) for $\gamma_{\mathrm{d}} \to \mu\mu$ events. A 6 GeV threshold on the second muon is requested. The uncertainties are statistical only.

5.2.2 3mu6 msonly Trigger

The tri-muon MS-only trigger selects events with at least three L1 muons with $p_{\mathrm{T}} \geq 6$ GeV, confirmed at HLT using only the MS information. It is expected to be very effective in selecting events for the $H \to 4\gamma_{\mathrm{d}} + X$ process for dark photons decaying into muons, resulting in a efficiency which ranges between 6% and 10% depending on the dark photon boost. It is less effective in selecting events for the

$H \to 2\gamma_d + X$ where two close-by muons coming from the same dark photon need to fall in two separate RoI. The expected trigger efficiency in selecting events for the $H \to 2\gamma_d + X$ process ranges between 3% and 4%. This trigger was operating throughout the entire 2015–2016 data taking, as shown in Table 5.3.

Period	Trigger	Integrated Luminosity [fb^{-1}]
2015 - all periods	HLT_3mu6_msonly	3.2
2016 - all periods	HLT_3mu6_msonly	32.9

Table 5.3. Tri-muon MS-only trigger in the 2015-2016 data taking periods.

5.2.3 CalRatio Trigger

The CalRatio trigger [90] is designed to target hadronic displaced decays which, decaying directly in the HCAL, produce narrow jets. At L1, energy deposits are searched for in a region of dimension 0.2×0.2 ($\Delta\eta \times \Delta\phi$), smaller with respect to the standard searched region of 0.8×0.8, and requiring a total transverse energy deposit of $E_T \geq 60$ GeV. At HLT reconstructed jets, with the calorimeter response calibrated at the EM scale, are required to have a transverse energy of $E_T \geq 30$ GeV and a ratio of energy deposits in the HCAL to ECAL of $\log(E_{HCAL}/E_{ECAL}) \geq 1.2$. Jets need to not have any matched ID track with $p_T \geq 2$ GeV in a ΔR cone of size 0.2 around the jet axis, and to be in the region covered by the ID ($|\eta| \leq 2.4$). Finally, jets are required to pass a BIB removal algorithm, which vetoes jets with at least four HCAL cells at the same ϕ and in the same layer with timing consistent with that of a BIB energy deposit. Deposits due to BIB are expected to have a very specific time distribution [91]. Table 5.4 summarises the CalRatio trigger used during the data taking.

Period	Trigger	Integrated Luminosity [fb^{-1}]
2015 - all periods	HLT_j30_jes_PS_llp_L1TAU60	3.2
2016 - all periods	HLT_j30_jes_cleanLLP_PS_llp_L1TAU60	32.9

Table 5.4. CalRatio triggers in the 2015-2016 data taking periods.

The CalRatio trigger efficiency is evaluated for the $H \to 2\gamma_d + X$ process. At truth level, dark photon decaying into electrons and pions in the acceptance of the ID ($|\eta| \leq 2.4$) are selected. The efficiency as a function of the transverse and longitudinal decay position of the γ_d are shown in Figure 5.3.

Efficiencies as a function of the transverse momentum in the HCAL barrel region, with $2.05 \leq L_{xy} \leq 3.7$ m and $|\eta| \leq 1.1$ of the γ_d, and in the HCAL end-cap region, with $2.05 \leq L_{xy} \leq 7$ m and $|\eta| \geq 1.1$ of the γ_d, are shown in Figure 5.4.

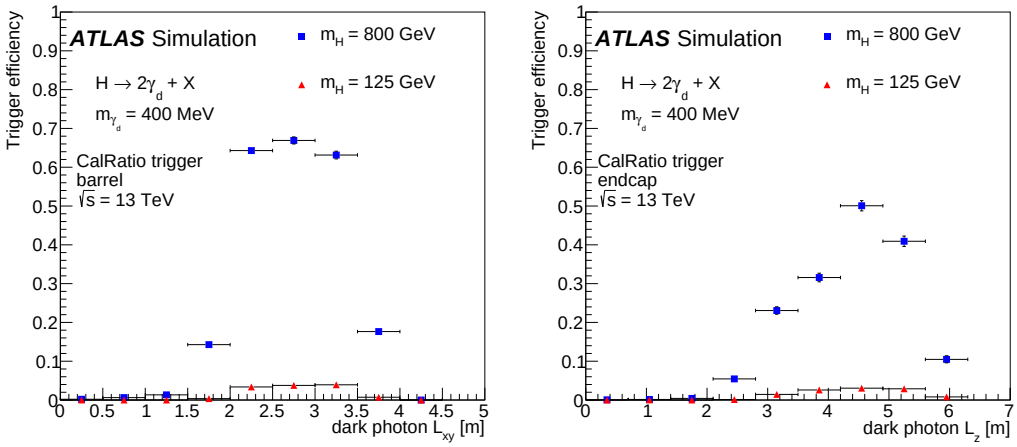

Figure 5.3. CalRatio trigger efficiency as a function of the transverse (left) and longitudinal (right) decay position of the γ_{d} for $\gamma_{\mathrm{d}} \to ee/\ \pi\pi$ events. The uncertainties shown by the error bars are statistical only.

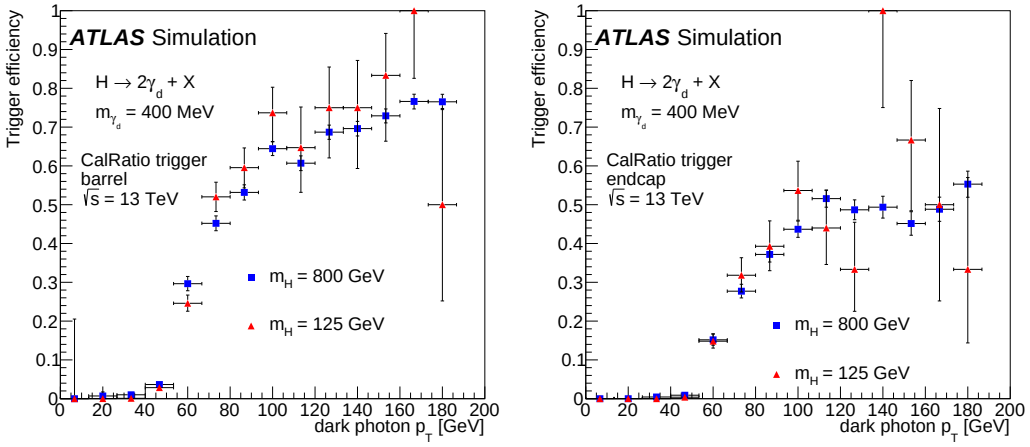

Figure 5.4. CalRatio trigger efficiency as a function of the transverse momentum of the γ_{d} in the barrel (left) and in the endcap (right) for $\gamma_{\mathrm{d}} \to ee/\ \pi\pi$ events. The calculation is limited to γ_{d} decays in the HCAL volume ($2.05 < L_{xy} < 3.7$). The uncertainties are statistical only.

5.2.4 Global efficiency

The resulting trigger acceptance times efficiency of the signal models, defined as the ratio between the number of triggered events to the total number of MC generated events, are shown in Table 5.5. The reported total efficiency corresponds to the logical OR of all the triggers.

Benchmark model	m_H [GeV]	$m_{f_{d_2}}$ [GeV]	m_{HLSP} [GeV]	$m_{s_{d_1}}$ [GeV]	m_{γ_d} [GeV]	$c\tau_{\gamma_d}$ [mm]	CalRatio efficiency	Tri-muon MS-only efficiency	Narrow-Scan efficiency	Total efficiency
$H \to 2\gamma_d + X$	125	5.0	2.0	-	0.4	49	0.4%	2.5%	1.4%	3.9%
$H \to 2\gamma_d + X$	125	5.0	2.0	-	0.4	4.9	0.4%	3.3%	1.5%	5.0%
$H \to 2\gamma_d + X$	125	5.0	2.0	-	0.4	492	0.0%	0.3%	0.2%	0.5%
$H \to 4\gamma_d + X$	125	5.0	2.0	2.0	0.4	82.4	0.1%	6.1%	1.4%	7.2%
$H \to 2\gamma_d + X$	800	5.0	2.0	-	0.4	12	9.9%	3.7%	3.0%	15.9%
$H \to 4\gamma_d + X$	800	5.0	2.0	2.0	0.4	21	7.6%	10.3%	6.7%	21.8%

Table 5.5. The acceptance times efficiency of the analysis triggers for MC signal samples.

5.3 DPJ reconstruction

The dark-photon jet topology is defined by the different couplings of the hidden sector and by the boost of the hidden particles, determined by the mass ratio of the decaying visible sector particles and the produced hidden sector one. A strong dynamics in the hidden sector may result in broader QCD-like jets with large multiplicity of particles within a DPJ. Moreover, hidden cascade decays and possible showering may result in very dense DPJs. Hidden particles might not interact with the detector or could decay outside the detector and result in missing transverse energy.

Among different hidden sector scenarios, the missing transverse energy can be extremely small, less than 10 GeV, or larger than the visible energy. Finally, the decay branching fractions into leptons and light mesons are determined by the dark photon mass [22, 25, 92].

Experimentally, it is helpful to characterize DPJs by some observable features:

- e, μ, π multiplicities;
- γ_d lifetime;
- dark-photon jet opening angle;
- dark-photon jet p_T, η.

Displaced DPJs are reconstructed according to these features. A γ_d decaying into a muon pair is searched for by looking for two closely spaced muon tracks in the MS, while a γ_d decaying into an electron or pion pair, given the high boost of the γ_d, is searched for as an energy deposit in the calorimeters identified as a single narrow jet. MC simulations show that DPJs containing two dark photons both decaying into an electron or pion pair are reconstructed as a single jet with radius $R = 0.4$.

The DPJs are then classified in categories according to the number of muons and jets found within a given cone of fixed angular size around a muon or jet candidate

with the highest transverse momentum. The size of the cone is fixed to be $\Delta R = 0.4$. This value has been tuned on the MC simulation to correctly reconstruct the dark photon in the investigated γ_d mass range. The total transverse momentum of the reconstructed DPJ is calculated as the vector sum of its constituents. The DPJ classification, shown schematically in Figure 5.5, is summarised as follows:

- **muonic-DPJ (μDPJ)** – At least two muons are required and no jets are allowed to be in the DPJ cone.
- **hadronic-DPJ (hDPJ)** – One jet is required and no muons are allowed to be in the DPJ cone.

Reconstructed DPJs with both muon and jet constituents are not considered in this analysis.

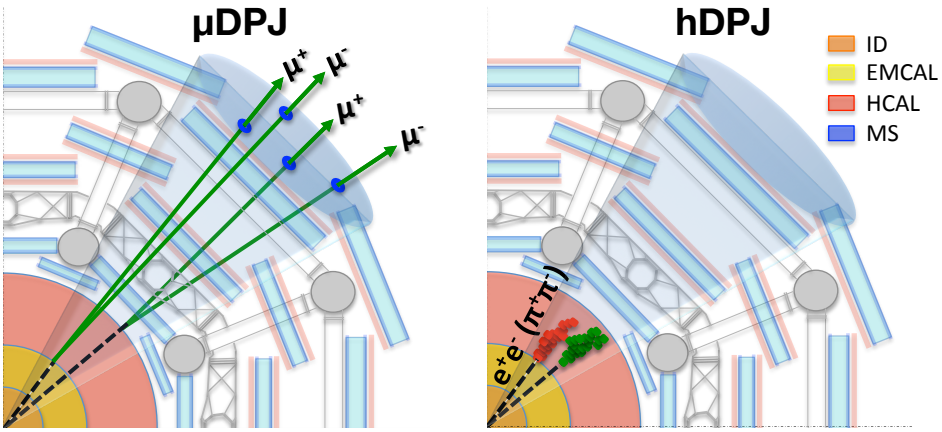

Figure 5.5. Schematic picture of the lepton-jet classification according to the decay final state: muons only (left) and jets only (right).

5.3.1 Muonic-DPJ

The muons used in this analysis are reconstructed using only tracks in the MS since the decay is expected to be displaced, out of the ID. The MS tracks are required to have at least one hit in two of the three MS tracking stations and not to be used in the reconstruction of a combined muon, this last requirement ensure that the MS tracks are not matched to a track in the ID. ID tracks [93] are reconstructed if at least one hit in one of the two innermost pixel layers is found. The reconstruction is therefore limited to displaced γ_d decays occurring after the first two pixel layers, and in the pseudorapidity interval $|\eta| < 2.5$, corresponding to the ID coverage. Finally, muons found inside the transition region of the MS, between the barrel and endcap, in the pseudorapidity range $1.0 \leq |\eta| \leq 1.1$, are rejected.

Muons are clustered in muonic-DPJs using a Cambridge–Aachen clustering algorithm [94]. The algorithm starts from the highest p_T muon and then searches for additional muons lying within a cone of size $\Delta R = 0.4$ opened around the muon momentum vector. If an additional muon is found, the vector sum of the momenta

of the two objects is taken as the new DPJ momentum. The clustering stops when no additional muon is found in the cone. If a jet is found in the cone, the DPJ is discarded.

The main source of background to the signal μDPJs are cosmic-ray muons that cross the detector in time coincidence with a pp interaction. These are discriminated using a Boosted Decision Tree (BDT) with gradient boosting, an algorithm known to provide state of the art performance in classification tasks without suffering from large overfitting, implemented in the TMVA framework [66]. The BDT training is configured to use 1000 of trees in the forest with a minimum percentage of training events required in a leaf node of 2.5%. The maximum depth allowed for each decision tree is set to 2 as the gradient boosting works best on weak classifiers and small individual decision trees are much less prone to overtraining. The method robustness is enhanced by reducing the learning rate of the algorithm by setting the parameter which controls the weight of the individual trees to 0.1. This demands more trees to be grown but can significantly improve the accuracy of the prediction in difficult settings. The gradient boosting algorithm may also benefit from the introduction of a bagging-like resampling to use random subsamples of the training events for growing the trees for each iteration. The relative size of the bagged event sample to the original size of the dataset is set to 0.5. The training of the μBDT uses half of the available statistics in the samples, the other half being used for validation. Events are chosen in alternating turns for the training and test samples as they occur in the source. The training uses as input the cosmic dataset as background sample and the MC sample with $m_{\mathrm{H}} = 125$ GeVas signal. The following properties of the constituent muon tracks of the DPJ are used as BDT input variables to distinguish a signal μDPJ from background:

- z_0, longitudinal impact parameter: the minimum separation in the z-coordinate between the muon track and the primary vertex[1] (PV) measured at the point of closest approach of the muon track to the beam line. Signal muons, despite being displaced, are expected to point to the PV due to the high boost, resulting in a peaked distribution around zero. Given the displacement of the dark photon, no inner detector hits are expected and the correct PV identification relies on initial state radiation (ISR) jets. The systematic uncertainty associated to ISR jets and its impact on the final results are discussed in Section 5.6. Cosmic-ray muons do not have a preferred direction along the z-coordinate, resulting in a broad, almost flat, z_0 distribution.

- muon timing: time of the muon track corrected by the time of flight from the interaction point [95]; looking at the time differences between the RPC middle layer (t_1^*) and RPC outer layer (t_2^*) of the MS, it is possible to identify the direction of flight of the muon (outgoing or incoming), as described in equation 5.2. This variable is important only in the north hemisphere, $\phi > 0$, where signal muons and cosmic muons have opposite directions. Two peaks are expected: one for the cosmic-ray muons, peaked at ~ 20 ns (twice the time

[1]The primary interaction vertex is defined as the vertex with the largest value of Σp_{T}^2, the sum of the squared transverse momenta of all the tracks originating from the vertex.

of flight from the RPC middle layer to the RPC outer layer), and one for the signal muons, peaked at ~ 0 ns.

$$
\begin{aligned}
&T(\text{High Pt}) = t_2^* - t_2^{\text{flight}} \\
&T(\text{Low Pt}) = t_1^* - t_1^{\text{flight}} \\
&\Delta T(\text{High-Low})(\text{for collisions}) = 0 \\
&\Delta T(\text{High-Low})(\text{for cosmics}) = -2(t_2^{\text{flight}} - t_1^{\text{flight}}) = \\
&-2(\text{time of flight})
\end{aligned}
\tag{5.2}
$$

- η, pseudorapidity: cosmic-ray muons are expected to come from the top of the ATLAS detector resulting in a peaked distribution.

- ϕ, azimuthal angle: signal muons are expected to have no preferred direction in the azimuth angle, resulting in a flat distribution. Cosmic-ray muons cross the detector from the top of the ATLAS detector, resulting in a double peak distribution.

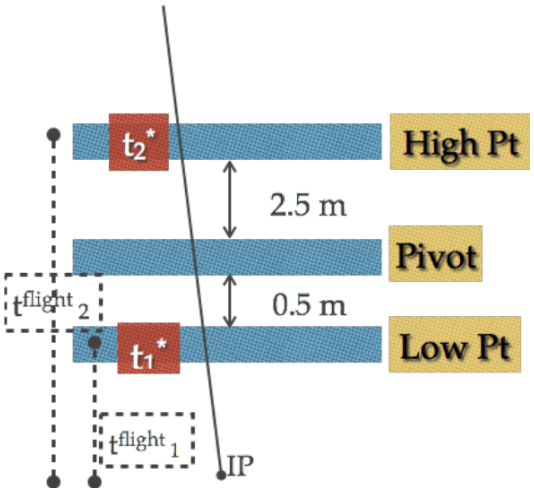

Figure 5.6. Visual scheme of the muon timing variable computation described in Equation 5.2. The pivot layer corresponds to the top layer of the RPC middle station of the MS.

All muonic-DPJ BDT (μBDT) input variables are shown in Figure 5.7.

The μBDT output is shown in Figure 5.8 (left) for both the cosmic-dataset, in red, and the $H \rightarrow 2\gamma_{\text{d}} + X$ signal sample with $m_H = 125$ GeV , in blue. Background-like DPJ muons are given negative values, while signal like muons are given positive values. A clear separation between signal and background muons of the μDPJs is seen.

Figure 5.8 (right) shows the selection efficiencies and significance, when assuming the same number of events for signal and background.

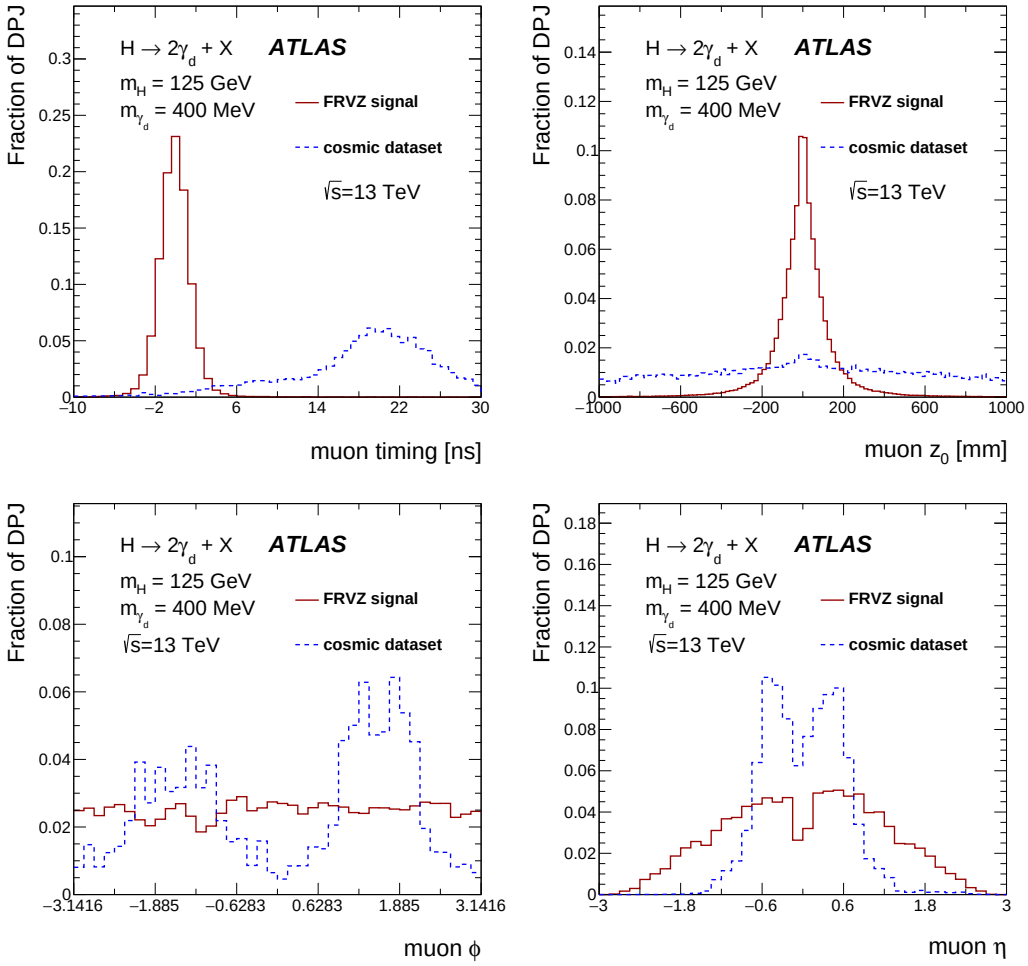

Figure 5.7. μDPJ discriminating variables used as input for the μBDT.

The cut on this output is chosen to be $\mu\text{BDT} > 0.21$; the value that yields the highest signal significance, $S/\sqrt{S+B}$, where S is the number of signal events and B the number of background events. The significance as a function of the μBDT cut, with the number of signal and background events normalised to 36.1 fb^{-1}, is shown in Figure 5.9

The correlation between the variables used in the μBDT definition is evaluated and reported in Figure 5.10.

An alternative μBDT is trained with a heavy scalar signal sample with $m_{\text{H}} = 800$ GeV, to study the μBDT output dependence on the training sample. The relative significance variation by adopting the alternative μBDT is checked and results are shown in Fig. 5.11. The signal significance is found to be only mildly dependent on the input model, thus the standard μBDT trained on the signal sample with $m_H = 125$GeV will be used for all samples.

The outputs of the μBDT for the different FRVZ signal samples used in the analysis are shown in Fig. 5.12.

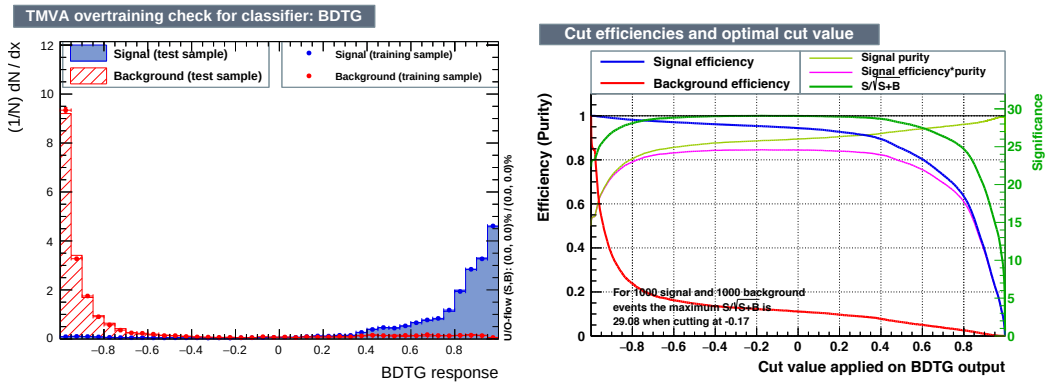

(a) (b)

Figure 5.8. (a): μBDT distribution for signal and background (test and training samples); (b): efficiency, purity and significance.

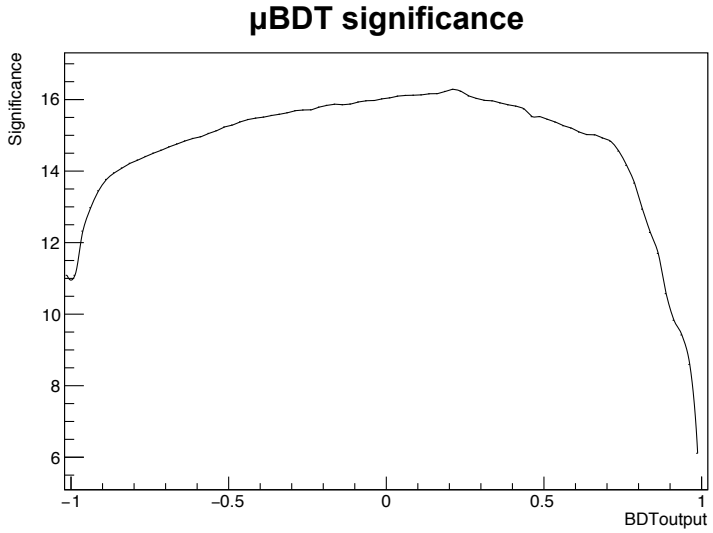

Figure 5.9. Significance as a function of the μBDT cut, computed using the $H \to 2\gamma_{\mathrm{d}} + X$ signal model with $m_{\mathrm{H}} = 125$ GeV and the data as background. The working point has been set at 0.21.

5.3.2 Hadronic-DPJ

Jets used in this analysis are reconstructed with an anti-k_t calorimetric algorithm [62, 63], with a ΔR cone of 0.4. These jets are expected to have no associated activity in the ID, a large fraction of the total deposited energy in the hadronic calorimeter (HCAL) and to be narrower than ordinary jets. Jets are required to have a transverse momentum $p_{\mathrm{T}} \geq 20$ GeV and $|\eta| < 2.5$. The weighted time difference between the bunch crossing time and the time of energy deposition in the calorimeter cells is required to be $|t| < 4$ ns, to reduce the out-of-time cosmic-ray background. Finally, fake jets in the transition region between barrel and end-cap are removed by requiring the fraction of deposited energy in the Tile Gap scintillators to be less than 0.9 of

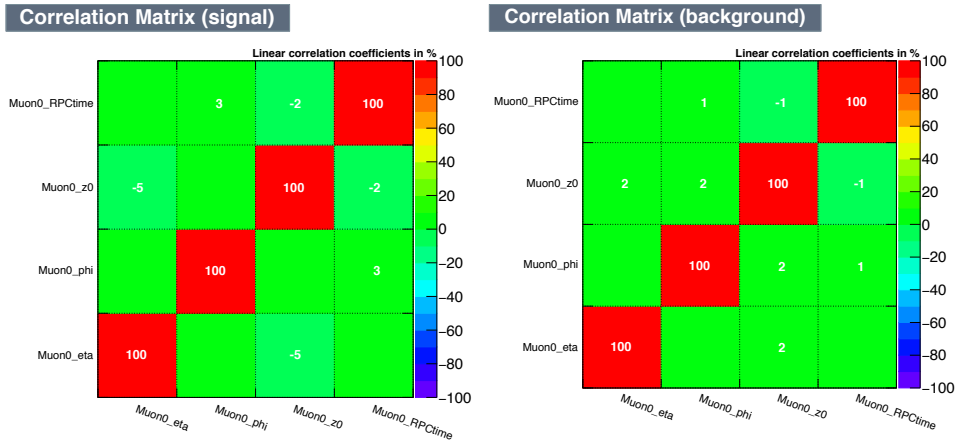

(a) signal (b) background

Figure 5.10. Correlation between the variables used in the μBDT for muonic dark-photon jets.

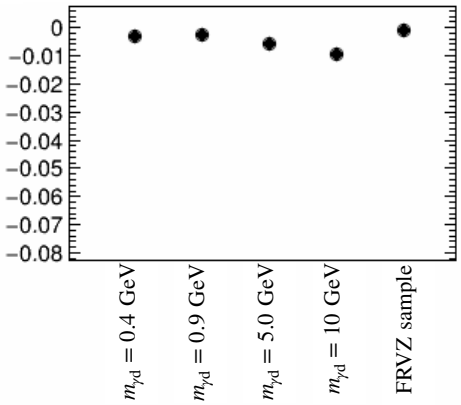

Figure 5.11. Significance variation for the μBDT selection, when the training is performed on FRVZ model with heavy Higgs $m_H = 800$GeV. The variation has to be considered with respect to the standard μBDT trained on FRVZ with $m_H = 125$GeV.

the total energy.

The main source of background for the signal jets are rare QCD multi-jet events with in-flight decays and punch through. These jets are separated from the expected signal jets using a BDT discriminant, with the same configuration of the μBDT, trained on the signal sample and multi-jet MC samples. The hadronic-DPJ BDT (hBDT) exploits the following features of the jets for the discrimination:

- jet width: the p_{T}-weighted sum of the ΔR between each energy cluster and the jet axis. Signal jets are expected to be narrower on average than ordinary jets since they are produced just before or inside the calorimeters;

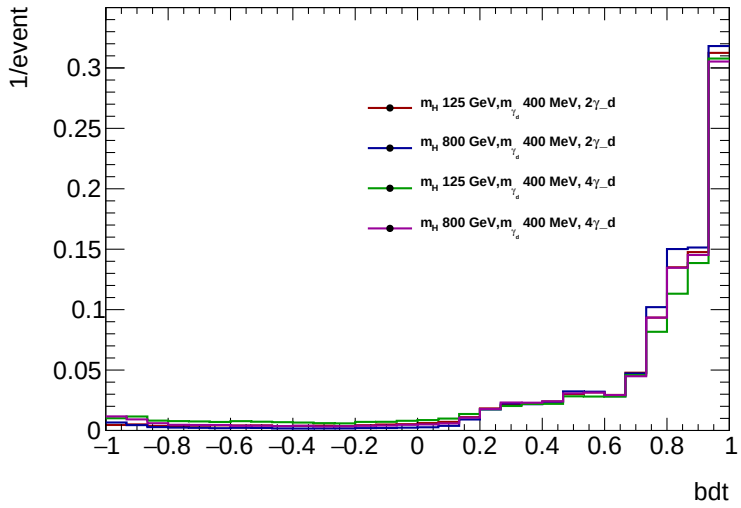

Figure 5.12. μBDT output for the different signal MC samples.

- jet vertex tagger (JVT) output [64]: the JVT is designed to distinguish pile-up jets from jets originating from the PV. It exploits a multivariate combination of track variables, like the p_{T}-weighted sum of the tracks from the primary vertex, that is sensitive to pile-up. Signal like jets mimic pile-up jets, due to their displacement, therefore this variable is used oppositely to its typical usage in ATLAS. The possible pile-up contamination due to its atypical usage has been checked on the zero-bias dataset and found to be negligible;

- $E_{\mathrm{ECAL}}/E_{\mathrm{total}}$, electromagnetic fraction: ratio of the energy deposition in the ECAL to the total energy. Signal jets coming from a displaced decay, just before or inside the hadronic calorimeter, are expected to have a low electromagnetic energy deposit but a high energy deposited in the hadronic calorimeter. A pre-selection cut on this variable $E_{\mathrm{ECAL}}/E_{\mathrm{total}} \leq 0.4$ is applied before the hBDT training;

- jet mass: as defined by the jet clustering algorithm [96] as the norm of the four-momentum sum of constituents inside a jet;

- jet charge: momentum-weighted charge sum constructed from tracks associated [97] with the jet;

- jet timing: energy-weighted average of the timing for each cell in the jet.

All hBDT input variables are shown in Figure 5.13.

The hBDT is trained, validated and optimised following the same procedure as the μBDT. The hBDT output is shown in Figure 5.14 (left) for the multi-jet background, in red, and the $H \rightarrow 2\gamma_{\mathrm{d}} + X$ signal sample with $m_H = 125$ GeV , in blue. The computed selection efficiencies and signal purity as a function of the output value are shown in Figure 5.14 (right). The peak at –0.2 in the BDT output distributions corresponds to jets with a JVT output that indicates a low pile-up

probability. The cut value on the output is chosen to be hBDT $>$ 0.91, value that yield the highest signal significance as can be seen in Figure 5.15.

The correlation between the variables used in the hBDT definition is evaluated and shown in Figure 5.16.

A dedicated hBDT, trained with an alternative signal sample with a heavy scalar with $m_{\mathrm{H}} = 800$ GeV, is studied to verify the output dependence from the training sample. Results are shown in Fig. 5.17, where a dependence on the Higgs mass is seen. This results in an overall improvement by 18 % when optimising the hBDT for a different mass point. For this search, the hBDT has been optimised for the selection of the $m_{\mathrm{H}} = 125$ GeV Higgs model and not optimised for the BSM heavy scalar.

The different outputs of the hBDT for the different FRVZ signal samples used in the analysis are shown in Fig. 5.18

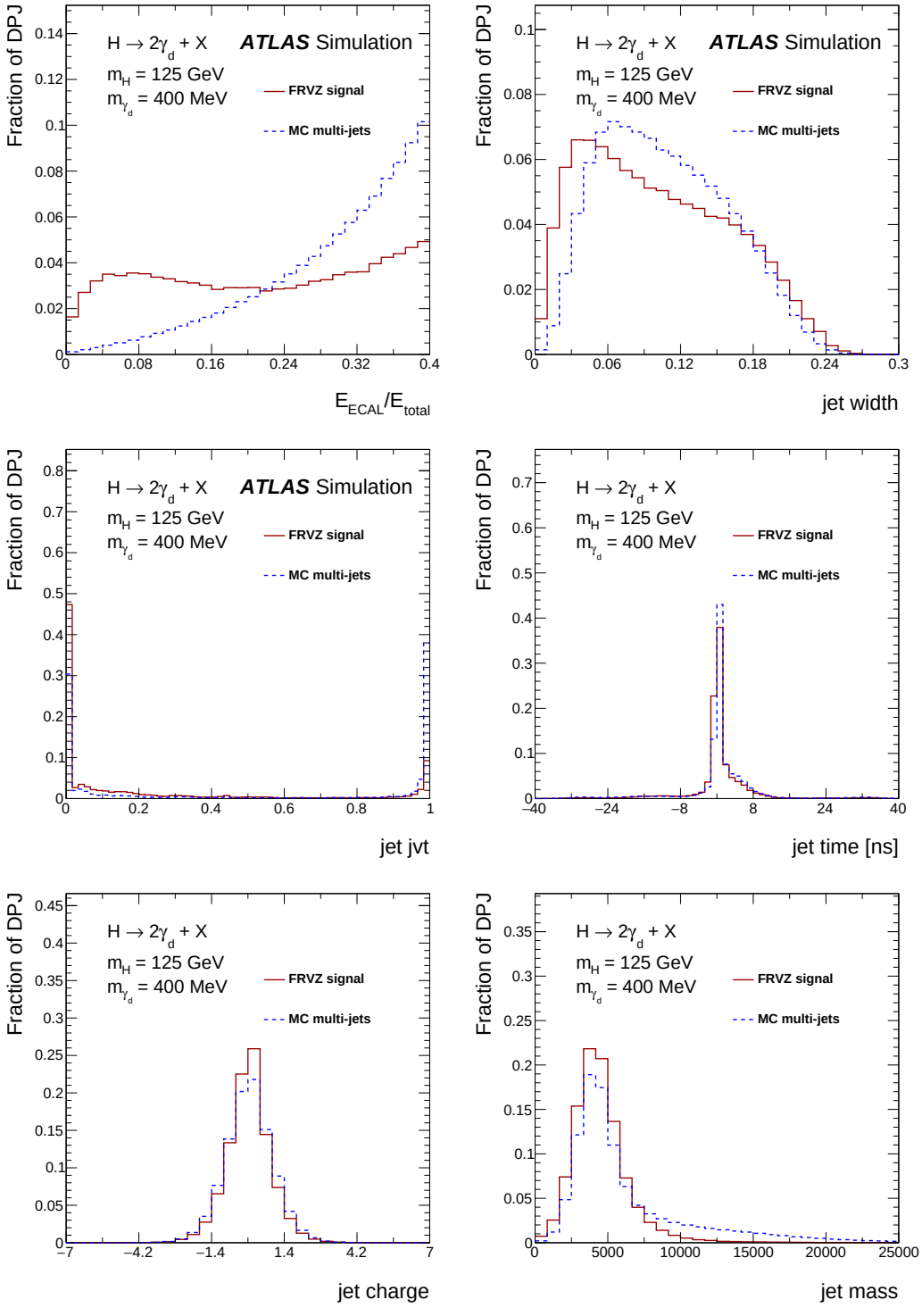

Figure 5.13. hDPJ discriminating variables.

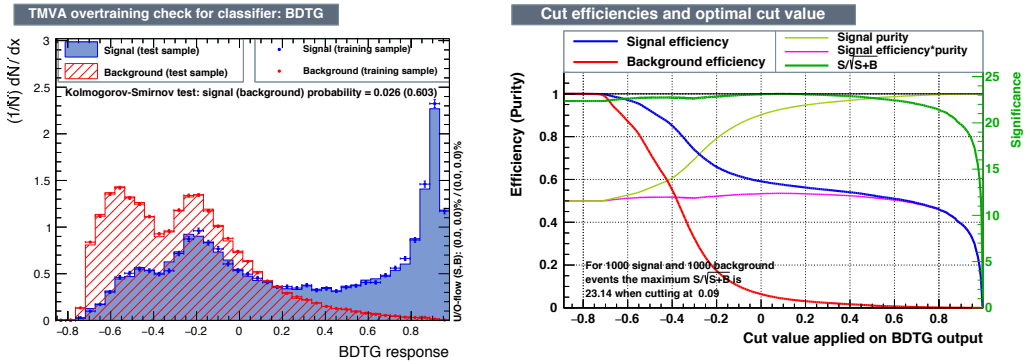

(a) (b)

Figure 5.14. (a): hBDT distribution for signal and background (test and training samples); (b): efficiency, purity and significance for the hBDT cuts.

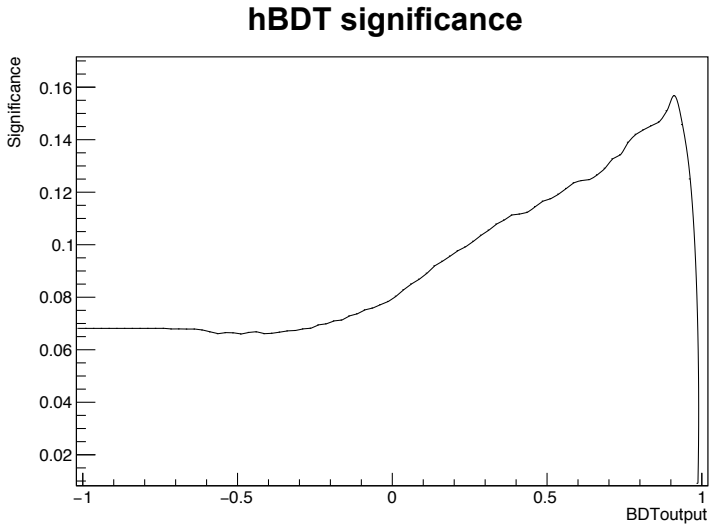

Figure 5.15. Significance (Eq. 5.2) as a function of the hBDT cut, using the benchmark model as signal and the data as background. The working point has been set at 0.91.

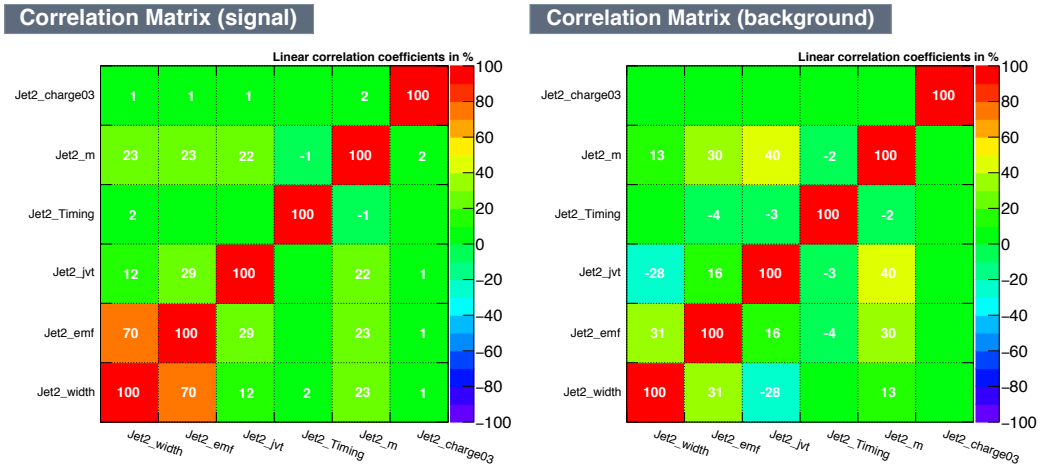

(a) signal (b) background

Figure 5.16. Correlation between the variables used in the hBDT for hadronic dark-photon jets.

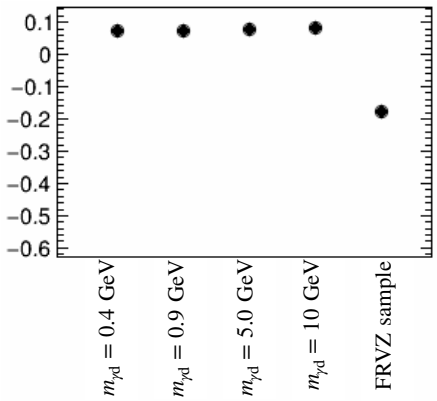

Figure 5.17. Significance variation for the hBDT selection, when training is performed on FRVZ model with heavy Higgs $m_{\mathrm{H}} = 800\mathrm{GeV}$. The variation has to be considered with respect to the standard hBDT trained on FRVZ with $m_{\mathrm{H}} = 125\mathrm{GeV}$.

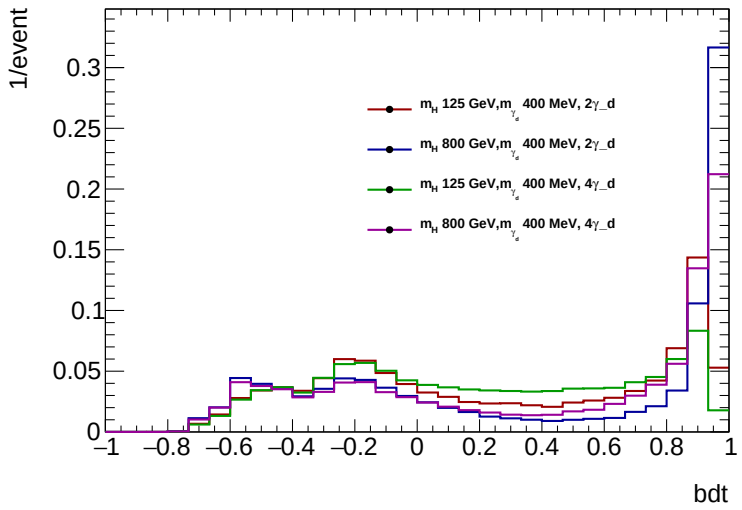

Figure 5.18. hBDT output for different FRVZ signal samples.

5.4 Event selection

Events selected by the triggers are required to have a good reconstructed PV and the presence of at least two reconstructed DPJs. Events with more than two reconstructed DPJs are included in the analysis. The DPJ with the highest transverse momentum is tagged as the leading one and the DPJ with largest $\Delta\phi$ to the leading one is tagged as the subleading. In the $H \to 2\gamma_{\mathrm{d}} + X$ with $m_{\mathrm{H}} = 125$ GeV benchmark model, more than two DPJs are found in 9% of the events.

Three channels are then considered:

- μDPJ–μDPJ;
- μDPJ–hDPJ, either the μDPJ or the hDPJ may be the leading DPJ;
- hDPJ–hDPJ.

A final selection is then applied on the single DPJ depending on its type, as described in Section 5.3 and summarised here:

- **μDPJ:**
  1. *muon η cut*: $|\eta| \leq 1.0$ or $|\eta| \geq 1.1$.
  2. *noCB cut*: veto on combined muon inside the μDPJ.
  3. *μBDT cut*: $\mu BDT \geq 0.21$.
- **hDPJ:**
  1. *Tile gap* cut: $E_{tilegap}/E_{tot} \leq 0.9$.
  2. *Jet timing* cut: $|t| \leq 4$ns.
  3. *hBDT* cut: $hBDT \geq 0.91$.

In Table 5.6 the pre-selection for all the signal samples is reported, rescaled to the nominal integrated luminosity of 36.1 fb^{-1}. The detailed cut-flows per signal sample are given in Tables 5.7 to 5.12.

	$H \to 2\gamma_{\mathrm{d}} + X$ $m_H = 125$ GeV $m_{\gamma_{\mathrm{d}}} = 0.4$ GeV $c\tau_{\gamma_{\mathrm{d}}} = 49$ mm	$H \to 2\gamma_{\mathrm{d}} + X$ $m_H = 125$ GeV $m_{\gamma_{\mathrm{d}}} = 0.4$ GeV $c\tau_{\gamma_{\mathrm{d}}} = 4.9$ mm	$H \to 2\gamma_{\mathrm{d}} + X$ $m_H = 125$ GeV $m_{\gamma_{\mathrm{d}}} = 0.4$ GeV $c\tau_{\gamma_{\mathrm{d}}} = 492$ mm	$H \to 4\gamma_{\mathrm{d}} + X$ $m_H = 125$ GeV $m_{\gamma_{\mathrm{d}}} = 0.4$ GeV $c\tau_{\gamma_{\mathrm{d}}} = 82.4$ mm	$H \to 2\gamma_{\mathrm{d}} + X$ $m_H = 800$ GeV $m_{\gamma_{\mathrm{d}}} = 0.4$ GeV $c\tau_{\gamma_{\mathrm{d}}} = 12$ mm	$H \to 4\gamma_{\mathrm{d}} + X$ $m_H = 800$ GeV $m_{\gamma_{\mathrm{d}}} = 0.4$ GeV $c\tau_{\gamma_{\mathrm{d}}} = 21$ mm
initial	174702 ± 417	174612 ± 417	174664 ± 417	174682 ± 417	14461 ± 120	14454 ± 120
trigger	6940 ± 83	8797 ± 93	894 ± 30	12493 ± 112	2295 ± 48	3151 ± 56
PV	6940 ± 83	8797 ± 93	894 ± 30	12493 ± 112	2295 ± 48	3151 ± 56
2 DPJs	2631 ± 51	4173 ± 65	163 ± 13	5261 ± 73	771 ± 28	1611 ± 40

Table 5.6. Analysis selections on the FRVZ signal model rescaled to the integrated luminosity of 36.1 fb^{-1}. All DPJ pair combinations are taken into account.

	$H \to 2\gamma_d + X$ $m_H = 125$ GeV, $m_{\gamma_d} = 0.4$ GeV, $c\tau_{\gamma_d} = 49$ mm		
	muonic-muonic	muonic-hadronic	hadronic-hadronic
2 DPJ	1329 ± 36	583 ± 24	148 ± 12
muon η	1148 ± 34	553 ± 24	–
no CB muon	811 ± 28	476 ± 22	–
gap ratio	–	466 ± 22	141 ± 12
jet timing	–	466 ± 22	141 ± 12
BDT	691 ± 26	82 ± 9	9 ± 3

Table 5.7. Event selection for the $H \to 2\gamma_d + X$ process with $m_H = 125$ GeV, $m_{\gamma_d} = 0.4$ GeV, and $c\tau_{\gamma_d} = 49$ mm. A luminosity of 36.1 fb^{-1} is assumed.

	$H \to 2\gamma_d + X$ $m_H = 125$ GeV, $m_{\gamma_d} = 0.4$ GeV, $c\tau_{\gamma_d} = 4.9$ mm		
	muonic-muonic	muonic-hadronic	hadronic-hadronic
2 DPJ	2212 ± 47	676 ± 26	128 ± 11
muon η	2014 ± 45	648 ± 26	–
no CB muon	686 ± 26	409 ± 20	–
gap ratio	–	407 ± 20	120 ± 11
jet timing	–	407 ± 20	120 ± 11
BDT	634 ± 25	48 ± 7	1 ± 1

Table 5.8. Event selection for the $H \to 2\gamma_d + X$ process with $m_H = 125$ GeV, $m_{\gamma_d} = 0.4$ GeV, and $c\tau_{\gamma_d} = 4.9$ mm. A luminosity of 36.1 fb^{-1} is assumed.

	$H \to 2\gamma_d + X$ $m_H = 125$ GeV, $m_{\gamma_d} = 0.4$ GeV, $c\tau_{\gamma_d} = 492$ mm		
	muonic-muonic	muonic-hadronic	hadronic-hadronic
2 DPJ	66 ± 8	61 ± 8	13 ± 4
muon η	58 ± 8	57 ± 8	–
no CB muon	48 ± 5	49 ± 7	–
gap ratio	–	49 ± 7	12 ± 4
jet timing	–	49 ± 7	12 ± 4
BDT	39 ± 6	2 ± 1	0

Table 5.9. Event selection for the $H \to 2\gamma_d + X$ process with $m_H = 125$ GeV, $m_{\gamma_d} = 0.4$ GeV, and $c\tau_{\gamma_d} = 492$ mm. A luminosity of 36.1 fb^{-1} is assumed.

	$H \to 4\gamma_d + X$ $m_H = 125$ GeV, $m_{\gamma_d} = 0.4$ GeV, $c\tau_{\gamma_d} = 82.4$ mm		
	muonic-muonic	muonic-hadronic	hadronic-hadronic
2 DPJ	1324 ± 36	971 ± 31	142 ± 12
muon η	1109 ± 33	881 ± 30	–
no CB muon	765 ± 28	717 ± 27	–
gap ratio	–	702 ± 27	137 ± 12
jet timing	–	702 ± 27	137 ± 12
BDT	548 ± 23	25 ± 5	0

Table 5.10. Event selection for the $H \to 4\gamma_d + X$ process with $m_H = 125$ GeV, $m_{\gamma_d} = 0.4$ GeV, and $c\tau_{\gamma_d} = 82.4$ mm. A luminosity of 36.1 fb^{-1} is assumed.

	$H \to 2\gamma_d + X$ $m_H = 800$ GeV, $m_{\gamma_d} = 0.4$ GeV, $c\tau_{\gamma_d} = 12$ mm		
	muonic-muonic	muonic-hadronic	hadronic-hadronic
2 DPJ	107 ± 10	254 ± 16	258 ± 16
muon η	97 ± 10	240 ± 16	–
no CB muon	60 ± 8	205 ± 14	–
gap ratio	–	204 ± 14	251 ± 16
jet timing	–	204 ± 14	251 ± 16
BDT	54 ± 7	132 ± 12	51 ± 7

Table 5.11. Event selection for the $H \to 2\gamma_d + X$ process with $m_H = 800$ GeV, $m_{\gamma_d} = 0.4$ GeV, and $c\tau_{\gamma_d} = 12$ mm. A luminosity of 36.1 fb^{-1} is assumed.

	$H \to 4\gamma_d + X$ $m_H = 800$ GeV, $m_{\gamma_d} = 0.4$ GeV, $c\tau_{\gamma_d} = 21$ mm		
	muonic-muonic	muonic-hadronic	hadronic-hadronic
2 DPJ	136 ± 12	250 ± 16	170 ± 13
muon η	118 ± 11	233 ± 15	–
no CB muon	70 ± 8	188 ± 14	–
gap ratio	–	184 ± 14	164 ± 13
jet timing	–	184 ± 14	164 ± 13
BDT	57 ± 8	85 ± 9	30 ± 6

Table 5.12. Event selection for the $H \to 4\gamma_d + X$ process with $m_H = 800$ GeV, $m_{\gamma_d} = 0.4$ GeV, and $c\tau_{\gamma_d} = 21$ mm. A luminosity of 36.1 fb^{-1} is assumed.

5.5 Background estimation

The main sources of background for the DPJ signal are cosmic-ray muons for the μDPJ and QCD multi-jet production for the hDPJ and μDPJ. The second leading background for both DPJ types is beam induced background (BIB).

The cosmic-ray background is composed of a bundle of high-energy muons coming from above that cross the detector in time coincidence with a bunch-crossing interaction [98]. These muons are mostly concentrated in the barrel region and although the rate is low, after the event selection they account for up to 7% of the total background in all the channels. Cosmic-ray muons can also contribute as sub-dominant background for the hDPJ in the event of a hard bremsstrahlung in the HCAL that may produce a fake jet.

Rare QCD multi-jet events are the dominant background source for the hDPJ due to the very high production cross-section. They consist of high-energy jets produced by the pp interaction that give rise to in-flight decays of K/π and heavy flavour quarks, and punch-through events. These result in displaced jets that could pass the event selection. Since the cosmic-ray background is strongly reduced by the event selection, multi-jet becomes the main background also to the μDPJ signature in the signal region.

BIB background [71] is a non-collisions background produced by the interaction of protons with residual beam gas or beam pipe elements, e.g. with beam collimators. In such an occurrence high-energy muons that cross the detector horizontally, parallel to the beam pipe, are produced. When this happens in the HCAL a displaced jet may be reconstructed mimicking a hDPJ. An event display of a BIB jet event is shown in Figure 5.19. This background is strongly reduced by the event selection, leading to a negligible contribution to the final background estimation.

5.5.1 ABCD method

To estimate the multi-jet background in the signal region a data-driven method called ABCD is used. This method relies on the definition of two discriminating variables uncorrelated for background events. A cut on each of these two variables is defined to form a 2×2 matrix with four well defined and non-overlapping regions: a signal region, A, which contains the majority of signal events, and three control regions, B, C, D, which contain mostly background events. The number of background events in the signal region can thus be evaluated as $N_A = N_D \times N_B/N_C$. The presence of multiple sources of background may lead to correlations in the two ABCD variables, invalidating the background estimation. If present, a well-known secondary source of background should be subtracted from the observation before applying the method. This is the case for this study where the cosmic-ray background is subtracted form the considered multi-jet QCD background estimation.

The two variables used to perform the method and define the ABCD plane are $\max(\Sigma p_{\mathrm{T}})$ and $|\Delta\phi|_{DPJ}$, defined in the following:

Isolation in the inner detector ($\max(\Sigma p_{\mathrm{T}})$)

The DPJ track isolation in the inner detector Σp_{T} is defined as the scalar sum of the transverse momenta of the tracks with $p_{\mathrm{T}} > 0.5$ GeV, reconstructed in the

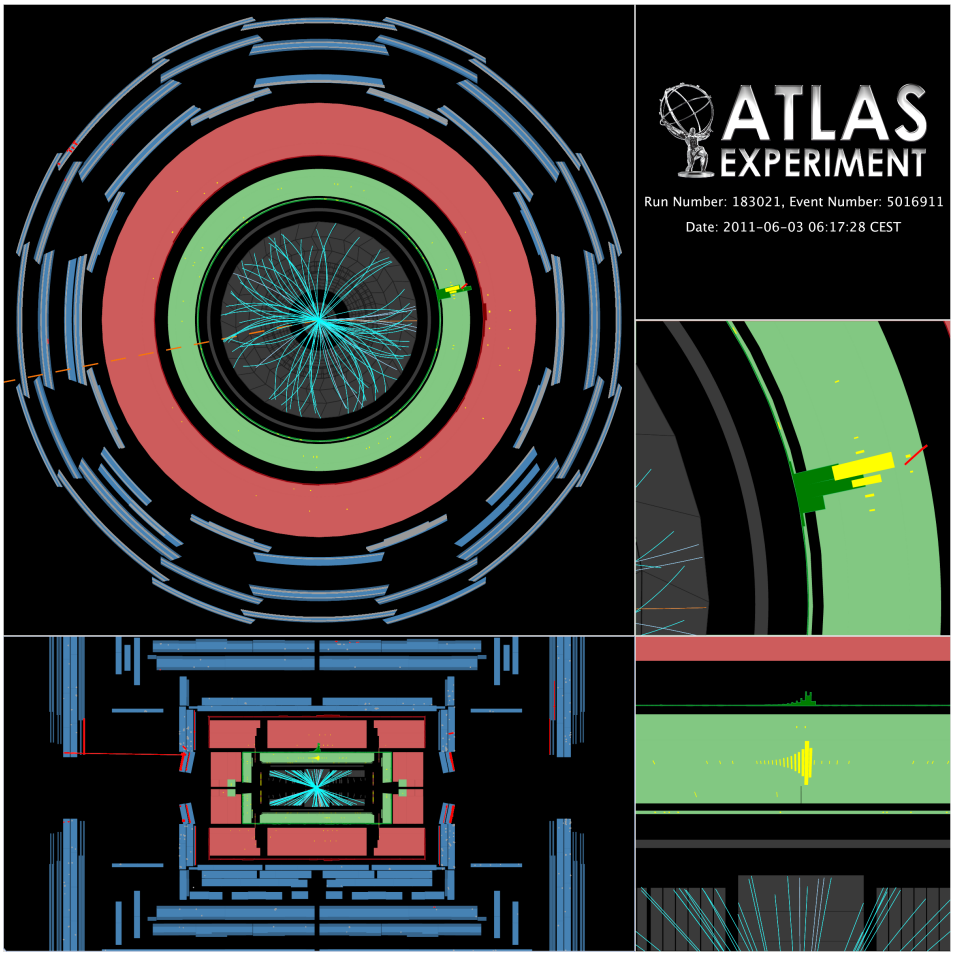

Figure 5.19. Example of an event with a BIB muon entering from the right and causing a fake jet [71].

ID and matched to the PV of the event within a $\Delta R = 0.4$ cone around the DPJ direction. The PV matching helps to reducing the dependence of Σp_{T} on the amount of pile-up. $\max(\Sigma p_{\mathrm{T}})$ is chosen as discriminating variable in the ABCD plane, where *max* indicates the highest Σp_{T} of the DPJs in the event. The Σp_{T} for the signal benchmark model and for multi-jet background events are shown in Figure 5.20. Displaced DPJs are expected to be highly isolated in the ID and a cut on this variable is highly effective in rejecting multi-jet background events.

Azimuthal opening angle ($\Delta\phi$)

It is defined as the opening angle between the two DPJs in the transverse plane. The reconstructed $\Delta\phi$ for the signal benchmark model and multi-jet background events is shown in Figure 5.21. Signal DPJs are expected to be back-to-back in the transverse plane, due to the production mode in the two-body decay of a Higgs boson generated at rest, hence a cut on $\Delta\phi$ reduces the background without significantly affecting the signal efficiency.

An example of the ABCD matrix is shown in Figure 5.22. The correlation

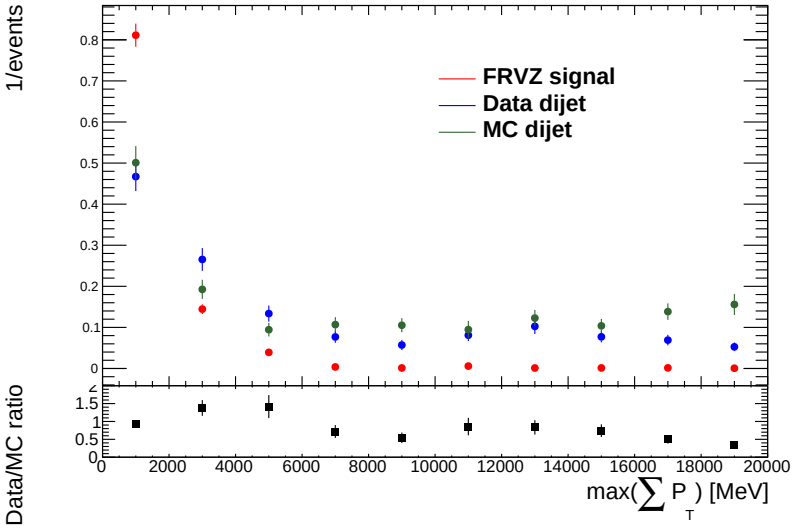

Figure 5.20. Distributions of Σp_{T} from MC QCD dijet sample (green), di-jet dataset (blue) and from DPJs in FRVZ MC (red). Ratio of the di-jet dataset to the QCD MC sample is also shown. All distributions are normalized to unit area.

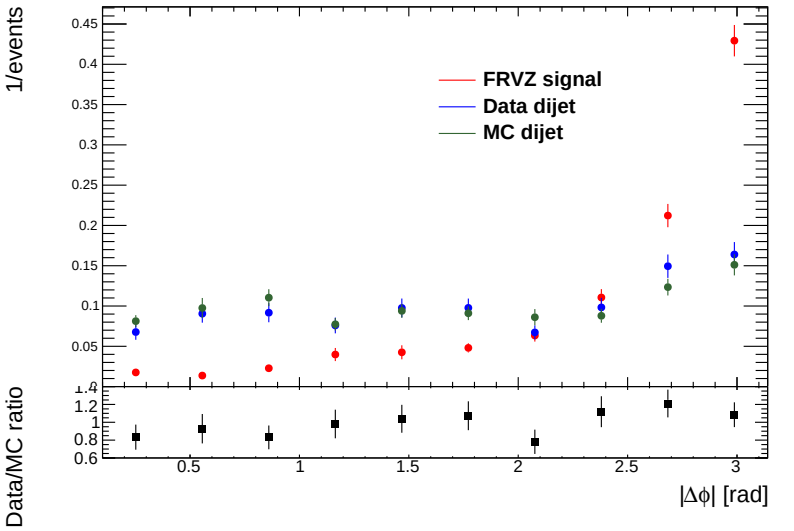

Figure 5.21. $\Delta\phi$ between the two DPJs in MC signal sample (red), dijet QCD MC sample (green) and di-jet dataset (blue). Ratio of the di-jet dataset to the QCD MC sample is also shown. All distributions are normalized to unit area.

between these two variables have been checked in a subset of 3.7 fb^{-1} of the 2016 dataset, and the results are shown in Figure 5.23. The linear correlation factor is found to be 6% for the muonic-muonic and muonic-hadronic channels and 5% for the hadronic hadronic channel. The effect of this correlation on the final result is found to be negligible compared to the statistical accuracy and hence not included in the final fit. The possible pile-up contamination in the ABCD plane is estimated

in the zero-bias dataset and results to be negligible.

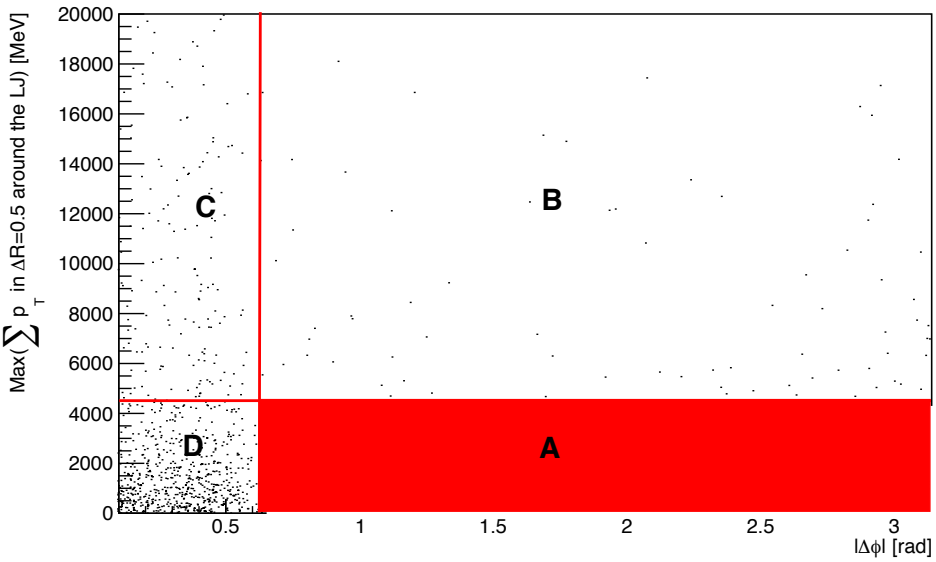

Figure 5.22. Scheme of the ABCD plane defined the $\Delta\phi$ and $\max(\Sigma p_{\mathrm{T}})$ variables.

The cuts defining the four regions are chosen to maximise the signal significance. Signal region A is defined by $\max(\Sigma p_{\mathrm{T}}) < 4.5$ GeV and $\Delta\phi > 0.625$ rad. Reversing one or both of the requirements regions B, C and D are defined: $\max(\Sigma p_{\mathrm{T}}) > 4.5$ GeV and $\Delta\phi > 0.625$ rad, $\max(\Sigma p_{\mathrm{T}}) > 4.5$ GeV and $\Delta\phi < 0.625$ rad, $\max(\Sigma p_{\mathrm{T}}) < 4.5$ GeV and $\Delta\phi < 0.625$ rad respectively.

Studies using the BIB dataset show a narrow distribution of events at small $\Delta\phi$, shown in Figure 5.24, that would contaminate the method in the hadronic-hadronic channel. Finally the requirement $\Delta\phi > 0.1$ rad is imposed in the ABCD plane to remove possible BIB contamination. This cut has no effect on the signal.

5.5.2 Beam induced background estimation

Beam induced background events are estimated in the BIB dataset by applying the event selection. The results are reported in Tables 5.13 and 5.14. No events survive the BDT cuts and enter any of the ABCD regions. The tight cut applied to the hBDT discriminant is observed to be very effective in the removal of BIB jets. The hBDT distribution of the two DPJs in the events is shown in Figure 5.25.

Additional cross-checks

Further checks on possible BIB event contamination are performed on collision data, collecting a BIB enriched data sample using an alternative version of the CalRatio trigger without isolation requirements, and vetoing the standard CalRatio trigger. BIB jet calorimeter deposits are expected to have an earlier reconstructed time with respect to objects from collisions. All physics object's timing measurements are corrected for the time-of-flight (TOF) from the interaction point, defined as

	BIB events
initial	2.71E+06
trigger	1.13E+06
PV	1.13E+06
2 DPJs	17071

Table 5.13. Result of the cut flow on the BIB dataset events. All DPJ pair combinations are taken into account.

	BIB events		
	muonic-muonic	muonic-hadronic	hadronic-hadronic
2 DPJ	0	2033	14858
muon η	0	1983	–
no CB muon	0	1983	–
gap ratio	–	1974	14552
jet timing	–	596	854
BDT	0	0	0
region A	0	0	0
region B	0	0	0
region C	0	0	0
region D	0	0	0

Table 5.14. DPJ pairs in each region of the ABCD plane for the 2015-2016 data sample, collected in the BIB dataset.

$t_{TOF} = \sqrt{(r^2 + z^2)}/c$ where r and z are the object positions and c the speed of light. The timing for objects coming from the hard scatter is therefore expected to be $t \sim 0$ (ns), while for BIB events it is expected to be $t = t_{TOF}^{BIB} - t_{TOF}$, where the BIB TOF is $t_{TOF}^{BIB} = \pm|z|/c$. BIB jet events may then be identified by looking for anomalous jet z-position versus timing distribution. A typical BIB jet distribution is shown in Figure 5.26 (the "banana plot").

The *banana plot* is checked in a subset of the collision data collected with the standard *CalRatio* trigger. Results are shown in Figure 5.26 before and after event selection. The effect of the $\Delta\phi$ cut is also shown. After the event selection, jets do not show any BIB behaviour.

Finally, the hBDT distribution for BIB events is investigated in the BIB enriched collision dataset. The hBDT output value for the two DPJs in the event are shown in Figure 5.27. The $\Delta\phi > 0.1$ cut is not included. The hBDT discriminant for the subleading DPJ is observed to be a powerful discriminant against BIB jets.

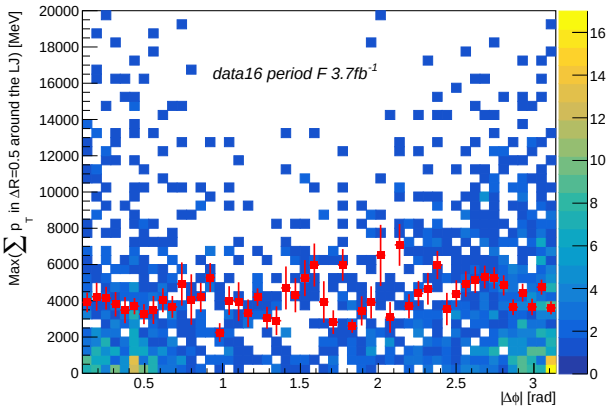

(a) muonic-muonic

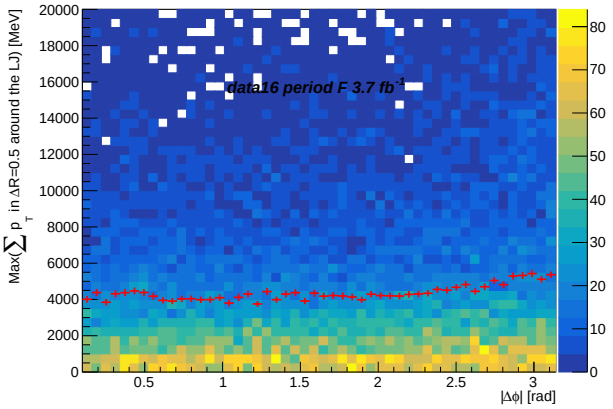

(b) muonic-hadronic

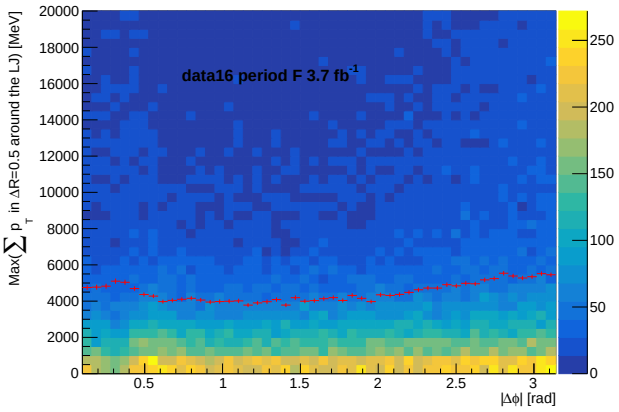

(c) hadronic-hadronic

Figure 5.23. Correlation between $\max(\Sigma p_{\mathrm{T}})$ and $\Delta\phi$ used in the ABCD method, on 16 period F of 2016 data corresponding to 3.7fb^{-1}. The points with error bars represent the profile histogram of $\max(\Sigma p_{\mathrm{T}})$ as a function of $\Delta\phi$.

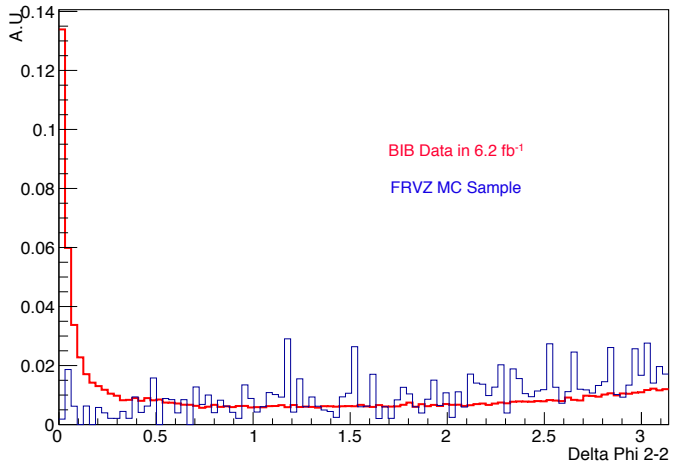

Figure 5.24. Residual BIB contamination in data (red) and signal MC sample (blue). An additional cut $|\Delta\phi| > 0.1$ has been imposed to remove these residual BIB events.

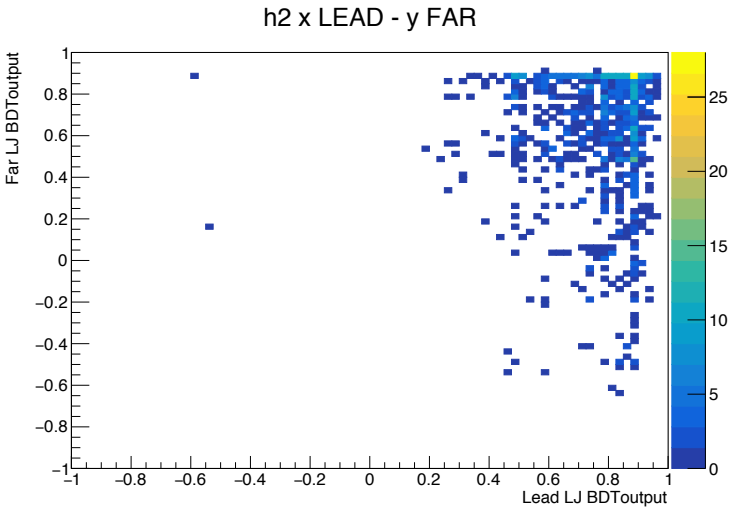

Figure 5.25. hBDT distribution for the two hadronic dark-photon jets in the BIB dataset events.

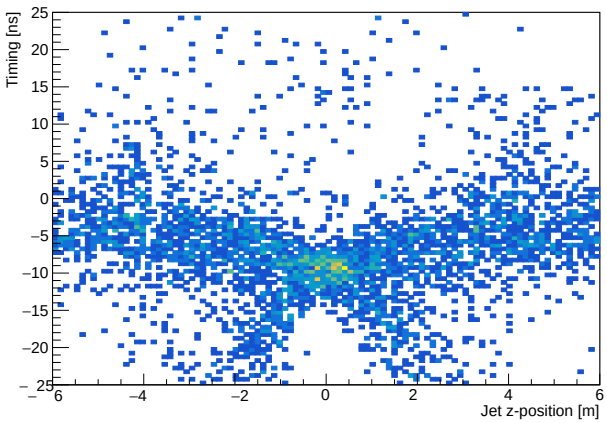

Figure 5.26. BIB jet time as a function of its z-position in the LAr and TileCal. The bands cover the radial extent of the detectors. The events shown are collisions data before the hBDT cut by using the *CalRatio* trigger without isolation and the cut $|\Delta\phi| < 0.1$.

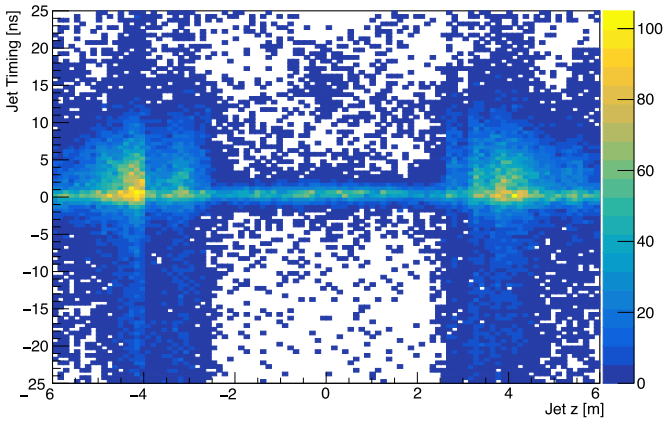

(a) All period A

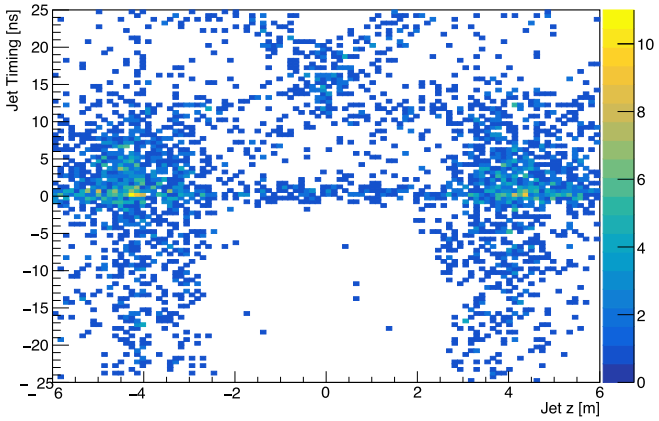

(b) $\Delta\phi < 0.1$

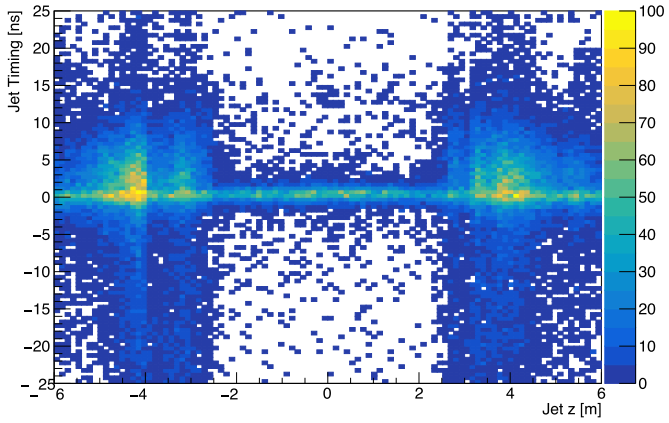

(c) $\Delta\phi \geq 0.1$

Figure 5.26. Subset of the collision sample corresponding to the period A of 2016 data taking. Data were collected with the standard *CalRatio* trigger. The jet z-position against the time distribution is shown for the full sample (a), for $\Delta\phi \leq 0.1$ (b), and for $\Delta\phi \geq 0.1$ (c).

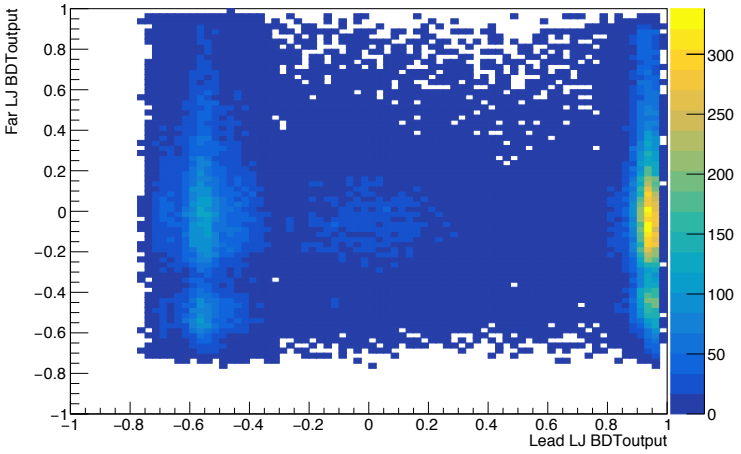

Figure 5.27. hBDT distribution for the two hadronic dark-photon jets in the BIB enriched dataset collected in collisions data. Additional $\Delta\phi > 0.1$ cut not imposed.

5.5.3 Estimation of contamination from cosmic rays

The number of cosmic-ray background events in the search region are estimated in the cosmic dataset by applying the event selection. Results are reported in Tables 5.15 and 5.16. These yields have to be scaled to the number of events in the *pp* collision data, considering the scale factor $F_{\mathrm{CR}} = 2.1$, introduced in Section 5.1.4.

The estimated cosmic-ray event yields are subtracted from each of the ABCD regions before using the ABCD method to estimate the multi-jet background yield.

	Cosmic events
initial	2.71E+06
trigger	2.25E+06
PV	2.25E+06
2 DPJs	30145

Table 5.15. Result of the cut-flow on the empty bunches triggered events (cosmic dataset). All DPJ pair combinations are taken into account. The ratio $F_{\mathrm{CR}} = 2.1$ between filled and empty bunch crossings is not considered in this table.

	Cosmic events		
	muonic-muonic	muonic-hadronic	hadronic-hadronic
2 DPJ	890	4026	24756
muon η	865	3916	–
no CB muon	865	3916	–
gap ratio	–	3902	24383
jet timing	–	1162	1140
BDT	5	5	1
region A	4	4	1
region B	0	0	0
region C	0	0	0
region D	1	1	0

Table 5.16. DPJ pairs in each region of the ABCD plane for the 2015-2016 data sample collected in the empty bunch crossings. The ratio $F_{\mathrm{CR}} = 2.1$ between filled and empty bunch crossings is not considered in this table.

5.5.4 Other negligible backgrounds

Additional potential backgrounds from SM processes are considered and studied with MC samples. The following processes, that could lead to multiple muons and jets, are evaluated: J/ψ, W+jets, Z+jets, $t\bar{t}$, single-top-quark, WW, WZ, and ZZ events. None of these processes has a non-negligible contribution after the trigger selection.

5.5.5 ABCD method validation

The validation of the ABCD method is performed in the validation regions (VRs), defined by the selection criteria described in Section 5.4 except for the BDT cuts which are inverted. These are defined in order to be as close as possible to the SR kinematic region and to have negligible signal and cosmic-ray contamination, which otherwise can bias the ABCD method validation. The μBDT cuts in the μDPJ–μDPJ VR are loosened for a statistically significant validation. The VR definitions are summarised in Table 5.17; the SRs are also reported for comparison.

Table 5.17. Summary of the definitions of the signal regions (SRs) and validation regions (VRs) used in the ABCD method.

Region	Channel	Criteria
SR	μDPJ–μDPJ	μBDT > 0.21 for both DPJs
	μDPJ–hDPJ	μBDT > 0.21 and hBDT > 0.91
	hDPJ–hDPJ	hBDT > 0.91 for both DPJs
VR	μDPJ–μDPJ	$-0.75 <$ μBDT < 0.35 for leading μDPJ, μBDT > -0.7 for subleading μDPJ
	μDPJ–hDPJ	$-0.5 <$ μBDT < 0.8 and $0.2 <$ hBDT < 0.8
	hDPJ–hDPJ	hBDT < 0.91 for both DPJs

In the VRs the linear correlation between the $\max(\Sigma p_{\mathrm{T}})$ and $\Delta\phi$ variables is checked to be less than 6% and the signal contamination to be less than 5%. The predicted yields in each of the ABCD regions in the VRs and the expected number of background events in region VR-A are reported in Table 5.18. The estimated cosmic-ray event yields are subtracted from each of the ABCD regions before using the method to estimate the multi-jet background yield. The observed number of events and the predicted number of events by the ABCD method are in full agreement within the statistical uncertainty.

DPJ pair type	B	C	D	Expected background in A	A
μDPJ–μDPJ	4	15	59	16 ± 9	13
μDPJ–hDPJ	455	87	308	1610 ± 210	1573
hDPJ–hDPJ	2556	536	14	67 ± 18	57

Table 5.18. Event count in each of the four regions of the ABCD plane in the validation regions and expected number of background events in region A. Statistical uncertainties are shown, these include also the statistical uncertainty on cosmic-ray events. The expected contribution from cosmic rays is included in all the regions, and in the background estimation.

5.5.6 QCD multi-jet background estimation

The QCD multi-jet background is estimated from the collision dataset by applying the ABCD method. The event distribution in the ABCD regions and the event

selection for the collision dataset are shown in Tables 5.19-5.20.

	2015 and 2016 data events
initial	3.04E+08
trigger	1.31E+08
PV	1.31E+08
2 DPJs	7.06E+06

Table 5.19. Result of the cut flow on 2015 and 2016 data. All DPJ pair combinations are taken into account.

	2015 and 2016 data events		
	muonic-muonic	muonic-hadronic	hadronic-hadronic
2 DPJ	18872	6.72E+05	1.75E+06
muon η	17672	6.55E+05	–
no CB muon	4065	1.56E+05	–
gap ratio	–	1.56E+05	1.72E+06
jet timing	–	8.71E+04	6.66E+05
BDT	946	244	105
region A	113	179	69
region B	24	8	13
region C	92	2	2
region D	463	45	15

Table 5.20. DPJ pairs in each region of the ABCD plane for the 2015-2016 data sample.

In Table 5.21 the final ABCD plane is reported with both the sources of background included and the total background estimation. The observed number of events in region A is in agreement with the predicted number of background events.

DPJ pair type	B	C	D	Expected A	A
μDPJ–μDPJ	24	92	463	128 ± 28 (stat.)	113
μDPJ–hDPJ	8	2	45	180 ± 138 (stat.)	179
hDPJ–hDPJ	13	2	15	100 ± 79 (stat.)	69

Table 5.21. Observed numbers of events in the ABCD regions and expected number of background events in region A. The expected contribution from cosmic rays is included in all the regions.

The distribution for events in the ABCD plane for both collision data and signal MC, $H \to 2\gamma_{\mathrm{d}} + X$ with $m_H = 125$ GeV, is shown for the μDPJ–μDPJ channel in Figure 5.28.

5.5.7 Signal yields

The yields in the ABCD plane for the signal MC benchmarks after the event selection are shown in Tables 5.22, 5.23, 5.24 and 5.25.

	$H \to 2\gamma_d + X$ $m_H = 125$ GeV, $m_{\gamma_d} = 0.4$ GeV, $c\tau_{\gamma_d} = 49$ mm		
	muonic-muonic	muonic-hadronic	hadronic-hadronic
region A	639 ± 25	74 ± 9	8 ± 3
region B	29 ± 5	0	1 ± 1
region C	0	0	0
region D	13 ± 4	7 ± 3	0

Table 5.22. Signal events distribution in the ABCD region for the FRVZ models assuming an luminosity of 36.1 fb^{-1}.

	$H \to 4\gamma_d + X$ $m_H = 125$ GeV, $m_{\gamma_d} = 0.4$ GeV, $c\tau_{\gamma_d} = 82$ mm		
	muonic-muonic	muonic-hadronic	hadronic-hadronic
region A	519 ± 23	22 ± 5	0
region B	11 ± 3	1 ± 1	0
region C	0	0	0
region D	13 ± 4	2 ± 1	0

Table 5.23. Signal events distribution in the ABCD region for the FRVZ models assuming an luminosity of 36.1 fb^{-1}.

	$H \to 2\gamma_d + X$ $m_H = 800$ GeV, $m_{\gamma_d} = 0.4$ GeV, $c\tau_{\gamma_d} = 12$ mm		
	muonic-muonic	muonic-hadronic	hadronic-hadronic
region A	610 ± 87	1544 ± 137	560 ± 87
region B	37 ± 22	62 ± 28	50 ± 25
region C	0	0	0
region D	0	0	0

Table 5.24. Signal events distribution in the ABCD region for the FRVZ models assuming an luminosity of 36.1 fb^{-1}.

	$H \to 4\gamma_{\mathrm{d}} + X$ $m_H = 800$ GeV, $m_{\gamma_{\mathrm{d}}} = 0.4$ GeV, $c\tau_{\gamma_{\mathrm{d}}} = 21$ mm		
	muonic-muonic	muonic-hadronic	hadronic-hadronic
region A	660 ± 91	996 ± 111	336 ± 65
region B	25 ± 18	50 ± 25	25 ± 18
region C	0	0	0
region D	0	0	0

Table 5.25. Signal events distribution in the ABCD region for the FRVZ models assuming an luminosity of 36.1 fb^{-1}.

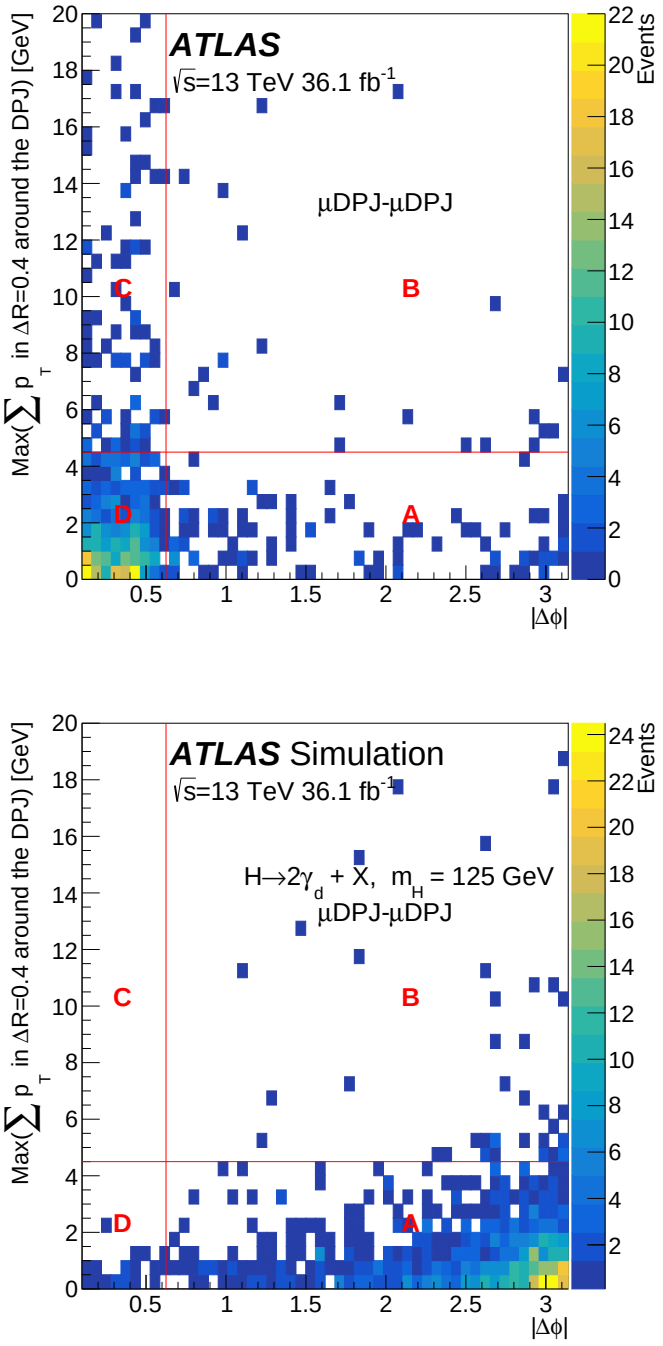

Figure 5.28. Opening angle between the two DPJs, $\Delta\phi$, vs inner-detector isolation, $\max(\Sigma p_{\mathrm{T}})$, for data (top) and MC signal $H \to 2\gamma_{\mathrm{d}} + X$ with $m_H = 125$ GeV (bottom) in the μDPJ–μDPJ channel. The red (solid) lines show the boundaries of the ABCD regions.

5.6 Systematic uncertainties

This section presents an overview of sources of systematic uncertainty studied for the dark-photon jet analysis.

Luminosity
The systematic uncertainty on the integrated luminosity measurement is 2.1%. It is derived following a methodology similar to that detailed in [99], based on a calibration of the luminosity scale using a x-y beam-separation scan with the LUCID-2 detector [100].

Muon reconstruction
The systematic uncertainty on the reconstruction of muons using only information from the MS is evaluated using a tag-and-probe method applied on $J/\psi \to \mu\mu$ data and MC samples, described in detail in [101]. J/ψ decay process shows similar topology and kinematics as the expected signal muons. The selection of a J/ψ event starts by requiring a combined muon with $p_{\mathrm{T}} \geq 4$ GeV reconstructed in the acceptance of the ID and firing a J/ψ low-mass di-muon trigger ("HLT MU4 BJPSI TRKLOOSE"). A matching is defined between the trigger object and the reconstructed muon by requiring a $\Delta R \leq 0.005$. The matched muon will be chosen as the tag. All reconstructed muon with opposite charge to the tag are then searched and the invariant mass with the tag muon computed. The muon which invariant mass with the tag is the closest to the J/ψ mass (3.1 GeV), in the invariant mass region between 2.7 GeV and 3.5 GeV, is chosen as the probe. Finally, the probe muon is required to match a MS track. Only highly boosted decays with an angular opening ΔR less than 0.6 are selected and only information from the MS is used for the reconstruction. The selection efficiency as a function of the opening angle ΔR between the two muons is shown in Figure 5.29. The reconstruction efficiency decreases for small ΔR values. In this region the MS limitations of reconstructing two separate tracks with small angular separation can be observed. The difference between data and MC in the ΔR interval between 0.02 and 0.06, where the signal sample is expected, is taken as systematic uncertainty and is found to be 15%.

3mu6 msonly trigger efficiency
The systematic uncertainty on the tri-muon MS-only trigger efficiency is 5.8%, taken from the Run-1 analysis [70] since the algorithm has not undergone any major change since then. In the Run-1 analysis, it was assumed to be dominated by the systematic uncertainty on the 2MU6 trigger, which was evaluated using a tag-and-probe method applied to $J/\psi \to \mu\mu$ events in data and MC samples following the same approach as the measurement of the muon reconstruction efficiency. Possible effects due to pile-up increase in Run-2 with respect to Run-1 are checked to be negligible. The trigger efficiency as a function of the opening angle the dark photons is shown in Figure 5.30 for two different pile-up regimes, 10-20 and 20-30 interactions per bunch crossing. It is confirmed that the difference between the two algorithms is within the considered systematic uncertainty.

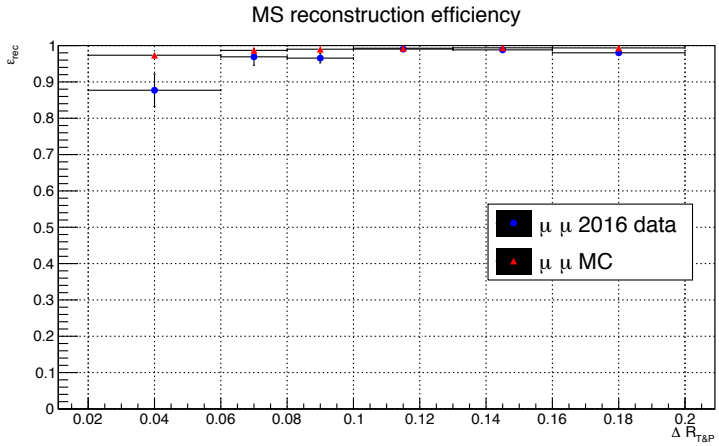

Figure 5.29. Reconstruction efficiency of standalone muon associated to γ_d evaluated using the tag-and-probe method as a function of the angular aperture ΔR between the decay muons of J/ψ for data and Monte Carlo samples.

Narrow-scan trigger efficiency

The systematic uncertainty on the narrow-scan trigger efficiency is estimated to be 6% by using a tag-and-probe method on $J\psi \to \mu\mu$ events in data and MC samples following the same approach as the measurement of the muon reconstruction efficiency. The trigger efficiency is studied as a function of the muons opening angle, and the results are shown in Figure 5.31. The data to MC difference in the region $0.02 \leq \Delta R \leq 0.06$, corresponding to the ΔR expected for signal events, is taken as systematic uncertainty. As expected, the trigger is fully efficient for highly collimated muons, ΔR <0.1.

CalRatio trigger efficiency

The systematic uncertainty on the CalRatio trigger efficiency is taken from Ref. [102]. It is computed on a very similar signal process and the result is 2%. This uncertainty is expected to be sub-dominant and was not recomputed for this analysis.

BDT shape

The systematic uncertainty which takes into account the mis-modelling of the MC input variables used for the BDT training is evaluated for both μBDT and hBDT.

- μBDT

  Muon variables used as input for the μBDT are studied using samples of $Z \to \mu\mu$ events in MC and data. Only information from the MS are used to reconstruct muons from the Z boson decay. The variables are shown in Fig 5.31 for reconstructed $Z \to \mu\mu$ events together with the ratio of the distributions in data to those in simulation.

  A shifted μBDT is trained with MC signal input variables rescaled to the data. The resulting output and efficiencies are shown in Fig. 5.32, these have to be compared with the standard μBDT. No significant change in signal and

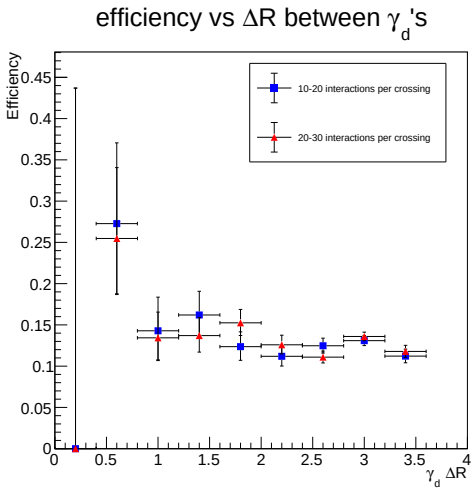

Figure 5.30. 3MU6 trigger efficiency as a function of the opening of the dark photons. Two different pile-up regimes are considered: 10-20 interactions per bunch crossings (in blue), 20-30 interactions per bunch crossings (in red).

background efficiency is seen. The systematic uncertainty is evaluated to be by 3% from the variation on the final yields when using the shifted μBDT compared to the standard analysis.

- hBDT

  Jet variables used as input for the hBDT are studied using multi-jet events in MC and data. The distribution and the ratio of the distributions in data to those in simulation are shown in Figure 5.32 .

  The hBDT discriminant for the multi-jet samples and the ratios of the MC to data are shown in Figure 5.33. The systematic uncertainty is evaluated to be by 14% from the variation on the final yields for the analysis when rescaling the hBDT output distribution of data to MC.

Jet energy scale and jet energy resolution

The systematic uncertainties which take into account the estimation of Jet Energy Scale (JES) and Jet Energy Resolution (JER) affect all signal processes in the analysis. These are evaluated following the procedure detailed in Ref. [67]. Depending on the signal process the uncertainty results range between 1% and 8% for the JES and between 1% and 7% for the JER. Detailed information are reported in Table 5.26 for the JES and in Table 5.27 for the JER.

Jets used in this analysis are required to have low electromagnetic fraction of energy. To take into account a possible dependence of this variable on the JES an additional uncertainty is applied. This uncertainty is estimated following the procedure used in the 2012 analysis [103], which compares the nominal scale with four reduced uncertainty sets, resulting in a systematic variation between 1% and 5% depending on the model. This additional uncertainty is summed in quadrature with the regular uncertainties of JES and JER. The size of the uncertainties applied to each signal process are reported in Table 5.28.

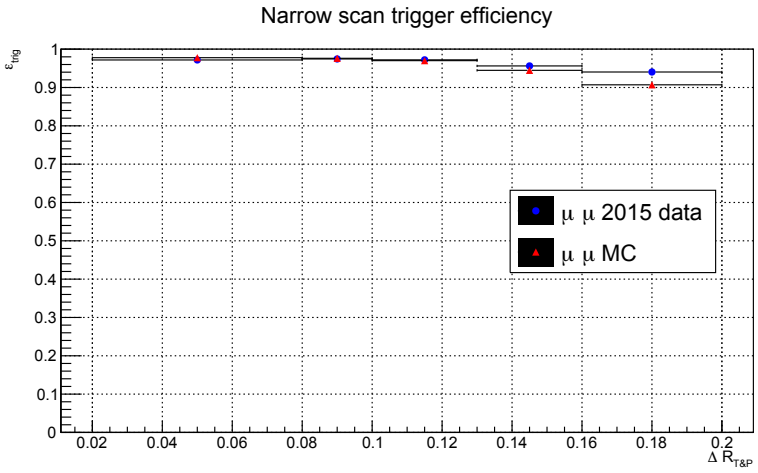

Figure 5.31. Narrow-Scan trigger efficiency evaluated using the tag-and-probe method as a function of the opening angle ΔR between the decay muons of J/ψ for data and Monte Carlo samples.

MC Signal Samples	JES Systematics Uncertainties		
decay,m_H,m_{γ_d},$c\tau$	muonic-muonic	muonic-hadronic	hadronic-hadronic
$H \to 2\gamma_d + X$,125 GeV,0.4 GeV, 49.23 mm	5%	1%	6%
$H \to 4\gamma_d + X$,125GeV, 0.4 GeV, 82.4 mm	7	5%;	0%
$H \to 2\gamma_d + X$,800GeV, 0.4 GeV, 11.76 mm	3%	0%	0%
$H \to 4\gamma_d + X$,800GeV, 0.4 GeV, 21.04 mm	8%	2%	0%

Table 5.26. Variation in the final yield due to the JES.

MC Signal Samples	JER Systematic Uncertainties		
decay,m_H,m_{γ_d},$c\tau$	muonic-muonic	muonic-hadronic	hadronic-hadronic
$H \to 2\gamma_d + X$,125 GeV,0.4 GeV,49.23 mm	1%	1%	0%
$H \to 4\gamma_d + X$,125GeV, 0.4 GeV, 82.4 mm	5%	4%	0%
$H \to 2\gamma_d + X$,800GeV, 0.4 GeV, 11.76 mm	3%	7%	0%
$H \to 4\gamma_d + X$,800GeV, 0.4 GeV, 21.04 mm	0%	2%	3%

Table 5.27. Variation in the final yield due to JER.

MC Signal Samples	JES_{EMF} Systematics Uncertainties		
decay,m_H,m_{γ_d},$c\tau$	muonic-muonic	muonic-hadronic	hadronic-hadronic
$H \to 2\gamma_d + X$,125 GeV,0.4 GeV,49.23 mm	-1%; +2%;	-5%; +2%	0%; 0%
$H \to 4\gamma_d + X$,125GeV, 0.4 GeV, 82.4 mm	-3%; +2%	-4%; +1%	0%;0%
$H \to 2\gamma_d + X$,800GeV, 0.4 GeV, 11.76 mm	0%; +1%	0%; +4%	0%; 0%
$H \to 4\gamma_d + X$,800GeV, 0.4 GeV, 21.04 mm	-3%; +2%	-1%; +2%	0%; 0%

Table 5.28. Variation in the final yield due to the low EMF JES.

Effect of pile-up on Σp_T

The selection efficiency on the Σp_T variable can be affected by the pile-up profile

in MC events. The systematic uncertainty which covers this effect is evaluated comparing the Σp_{T} variable as a function of pile-up, for reconstructed muons from $Z \to \mu\mu$ events in MC and in data. The study is shown in Figure 5.34. The maximum difference at the value of the analysis selection requirement on $\max(\Sigma p_{\mathrm{T}})$ is taken as systematic uncertainty and is found to be 5.1%.

Pile-up reweighting

The MC samples are reweighted by the ratio between the predicted and measured distribution of the number of primary vertices in the events, in order to match the 2015-2016 dataset. The systematic uncertainty associated to this process is evaluated by including a variation in the reweighting process, assigning a $\pm 1\sigma$ uncertainty to the ratio between the predicted and measured distributions of the number of primary vertices as a function of the instantaneous luminosity. Depending on the signal process the uncertainty is estimated to range from 1% to 14%. A more detailed information for each process is reported in Table 5.29.

MC Signal Samples	Pile-Up Reweighting Systematic Uncertainties		
decay,m_H,m_{γ_d},$c\tau$	muonic-muonic	muonic-hadronic	hadronic-hadronic
$H \to 2\gamma_{\mathrm{d}} + X$,125 GeV,0.4 GeV,49.23 mm	-2%; +2%;	-8%; +3%	-2%; +3%
$H \to 4\gamma_{\mathrm{d}} + X$,125GeV, 0.4 GeV, 82.4 mm	-6%; 0%	0%; 0%	0%; 0%
$H \to 2\gamma_{\mathrm{d}} + X$,800GeV, 0.4 GeV, 11.76 mm	-10%; +3%	-2%; +1%	-2%; +3%
$H \to 4\gamma_{\mathrm{d}} + X$,800GeV, 0.4 GeV, 21.04 mm	-1%; 0%	-14%; +0%	-8%; 0%

Table 5.29. Variation in the final yield due to pile-up reweighting shifts.

Initial state radiation jet effects on PV and event selection

Since no inner detector hit is expected for signal DPJs, the PV algorithm to identify the correct vertex may rely significantly on ISR jets. Therefore the systematic uncertainty on the MC signal samples ISR modelling is likely to have a significant impact on the final result. An increase of the ISR jets radiation could raise the Σp_{T}, and thus decrease the signal efficiency when the ISR jet falls in the same cone of the DPJ. A decrease of the ISR could only reduce the Σp_{T}, which would improve signal efficiency. The PV selection efficiency and ISR effects on the MC signal samples are checked. After the trigger request, the correct primary vertex is selected with an efficiency of $\sim 56\%$. Among these events, the presence of at least one ISR jet with $p_{\mathrm{T}} \geq 20$ GeV from the right PV is found in 81% of the cases. In the 44% of events where the wrong primary vertex is selected, the presence of ISR jet with $p_{\mathrm{T}} \geq 20$ GeV from the right PV is found only in 2% of the cases. These numbers do not vary significantly at the different steps of the event selection. Only 46% of the total events that pass the event selection show a presence of ISR jets from the PV. The correct PV can be identified in signal events when there is a presence of ISR jets, but the analysis does not rely on ISR jets for the events to pass the event selection. The results are thus not affected by ISR jets and no additional systematic uncertainty is taken into account.

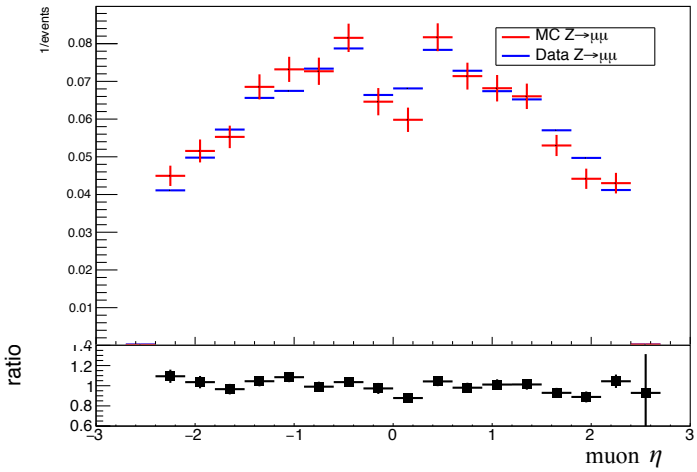

(a) η

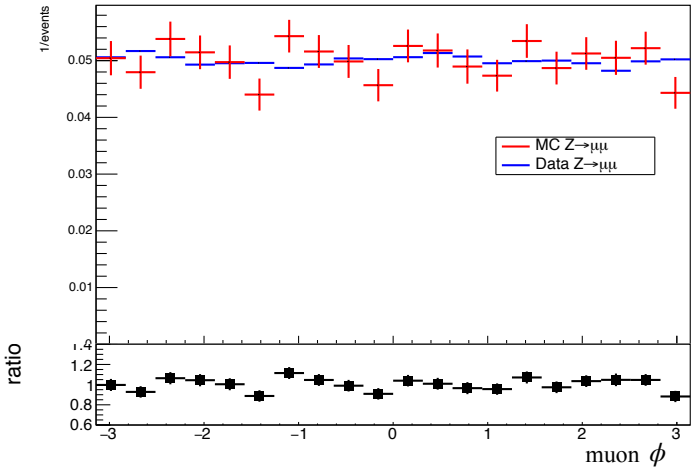

(b) ϕ

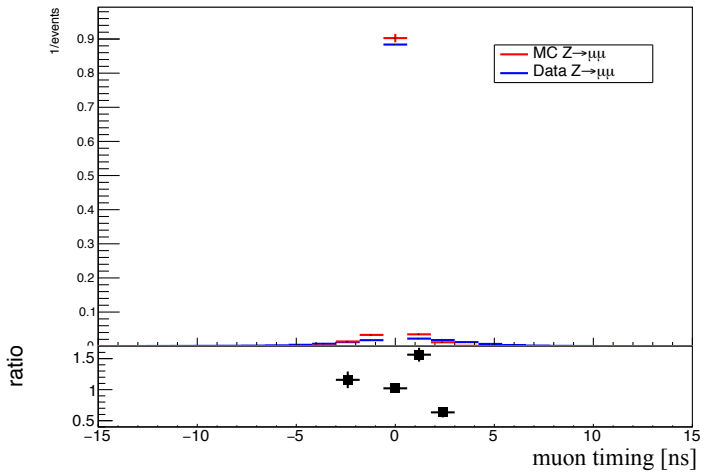

(c) RPC timing

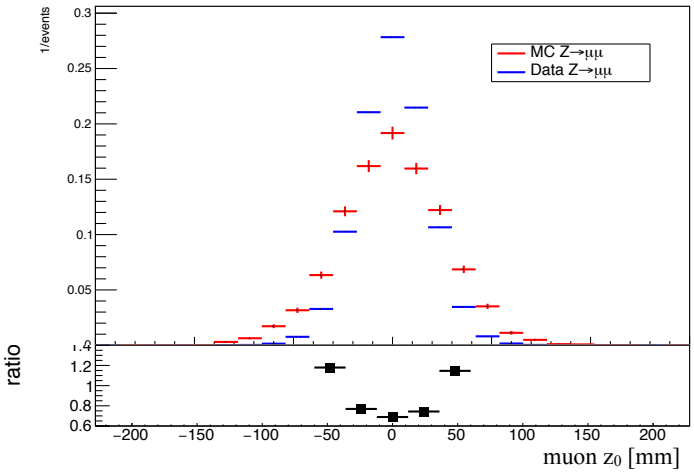

(d) z0

Figure 5.31. Muon track parameters of reconstructed $Z \to \mu\mu$ process in MC events (red) and 2016 data control sample (blue): pseudorapidity (a), azimuthal angle (b), RPC timing (c) and impact parameter z_0 (d).

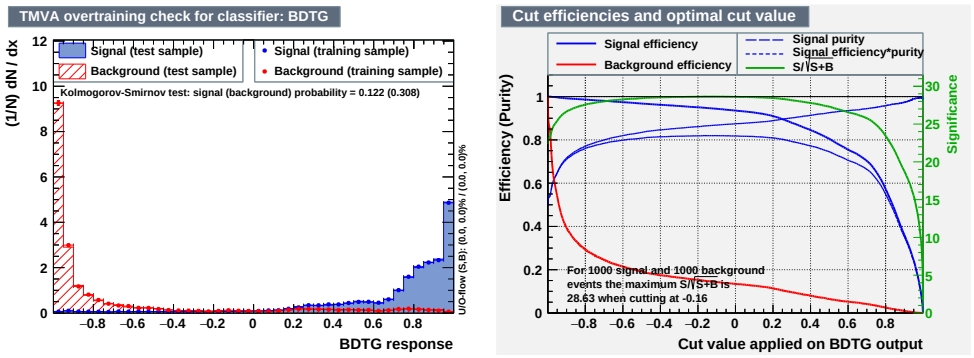

(e) (f)

Figure 5.32. Results for the-data-to-MC-rescaled-BDT used to estimate the systematic uncertainty to be compared to the standard μBDT used in the analysis 5.8. (a) μBDT output distribution for signal and background (test and training samples). (b) Signal and background cut efficiencies.

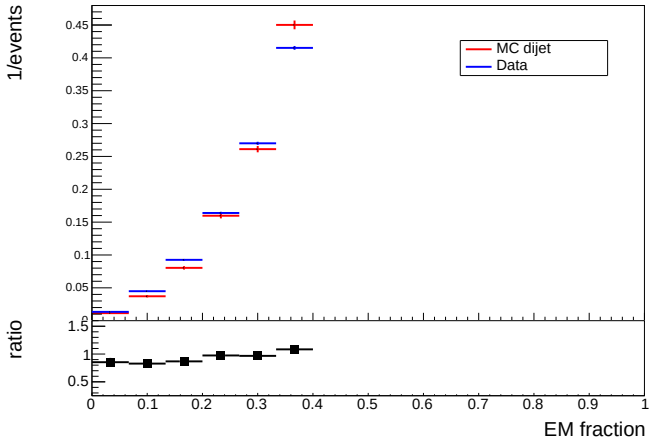

(a) EM fraction

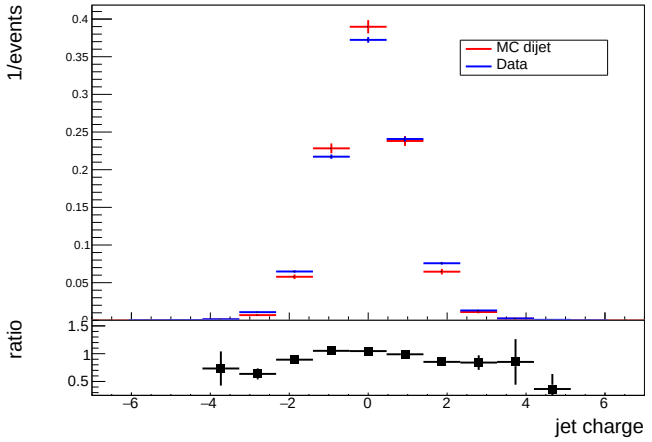

(b) Jet charge

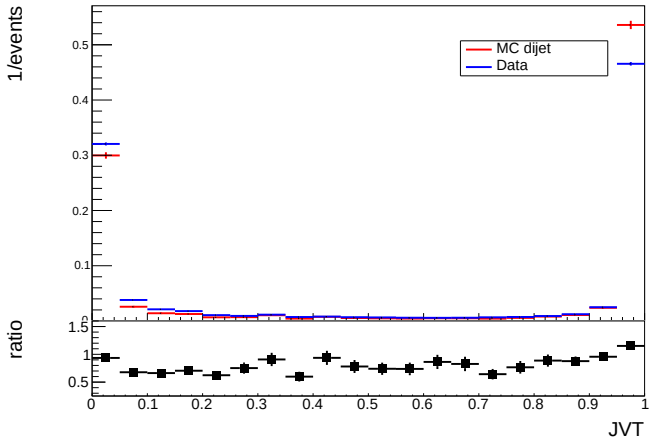

(c) JVT

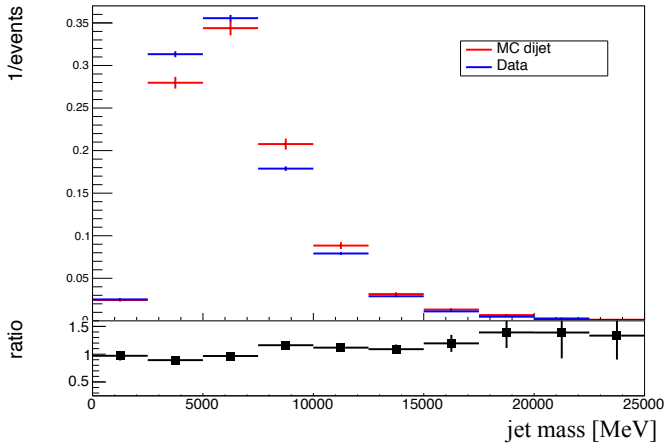

(d) Jet mass

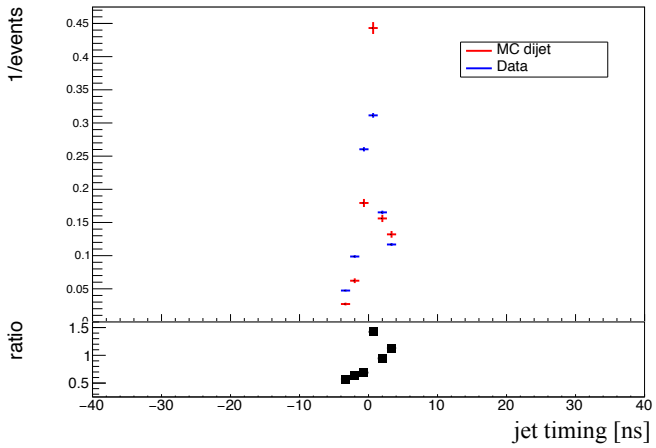

(e) Jet timing

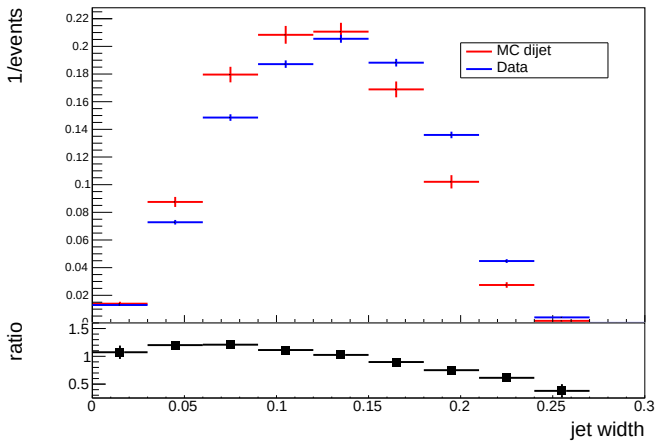

(f) Jet width

Figure 5.32. Jet features comparison between multi-jet MC (red) and di-jet dataset (blue): EM fraction(a), jet charge (b), jet vertex tagger (c), jet mass (d), jet timing (e) and jet width (f).

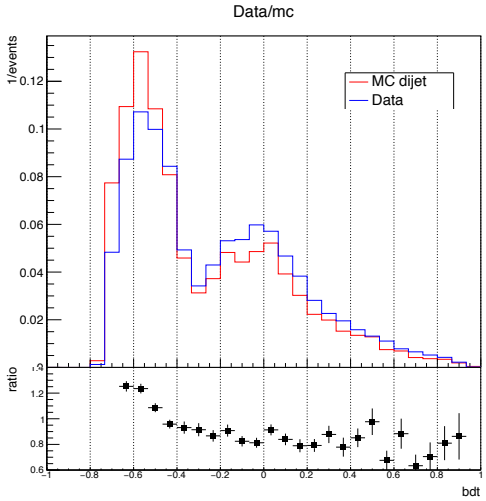

Figure 5.33. Data over MC ratio for the hBDT output.

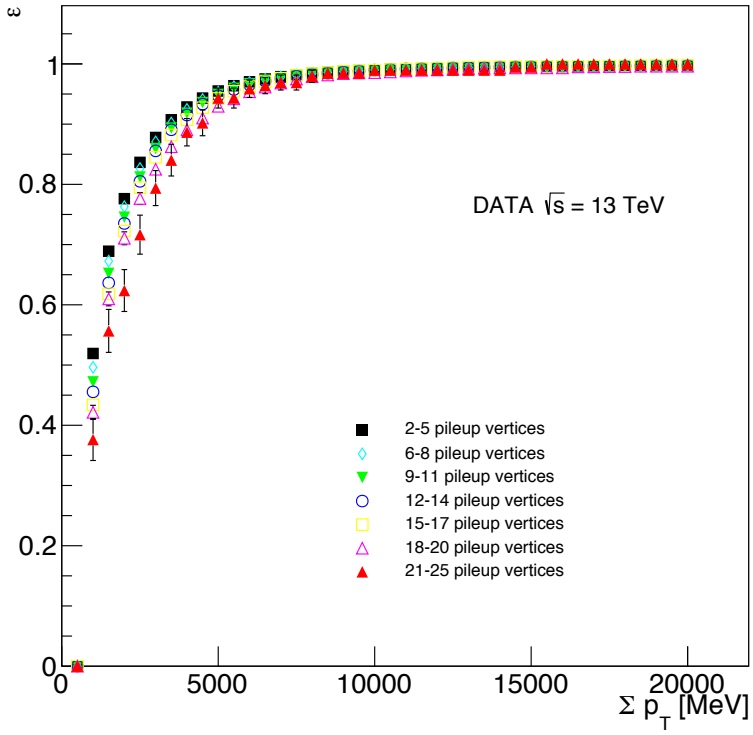

Figure 5.34. Isolation efficiency as a function of Σp_{T} in four intervals of the number of reconstructed interaction vertices per event in a $Z \to \mu\mu$ data sample.

5.7 Results and interpretation

5.7.1 Likelihood fit

A likelihood based ABCD method has been developed for the simultaneous data-driven background estimation and signal hypothesis test. This method is robust against control regions with small number of events and takes into account a possible small signal contamination in the control regions. For all MC signal samples a contamination lower than 10% is thus allowed.

The background estimation in signal region A is obtained by performing a fit to the background and signal yields in the four regions. The fitted likelihood describes the signal and background expectation in each region, defined by products of Poisson functions, and takes the following form:

$$\mathcal{L}(n_{\mathrm{A}}, n_{\mathrm{B}}, n_{\mathrm{C}}, n_{\mathrm{D}} | s, b, \tau_{\mathrm{B}}, \tau_{\mathrm{C}}) = \prod_{i=\mathrm{A,B,C,D}} \frac{\mathrm{e}^{-N_i} N_i^{n_i}}{n_i!} \quad ,$$

where n_{A}, n_{B}, n_{C}, n_{D} are the number of events observed in each region in data, τ_{B} and τ_{C} are the nuisance parameters that describe the ABCD ansatz. N_i are linear combinations of the signal and background expectation in each region, defined as follows:

$$\begin{aligned} N_{\mathrm{A}} &= s + b \\ N_{\mathrm{B}} &= s\,\varepsilon_{\mathrm{B}} + b\,\tau_{\mathrm{B}} \\ N_{\mathrm{C}} &= s\,\varepsilon_{\mathrm{C}} + b\,\tau_{\mathrm{C}} \\ N_{\mathrm{D}} &= s\,\varepsilon_{\mathrm{D}} + b\,\tau_{\mathrm{C}} \,/\, \tau_{\mathrm{B}} \end{aligned}$$

where s is the signal and b is the background yield in region A. The signal contamination in the region i is described by ε_i. All the parameter values are allowed to float in the fit to the four data regions.

The upper limit on the signal strength is obtained with the $\mathrm{CL_s}$ method [104], performing a global simultaneous fit based on the profile likelihood method [105] in order to normalise the observed data in all the regions to the signal expectation. The presence of an excess generated by the signal is then evaluated by comparing the estimated number of events in the SR to the observed data. All systematic uncertainties described in Section 5.6 are included in the fit as nuisance parameters, parametrised with gaussian probability density functions that multiply the fit likelihood. The gaussian probability distribution function mean value is constrained by the parameter nominal value and the variance is defined by the 68% of the systematic uncertainty associated to the parameter.

5.7.2 Background-only result

The observed number of events and the expected number of events in region A estimated with the likelihood-based ABCD are summarised in Table 5.30. The numbers reported are extrapolated by the fit assuming no signal and including only

control regions B, C, D in the fit. The expected background includes both multi-jet and cosmic backgrounds, obtained as described in Section 5.5.

DPJ pair type	B	C	D	Expected A	A
μDPJ–μDPJ	24	92	463	128 ± 26 (stat.)	113
μDPJ–hDPJ	8	2	45	177 ± 86 (stat.)	179
hDPJ–hDPJ	13	2	15	97 ± 48 (stat.)	69

Table 5.30. Observed numbers of events in the ABCD regions and expected number of background events in region A. In the estimate, the data in region A are not considered and the signal strength is fixed to zero. The statistical uncertainty in the background expectations is given. The expected contribution from cosmic rays is included in all the regions.

As no excess is observed in data over the estimated background, the results of the search for DPJ production are used to set upper limits on the production cross-section times branching fraction $\sigma \times \mathcal{B}$ as a function of the γ_{d} proper decay length using the $\mathrm{CL_s}$ method.

5.7.3 Lifetime reweighting

In order to obtain limits as a function of $\mathrm{c}\tau$, the signal efficiency for different proper lifetimes is extrapolated from the MC signal samples. To extrapolate the events from a specific lifetime of reference, τ_{ref}, to a different lifetime a weight w_i, derived from the ratio of the Poissonian decay probabilities, is applied:

$$w_i(t_i) = \frac{\tau_{\mathrm{ref}}}{\tau_{\mathrm{new}}} \cdot \mathrm{e}^{-(\frac{1}{\tau_{\mathrm{new}}} - \frac{1}{\tau_{\mathrm{ref}}})t_i},$$

where τ_{ref} is the proper time with which the reference sample was generated, τ_{new} is the proper time to which the event is rescaled, and t_i is the decay time of the i-th dark photon. This weight is multiplicative for the two dark photons considered in the event. The reweighting process is validated with alternative MC samples generated with the same mass points but different $\mathrm{c}\tau$. Results are shown in Figure 5.35, where the ratio $\varepsilon(\mathrm{c}\tau)/\varepsilon(49\text{ mm})$ as a function of $\mathrm{c}\tau$ for the signal benchmark model is shown. The validation samples with $\mathrm{c}\tau$ =4.9mm, 49mm, and 492mm are shown with black markers. Good agreement is observed within statistical uncertainties.

The extrapolated signal efficiencies for the $H \rightarrow 2\gamma_{\mathrm{d}} + X$ and $H \rightarrow 4\gamma_{\mathrm{d}} + X$ processes as a function of $\mathrm{c}\tau$ for the different channels are shown in Figure 5.36.

The higher efficiency of the $H \rightarrow 4\gamma_{\mathrm{d}} + X$ processes in the muonic channels is due to a better selection from the 3MU6 msonly trigger. In the hadronic channels the CalRatio trigger is seen to be very inefficient for the models with $m_{\mathrm{H}} = 125$ GeV Higgs boson due to the lower p_{T} of the jets. This effect is less visible in the μDPJ - hDPJ channel where the efficiency is recovered by the narrow-scan trigger.

5.7.4 Interpretation within the FRVZ simplified model

The results for the FRVZ model are obtained from the likelihood-based ABCD fit assuming the expected signal yields, reported in Section 5.5.7, and the observed

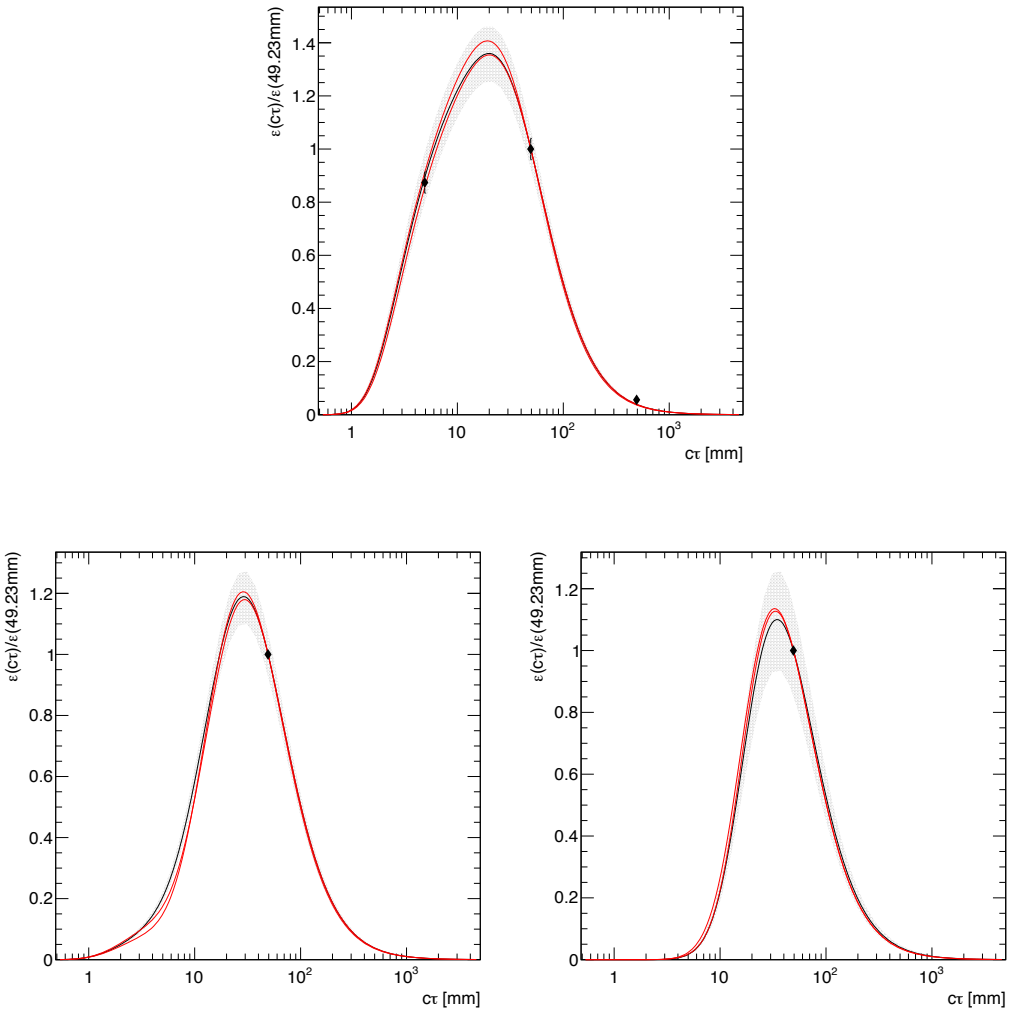

Figure 5.35. Ratio of the integrated detection efficiency at a given $c\tau$ to the detection efficiency at $c\tau = 49$ mm of the SM 125 GeV $H \to 2\gamma_d + X$ MC sample. The ratio is shown for the fully muonic-channel (top), muonic-hadronic channel (left) and fully hadronic-channel (right). The markers show the relative efficiency found using full simulation MC samples with $c\tau$ =4.9mm, 49mm, and 492mm, indicating good agreement with the reweighting curve.

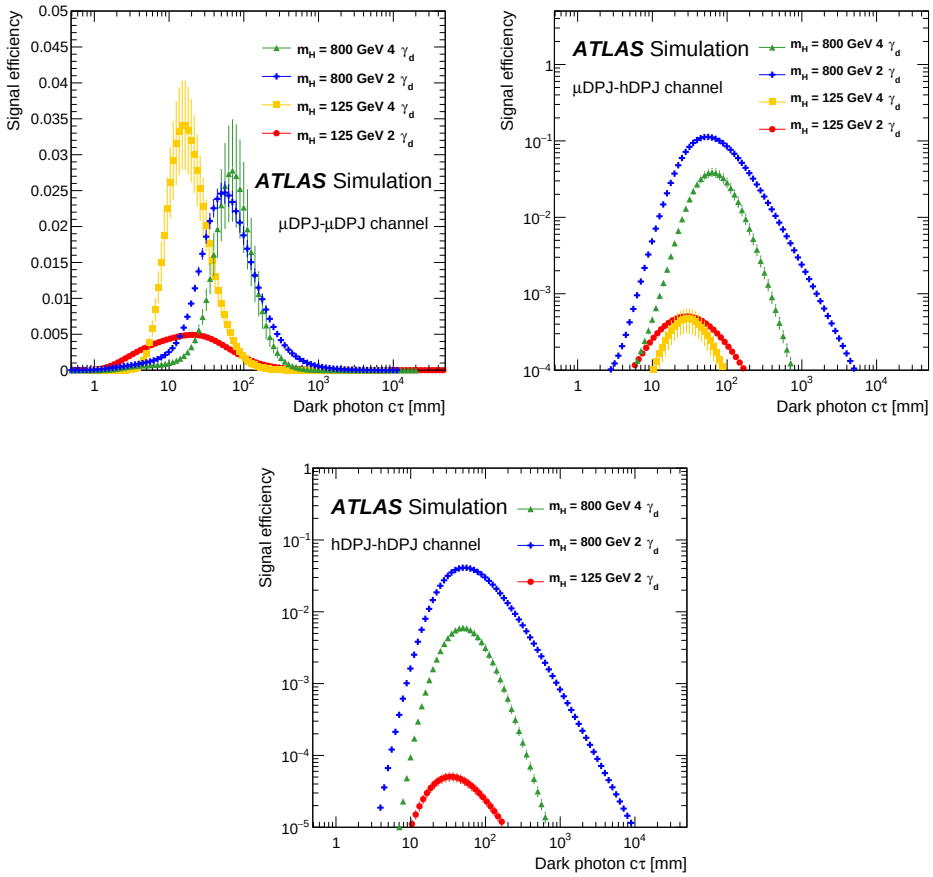

Figure 5.36. Extrapolated signal efficiencies as a function of proper decay length of the γ_{d} for the $H \to 2\gamma_{\mathrm{d}} + X$ and $H \to 4\gamma_{\mathrm{d}} + X$ processes and for the three different channels: μDPJ–μDPJ (left), μDPJ–hDPJ (right) and hDPJ–hDPJ (bottom). The signal efficiency in the hDPJ–hDPJ channel for $m_H = 125$ GeV $H \to 4\gamma_{\mathrm{d}} + X$ process is small compared with the other channels and is not shown. The vertical bars represent the statistical uncertainties.

data in the four ABCD regions. The μDPJ - μDPJ channel 95% CL cross-section upper limits are shown in Figure 5.37 for the $H \to 2\gamma_{\mathrm{d}} + X$ and $H \to 4\gamma_{\mathrm{d}} + X$ processes with $m_H = 125$ GeV. Upper limits for the $H \to 2\gamma_{\mathrm{d}} + X$ process with $m_H = 800$ GeV are shown in Figure 5.38. Upper limits for the $H \to 4\gamma_{\mathrm{d}} + X$ process with $m_H = 800$ GeV are shown in Figure 5.39. The complete results in terms of excluded $c\tau$ ranges are summarised in Table 5.31, assuming a branching fraction to dark sector of 10% for the Higgs boson with $m_H = 125$ GeV and 100% for the $m_H = 800$ GeV BSM heavy scalar.

The reported results significantly extend the current ATLAS $c\tau$ range of exclusion contour from Run-1 lepton-jet searches. The prompt lepton-jet search result [106], based on 20.3 fb^{-1} of data collected at $\sqrt{s} = 8$ TeV for the $H \to 2\gamma_{\mathrm{d}} + X$ channel with $m_H = 125$ GeV, is shown in Figure 5.40. The sensitivity reach of the prompt search up to $c\tau \sim 5$mm, assuming a Higgs boson decay branching fraction into dark fermions of 10 %, is completely complementary to the displaced dark-photon jet limit

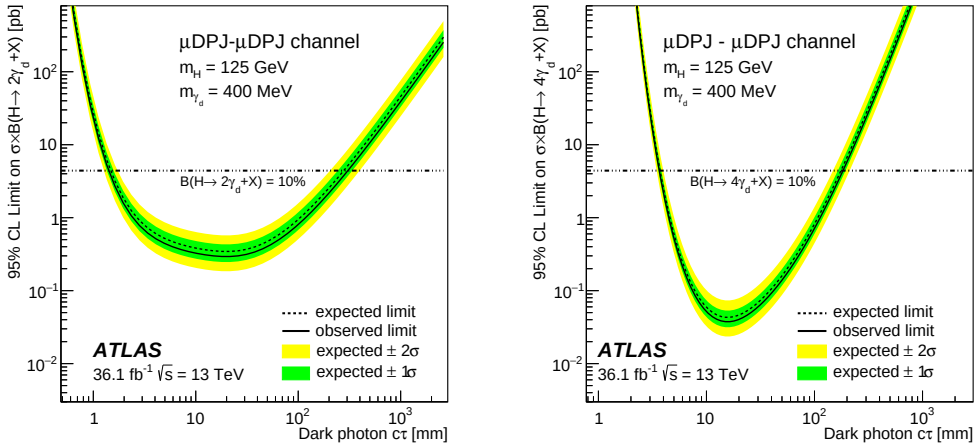

Figure 5.37. Upper limits at 95% CL on the cross-section times branching fraction for the processes $H \to 2\gamma_\mathrm{d} + X$ (left) and $H \to 4\gamma_\mathrm{d} + X$ (right) in the μDPJ–μDPJ final states for $m_H = 125$ GeV. The horizontal lines correspond to the cross-section times branching fraction for a value of the branching fraction of the Higgs boson decay into dark fermions of 10%.

Model	Excluded $c\tau$ [mm] $m_H = 125$ GeV $H \to 2\gamma_\mathrm{d} + X$	Excluded $c\tau$ [mm] $m_H = 125$ GeV $H \to 4\gamma_\mathrm{d} + X$	Excluded $c\tau$ [mm] $m_H = 800$ GeV $H \to 2\gamma_\mathrm{d} + X$	Excluded $c\tau$ [mm] $m_H = 800$ GeV $H \to 4\gamma_\mathrm{d} + X$
μDPJ–μDPJ	$1.5 \leq c\tau \leq 307$	$3.7 \leq c\tau \leq 178$	$5.0 \leq c\tau \leq 1420$	$10.5 \leq c\tau \leq 312$
μDPJ–hDPJ	–	–	$7.2 \leq c\tau \leq 1234$	$14.5 \leq c\tau \leq 334$
hDPJ–hDPJ	–	–	$7.3 \leq c\tau \leq 1298$	$13.6 \leq c\tau \leq 231$

Table 5.31. Ranges of γ_d $c\tau$ excluded at 95% CL for $H \to 2\gamma_\mathrm{d} + X$ and $H \to 4\gamma_\mathrm{d} + X$. A branching fraction value of $\mathcal{B}(H \to f_{\mathrm{d}_2}\,\bar{f}_{\mathrm{d}_2}) = 10\%$ is assumed for DPJ production in the decay of a $m_H = 125$ GeV Higgs boson. For DPJ production in the decay of a $m_H = 800$ GeV BSM scalar boson, a value of $\mathcal{B}(H \to f_{\mathrm{d}_2}\,\bar{f}_{\mathrm{d}_2}) = 100\%$ and a production cross-section of $\sigma = 5$ pb are assumed.

which extends the exclusion up to $c\tau \sim 300$ mm. Moreover, this search significantly improves the previous ATLAS Run-1 result from displaced lepton-jet searches [70], extending the excluded $c\tau$ range from 14 mm $\leq c\tau \leq$ 40 mm to 1.5 mm $\leq c\tau \leq$ 307 mm.

Vector portal exclusion

The upper limit in the μDPJ - μDPJ channel for the $H \to 2\gamma_\mathrm{d} + X$ process and $m_H = 125$ GeV is also interpreted in the context of the FRVZ vector portal model, in terms of kinetic mixing parameter ϵ and γ_d mass limit. The result is shown in Figure 5.41, in terms of exclusion contours for different Higgs decay branching fractions into γ_d, ranging from 1% to 20%. The signal efficiency as a function of γ_d mass is expected to be constant over the interval from 0.2 GeV to 2 GeV [70]. Hence, only the branching fraction variations [22] are considered for the extrapolation of the signal efficiency as a function of the γ_d mass. The dependence on the kinetic mixing

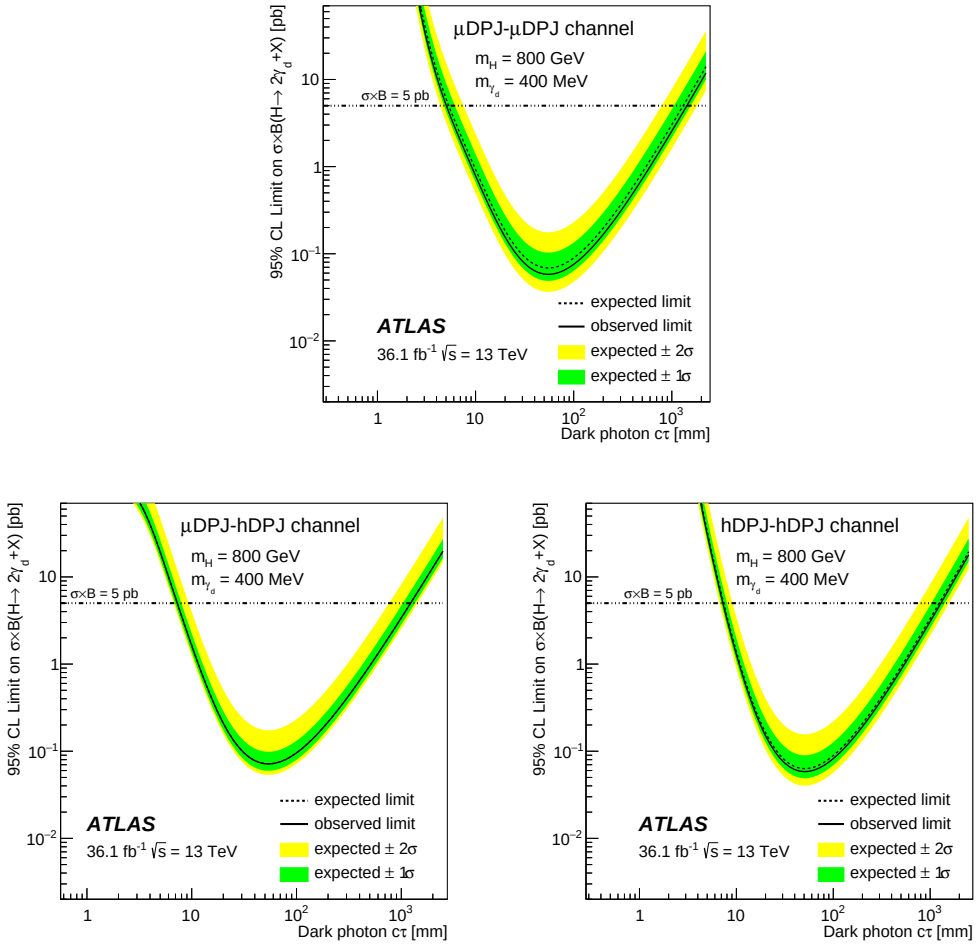

Figure 5.38. Upper limits at 95% CL on the cross-section times branching fraction for the process $H \rightarrow 2\gamma_{\mathrm{d}} + X$, where H is a BSM heavy scalar with $m_{\mathrm{H}} = 800$ GeV, in the μDPJ–μDPJ (top), μDPJ–hDPJ (left) and hDPJ–hDPJ (right) final states. The horizontal lines correspond to a cross-section times branching fraction of 5 pb.

parameter ϵ is extrapolated from the cτ signal efficiency, exploiting Equation 3.12 introduced in Section 3.2.1.

The muonic channel does not allow to provide an exclusion limit in the mass range in which the γ_{d} decays into the ρ, ω, and ϕ resonances around 0.8 and 1.0 GeV. Exclusion from previous Run-1 ATLAS searches for dark-photon jets are shown for the displaced search [70] and for the complementary prompt search [106].

Significant improvements with respect to the constraints set in the previous ATLAS searches using 8 TeV data are observed. The great sensitivity of the analysis μDPJ–μDPJ channel allows to exclude a cτ range that covers the entire ATLAS detector dimensions up to $\epsilon \sim 10^{-7}$ for 20%, 10%, 5% branching fraction of the SM Higgs decay into dark fermions. Moreover, for the first time an exclusion sensitivity has been reached when considering the SM Higgs BR into dark fermions of 1%.

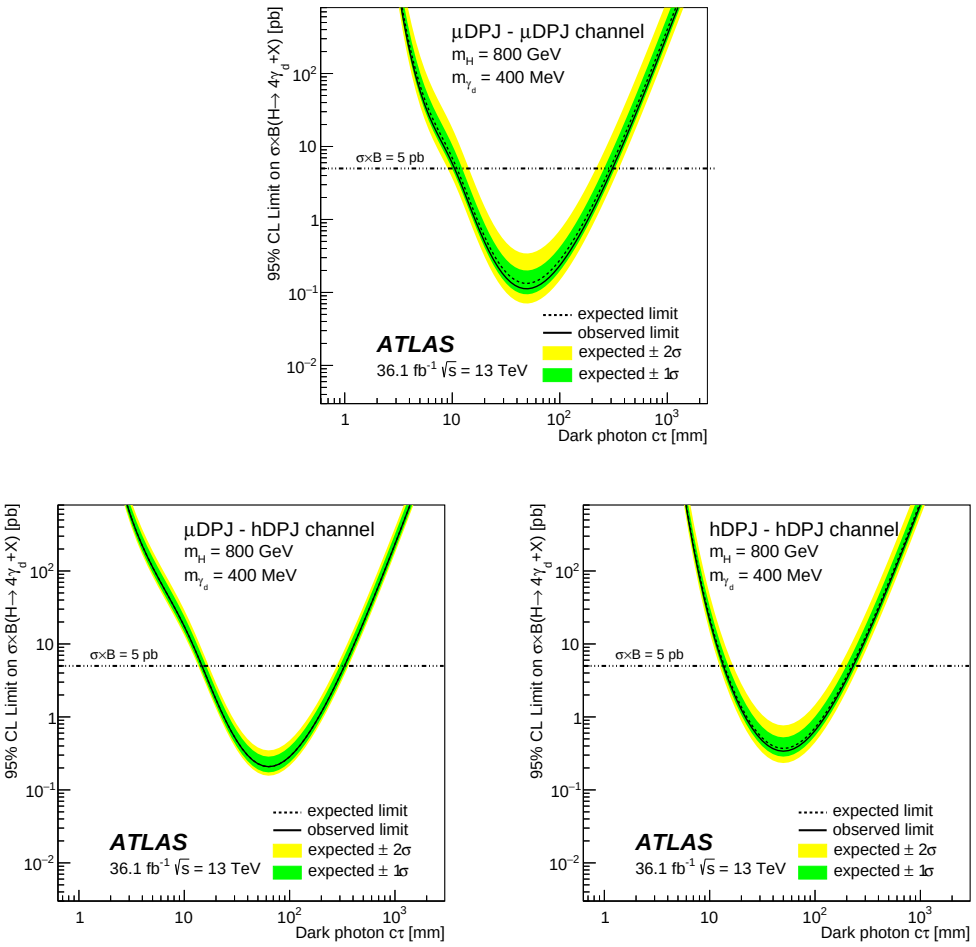

Figure 5.39. Upper limits at 95% CL on the cross-section times branching fraction for the process $H \rightarrow 4\gamma_{\mathrm{d}} + X$, where H is an 800 GeV BSM Higgs boson, in the μDPJ–μDPJ (top), μDPJ–hDPJ (left) and hDPJ–hDPJ (right) final states. The horizontal lines correspond to a cross-section times branching fraction of 5 pb.

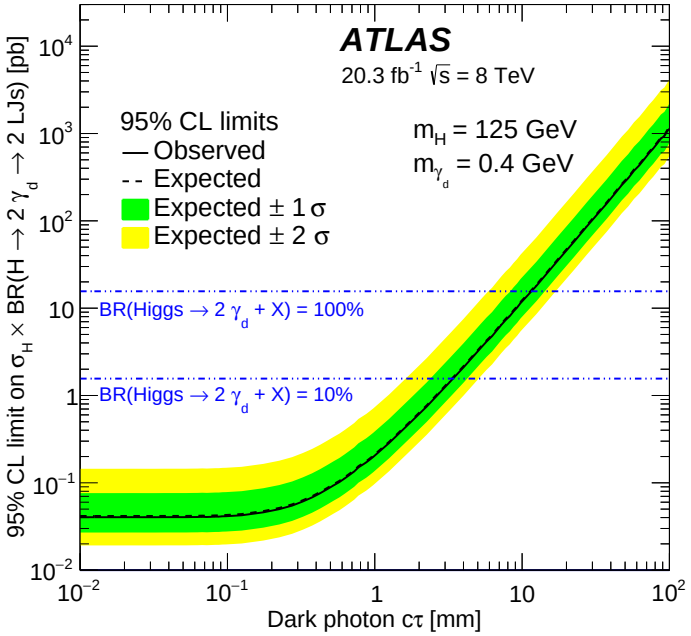

Figure 5.40. Results of the Run-1 prompt lepton-jet search [106]. Upper limits at 95% CL on the cross-section times branching fraction for the process $H \to 2\gamma_{\mathrm{d}} + X$ with $m_H = 125$ GeV and $m_{\gamma_{\mathrm{d}}} = 0.4$ GeV. The result is based on the combination of the eDPJ–eDPJ, μDPJ–μDPJ, eDPJ–μDPJ channels.

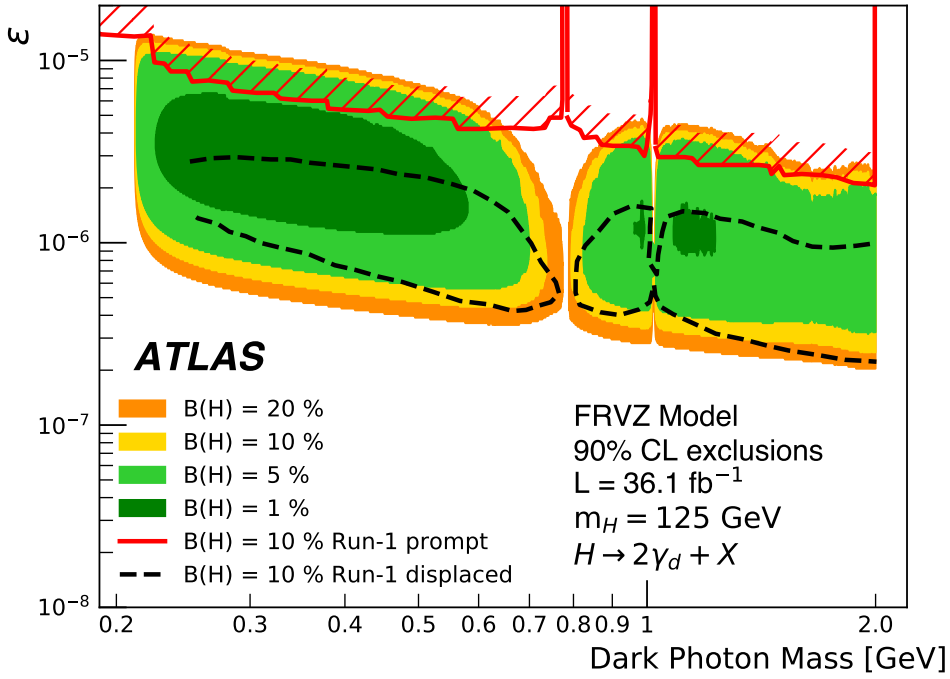

Figure 5.41. The 90% CL exclusion contours regions of the SM Higgs boson as a function of the γ_d mass and of the kinetic mixing parameter ϵ for the $H \to 2\gamma_d + X$ process. These limits are obtained assuming the FRVZ model with decay branching fractions of the Higgs boson into γ_d which range between 1% and 20%, and the NNLO Higgs boson production cross-sections via gluon–gluon fusion. The figure also shows excluded regions from the Run-1 ATLAS displaced [70] (black line) and prompt [106] (red line) dark-photon jets searches.

5.7.5 Results in the context of LHC dark photon searches

The displaced lepton-jet search results have to be evaluated in the context of the full LLP programme. ATLAS, CMS, and LHCb results show great complementarity and their comprehension are critical for a complete coverage of dark photon models. All of these searches focus on leptonically decaying dark photons and displaced vertices.

ATLAS

The already discussed ATLAS Run-1 lepton-jet results are shown in Figure 5.42 for both the prompt and displaced search. Vector portal only exclusions from beam-dump experiments are also shown to provide an overview of the different regions explored by the various types of experiments. The comparison between the Run-1 and the Run-2 results must take into account several factors. Run-1 searches included the mixed-DPJ in the analysis and did not use separate channels in the final background estimation.

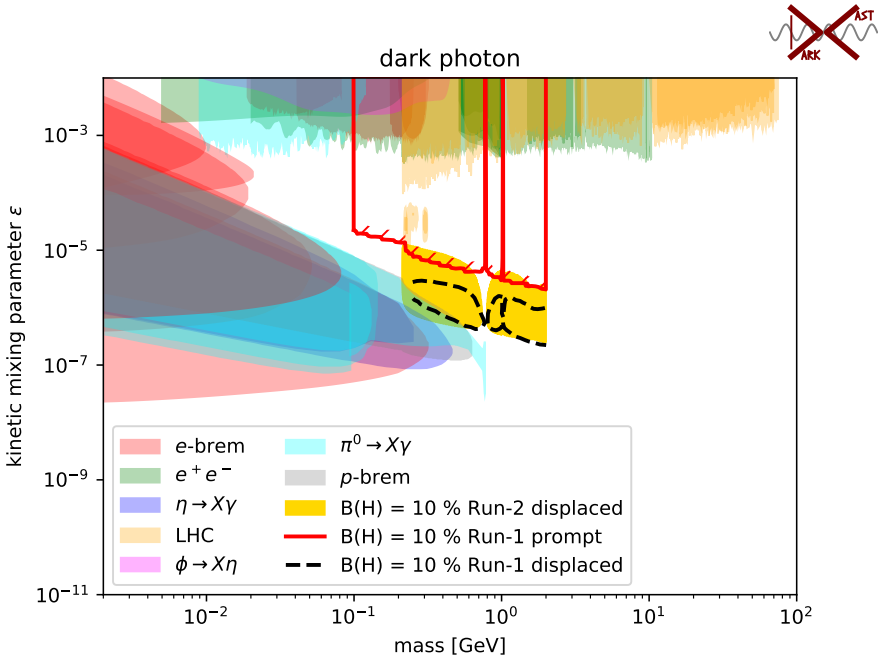

Figure 5.42. 90% CL exclusion contours of the ATLAS Run-1 lepton-jet search of the Higgs boson as a function of the γ_d mass and of the kinetic mixing parameter ϵ for the $H \to 2\gamma_d + X$ process. These limits are obtained assuming the FRVZ model with decay branching fractions of the Higgs boson into γ_d of 10%, and the NNLO Higgs boson production cross-sections via gluon–gluon fusion [106]. Plot made with DarkCast [26] tool.

Vector portal models in ATLAS are also probed in a higher mass regime where the out-going muons are not collimated. The search for displaced di-muon vertices [107] is sensitive to displaced decays from dark photon masses of about 15 GeV up to 60 GeV. The low mass final states are triggered on two msonly muons with $p_T >$ 15 GeV requiring a $\Delta R < 0.5$ between the muons, or with the 3MU6 msonly. Instead, to select high masses final states high-p_T single muon triggers are used. Muons are

then required to be highly isolated in the ID, reconstructing displaced decays up to $|d_0| \sim 200$cm. An interpretation in a vector portal simplified model where a BSM scalar decay directly to two dark photons, also named dark Z (Z_d), is shown in Figure 5.43.

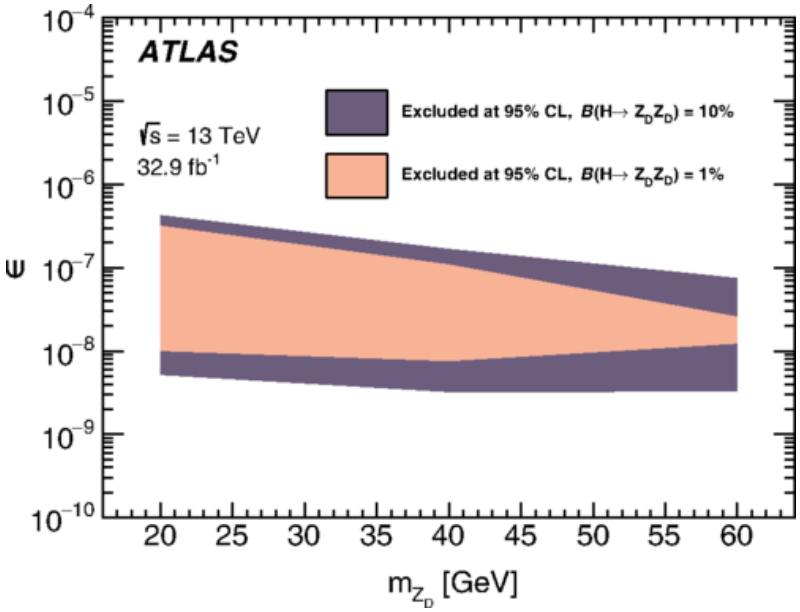

Figure 5.43. The observed 95% CL excluded regions in the plane of ϵ versus dark photon mass (m_{Z_d}), for $BR(H \to Z_d Z_d)$ values of 10% and 1%, and $m_H = 300$ GeV [107].

CMS

The CMS experiment performed two prompt muonic lepton-jet searches with Run-1 [108] and early Run-2 [109] dataset. These searches exploit a standard di-muon trigger to select events with at least two pairs of oppositely charged muons. The Run-2 search is sensitive to dark photon masses up to 8.5 GeV reaching an exclusion for SM Higgs branching fractions below 0.1% in the low mass region. Figure 5.44 show a naive comparison between the CMS lepton-jet search and ATLAS Run-2 search. ATLAS and CMS analyses investigate the same signal topologies however interpret the results in different models. CMS lepton-jet search considers a dark SUSY [110] scenario where a dark photon is assumed together with an undetected dark neutralino.

LHCb

The LHCb experiment performed a dark photon search with Run-2 data [111] looking for inclusive di-muon production. The analysis searches for prompt direct production of a dark photon in a mass range from the di-muon threshold up to 70 GeV, and a displaced search in the low-mass range. Events are required to have a muon with $p_{\mathrm{T}} \geq 1.8$GeV or a di-muon system in which the product of the p_{T} of each muon is $\geq (1.5\text{GeV})^2$. Results are then interpreted in a minimal dark photon model where only a new $U(1)'$ is assumed and dark photons are produced via Drell-Yan processes. This interpretation do not assume any dark Higgs sector and therefore

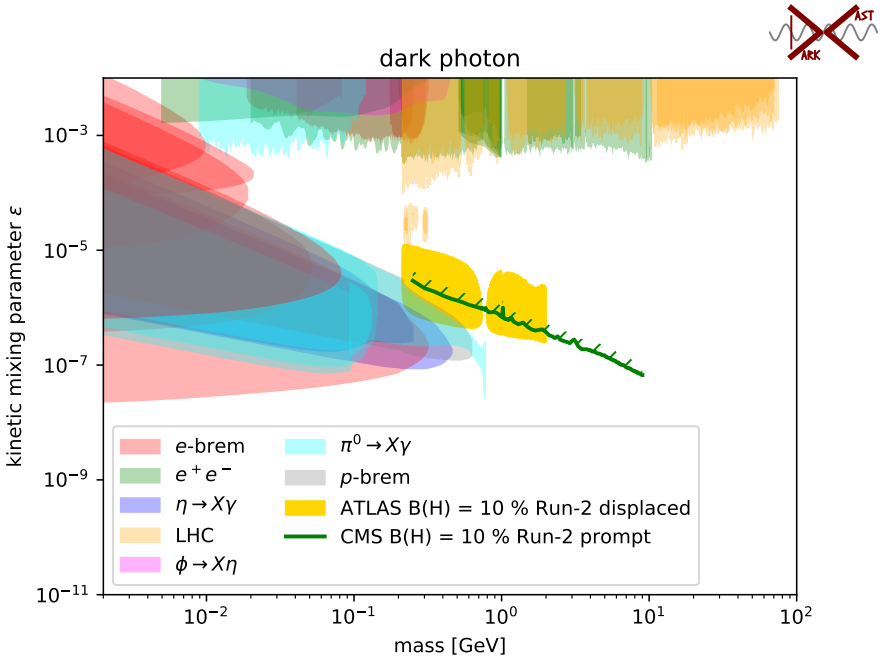

Figure 5.44. The 90% CL upper limits (green solid curve) from the lepton-jet CMS search with 36 fb^{-1} of data [109]. ATLAS Run-2 lepton-jet search (yellow contour) is also reported for comparison. ATLAS and CMS analyses investigate the same signal topologies however interpret the results in different theory models. Plot made with DarkCast [26] tool.

is less stringent then the ATLAS and CMS probed models, allowing also a direct comparison with BaBar [28] and KLOE-2 results [112]. BaBar and KLOE-2 search for dark photons in the e^+e^- annihilation looking at $\gamma A'$ with $A' \to l^+l^-$ final states. LHCb results, shown in Figure 5.45, supersede both BaBar and KLOE-2 excluded regions in the ϵ versus dark photon mass $m(A')$ parameter plane.

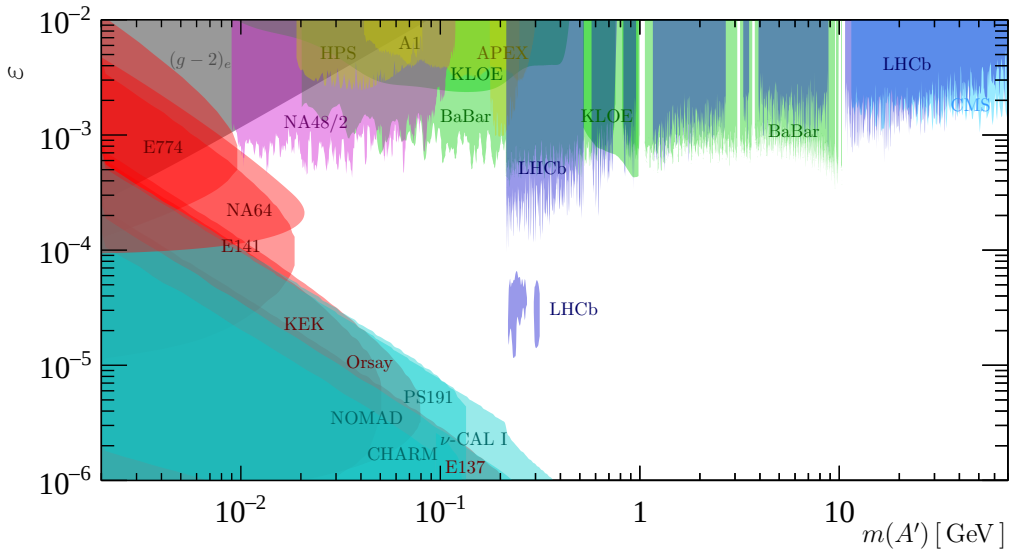

Figure 5.45. Regions of the ϵ versus dark photon mass $m(A')$ parameter space excluded at 90% CL by the prompt and displaced LHCb search (blue) [111] compared to the best existing limits.

Chapter 6

Improvements for dark-photon jets search in the full Run-2 dataset

The first Run-2 displaced dark-photon jet results based on 36.1 fb^{-1} of data collected in pp collisions at $\sqrt{13}$ TeV with the ATLAS detector have laid the ground for the legacy analysis with the full Run-2 dataset composed of 139 fb^{-1}. In this chapter the status and several improvements for the full Run-2 analysis are discussed.

The increase by a factor 4 of the total integrated luminosity will offer a great opportunity to probe the yet unexplored electron channel, crucial to cover the mass range below twice the muon mass, and to improve the hadronic channel, essential to exclude the mass range where γ_{d} decays to hadronic resonances. This will be backed up by an improved selection of hDPJ based on a novel machine learning (ML) technique dependent on convolutional neural networks. This technique exploits multi-dimensional jet images, where one image whose pixel are composed by calorimeter cell is constructed for each sampling layer of the calorimeter, to discriminate between hadronic decays of dark photon and QCD jets.

The new analysis will include the mixed dark-photon jet to select events with both jets and muons in a single DPJ.

To further increase the dataset size, the full Run-2 analysis will try to overcome the major bottleneck of trigger selection. This will be achieved by considering additional Higgs production modes, beside the ggF mode, that will allow to use more efficient standard triggers. The plan is to include the Higgs production in association with a vector boson (VH) and through vector boson fusion (VBF).

To extend the reach of the analysis to smaller values of epsilon, thus probing more displaced decays, a new topological signature called "mono displaced-DPJ" will be studied. The mono displaced-DPJ will consider events with a DPJ back-to-back with missing transverse momentum (MET), studying the case where one of the two dark photons decay outside the detector. Moreover, events tagged by an ISR jet where both dark-photon jets decay outside the detector will also be considered, performing a dark photon reinterpretation of the mono-jet analysis [113] results.

The interpretation of the results in vector portal models will be significantly improved by a newly developed deep-learning based tool, designed to parametrise the

analysis efficiencies and channel contaminations across the vector portal phase-space.

Finally, the increase of luminosity will lead to a better knowledge of the data-driven background predictions reducing the statistical uncertainty, the dominant uncertainty in 2015–2016 analysis.

6.1 VH production

The SM VH total cross section in pp collisions at $\sqrt{s} = 13$ TeV, estimated at NNLO QCD and NLO EWN [114], is $\sigma = 1.369$ pb for WH and $\sigma = 0.882$ pb for ZH (qqZH and the smaller ggZH processes are included in the computation). The smaller cross section with respect to the ggF production, by a factor of ~ 35 for WH and ~ 55 for ZH process, is recovered by a more efficient trigger selection. VH events involving muon or electron decays are selected by single-lepton triggers with a $p_{\mathrm{T}} = 24$ GeV threshold, which was active during the 2015-2016 data taking. During the 2017-2018 data taking the single-lepton triggers threshold has been increased to $p_{\mathrm{T}} = 26$ GeV but no significant difference is expected in terms of trigger efficiency for FRVZ signal samples. Tests on FRVZ samples generated with VH production mode show a single-lepton trigger total efficiency of 50–80 % for the vector boson decay to electrons and of 60–70 % for decay to muons, depending on the displacement of the dark photons. This single-lepton selection greatly improves the efficiency of the Run-2 specialised triggers, described in Section 5.2, by almost a factor 10. A comparison between the ggF and the VH topology is presented in Figure 6.1. In VH events the Higgs boson is emitted with a higher boost than in the ggF scenario, and its direct decay products are expected to be more collimated. This behaviour is expected also in the dark photons kinematics, presenting a smaller ΔR in VH events.

Kinematic distributions of the Z and W boson are reported in Figure 6.2 and Figure 6.3, respectively. The vector boson is likely to be emitted back-to-back with respect to the Higgs boson.

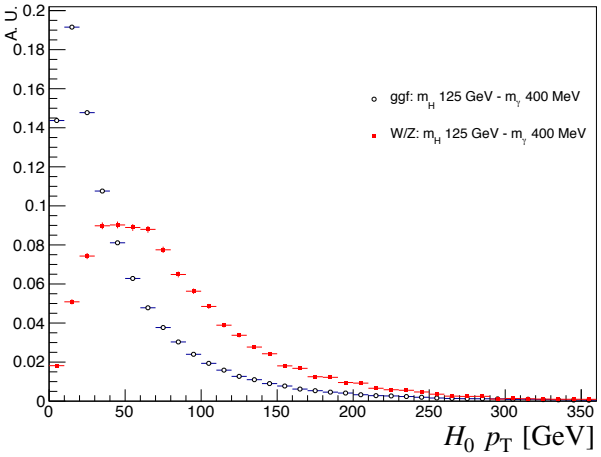

(a) H0 p_{T}

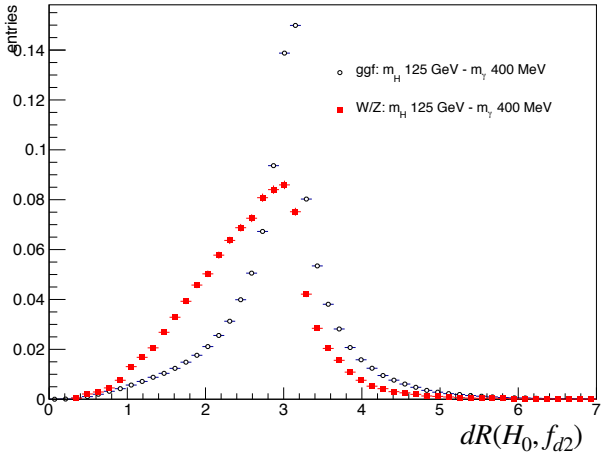

(b) H0 children ΔR

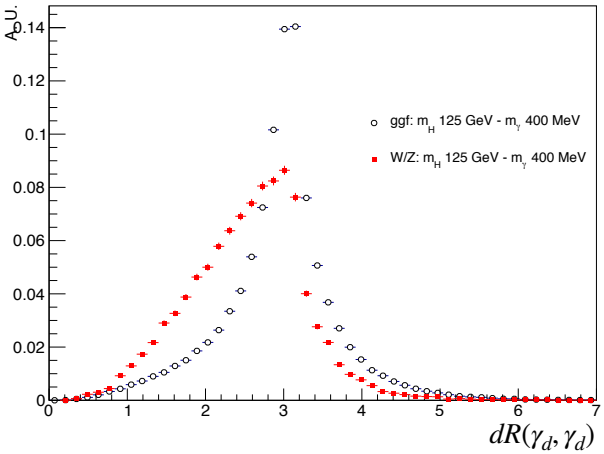

(c) ΔR between 2 γ_{d}

Figure 6.1. Higgs truth kinematic variables in gluon-fusion sample (black open circles) and associated production sample (red squares). For both production mechanisms, m_H = 125 GeV and $m_{\gamma_{\mathrm{d}}} = 0.4$ GeV are chosen.

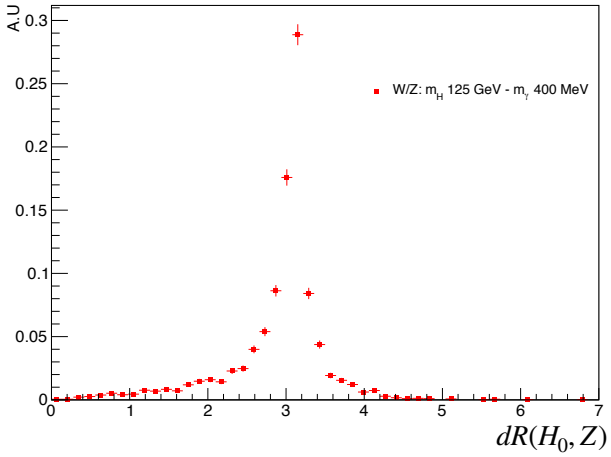

(a) H-Z ΔR

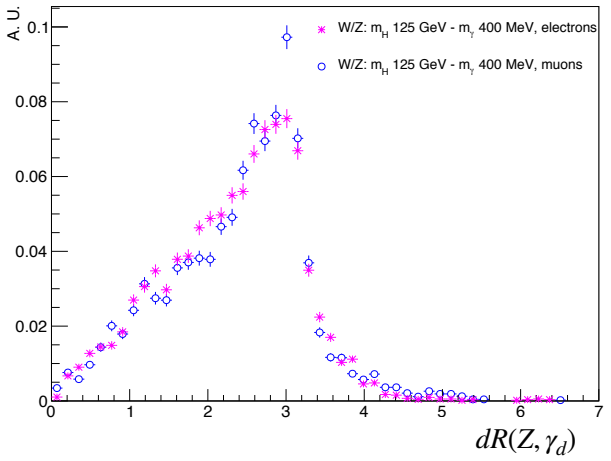

(b) Z-γ_{d} ΔR

Figure 6.2. In events with a truth Z, ΔR between following truth particles: Z and Higgs (a); γ_{d} and Z (b).

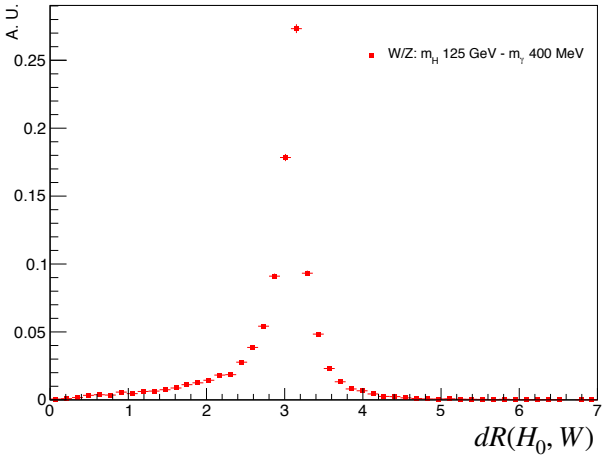

(a) H-W ΔR

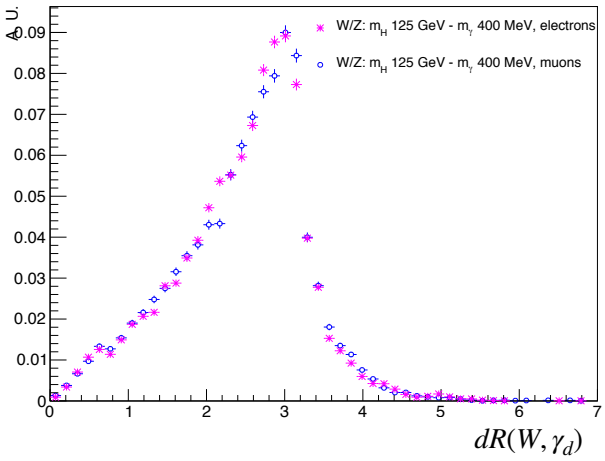

(b) W - γ_{d} ΔR

Figure 6.3. In events with a truth W, ΔR between following truth particles: W and Higgs (a); γ_{d} and W (b).

6.2 Hadronic CNN

One of the main goals of the legacy analysis is the exploitation of the hadronic channel to significantly improve the current results. The new selection is based on advanced deep learning algorithms running on multi-dimensional jet cluster images, a low level input that allows to fully exploit the calorimeter information. The idea is to map a jet on a $\eta \times \phi$ plane with transverse momentum as pixel intensity, a schematic example of mapping is presented in Figure 6.4.

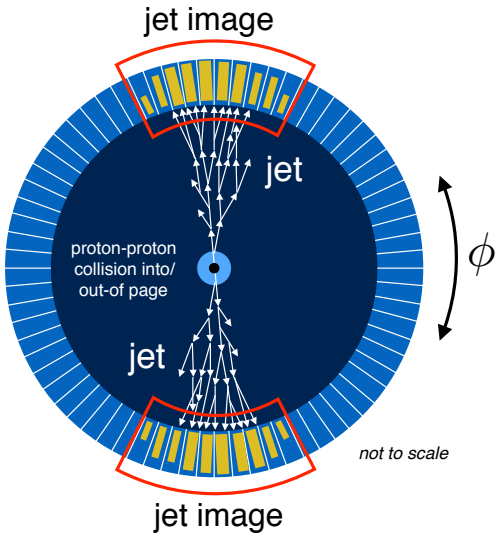

Figure 6.4. Schematic example of jet image capture on the calorimeter.

On this input, a per-jet convolutional neural network (CNN) image recognition algorithm is trained to discriminate between hadronic dark-photon jet and QCD jet. Four-dimensional jet images are used for this study, the first dimension being composed of all ECAL layers collapsed in one and the remaining three of each HCAL sampling layer. Figure 6.5 show an example hadronic dark-photon jet image and an average sum of 16k hadronic dark-photon jet images.

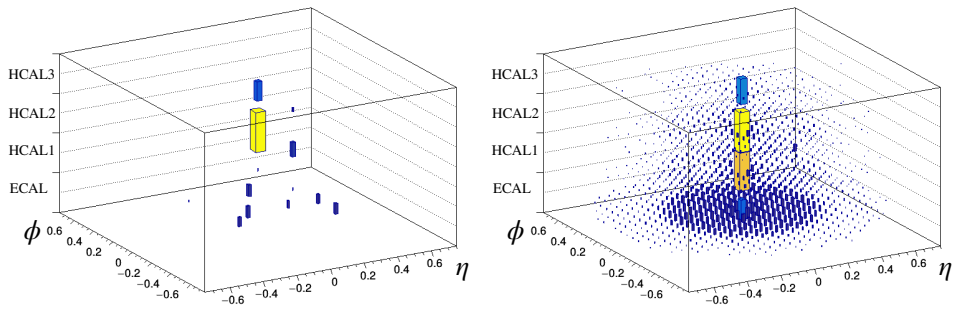

Figure 6.5. Hadronic dark-photon jet image used as input for the CNN (left) and an average sum of 16k hadronic jet images (right).

The CNN is trained on a FRVZ dark-photon signal sample and on QCD multi-jet background sample, the same used in the 2015–2016 analysis. For the preliminary test presented here, a total statistics of $\sim$ 20 k jet images have been used for each sample. The method is tested against overtraining and an accuracy of 93% is achieved. The discriminant output and the relative ROC curve are presented in Figure 6.6. Preliminary studies show a good response in discrimination power between displaced jets and multijet QCD jets in calorimetric deposits. A significant improvement is achieved with respect to the BDT discriminant used in the previous Run-2 analysis. The CNN algorithm will be further improved and optimised on a larger jet image sample. Deep neural networks seem to have good performance in managing sparse images from jet clusters.

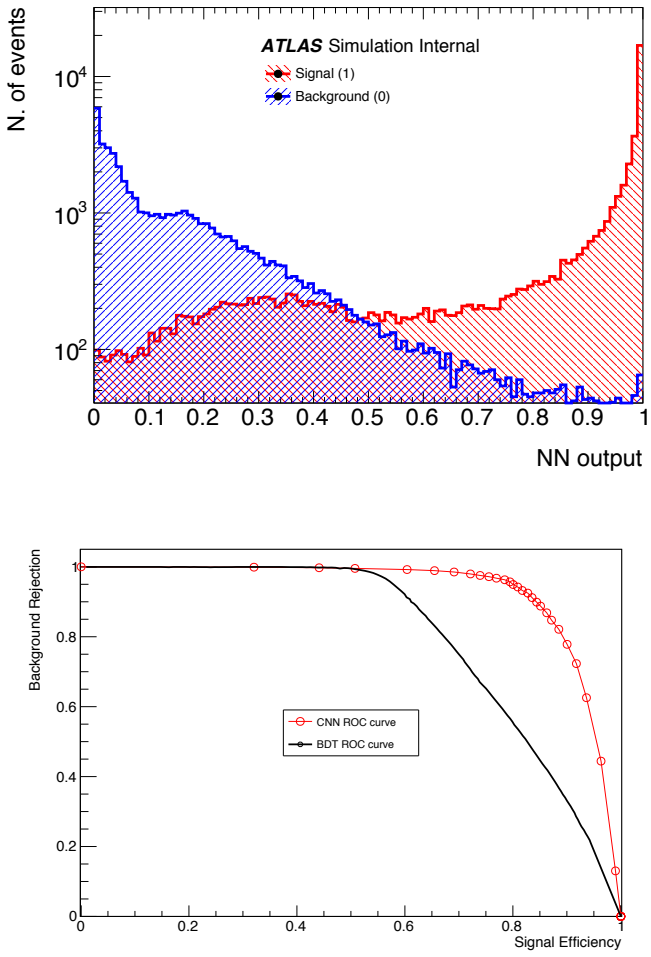

Figure 6.6. CNN discriminator output (left) for signal hadronic dark-photon jet in red and background QCD jet in blue. ROC curve comparison between CNN (red) and Run-2 BDT (red).

6.3 Mixed DPJ

The possibility to include in the analysis a mixed-DPJ to have a more complete dark-photon phenomenology is currently under study. The mixed-DPJ topology is designed to select close-by dark photons, one γ_d decaying to a muon pair and one γ_d decaying to an electron/pion pair. It is especially important for the $H \to 4\gamma_d + X$ process, where it would significantly increase the number of signal events in the final selection. This selection is orthogonal to the μDPJ and hDPJ, as it requires one jet and at least one muon in the DPJ cone of size $\Delta R = 0.4$. A schematic picture of the mixed-DPJ reconstruction is shown in Figure 6.7.

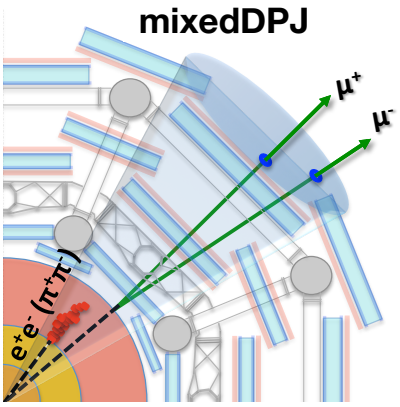

Figure 6.7. Schematic picture of the mixed dark-photon jet classification of the decay final state.

Mixed-DPJs are found also in $H \to 2\gamma_d + X$ events, arising from several different processes. The most common process being when one of the two muons coming from a dark photon decay has a non-negligible energy loss in the calorimeter mimicking a displaced jet and the second one is correctly reconstructed in the MS.

Considering the new DPJ topology, three new channels are taken into account: muonic-mixed, mixed-mixed, and mixed-hadronic.

A preliminary event selection based on the 36 fb^{-1} is made requiring the mixed-DPJ to pass both μDPJ and hDPJ cuts. Results are reported in Table 6.1 and Table 6.3 for the $H \to 2\gamma_d + X$ signal process, and in Table 6.2 and Table 6.4 for the $H \to 4\gamma_d + X$ signal process.

A potential increase on the number of signal events by 30% is observed, which will be further improved by optimising the selection cuts for the mixed-DPJ.

The mixed-DPJ reconstruction and selection is preliminarily performed also in the 2015-2016 collision dataset, and the distribution in ABCD regions are reported in Table 6.5. No events are observed in the ABCD regions for the cosmic and BIB datasets.

A preliminary exclusion on the muonic-mixed channel is made for the $H \to 2\gamma_d + X$ process with $m_H = 125$ GeV, and shown in Figure 6.8. Although validation and cross-check are yet to be made, a great potential sensitivity is observed. The mixed-mixed and mixed-hadronic channels are not exploitable for any test due to the low statistics in the 36fb^{-1} data.

	$H \to 2\gamma_d + X$ $m_H = 125$ GeV, $m_{\gamma_d} = 0.4$ MeV, $c\tau_{\gamma_d} = 49.23$ mm		
	muonic-mixed	mixed-mixed	mixed-hadronic
2LJ	1329 ± 37	39± 6	107 ± 10
muon η	1148± 34	32± 6	98 ± 10
no CB muon	811 ± 29	16± 4	73± 9
gap ratio	–	–	72± 9
jet timing	–	16± 4	72± 9
BDT	691 ± 26	1 ±1	1 ±1
region A	639 ± 26	1±1	1 ± 1
region B	29 ± 5	0	0
region C	0	0	0
region D	13 ± 4	0	0

Table 6.1. Event selection for the $H \to 2\gamma_d + X$ process with $m_H = 125$ GeV, $m_{\gamma_d} = 0.4$ GeV, and $c\tau_{\gamma_d} = 49.23$ mm. A luminosity of 36.1 fb^{-1} is assumed.

	$H \to 4\gamma_d + X$ $m_H = 125$ GeV, $m_{\gamma_d} = 0.4$ GeV, $c\tau_{\gamma_d} = 82.4$ mm		
	muonic-mixed	mixed-mixed	mixed-hadronic
2LJ	1758 ±42	482 ± 22	584 ± 24
muon η	1454 ± 31	387 ± 20	521 ± 23
no CB muon	962 ±31	263 ± 16	423 ±21
gap ratio	–	–	414 ±20
jet timing	958 ± 31	260 ± 16	414 ±20
BDT	216 ± 15	22 ± 5	5 ± 2
region A	199 ± 14	19 ± 4	5 ± 2
region B	6 ±2	2 ± 1	0
region C	0	0	0
region D	6 ±2	0	0

Table 6.2. Event selection for the $H \to 4\gamma_d + X$ process with $m_H = 125$ GeV, $m_{\gamma_d} = 0.4$ GeV, and $c\tau_{\gamma_d} = 82.4$ mm. A luminosity of 36.1 fb^{-1} is assumed.

	$H \to 2\gamma_d + X$ $m_H = 800$ GeV, $m_{\gamma_d} = 0.4$ GeV, $c\tau_{\gamma_d} = 11.76$ mm		
	muonic-mixed	mixed-mixed	mixed-hadronic
2LJ	64 ± 8	9 ± 3	80 ± 9
muon η	56 ±8	8 ± 3	75± 9
no CB muon	32 ± 6	5 ± 2	57± 8
gap ratio	–	–	57± 8
jet timing	32 ±6	5 ±2	57 ±8
BDT	8 ± 3	0	10 ± 3
region A	7 ± 3	0	9 ± 3
region B	1 ± 1	0	1± 1
region C	0	0	0
region D	0	0	0

Table 6.3. Event selection for the $H \to 2\gamma_d + X$ process with $m_H = 800$ GeV, $m_{\gamma_d} = 0.4$ GeV, and $c\tau_{\gamma_d} = 11.76$ mm. A luminosity of 36.1 fb^{-1} is assumed.

	$H \to 4\gamma_d + X$ $m_H = 800$ GeV, $m_{\gamma_d} = 0.4$ GeV, $c\tau_{\gamma_d} = 21.04$ mm		
	muonic-mixed	mixed-mixed	mixed-hadronic
2LJ	399 ± 20	263 ± 16	394 ±20
muon η	347 ± 19	222 ± 15	364 ±19
no CB muon	208 ± 14	130 ±11	296 ± 17
gap ratio	–	–	289 ± 17
jet timing	205 ± 14	128 ± 11	289 ±17
BDT	51 ± 7	13 ± 4	31 ± 6
region A	46 ± 7	11 ± 3	27 ±5
region B	2 ± 1	1 ±1	2 ± 1
region C	0	0	0
region D	0	0	0

Table 6.4. Event selection for the $H \to 4\gamma_d + X$ process with $m_H = 800$ GeV, $m_{\gamma_d} = 0.4$ GeV, and $c\tau_{\gamma_d} = 21.04$ mm. A luminosity of 36.1 fb^{-1} is assumed.

	2015 and 2016 data events		
	muonic-mixed	mixed-mixed	mixed-hadronic
region A	16	0	4
region B	8	0	5
region C	44	0	0
region D	48	1	1

Table 6.5. Mixed-DPJ pairs in each region of the ABCD plane for the 2015-2016 data sample.

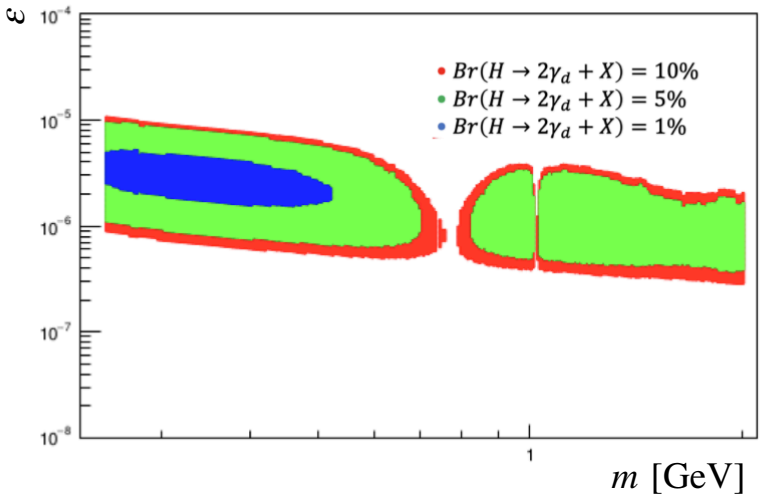

Figure 6.8. The 95% CL exclusion contours regions of the SM Higgs boson as a function of the γ_{d} mass and of the kinetic mixing parameter ϵ for the muonic-DPJ–mixed-DPJ channel in the $H \to 2\gamma_{\mathrm{d}} + X$ process.

6.4 Deep learning interpretation tool

A dark photon interpretation tool based on novel ML techniques is currently under development and study. The tool is designed to exploit DPJs channel's cross-contamination, extrapolating the most information form the data, and to perform an accurate dark photon mass reweighting. It will lead to a significant improvement in the result interpretation in vector portal models, overcoming the assumptions made in the current Run-2 analysis limits. In the current results, the signal efficiency as a function of γ_{d} mass is assumed to be constant over the interval from 0.2 GeV to 2 GeV and the μDPJ–μDPJ to be populated only from $\gamma_{\mathrm{d}} \to \mu\mu$ events. A neural network will be trained for each analysis channel, taking as input the signal efficiencies, the channel contaminations, and the vector portal parameters. It will be trained on several MC signal samples with different dark photon masses, spanning the analysis mass range. The final tool will be able to yield for any given $m_{\gamma_{\mathrm{d}}}$ and ϵ the analysis efficiency and channel contaminations, that can be used to set a limit in the vector portal model.

Preliminary tests are performed with a deep neural network trained on a signal MC sample with a dark photon mass of $m_{\gamma_{\mathrm{d}}}$=0.4 GeV. The channel contaminations studied at truth level for this sample are reported in Table 6.6.

Analysis channel	$\gamma_{\mathrm{d}}\gamma_{\mathrm{d}} \to 4\mu$	$\gamma_{\mathrm{d}}\gamma_{\mathrm{d}} \to 2\mu 2h$	$\gamma_{\mathrm{d}}\gamma_{\mathrm{d}} \to 4h$	fake
muonic-muonic	90%	7%	0%	3%
muonic-hadronic	0%	92%	6%	2%
hadronic-hadronic	0%	0%	100%	0%

Table 6.6. Analysis channel contaminations for the $H \to 2\gamma_{\mathrm{d}} + X$ process with $m_H = 125$ GeV, $m_{\gamma_{\mathrm{d}}} = 0.4$ GeV, and $c\tau_{\gamma_{\mathrm{d}}} = 49.23$ mm.

Considering only the μDPJ–μDPJ channel, the hadronically decayed dark photon misreconstructed as a μDPJ in the $\gamma_{\mathrm{d}}\gamma_{\mathrm{d}} \to 2\mu 2h$ process can thus be used to set a limit on γ_{d} hadronic decays.

A preliminary contour exclusion exploiting contamination in the muonic-muonic channel is made for the $H \to 2\gamma_{\mathrm{d}} + X$ process with $m_H = 125$ GeV, and shown in Figure 6.9. A significant improvement is observed in the mass range where the dark photon decays mainly to hadronic resonances.

In the full Run-2 dark-photon jet search, this tool will allow to perform a complete combination of all analysis channels and will help to improve the exclusion of dark photon hadronic decays.

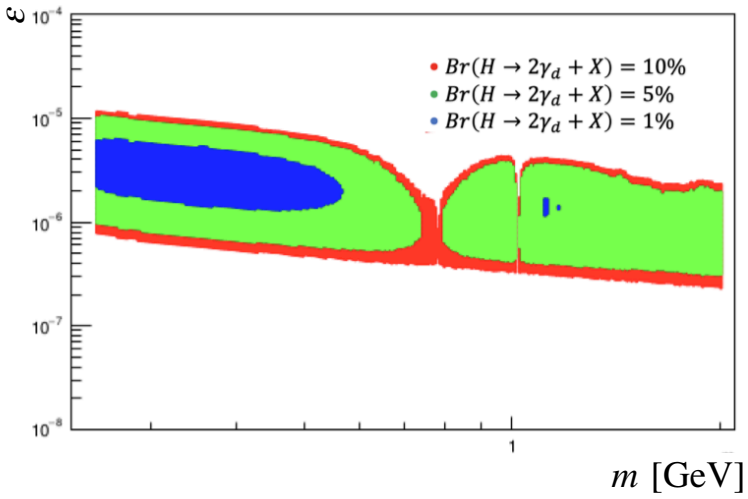

Figure 6.9. The 95% CL exclusion contours regions of the SM Higgs boson as a function of the γ_{d} mass and of the kinetic mixing parameter ϵ for the muonic-DPJ–muonic-DPJ channel in the $H \rightarrow 2\gamma_{\mathrm{d}} + X$ process.

Chapter 7

Search prospects at Run-3 and HL-LHC

7.1 HL-LHC upgrade

An extensive ATLAS detector and trigger upgrade plan is designed to cope with the extreme conditions of the High-Luminosity LHC (HL-LHC), a major upgrade of the LHC which is expected to operate at a centre-of-mass energy of $\sqrt{s} = 14$ TeV providing a peak instantaneous luminosity of $\sim 5 \times 10^{34}$ cm^{-2}s^{-1} [115], without significant performance losses. A detailed description of the upgrade plan can be found in the Phase-II Scoping Document [116]. This Section will give an overview of the upgrade plans for the systems of interest for the DPJ search: the ATLAS muon spectrometer in the barrel region [117] and the muon trigger and data acquisition [118].

The goal for the MS upgrade is to maintain the full muon reconstruction and identification efficiency of the present ATLAS setup. It will be crucial to preserve the low-p_{T} trigger threshold with sustainable rates. The lowest threshold for a single muon trigger will be $p_{\mathrm{T}} = 20$ GeV, which will need to keep a rate at the hardware-trigger level of less than 40 kHz [118]. It is also relevant to maintain multi-muon triggers with low p_{T} threshold. The detector upgrade will recover the Run-2 geometrical acceptance limit in the barrel region of the Resistive Plate Chamber (RPC) system, which is below 80%. Finally, the trigger and readout system will be improved. The new scheme will start with a single-level hardware trigger (L0 trigger) based on muon and calorimeter information with a latency of 10μ. L0 trigger will send events to the high-level trigger (HLT) at a rate of 1 Mhz.

7.1.1 Muon Spectrometer barrel upgrade

The main MS upgrade will affect the barrel region where new chambers will be installed and the front-end and readout electronics replaced. The present RPC system geometrical acceptance will be extended with the installation of an additional thin gap RPC layer. The layout of the ATLAS MS transverse section with the new RPC detectors is shown in Figure 7.1. The four layers composing the RPC system are shown in red: the new Barrel Inner (BI) RPC0 layer, the two Barrel Middle (BM)

RPC1-2 layers and the Barrel Outer (BO) RPC3 layer. A new electronic system is required to provide the necessary improvement in the trigger and data acquisition to reach the proposed goal of maintaining low trigger thresholds at sustainable rates in the HL-LHC environment.

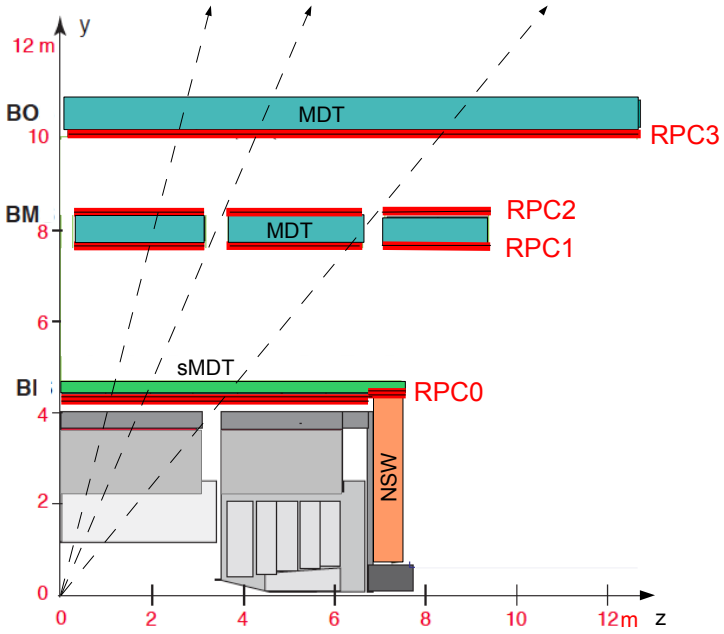

Figure 7.1. Transverse section of a small sector in the barrel region showing the four layers of RPC chambers: RPC0 in the barrel-inner (BI), RPC1-2 in the barrel-middle (BM), and RPC3 in the barrel-outer (BO) layers. The three dashed lines represent muon trajectories traversing two, three and four RPC chambers [118].

The readout of the RPC and TGC chambers will be replaced with Field Programmable Gate Array (FPGA) based boards. The system will exploit a data collector and transmitter (DCT) on-detector board, which will serialise the collected data to the counting room USA15, and an off-detector board where all information is collected and trigger algorithms are run. The possibility of modifying the firmware of the FPGA provides a solution for unexpected problems and changes in experimental conditions. The new scheme will allow more complex and flexible algorithms to be used compared to the current setup.

7.1.2 L0 muon trigger

The new hardware-based single-level trigger will be capable of handling a maximum rate of 1 MHz with a 10 μs latency; 200 kHz of the whole bandwidth will be assigned to muon triggers. The new L0 muon barrel trigger is planned to operate the same identification algorithm used in Run-2, based on hits coincidences in the different RPC layers within a $\Delta\eta \times \Delta\phi$ window pointing to the IP. The trigger will use a total of nine measurements planes distributed in the four RPC layers: three in the

BI, two in each BM layer, and two in the BO layer. Coincidence windows are tuned to select at least 95% of muons coming from the IP with a transverse momentum greater than the reference threshold. The windows effectively measure the muon momentum through the deflection of the trajectory with respect to a straight line from the IP.

The new BI layer will extend the Run-2 coincidence requirements, based on a 3 out of 3 layers ("3/3 chambers") algorithm, to a 3 out of 4 layers ("3/4 chambers") algorithm. The different requirements on the number of hits in the four RPC layers define the quality of the trigger selection and are summarised in Figure 7.2.

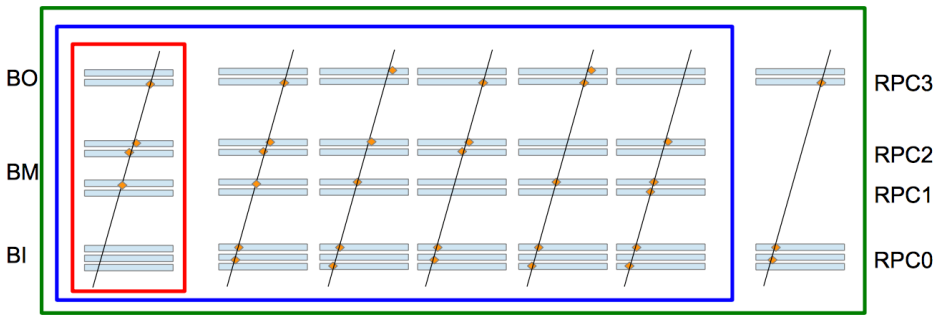

Figure 7.2. Schematic picture of the number of hits in the RPC layers required by the trigger: Run-2 "3/3 chambers" selection (red), 3 out of 4 layers ("3/4 chambers") selection (blue) and inner most and outermost layers ("BI-BO") selection.

The performance of this setup is studied using a MC simulation which includes the description of the new BI RPC layer in the detector geometry. The L0 muon trigger algorithm was implemented to include the new selections, and operates as follows. First the algorithm searches for hits in all RPC planes within the defined coincidence window opened from the innermost hit. The search is run independently for η and ϕ. The coincidence window requirement is then applied to each pair of hits in consecutive planes. In each iteration, a new coincidence window is opened on the hit in the current plane pointing to the IP. A schematic view of the steps is shown in Figure 7.3. If a hit pattern is found both for the η and ϕ plane, a muon candidate is found. If more than one pattern is found, the one with the greatest number of hits is considered.

The expected L0 trigger efficiency as a function of the muon pseudorapidity for the different qualities is shown in Figure 7.4 for prompt muons with $p_{\mathrm{T}} = 25$ GeV. The "3/4 chambers + BI-BO" selection is expected to improve the trigger acceptance $\times$ efficiency of the current Run-2 setup, "3/3 chambers", from 78% up to 96%. The L0 trigger will provide good efficiency at a moderate rate for low threshold single muon triggers.

7.1.3 RPC trigger and readout system

The current RPC on-detector trigger and readout electronics must be replaced to comply with the TDAQ requirements for HL-LHC operations. The on-detector electronics need to be simplified to minimise the radiation damage from the cavern background, retaining only the task of digitization of the front-end signals and of

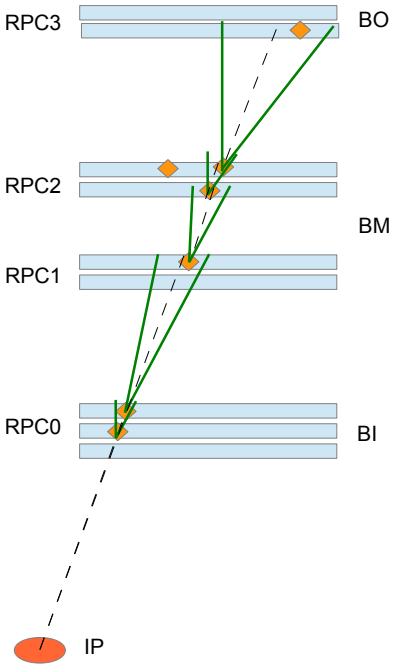

Figure 7.3. Illustration of the RPC L0 barrel trigger algorithm. Hits are associated between consecutive planes if the hit in the next (outer) plane lies inside a coincidence window around the straight line from the IP to the hit in the current (inner) plane. The width of the coincidence windows defines the p_{T} threshold.

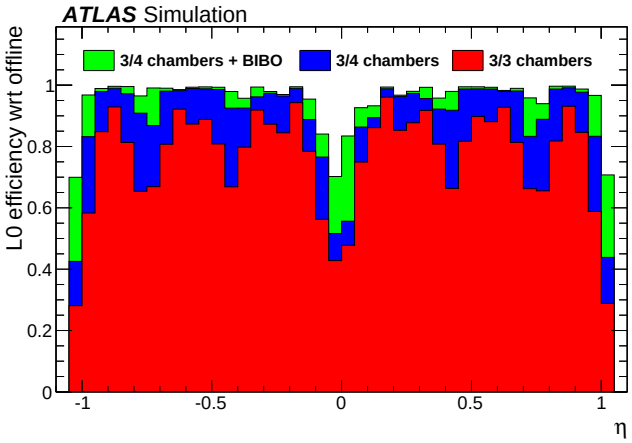

Figure 7.4. Acceptance × efficiency of the RPC trigger system as a function of η for the Run-2 system "3/3 chambers" trigger (red), for the HL-LHC "3/4 chambers" trigger (blue) and for the HL-LHC "3/4 chambers + BI-BO" trigger (green). The efficiency is evaluated using Monte Carlo simulation of single muons with a fixed transverse momentum of 25 GeV [118].

sending data off-detector at high speed. Trigger algorithms will then be executed on dedicate boards off-detector. A simplified scheme of the RPC readout system is shown in Figure 7.5. Front-end data from the RPC is digitised and serialised by the on-detector Data Collector Transmitter (DCT) to the off-detector barrel Sector Logic (SL) boards, where the trigger and readout is implemented. The SL boards run the L0 algorithm to select the muon candidates and send them, together with the information received from the Tile Calorimeter barrel outer layer, to the Monitored Drift Tube (MDT) trigger processor boards. The MDT trigger processor sends a signal back to the SL whether the muon candidate is confirmed or rejected, which in turn sends all the barrel L0 candidates to the Muon to Central Trigger Processor interface (MuCTPi). If the L0-accept confirmation is received, the SL sends the readout data, which was stored in local buffer, to the Front-End Link interface eXchange [119] (FELIX) system.

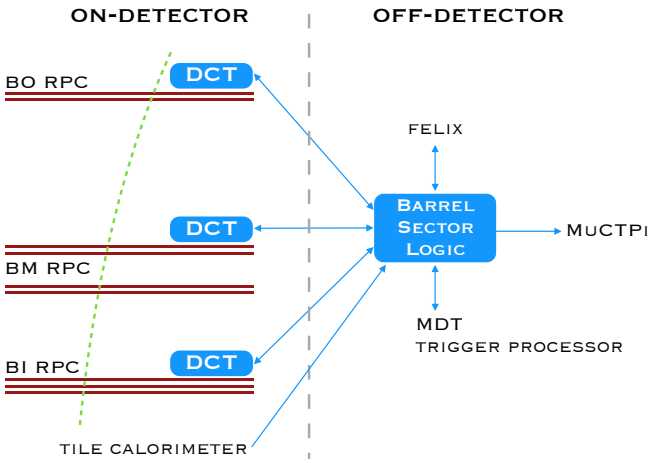

Figure 7.5. L0 RPC readout scheme in the barrel for HL-LHC. The on-detector DCT boards sample the RPC front-end data and send the digitized data on optical fibres to the off-detector Sector Logic boards which perform the trigger algorithm and readout logic.

DCT board

The DCT collects the data from the RPC front-end and sends the hit information off-detector on an optical fibre. Front-end data from the RPC is digitised and serialised by the on-detector DCT to the off-detector barrel SL boards, where the trigger and readout is implemented. A block diagram of the board is shown in Figure 7.6. The DCT board hosts one FPGA performing the digital logic and one high-speed bi-directional Gigabit Transceiver (GBTx) for serial data transmission, interfaced to a slow control unit (GBT- SCA) for monitoring and configuration. The GBT optical fibre's bandwidth limit is foreseen at 9.6 Gb/s. Through an electrical-to-optical transceiver (VTRx), the DCT receives the trigger, timing and control (TTC) signals from the SL and sends the zero-suppressed hit information.

The final configuration of the DCT boards is currently under development.

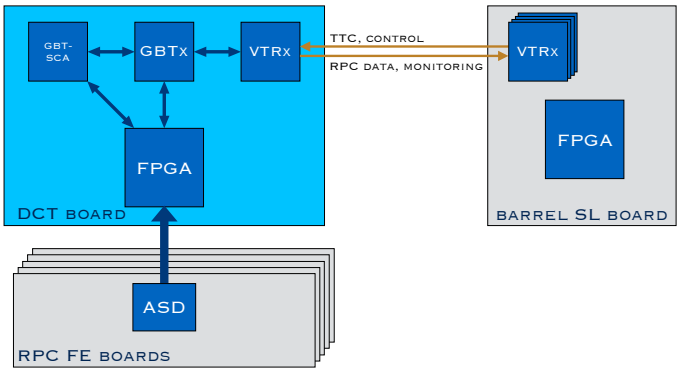

Figure 7.6. Block diagram of the DCT board. The FPGA is used to sample and zero-suppress the RPC front-end data. The GBTx serializes the FPGA input and output data. The GBT-SCA chip is used for board control and monitoring.

DCT hardware simulation

The first hardware simulation of a RPC DCT board is performed in order to help to define the final configuration, to evaluate the electronic components and to estimate the expected data bandwidth. The simulation, programmed in VHDL (VHSIC Hardware Descriptive Language), comprises a simulation of the input channels from the RPC and a hardware simulation, synthesizable in the FPGA, of the DCT digital logic. VHDL is a versatile and powerful hardware description language which is useful for modelling electronic systems at various levels of design abstraction. The RPC front-end sends hit information from each strip of the RPC detector, which are arranged along the η and ϕ direction, as input to the DCT. The number of front-end RPC strips connected to a DCT board depends on the type and location of the RPC chamber. The maximum number of channels for a BM sector is 512 channels: 32 strips along η and 32 strips along ϕ are read for each layer (GasGap) of the two BM layers, covering half of the sector surface. A BM RPC sector is composed of four single RPC chambers, arranged along the longitudinal (DoubletZ) and transversal (DoubletR) direction with respect to the beam pipe. The maximum number of channels for a BI sector is 408 channels: 48 strips along η and 88 strips along ϕ are read for each layer (GasGap) of the three BI layers, covering the whole sector surface (BI RPC sectors are composed of a single RPC chamber). DCT input for the BM and BI RPC sectors are schematically summarised in Figure 7.7. The hardware simulation, as illustrated in Figure 7.8, is composed of a readout block, a first-in-first-out (FIFO) buffer and a encoder. The FPGA will operate at a clock frequency of 500 MHz and will sample RPC hit times on both the rising edge and falling edge of the clock. The readout block is designed to sample the RPC front-end input, with a resolution of 1 ns and pushes all the information into a FIFO buffer.

The encoder pulls the data from the buffer to perform a zero-suppression and serialise the data, following a well defined transmission protocol, to the output.

The output is transmitted synchronously using the clock in a continual stream of 18 bit words, for a total bandwidth of 9 GB/s. The output data format is: 6-bit header for alignment, 2-bit index, 12-bit bunch crossing time (LHC operates at 40 MHz), 2-bit index, 2-bit hit time, 5-bit index (14-bit for BI RPC as sampled on both

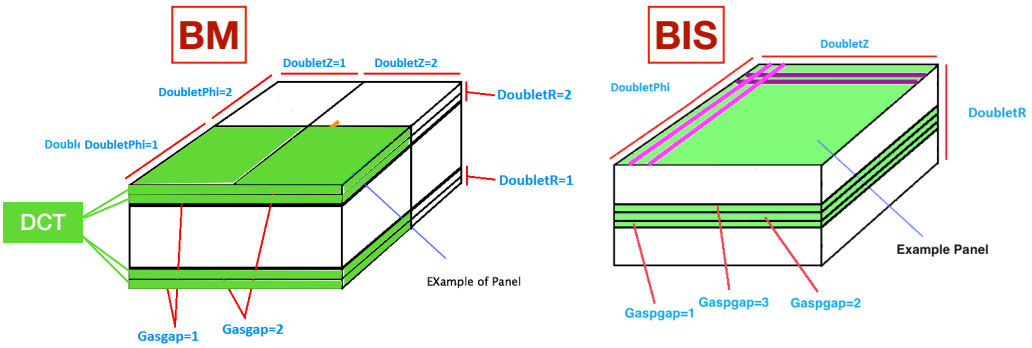

Figure 7.7. Picture of DCT board input sections in BM (left) and BI small (right) RPC station. In the BM station, a single DCT unit collects data from each hit measurement plane of the two RPC layers, covering half of the sector surface. In the BI station, a single DCT unit collects data from each hit measurement plane of the RPC layer, covering the total sector surface.

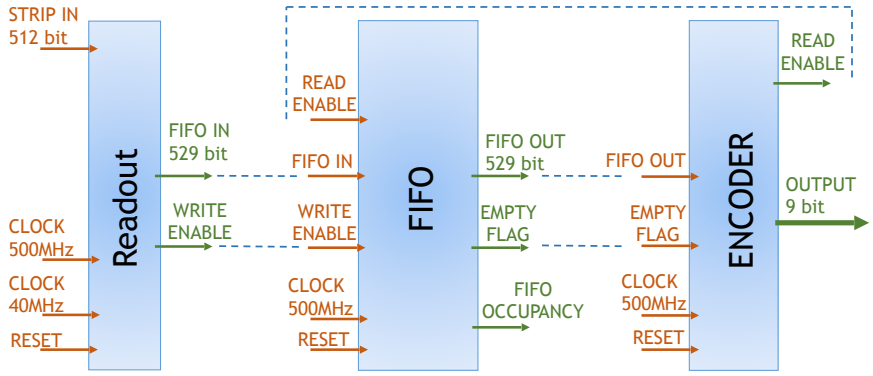

Figure 7.8. Block diagram of DCT board simulation. System operates at a clock frequency of 500 MHz. Readout block samples the RPC front-end input to push it into a FIFO buffer. The data is then pulled and serialised by the encoder.

leading and trailing edge), 2-bit index, 9-bit strip ID (the last two words may be repeated in case of multiple hits at the same time). A visual scheme of the protocol is shown in Figure 7.9 for a BM station. The DCT performance is tested in a realistic configuration of the expected conditions of HL-LHC environment. RPC hits are taken from MC samples generated at HL-LHC conditions, shown in Section 7.2.1, and used as input to the simulation. Assuming the worst-case scenario, one of the most exposed chambers are selected from the large BM and BI sector.

The BML chamber situated in ϕ-sector 3.01 and in z-sector -5, see Figure 7.10, has an expected rate of 195 Hz/cm^2 (considering a safety factor of two and a simulated cluster size of 1.5), with an average strip occupancy per bunch crossing of 0.5% and a hit rate of 0.096 hits/ns. The BIS chamber, situated in the same sectors as the selected BML, has an expected rate of 152 Hz/cm^2, with an average strip occupancy per bunch crossing of 0.1% and a hit rate of 0.014 hits/ns.

First the buffer depth and possible overflow is checked. A buffer overflow occurs

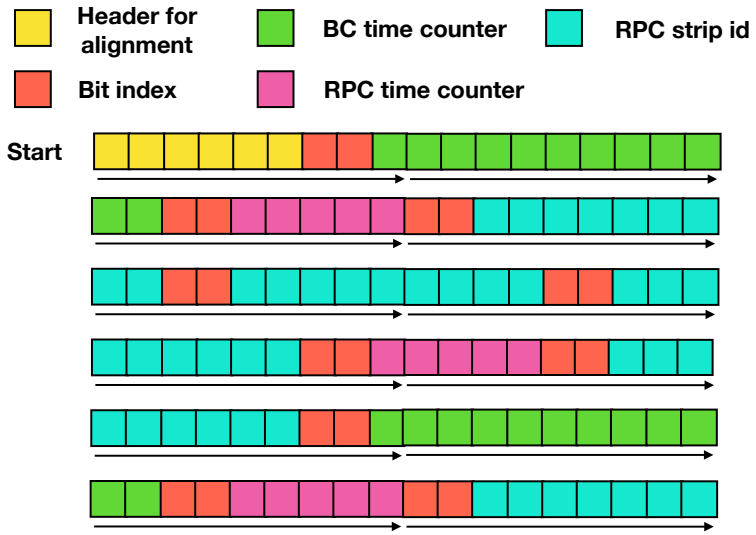

Figure 7.9. Visual scheme of the output data format for a BM station. The protocol accounts for: 6-bit header for alignment, 2-bit index, 12-bit bunch crossing time (LHC operates at 40 MHz), 2-bit index, 2-bit hit time, 5-bit index, 2-bit index, 9-bit strip ID (the last two words may be repeated in case of multiple hits at the same time).

Sector	RPC unit Id. along Z direction																			
Id.	-6.2	-6.1	-5.0	-4.0	-3.2	-3.1	-2.2	-2.1	-1.2	-1.1	1.1	1.2	2.1	2.2	3.1	3.2	4.0	5.0	6.1	6.2	Average
01.01	342	280	301	225	145	114	128	101		61	61	71	113	122	127	136	214	276	269	285	180
01.02	293	281	303	218	159	133	129	143		76	71	75	127	143	140	148	215	295	278	297	188
2	168	204	188	138	109	90	77	63	55	56	45	48	61	79	94	104	140	207	196	152	115
03.01	297	296	281	198	148	128	119	119	68	67	65	71	131	125	114	125	207	329	268	290	177
03.02	300	243	277	210	151	129	155	122	85	75	75	70	122	127	152	132	207	315	243	299	179
4	112	166	158	151	101	83	65	77	41	53	46	41	73	68	92	108	160	196	175	112	101
05.01	171	173	263	138	105	102	140	127	68	60	60	69	124	177	102	137	185	290	173	171	149
05.02	227	198	237	158	109	105	136	143	77	61	63	71	111	136	108	141	200	267	255	282	159
6	175	186	208	163	105	95	90	95	77	59	52	59	84	81	106	124	189	200	227	167	131
07.01	305	263	288	191	154	129	131	114		76	78		122	139	124	148	185	261	268	305	183
07.02	327	258	216	203	141	112	129	108		74	77		105	114	112	152	184	278	276	279	175
8	146	196	195	161	103	85	80	70	50	57	54	54	67	74	85	108	168	196	194	156	118
09.01	319	246	301	206	155	117	149	119		46	64		106	134	124	135	197	283	262	297	181
09.02	347	258	287	205	143	95	107	103		58	67		99	112	95	137	188	285	265	292	174
10	174	201	207	147	99	86	68	71	46	43	41	50	64	69	80	103	148	193	201	170	115
11.01	308	244	237	157	97	84	81	87		40	43		83	94	92	94	148	227	215	278	132
11.02	196	193	157	105	78	66	55	57		33	31		50	62	58	71	98	151	160	185	98
12						80	81	66	51	36	36	51	75	87	80						64
13.01	291	278	253		140	102	96	84	43	41	47	50	87	95	99	123		249	263	319	149
13.02	299	264	262		104	97	105	86	49	48	50	56	93	103	97	110		252	227	294	146
14						142	68	64	52	41	40	49	63	68	136						76
15.01	196	221	148	113	76	71	67	49		38	36		50	59	86	87	104	156	173	196	104
15.02	183	159	246	164	116	98	103	75		44	43		75	106	112	107	158	248	159	183	133
16	173	214	216	173	108	89	54	75	56	59	50	50	77	54	87	103	177	209	208	154	124
Average	229	223	234	167	118	101	96	88	56	52	51	56	86	97	103	118	171	240	221	221	137

Figure 7.10. Averaged RPC hit rates in BM chambers, measured in Run 1 and extrapolated (including a safety factor of two) to a luminosity of $7.5 \times 10^{34}\text{cm}^{-2}\text{s}^{-1}$. The plot shows rates Hz/cm^2 as a function of the ϕ-sector (vertical axis) and of the station number along Z (horizontal axis).

every time the data are pushed into a buffer when there is no more space allocated in its memory, which would result in a data loss. For this test a 529 × 1024 bit buffer is considered. Buffer depth evolution during the simulation of few ms is shown in Figure 7.11, with minimum bias and $Z \to \mu\mu$ MC samples. The buffer is stable and no overflow that would result in data loss is observed.

The buffer latency is then studied to understand how many bunch crossings are needed to exit the serialised strip information. The time difference between hit arrival time and the time of the last strip information is pushed out in terms of

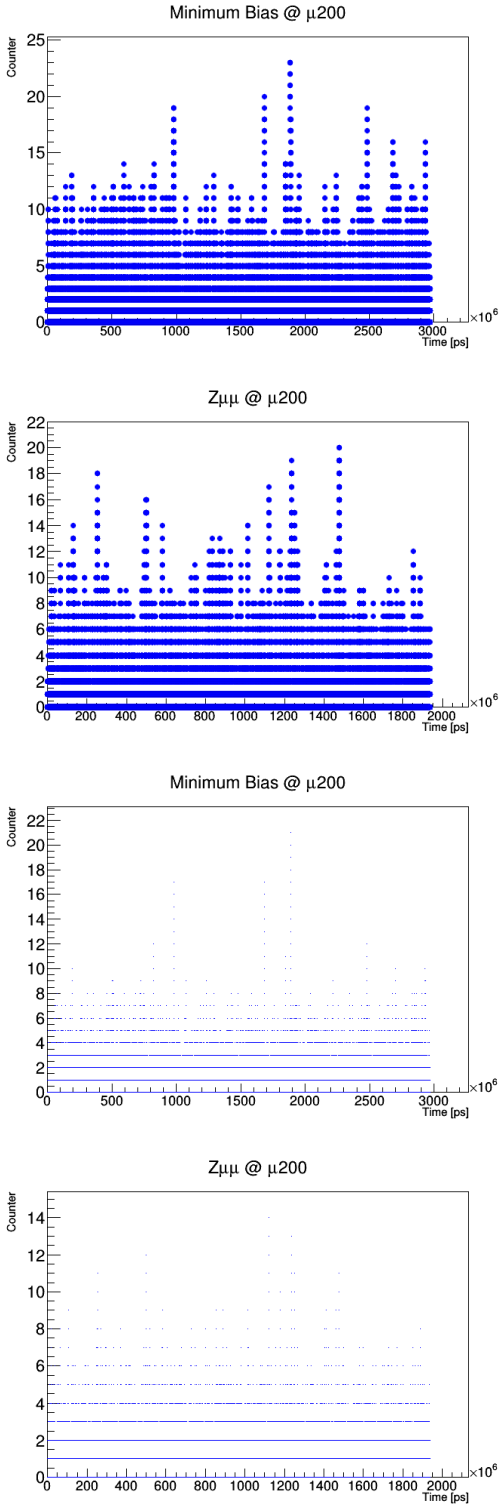

Figure 7.11. Buffer depth evolution tested for BM (top) and BI (bottom) scenario on a minimum bias (left) and a $Z \to \mu\mu$ (right) MC samples. No buffer overflow is seen.

bunch-crossing count is shown in Figure 7.12, for different simulated scenarios in the BM and BI simulation. In the worst case scenario, a latency of 14 BC for the BM and 10 BC for the BI would allow the buffer to push all the data without any loss.

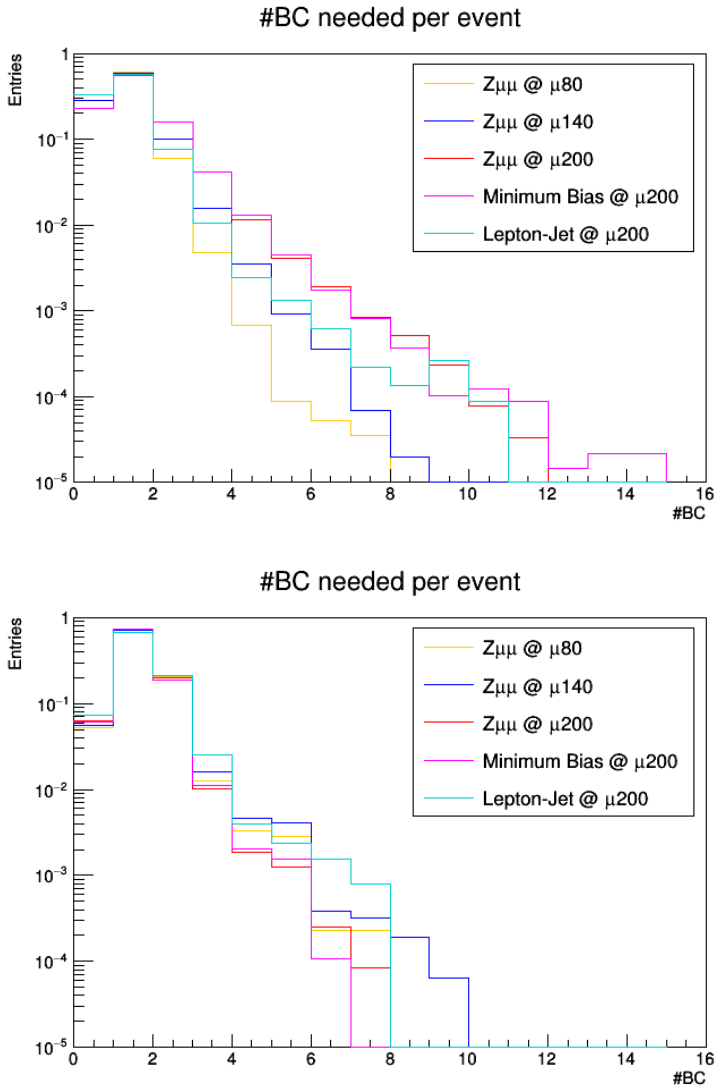

Figure 7.12. DCT latency in terms of bunch crossings counts for BM (top) and BI (bottom) scenario. Latency is considered as the time difference between hits arrival time and the time the last strip information is pushed out. A bunch crossing count consists of 25 ns.

The DCT system processing efficiency as a function of the BC latency counts is shown in Figure 7.13. The simulated DCT system and the implemented transmission protocol have shown that a FPGA-based system is suitable to serialise and transmit RPC hit data in a high rate and pile-up environment without data loss.

The total estimated processing time of the DCT FPGA is 15 bunch crossings: 4 BC for data manipulation, 1 BC for zero suppression, 10 BC for buffer latency. Considering 18 BC latency for signal transmission in the optical fibre from the DCT to USA15, assuming a maximum fibre length of 90 m, the total expected

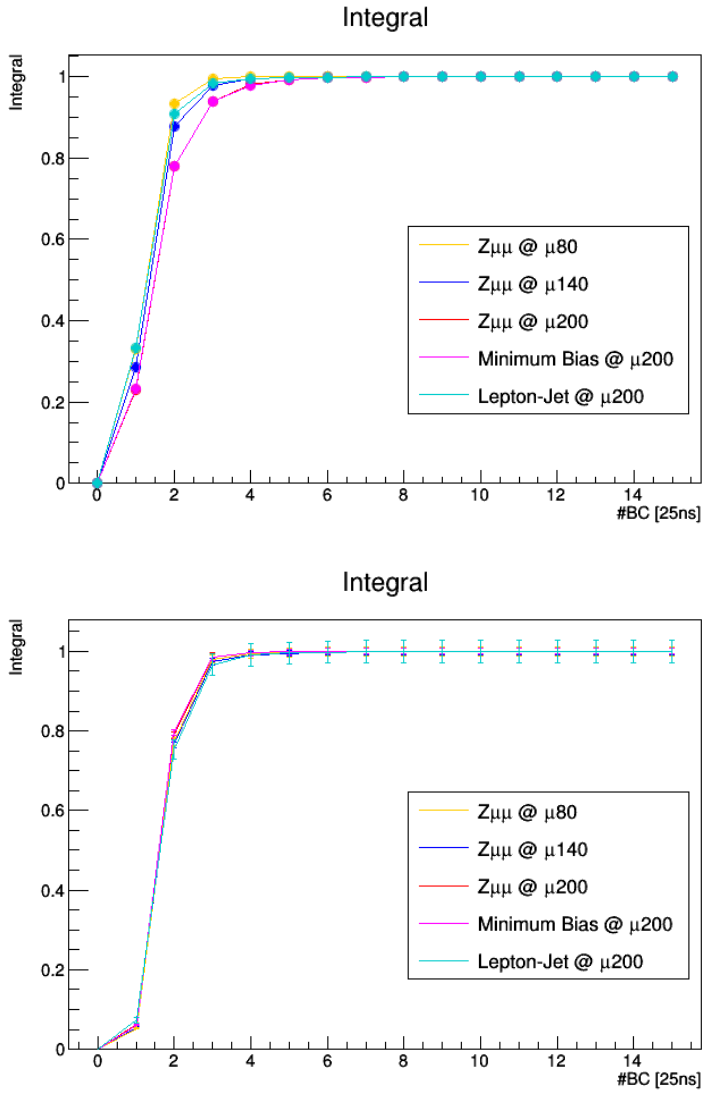

Figure 7.13. DCT selection efficiency for BM (top) and BI (bottom) scenario.

latency from DCT to the SL is 33 BC (0.825 μs). This complies with the required specification of the muon TDAQ for the barrel by using a single optical fibre.

7.2 HL-LHC trigger improvements

Long-lived particle searches are based on specialised triggers, designed to overcome the inefficiency of ATLAS Run-2 standard triggers [58] which are optimised for the selection of prompt particles from the interaction point. This is the case for the Run-2 dark-photon jet search presented in Chapter 5, which relies on the narrow-scan trigger to select dark photon decays into muons. However, the narrow-scan trigger is far from optimal. The ATLAS upgrade offers an incredible opportunity to exploit the new hardware changes to develop new ideas for signatures that might have been

missed.

In the boosted scenario, the out-going muons from a dark photon decay are very collimated and the Run-2 L1 trigger efficiency is limited by the finite granularity of the TDAQ system. The muon trigger is designed to yield a single muon candidate per Region of Interest (RoI), of dimension 0.2×0.2 ($\Delta\eta \times \Delta\phi$). The proposed muon-scan trigger will recover this inefficiency.

Oppositely, if the dark photon is not boosted sufficiently, the out-going muons from a displaced decay are not pointing to the IP. This scenario is very challenging for the current trigger, which is based on threshold windows opened towards the IP, resulting in a non-optimal selection for any non-pointing muon track. The suggested sagitta-muon trigger will extend the reach of the trigger system to these events.

These new proposed triggers will allow to choose a lower muon trigger p_{T} threshold compared to the Run-2 configuration, improving the selection efficiency of events with displaced muon pairs without increasing significantly the trigger rate.

7.2.1 MC samples

The simulation samples introduced in this Section are generated and processed for two different setups to reflect the Run-2 and the expected HL-LHC environments. The Run-2 setup samples are generated at a centre-of-mass energy of 13 TeV with a number of interactions per bunch crossing of $\langle\mu\rangle = 25$ and processed through a full simulation of the ATLAS detector geometry and response using the GEANT4 [86] toolkit. The HL-LHC setup samples are generated at a centre-of-mass energy of 14 TeV with a number of interactions per bunch crossing of $\langle\mu\rangle = 200$ and processed through the simulation framework developed for the expected HL-LHC upgraded detector using the GEANT4 toolkit. To model the effect of pile-up, additional collisions are overlaid on each generated signal and background event. The multiple interactions were simulated with PYTHIA 8.210 using the A2 tune [87] and the MSTW2008LO PDF set [88].

Signal Processes

The FRVZ model used for the Run-2 dark-photon jet search, introduced in Section 3.5, is used for the studies presented in this chapter. To obtain a boosted dark photon scenario, two samples are generated with a light mass of 400 MeV with different proper decay length: a very displaced ('medium') sample with $c\tau = 49$ mm and a less displaced ('short') sample with $c\tau = 4.9$ mm. Instead, a sample with a heavier dark photon with mass of 10 GeV is generated for the non boosted scenario and non pointing muons. All signal samples are generated at a centre-of-mass energy of 13 and 14 TeV and only the dominant ggF Higgs production mechanism is considered. The estimated cross sections, calculated at next-to-next-to-leading order (NNLO) [76], in pp collisions at $\sqrt{s} = 13$ TeV and $\sqrt{s} = 14$ TeV are respectively $\sigma_{\mathrm{SM}} = 43.87$ pb and $\sigma_{\mathrm{SM}} = 49.97$ pb assuming $m_{\mathrm{H}} = 125$ GeV. The samples are generated at leading order using MG5_aMC@NLO 2.2.3 [72] interfaced to the PYTHIA 8.210 [73] parton shower model. The A14 set of tuned parameters [74] are used together with the NNPDF2.3LO parton distribution function (PDF) set [75]. The list of the samples with all the generation parameters are summarised in Table 7.1.

$\sqrt{s}$ [TeV]	$< \mu >$	m_H [GeV]	$m_{f_{d_2}}$ [GeV]	m_{HLSP} [GeV]	m_{γ_d} [GeV]	$c\tau_{\gamma_d}$ [mm]
13	25	125	5.0	2.0	0.4	49
13	25	125	5.0	2.0	0.4	4.9
13	25	125	30	10	10	856
14	200	125	5.0	2.0	0.4	49
14	200	125	5.0	2.0	0.4	4.9
14	200	125	30	10	10	856

Table 7.1. Parameters used for the MC generation of the $H \rightarrow 2\gamma_d + X$ FRVZ benchmark samples.

Background

As addressed in the previous Chapters, the main background in the dark-photon jet analysis is due to multi-jet events. All multi-jet MC samples are generated for both Run-2 and HL-LHC setups with Pythia 8.210 and using the A14 tune with the NNPDF2.3LO PDF set.

Simulated sample of $Z \rightarrow \mu\mu$ events are used for trigger and systematic uncertainties studies. For the HL-LHC setup, four different pile-up conditions ranging from 30 to 200 interactions per bunch crossing are generated to study the effects of pile-up on signal and background efficiencies. These samples are generated with Powheg 1.2856 [120, 121] and Pythia 8.186 using the CT10 [122] PDF set and the AZNLO [123] tune.

Finally, a minimum bias sample is generated for trigger rate evaluation for the HL-LHC setup. The sample is generated with Pythia 8 with A2 [87] tune and MSTW2008LO [88] PDF.

All generated background samples are summarised in Table 7.2.

Sample	$\sqrt{s}$ [TeV]	$< \mu >$
QCD dijet	13	25
QCD dijet	14	200
$Z \rightarrow \mu\mu$	13	25
$Z \rightarrow \mu\mu$	14	30
$Z \rightarrow \mu\mu$	14	80
$Z \rightarrow \mu\mu$	14	140
$Z \rightarrow \mu\mu$	14	200
Minimum bias	14	200

Table 7.2. Parameters used for the Monte Carlo generation of the multijets, minimum bias and $Z \rightarrow \mu\mu$ samples.

7.2.2 Run-2 vs HL-LHC comparison

The HL-LHC simulation framework is validated by comparing the low-level single muon trigger efficiency to the Run-2 setup for the FRVZ 'medium' signal sample. The baseline trigger threshold of $p_{\mathrm{T}} = 20$ GeV is tested selecting at truth level only events with muons decays in the barrel region, $|\eta| < 1.05$. The muon trigger efficiency as a function of the truth transverse decay position (L_{xy}) of the dark photon is shown in Figure 7.14 for the Run-2 setup, in blue, and the HL-LHC setup, in red. The new BI RPC trigger layer situated at ~ 4.5 m in the transverse plane allows the HL-LHC setup to yield a higher efficiency with respect to Run-2 for decays that happen before this layer. For a transverse decay distance larger than ~ 4.5 m, the two setups show a comparable efficiency as expected. The efficiency drop at ~ 6.5 m corresponds to the position of the BM RPC layer, after which the system is no longer able to select these events. The low efficiency reported at small decay lengths is a feature of the model; indeed in this regime the dark photon has low boost which results in low p_{T} muons.

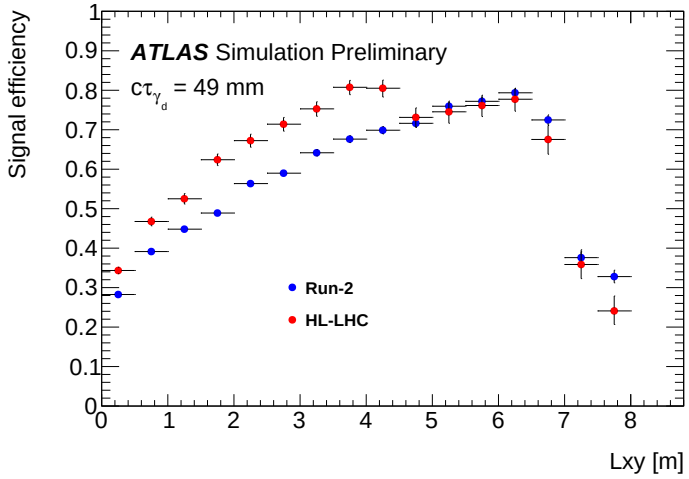

Figure 7.14. Efficiency for the single muon trigger with threshold $p_{\mathrm{T}} = 20$ GeV as a function of the truth transverse decay position of the γ_{d} for the Run-2 (blue) and the HL-LHC (red) setups.

7.2.3 Multi-muon scan

The Run-2 trigger system is able to select only a single muon candidate per RoI, of dimension 0.2×0.2 ($\Delta\eta \times \Delta\phi$), and is therefore very inefficient in the selection of close-by muons. This is the case for muons from a dark photon decay in a boosted scenario. The opening azimuthal angle between the two out-going muons of the dark photon decay as a function of the leading muon p_{T} is shown in Figure 7.15 for the signal 'medium' sample. Most of the signal events are likely to fall in the same RoI, thus could be selected only by a single muon trigger. Since it is not possible to choose a single muon p_{T} threshold lower than 20 GeV due to the high trigger rate, the Run-2 system is very inadequate in selecting low-p_{T} close-by muons, a typical signature of Dark Sector models.

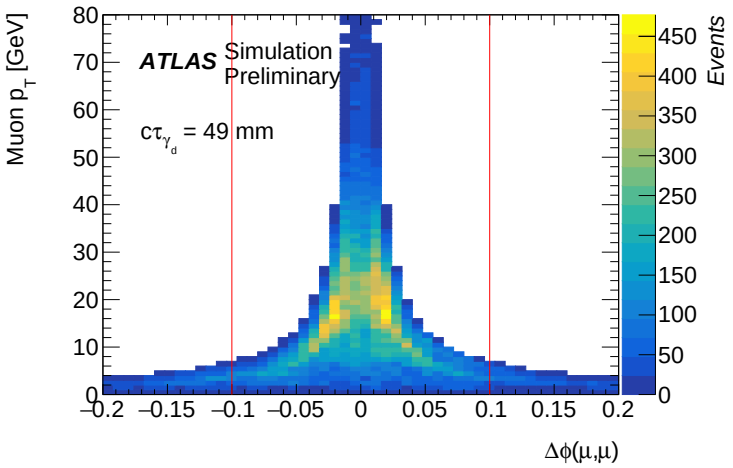

Figure 7.15. Truth transverse momentum distribution of the leading muon as a function of the opening angle in the ϕ plane of the two muons of the γ_{d} decay. Red lines show the RoI size. The 'medium' sample with average lifetime $c\tau = 49$ mm is used.

As a solution to this inefficiency, a new trigger at L0 called 'multi-muon scan' is developed. This trigger marks in the sector logic when multiple muon candidates are found in a single RoI. This selection would allow to use a lower p_{T} trigger threshold in order to reach a higher signal efficiency without increasing significantly the trigger rate.

L0 multi-muon algorithm

The multi-muon trigger algorithm is tested in the barrel, and designed to extend the standard triggering algorithm to seek additional muon patterns in the RoI. The standard algorithm processes all the hits that occurred in the nine RPC trigger layers, searching inside a window for the pattern with the highest number of hit points, called the best pattern, to form the primary muon candidate in the RoI. At this point the multi-muon algorithm searches for additional hit patterns not compatible with the best pattern. The two patterns are required not to share any hits. In addition, hits in at least three different RPC layers are required to reduce possible coincidence due to white noise. If at least one valid secondary pattern is found, an additional muon is assumed to be found in the RoI. The only free parameter to set in the algorithm is the minimal azimuthal angular separation between the secondary pattern and the best one ($\Delta\phi_{\mathrm{RoI}}$), hereafter called 'resolution parameter'. A cut on this parameter is required to reduce the fake rate.

A new L0 trigger is then defined by the logical OR of a single muon L0 with a $p_{\mathrm{T}} = 20$ GeV threshold and a multi-muon L0 with a $p_{\mathrm{T}} = 10$ GeV threshold.

The efficiency, defined as the number of triggered events over the number of total events, of the multi-muon trigger is evaluated as a function of the resolution parameter for the 'medium' signal sample and shown in Figure 7.16. It also shoes the fake rate as a function of the resolution parameter, estimated on single muon events from a simulated $Z \to \mu\mu$ sample.

A constraint on $\Delta\phi_{\mathrm{RoI}}$ is necessary to reduce the fake rate, keeping in mind

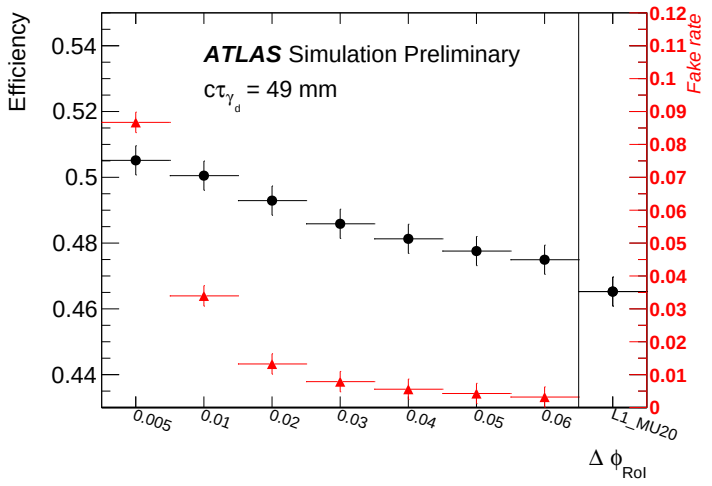

Figure 7.16. L0 multi-muon scan trigger efficiency for the 'medium' FRVZ signal sample in black (left axis) and fake rate in red (right axis) as a function of the resolution parameter $\Delta\phi_{\text{RoI}}$. In the separate box the Run-2 standard $p_{\text{T}} = 20$ GeV (L1_MU20) trigger efficiency is shown for comparison.

that a smaller resolution parameter yields a higher efficiency. The best compromise between signal efficiency and fake rate is found at the value $\Delta\phi_{\text{RoI}} = 0.01$, which is adopted as the working point for this study.

The rate of the L0 multi-muon scan is estimated to be 13 kHz at an luminosity of 5×10^{34} cm^{-2}s^{-1}. This is evaluated on the minimum bias MC sample assuming the multijet background contamination is negligible.

Trigger efficiency

The L0 multi-muon scan trigger efficiency is estimated as a function of the azimuthal opening angle $\Delta\phi(\mu,\mu)$ between the two muons of the dark photon decay, for both the 'short' and 'medium' signal samples. At truth level, events with a leading muon with $p_{\text{T}} > 10$ GeV and sub-leading muon with $p_{\text{T}} > 5$ GeV are selected, these are shown in Figure 7.17.

The efficiencies are shown in Figure 7.18 together with two single muon trigger selections with 10 and 20 GeV thresholds. The multi-muon selection improves the standard 20 GeV single muon trigger reducing the efficiency gap with respect to the 10 GeV single muon trigger, which cannot be used due to the high trigger rate at L0. A different behaviour is observed for the two different samples as $\Delta\phi(\mu,\mu)$ depends on both the decay distance and the γ_{d} transverse momentum. The 'short' sample is expected to have in average a larger p_{T} at small $\Delta\phi(\mu,\mu)$ with respect to the 'medium' sample, thus a greater efficiency is achieved in this regime. In the larger $\Delta\phi(\mu,\mu)$ regime both samples are expected to have the same trigger efficiency. A gain in signal efficiency of $\sim 7\%$ is achieved with respect to the single 20 GeV muon trigger, for the tested signal model.

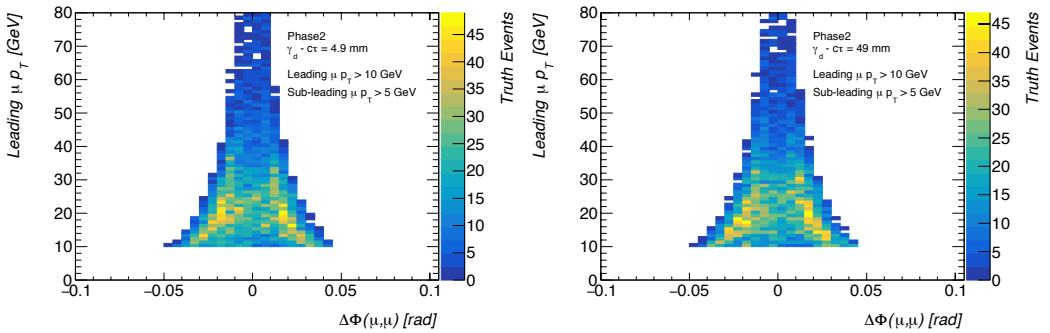

(a) 'short' sample $c\tau = 4.9mm$ (b) 'medium' sample $c\tau = 49mm$

Figure 7.17. Truth transverse momentum distribution of the leading muon as a function of the angular distance in the ϕ-plane of the two outcoming muons, decay products of the γ_d. Events with leading muon with $p_{\mathrm{T}} \geq 10$ GeV and sub-leading muon with $p_{\mathrm{T}} \geq 5$ GeV are selected at truth level.

7.2.4 L0 sagitta muon: a algorithm to select non pointing muons

As mentioned in Section 7.1.2, the Run-2 low level muon trigger threshold windows are designed to select muons coming from the interaction point, resulting in a very inefficient selection for non-pointing muons. A scenario with non-pointing dark photons is studied with the signal sample with a dark photon mass of 10 GeV where the γ_{d} are not boosted sufficiently. In this sample, highly boosted muons have a large longitudinal track impact parameter (z_0), defined as the minimum distance in the z coordinate of the muon track extrapolated to the IP. Figure 7.19 shows z_0 as a function of the muon transverse momentum for this sample. The single muon trigger efficiency would fall off approximately linearly with z_0 to zero for values of $|z_0| \geq$ 200 mm. Moreover, the transverse momentum of a non-pointing track would be mis-reconstructed underestimating its p_{T} value, due to the threshold window optimization. A muon with $p_{\mathrm{T}} = 20$ GeV non-pointing to the PV can be triggered by a low-p_{T} threshold, e.g. $p_{\mathrm{T}} = 5$ GeV , and not by a high-p_{T} one.

A new trigger based on the sagitta method is proposed, called 'L0 sagitta muon', to recover this loss of efficiency for high z_0 tracks.

Sagitta method

A viable strategy to recover this kind of events consists in selecting muons with a lower threshold trigger, and then recomputing the mis-reconstructed transverse momentum by the sagitta method. The sagitta (s) is defined as the vertical distance from the midpoint of the chord (L) to the arc of the muon trajectory itself. A schematic picture of the sagitta is shown in Figure 7.20. The $\eta - \phi$ information is needed for at least three points, thus a hit in each RPC station (BI-BM-BO) is required.

The sagitta as a function of the truth muon transverse momentum is studied for a MC sample of single muons generated according to a uniform transverse momentum distribution. The inverse of the sagitta distribution as a function of the truth

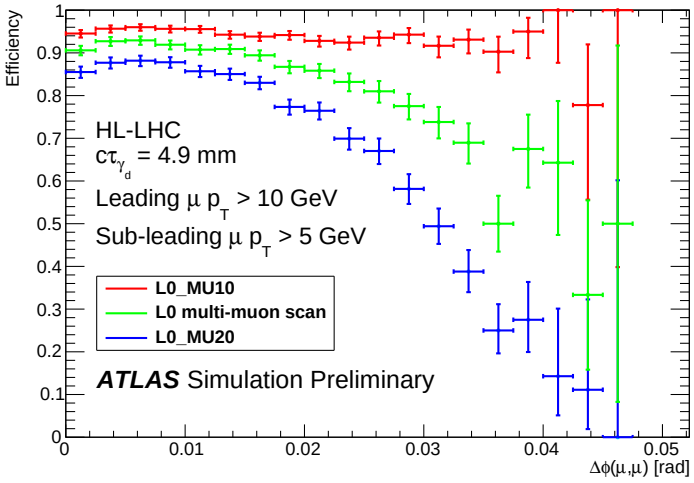

(a) 'short' sample, $c\tau = 4.9mm$

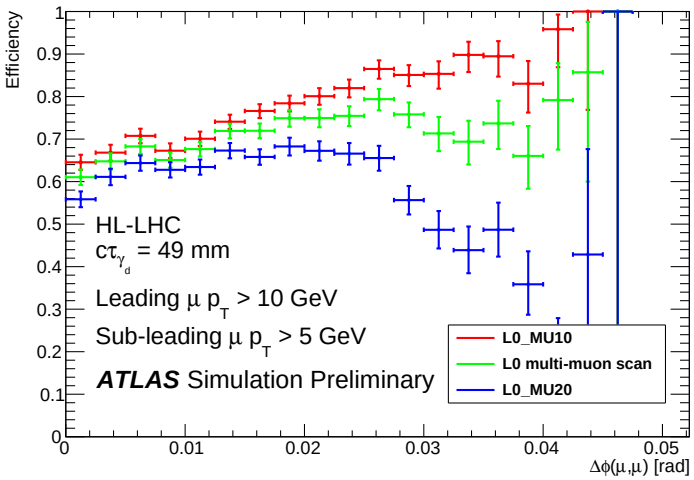

(b) 'medium' sample, $c\tau = 49mm$

Figure 7.18. Efficiency for different trigger selections as a function of the opening angle of the two muons of the γ_d decay. Single muon with 10 (L0_MU10) and 20 (L0_MU20) GeV p_T threshold are shown in red and blue, respectively. The L0 multi-muon scan trigger is shown in green.

muon transverse momentum is shown in Figure 7.21. The profile [1] is also shown superimposed.

The mean value of the inverse of the sagitta for a $p_T = 20$ GeV pointing muon is $s^{-1} = 9 \times 10^{-6}$ mm^{-1}. A cut on the inverse of the sagitta at this value can thus be used to select non-pointing muons with a p_T greater than 20 GeV.

[1] The profile show the mean value of Y and its error for each bin in X

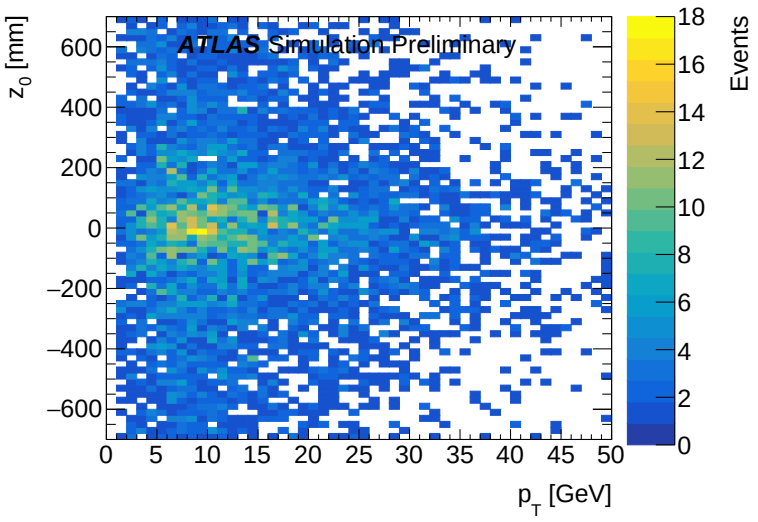

Figure 7.19. Muon longitudinal impact parameter z_0 as a function of the truth muon transverse momentum in the FRVZ MC sample with $m_{\mathrm{H}} = 10$ GeV.

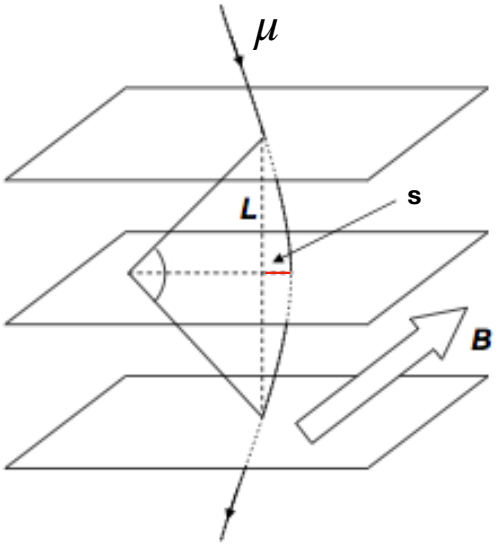

Figure 7.20. Schematic picture of the sagitta (s), defined as the vertical distance from the midpoint of the chord (L) to the arc of the muon trajectory itself.

Efficiency

The new L0 muon sagitta trigger selection is then defined as: the single muon trigger with a p_{T} threshold of 5 GeV and the sagitta cut $s^{-1} \leq 9 \times 10^{-6}$ mm^{-1}, for muons not selected by the single muon trigger with p_{T} threshold of 20 GeV. The efficiency is shown in Figure 7.22 as a function of the leading muon p_{T} for a signal sample with $m_{\gamma_d} = 10$ GeV. The single muon trigger with p_{T} threshold of 20 GeV and the logical OR of the two are also shown. A gain in signal efficiency of $\sim 20\%$ is reported for the L0 muon sagitta trigger with respect to the standard single muon

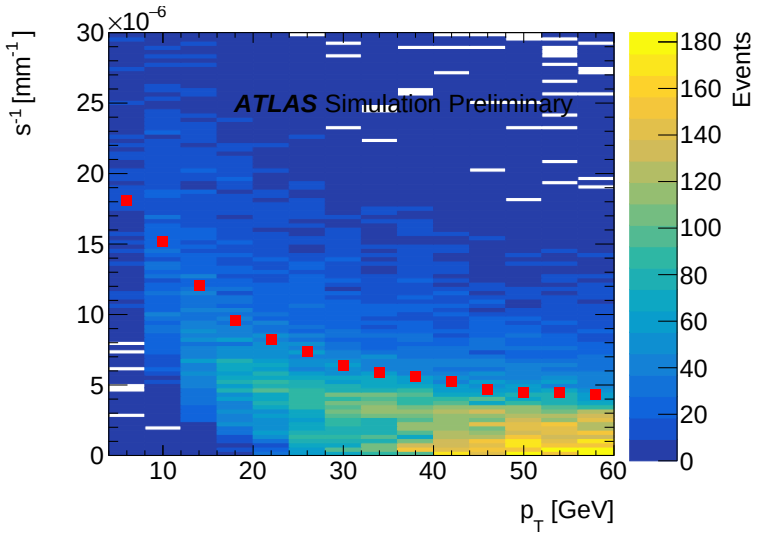

Figure 7.21. Inverse of the sagitta of pointing muons as a function of the muon truth transverse momentum. The profile of the inverse of the sagitta over the muon transverse momentum is overlaid in red.

trigger.

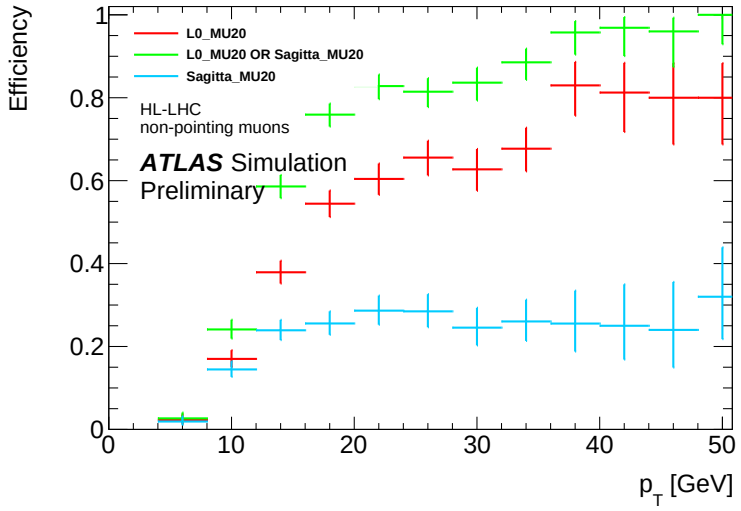

Figure 7.22. Trigger efficiency comparison for FRVZ sample with $m_{\gamma_d} = 10$ GeV: L0 $p_T = 20$ GeV threshold (red), L0 sagitta muon trigger (blue) and the OR of the two triggers (green).

Contamination from low p_T muons is estimated on a pointing muon MC sample generated according to a uniform transverse momentum distribution in the range 1-50 GeV. The efficiency as a function of the muon transverse momentum, tested on this sample, for the L0 sagitta muon and the standard 20 GeV single muon trigger is shown in Figure 7.23. Little contamination is seen from low p_T muons. This could be further reduced by optimising the tuning of the sagitta threshold.

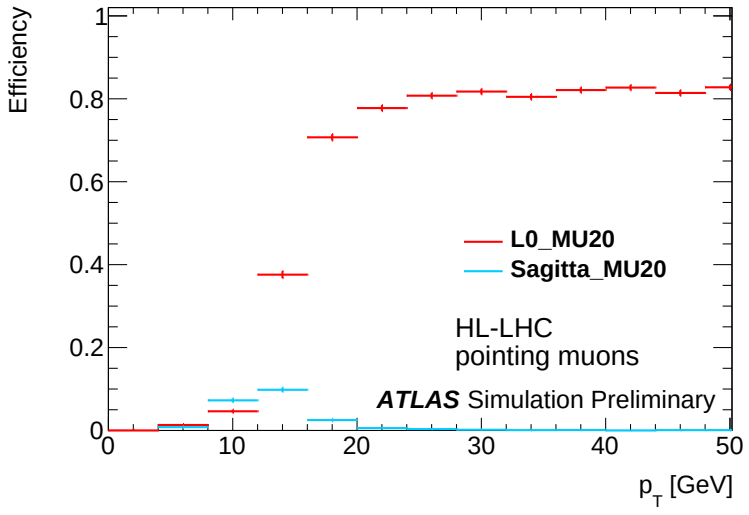

Figure 7.23. Muon trigger efficiency for MC single pointing muon events: standard 20 GeV threshold (red) and L0 sagitta muon trigger when the previous trigger is not fired (blue).

7.3 HL-LHC prospects for the displaced dark-photon search

The expected sensitivity of the displaced dark-photon jet analysis after Run-3 and HL-LHC operations is introduced in this section. This study is based on the 2015–2016 results presented in Chapter 5 focusing only on the μDPJ–μDPJ channel. Moreover, the trigger improvements introduced in Section 7.2 are exploited to improve the signal selection. The signal model used in the Run-2 search, generated for the HL-LHC setup, is considered for the study. All MC samples used are presented in Section 7.2.1.

Run-3 conditions are assumed to be the same as Run-2 with the exception of the increased centre-of-mass energy to 14 TeV and the total integrated luminosity of 300 fb^{-1}. The HL-LHC setup assumes a 14 TeV centre-of-mass energy with $\langle\mu\rangle = 200$ interactions per bunch crossing, the new detector setup explained in Section 7.1 and a total integrated luminosity of 3000 fb^{-1}.

7.3.1 Run-2 extrapolation to Run-3 and HL-LHC

The Run-2 analysis selection efficiency is considered to be unchanged for the Run-3 and HL-LHC setups in the extrapolation procedure. In the background extrapolation only the relevant multijet and cosmic-ray backgrounds are considered. The Run-3 and HL-LHC analyses are expected to be able to maintain the minor beam induced background to negligible level as in Run-2.

Being that Run-3 extrapolation does not consider any change in pileup with respect to Run-2, signal and mulitjet background events are rescaled according to the increased integrated luminosity and centre-of-mass energy. The cosmic-ray background is expected to scale with the duration of data taking. Comparing the

two years of data taking (2015+2016) used in the Run-2 analysis, to the two final years of Run-2 (2017–2018) and three years of expected data taking time of Run-3, a scaling factor of 2.5 is assumed.

The HL-LHC extrapolation exploits the simulated MC samples to compare directly the different working conditions with respect to Run-2. A scale factor of 1.13 is computed for signal events and of 1.25 for multijet background events. The cosmic-ray background is computed comparing the two years (2015–2016) of the Run-2 data taking, to the expected 12 years duration of the HL-LHC data taking, resulting in a scale factor of 6. The expected multi-muon scan trigger improvement by 7 %, introduced in Section 7.2.3, is adopted for the signal sample, since the Run-2 analysis searched for dark photons in the boosted regime.

Table 7.3 summarises the expected number of background and signal events after Run-3 and HL-LHC data taking.

Muonic channel	$\sqrt{s}$ TeV	Expected background	Expected signal FRVZ model
Run-3	14	930 ± 12 (stat.)	5325 ± 213 (stat.)
HL-LHC	14	11685 ± 48 (stat.)	65648 ± 2626 (stat.)

Table 7.3. Expected number of background and FRVZ signal events at the end of Run-3 and HL-LHC. Statistical errors only are presented and $BR(\gamma_d \to \mu\mu) = 45$ % is used. Cosmic-ray events are subtracted.

7.3.2 Statistical and systematic uncertainties

All statistical uncertainties are scaled with the expected integrated luminosity. For the Run-3 setup, systematic uncertainties are assumed to be the same as in Run-2, as presented in Section 5.6. For the HL-LHC setup the same systematic uncertainties are evaluated following ATLAS collaboration prescriptions adopted for upgrade studies [124]. Analysis specific systematic uncertainties are considered the same as in Run-2, assuming that the ATLAS detector performance will be kept close to the Run-2 one. The same considerations have been applied to the uncertainties related to the Boosted Decision Tree (BDT), trained to discriminate the signal μDPJ from the cosmic-ray background. The Run-2 systematic uncertainty on the pile-up mismodelling effects on the Σp_{T} selection efficiency is recomputed to take into account the higher pileup conditions of HL-LHC. This is evaluated following the same method reported in Section 5.6 for Run-2, using the $Z \to \mu\mu$ MC samples generated with different pileup conditions. The Σp_{T} variable as a function of pile-up is shown in Figure 7.24 for the four pile-up regimes. The maximum difference at the value of the analysis selection requirement $\max(\Sigma p_{\mathrm{T}}) \leq 4.5$ GeV is taken as systematic uncertainty and is found to be 18%. According to detailed simulation studies of the upgraded detector [124], the jet energy scale uncertainty is expected to decrease in the transition from Run-2 to the HL-LHC and is assumed to be 2.5%, half that of Run-2, while the jet energy resolution uncertainty is expected to be the same as in Run-2 and thus assumed to be 2%. The expected uncertainty on the integrated luminosity for the full HL-LHC dataset is 1%. All the adopted systematic

uncertainties are reported in Table 7.4

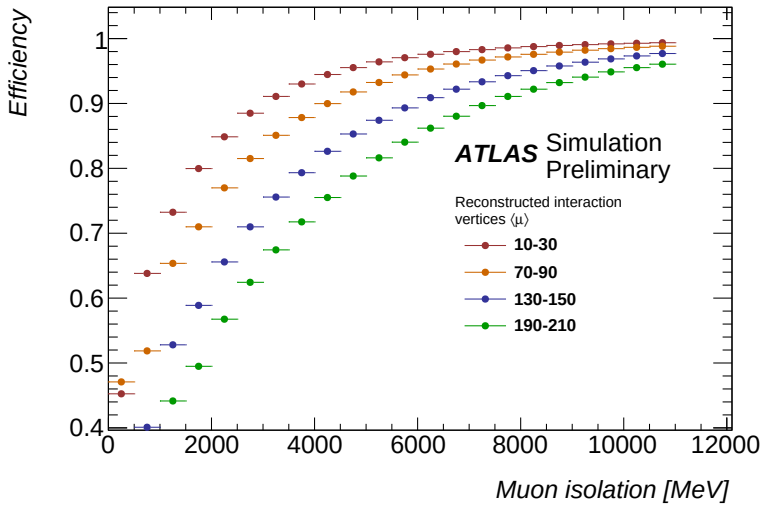

Figure 7.24. Isolation efficiency as a function of $\sum p_{\mathrm{T}}$ for four intervals of the number of reconstructed interaction vertices per event in a $Z \to \mu\mu$ MC sample.

Systematic uncertainty (in %)	Run-3	HL-LHC
Luminosity	2.2	1.0
Reconstruction efficiency γ_d	9.7	9.7
Effect of pile-up on Σp_T	10	18
Reconstruction of the p_T of the γ_d	5.1	5.1
Pile-up	2.0	2.0
Jet energy scale	5.0	2.5
Jet energy resolution	2.0	2.0

Table 7.4. Summary of the systematic uncertainties used for sensitivity extrapolation to Run-3 and HL-LHC.

7.3.3 Results

The same procedure adopted in Run-2, see Section 5.7, is used to set upper limits at 95% CL on the cross-section times branching fraction of $H \to 2\gamma_{\mathrm{d}} + X$ as a function of the dark photon proper lifetime.

The μDPJ–μDPJ results are shown in Figure 7.25 for the different setups, considering the $H \to 2\gamma_{\mathrm{d}} + X$ process and $m_H = 125$ GeV. The HL-LHC scenario is shown with and without the multi-muon scan trigger improvement. The results in terms of excluded $c\tau$ ranges are summarised in Table 7.5, assuming a branching fraction for the Higgs boson to the dark sector of 10% and 1%.

The upper limits are also interpreted in the context of the FRVZ vector portal model in terms of kinetic mixing parameter ϵ and γ_{d} mass limit. The Run-3 and

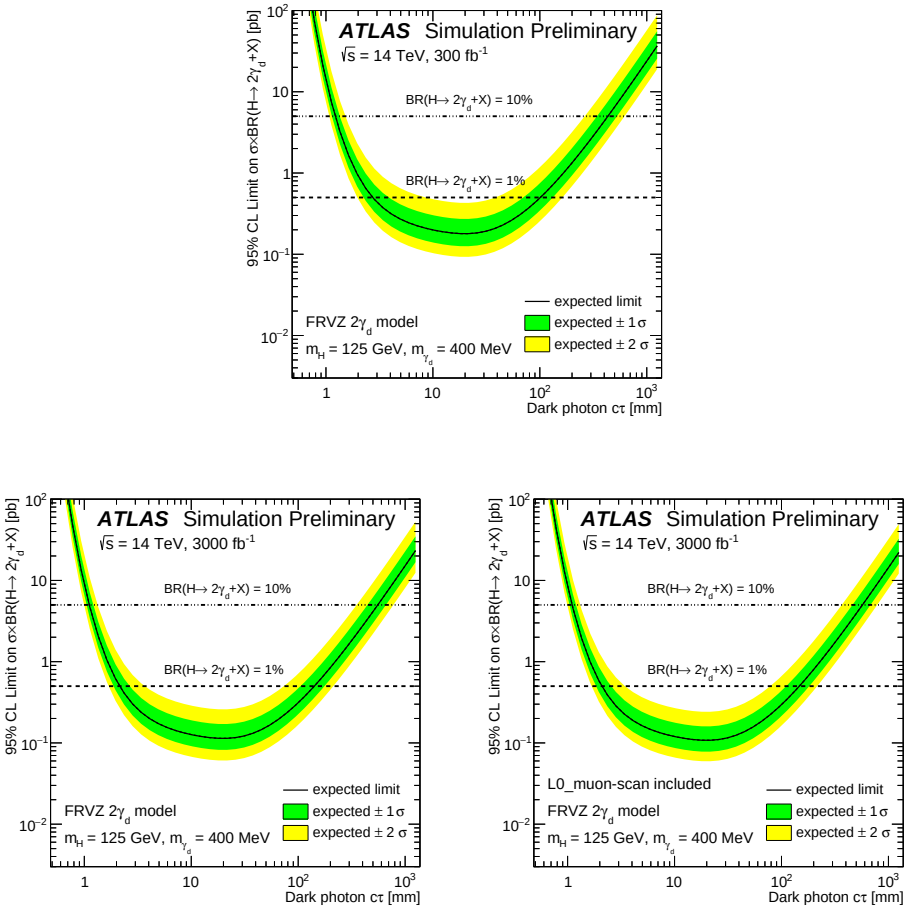

Figure 7.25. 95% CL upper limit on the cross-section times branching fraction of $H \rightarrow 2\gamma_{\mathrm{d}}+X$ as a function of the γ_{d} lifetime, considering 45% dark photon branching ratio to muons. Three different scenarios are considered: 300 fb^{-1}after Run-3 (top), 3000 fb^{-1}after HL-LHC (right) and 3000 fb^{-1}after HL-LHC including multi-muon scan trigger improvement (left).

Excluded $c\tau$ [mm] $H \rightarrow 2\gamma_{\mathrm{d}}+X$ muonic-muonic	Run-2	Run-3	HL-LHC	HL-LHC w/ L0 muon-scan
BR=10 %	$1.5 \leq c\tau \leq 307$	$1.15 \leq c\tau \leq 435$	$0.97 \leq c\tau \leq 553$	$0.97 \leq c\tau \leq 597$
BR=1 %	-	$2.76 \leq c\tau \leq 102$	$2.18 \leq c\tau \leq 142$	$2.13 \leq c\tau \leq 148$

Table 7.5. Ranges of γ_d $c\tau$ excluded at 95 % CL for $H \rightarrow 2\gamma_{\mathrm{d}}+X$ assuming BR($H \rightarrow 2\gamma_{\mathrm{d}}+X$) = 10 % and BR($H \rightarrow 2\gamma_{\mathrm{d}}+X$) = 1 %.

HL-LHC setup results are shown in Figure 7.26 as exclusion contours assuming a Higgs decay branching fraction into γ_{d} of 1%. The dark-photon jet search at the HL-LHC is expected to probe BR($H \rightarrow 2\gamma_{\mathrm{d}}+X$) down to 1% with the same sensitivity reached by the Run-2 analysis when considering a 10% branching ratio.

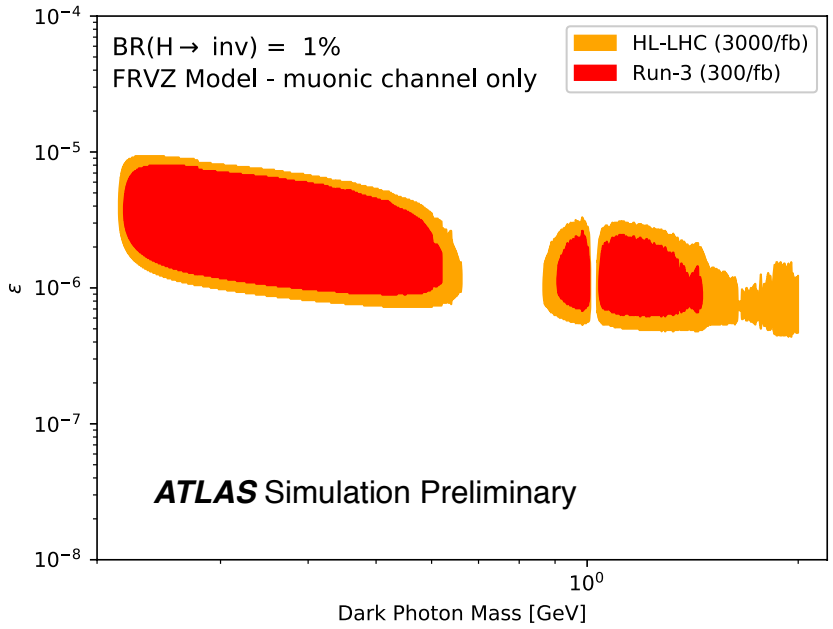

Figure 7.26. Exclusion contour plot in the plane defined by the γ_d mass and the kinetic mixing parameter ϵ. Two different scenarios are shown assuming a Higgs decay branching fraction to the hidden sector of 1%: 300 fb^{-1}after Run-3 (red) and 3000 fb^{-1}after HL-LHC including multi-muon scan trigger improvement (orange).

Chapter 8

Conclusions

Several promising theories beyond the Standard Model predict the existence of a light dark gauge boson γ_{d} that decays into collimated jet-like structures of leptons and light hadrons (dark-photon jets). These Dark Sector models can provide a solution to many open questions in particle physics such as Dark Matter and naturalness. The dark photon mixes kinetically with the SM photon and depending on the structure of the hidden sector can decay to SM particles. The kinetic mixing term ϵ determines the lifetime, for small values the dark photon may be produced with a macroscopic life-time. The search for these long-lived particles (LLP) depends on the decay length, which can range from few μm to several meters outside the ATLAS detector. LLP decaying outside of the interaction region give rise to striking signatures in the detector, representing a great challenge for both the trigger and the event reconstruction capabilities of the detector. This work presents the most recent ATLAS results [4] of the search for long-lived dark photons decaying into displaced dark-photon jets, based on 36 fb^{-1} of data collected in proton-proton collisions at $\sqrt{s} = 13$ TeV. No significant excess of events compared with the background expectation is observed, and upper limits are set on the production cross section times branching fraction of scalar bosons that decay into dark photons according to the FRVZ model. The upper limits are computed as a function of the proper decay length $c\tau$ of the dark photon γ_{d}. A cross section times branching fraction above 4 pb is excluded for a Higgs boson decaying into two dark photons for dark-photon decay lengths between 1.5 mm and 284 mm. Improvements in background suppression and the exploitation of hadronic γ_{d} decays result in a significantly increased sensitivity compared to the previous ATLAS Run-1 result from displaced lepton-jet searches [70] using 8 TeV *pp* data.

The full Run-2 dataset will allow to further increase the discovery potential of the analysis and to search for currently unexplored decay channels. The dark-photon jet analysis will explore the very well motivated low-mass dark photon region of fully electronic decays, a difficult region due to small angular separation between the two leptons. Moreover, to extend to smaller values of ϵ a new topological signature will be studied where a dark-photon jet is produced back-to-back with missing transverse momentum, studying the case where one of the two dark photon decays outside the detector. Other planned enhancements to the analysis include the study of the mono-DPJ and W/Z associated production channels. A new

interesting idea would be to include γ_d decaying into taus, a very interesting probe to more complete Dark Sector models where certain SM fields are charged under the new U(1) symmetry, exploiting the extra anomaly-free groups within the SM. In general, exploring the gauge couplings to SM particles could dramatically reshape the landscape of Dark sectors, and LHC searches could be complementary to dedicated dark photon experiments. In the context of a dark photon legacy paper, the full Run-2 dark-photon jet search is crucial to combine the discovery power of all ATLAS Run-2 different analyses in a common dark photon framework, an effort that has already started.

In the long-term picture, this work investigates the expected limits after Run-3 and HL-LHC [5] operations extrapolating the results of the Run-2 search, laying the groundwork for these future analyses. The 95% CL exclusion limit on the dark photon average $c\tau$ is expected to improve, extending the lower bound down to 0.97 mm and the upper bound up to 597 mm, assuming a branching ratio of the Higgs boson decay to the Hidden sector of 10%.

To overcome the inefficiency of ATLAS Run-2 triggers to select LLP, the main bottleneck of the Run-2 dark-photon jet analysis, two new muon trigger algorithms are developed to fully exploit the HL-LHC hardware improvements. The multi-muon scan trigger designed to improve the selection efficiency for close-by muon pairs, shows a gain in efficiency of $\sim$7% with respect to the baseline selection used in Run-2. The sagitta muon trigger designed to select displaced non-pointing muons, a signature not reachable by the current trigger system, for a total efficiency improvement of $\sim$20% with respect to the Run-2 baseline selection.

In the near future, searches must entail a shift towards innovative non-standard signature to expand ATLAS's lead role in the investigation of DM. The dark-photon jet signature will continue to be one of the most powerful tools to probe the intensity frontier at ATLAS.

Bibliography

[1] L. Evans et al. LHC Machine. *JINST*, 3:S08001, 2008.

[2] ATLAS Collaboration. The ATLAS Experiment at the CERN Large Hadron Collider. *JINST*, 3:S08003, 2008.

[3] R. Adam et al. Planck 2015 results. I. Overview of products and scientific results. *Astron. Astrophys.*, 594:A1, 2016.

[4] ATLAS Collaboration. Search for light long-lived neutral particles produced in pp collisions at $\sqrt{s} = 13$ TeV and decaying into collimated leptons or light hadrons with the ATLAS detector. 2019.

[5] ATLAS Collaboration. Search prospects for dark-photons decaying to displaced collimated jets of muons at HL-LHC. ATL-PHYS-PUB-2019-002, 2019.

[6] A. Pich. The Standard model of electroweak interactions. In *The Standard model of electroweak interactions*, pages 1–49, 2008. [,1(2007)].

[7] C. Quigg. Gauge theories of the strong, weak and electromagnetic interactions. *Front. Phys.*, 56:1–334, 1983.

[8] T. Muta. *Foundations of Quantum Chromodynamics: An Introduction to Perturbative Methods in Gauge Theories, (3rd ed.)*, volume 78 of *World scientific Lecture Notes in Physics*. World Scientific, Hackensack, N.J., 2010.

[9] W. Greiner et al. *Quantum Chromodynamics*. Springer Berlin Heidelberg, 2007.

[10] S. Weinberg. A Model of Leptons. *Phys. Rev. Lett.*, 19:1264–1266, 1967.

[11] A. Salam et al. Weak and electromagnetic interactions. *Nuovo Cim.*, 11:568–577, 1959.

[12] P. W. Higgs. Broken Symmetries and the Masses of Gauge Bosons. *Phys. Rev. Lett.*, 13:508–509, 1964. [,160(1964)].

[13] F. Englert et al. Broken Symmetry and the Mass of Gauge Vector Mesons. *Phys. Rev. Lett.*, 13:321–323, 1964. [,157(1964)].

[14] N. Bernal et al. The Dawn of FIMP Dark Matter: A Review of Models and Constraints. *Int. J. Mod. Phys.*, A32(27):1730023, 2017.

[15] E. W. Kolb et al. The Early Universe. *Front. Phys.*, 69:1–547, 1990.

[16] PandaX-II Collaboration. Dark Matter Results From 54-Ton-Day Exposure of PandaX-II Experiment. *Phys. Rev. Lett.*, 119(18):181302, 2017.

[17] XENON1T Collaboration. Light Dark Matter Search with Ionization Signals in XENON1T. 2019.

[18] R. Bernabei et al. Final model independent result of DAMA/LIBRA-phase1. *Eur. Phys. J.*, C73:2648, 2013.

[19] ATLAS Collaboration. Combination of searches for invisible Higgs boson decays with the ATLAS experiment. *Phys. Rev. Lett.*, 122(23):231801, 2019.

[20] M. Pospelov et al. Secluded WIMP Dark Matter. *Phys. Lett.*, B662:53–61, 2008.

[21] D. Curtin et al. Illuminating dark photons with high-energy colliders. *JHEP*, 02:157, 2015.

[22] B. Batell et al. Probing a secluded U(1) at B factories. *Phys. Rev. D*, 79:115008, 2009.

[23] M. J. Strassler et al. Echoes of a hidden valley at hadron colliders. *Phys. Lett. B*, 651:374–379, 2007.

[24] M. Buschmann et al. Lepton Jets from Radiating Dark Matter. *JHEP*, 07:045, 2015.

[25] A. Falkowski et al. Hidden Higgs decaying to lepton jets. *JHEP*, 05:077, 2010.

[26] P. Ilten et al. Serendipity in dark photon searches. *JHEP*, 06:004, 2018.

[27] LHCb Collaboration. Search for Dark Photons Produced in 13 TeV *pp* Collisions. *Phys. Rev. Lett.*, 120(6):061801, 2018.

[28] BABAR Collaboration. Search for a Dark Photon in e^+e^- Collisions at BaBar. *Phys. Rev. Lett.*, 113(20):201801, 2014.

[29] J. R. Batley et al. Search for the dark photon in π^0 decays. *Phys. Lett.*, B746:178–185, 2015.

[30] A. Konaka et al. Search for neutral particles in electron-beam-dump experiment. *Phys. Rev. Lett.*, 57:659–662, Aug 1986.

[31] E. M. Riordan et al. Search for short-lived axions in an electron-beam-dump experiment. *Phys. Rev. Lett.*, 59:755–758, Aug 1987.

[32] J. D. Bjorken et al. Search for neutral metastable penetrating particles produced in the slac beam dump. *Phys. Rev. D*, 38:3375–3386, Dec 1988.

[33] A. Bross et al. Search for short-lived particles produced in an electron beam dump. *Phys. Rev. Lett.*, 67:2942–2945, Nov 1991.

[34] M. Davier et al. An unambiguous search for a light higgs boson. *Physics Letters B*, 229(1):150 – 155, 1989.

[35] J. Blümlein et al. New exclusion limits for dark gauge forces from beam-dump data. *Phys. Lett. B*, 701:155–159, 2011.

[36] J. Blümlein et al. New exclusion limits on dark gauge forces from proton Bremsstrahlung in beam-dump data. *Phys. Lett. B*, 731:320–326, 2014.

[37] S. N. Gninenko. Constraints on sub-GeV hidden sector gauge bosons from a search for heavy neutrino decays. *Phys. Lett. B*, 713:244–248, 2012.

[38] C. Cheung et al. Lepton jets in (supersymmetric) electroweak processes. *JHEP*, 04:116, 2010.

[39] A. Falkowski et al. Discovering Higgs Boson Decays to Lepton Jets at Hadron Colliders. *Phys. Rev. Lett.*, 105:241801, 2010.

[40] M. Benedikt et al. LHC Design Report. 3. The LHC injector chain. 2004.

[41] LHC Guide. Mar 2017.

[42] S. Chatrchyan et al. The CMS Experiment at the CERN LHC. *JINST*, 3:S08004, 2008.

[43] K. Aamodt et al. The ALICE experiment at the CERN LHC. *JINST*, 3:S08002, 2008.

[44] J. Alveset al. The LHCb Detector at the LHC. *JINST*, 3:S08005, 2008.

[45] ATLAS Collaboration. Luminosity Public Results Run-2.

[46] ATLAS Collaboration. Luminosity determination in pp collisions at $\sqrt{s} = 13$ TeV using the ATLAS detector at the LHC. ATLAS-CONF-2019-021, 2019.

[47] H. Wiedemann. *Particle accelerator physics I.* Springer, Berlin, Germany, 1999.

[48] ATLAS magnet system: Technical design report. 1997.

[49] ATLAS Collaboration. Track Reconstruction Performance of the ATLAS Inner Detector at $\sqrt{s} = 13$ TeV. ATL-PHYS-PUB-2015-018, 2015.

[50] ATLAS Collaboration. ATLAS Insertable B-Layer Technical Design Report. ATLAS-TDR-19, 2010.

[51] B. Abbott et al. Production and integration of the ATLAS Insertable B-Layer. *JINST*, 13(05):T05008, 2018.

[52] ATLAS Collaboration. The Silicon microstrip sensors of the ATLAS semiconductor tracker. *Nucl. Instrum. Meth.*, A578:98–118, 2007.

[53] B. Aubert et al. Construction, assembly and tests of the ATLAS electromagnetic barrel calorimeter. *Nucl. Instrum. Meth.*, A558:388–418, 2006.

[54] ATLAS tile calorimeter: Technical design report. 1996.

[55] D. M. Gingrich et al. Construction, assembly and testing of the ATLAS hadronic end-cap calorimeter. *JINST*, 2:P05005, 2007.

[56] ATLAS Collaboration. ATLAS muon spectrometer: Technical design report. 1997.

[57] ATLAS Collaboration. 2015 start-up trigger menu and initial performance assessment of the ATLAS trigger using Run-2 data. ATL-DAQ-PUB-2016-001, 2016.

[58] ATLAS Collaboration. Performance of the ATLAS Trigger System in 2015. *Eur. Phys. J.*, C77(5):317, 2017.

[59] ATLAS Collaboration. Electron reconstruction and identification in the ATLAS experiment using the 2015 and 2016 LHC proton-proton collision data at $\sqrt{s}$ = 13 TeV. *Eur. Phys. J.*, C79(8):639, 2019.

[60] W. Lampl et al. Calorimeter clustering algorithms: Description and performance. 2008.

[61] ATLAS Collaboration. Muon reconstruction performance of the ATLAS detector in proton–proton collision data at $\sqrt{s} = 13\,\text{TeV}$. *Eur. Phys. J. C*, 76:292, 2016.

[62] M. Cacciari et al. The anti-k_t jet clustering algorithm. *JHEP*, 04:063, 2008.

[63] M. Cacciari et al. FastJet user manual. *Eur. Phys. J. C*, 72:1896, 2012.

[64] ATLAS Collaboration. Tagging and suppression of pileup jets with the ATLAS detector. ATLAS-CONF-2014-018, 2014.

[65] ATLAS Collaboration. Performance of pile-up mitigation techniques for jets in pp collisions at $\sqrt{s} = 8\,\text{TeV}$ using the ATLAS detector. *Eur. Phys. J. C*, 76:581, 2016.

[66] A. Hocker et al. TMVA - Toolkit for Multivariate Data Analysis. 2007.

[67] ATLAS Collaboration. Jet energy scale measurements and their systematic uncertainties in proton–proton collisions at $\sqrt{s} = 13\,\text{TeV}$ with the ATLAS detector. *Phys. Rev. D*, 96:072002, 2017.

[68] ATLAS Collaboration. Selection of jets produced in 13 TeV proton–proton collisions with the ATLAS detector. ATLAS-CONF-2015-029, 2015.

[69] ATLAS Collaboration. Search for displaced muonic lepton jets from light Higgs boson decay in proton–proton collisions at $\sqrt{s} = 7\,\text{TeV}$ with the ATLAS detector. *Phys. Lett. B*, 721:32, 2013.

[70] ATLAS Collaboration. Search for long-lived neutral particles decaying into lepton jets in proton–proton collisions at $\sqrt{s} = 8\,\text{TeV}$ with the ATLAS detector. *JHEP*, 11:088, 2014.

[71] ATLAS Collaboration. Characterisation and mitigation of beam-induced backgrounds observed in the ATLAS detector during the 2011 proton–proton run. *JINST*, 8:P07004, 2013.

[72] J. Alwall et al. The automated computation of tree-level and next-to-leading order differential cross sections, and their matching to parton shower simulations. *JHEP*, 07:079, 2014.

[73] T. Sjöstrand et al. An introduction to PYTHIA 8.2. *Comput. Phys. Commun.*, 191:159–177, 2015.

[74] ATLAS Collaboration. ATLAS Pythia 8 tunes to 7 TeV data. ATL-PHYS-PUB-2014-021, 2014.

[75] R. D. Ball et al. Parton distributions with LHC data. *Nucl. Phys. B*, 867:244–289, 2013.

[76] S. Dittmaier et al. Handbook of LHC Higgs Cross Sections: 1. Inclusive Observables. CERN-2011-002.

[77] T. Gleisberg et al. Event generation with sherpa 1.1. *JHEP*, 02:007, 2009.

[78] R. D. Ball et al. Parton distributions for the LHC run II. *JHEP*, 04:040, 2015.

[79] S. Frixione et al. A positive-weight next-to-leading-order monte carlo for heavy flavour hadroproduction. *JHEP*, 09:126, 2007.

[80] T. Sjöstrand et al. PYTHIA 6.4 physics and manual. *JHEP*, 05:026, 2006.

[81] P. Z. Skands. Tuning monte carlo generators: The perugia tunes. *Phys. Rev. D*, 82:074018, 2010.

[82] H. L. Lai et al. New parton distributions for collider physics. *Phys. Rev. D*, 82:074024, 2010.

[83] J. Pumplin et al. New generation of parton distributions with uncertainties from global qcd analysis. *JHEP*, 07:012, 2002.

[84] P. Golonka et al. PHOTOS Monte Carlo: A Precision tool for QED corrections in Z and W decays. *Eur. Phys. J.*, C45:97–107, 2006.

[85] ATLAS Collaboration. The ATLAS Simulation Infrastructure. *Eur. Phys. J. C*, 70:823, 2010.

[86] GEANT4 Collaboration. GEANT4–a simulation toolkit. *Nucl. Instrum. Meth. A*, 506:250–303, 2003.

[87] ATLAS Collaboration. Summary of ATLAS Pythia 8 tunes. ATL-PHYS-PUB-2012-003, 2012.

[88] A. D. Martin et al. Parton distributions for the LHC. *Eur. Phys. J. C*, 63:189–285, 2009.

[89] ATLAS Collaboration. Performance of the ATLAS Trigger System in 2010. *Eur. Phys. J. C*, 72:1849, 2012.

[90] ATLAS Collaboration. Triggers for displaced decays of long-lived neutral particles in the ATLAS detector. *JINST*, 8:P07015, 2013.

[91] ATLAS Collaboration. Characterisation and mitigation of beam-induced backgrounds observed in the ATLAS detector during the 2011 proton-proton run. *JINST*, 8:P07004, 2013.

[92] P. Meade et al. Dark matter sees the light. *JHEP*, 12:052, 2009.

[93] ATLAS Collaboration. Early Inner Detector Tracking Performance in the 2015 Data at $\sqrt{s} = 13$ TeV. ATL-PHYS-PUB-2015-051, 2015.

[94] Y. L. Dokshitzer et al. Better jet clustering algorithms. *JHEP*, 08:001–001, 1997.

[95] ATLAS Collaboration. The Level-1 Trigger Muon Barrel System of the ATLAS experiment at CERN. *JINST*, 4:P04010, 2009.

[96] ATLAS Collaboration. Jet mass reconstruction with the ATLAS Detector in early Run 2 data. ATLAS-CONF-2016-035, 2016.

[97] M. Cacciari et al. The catchment area of jets. *JHEP*, 04:005, 2008.

[98] ATLAS Collaboration. Beam-induced and cosmic-ray backgrounds observed in the ATLAS detector during the LHC 2012 proton–proton running period. *JINST*, 11:P05013, 2016.

[99] ATLAS Collaboration. Luminosity determination in pp collisions at $\sqrt{s} = 8\,\text{TeV}$ using the ATLAS detector at the LHC. *Eur. Phys. J. C*, 76:653, 2016.

[100] G. Avoni et al. The new LUCID-2 detector for luminosity measurement and monitoring in ATLAS. *JINST*, 13(07):P07017, 2018.

[101] ATLAS Collaboration. Muon reconstruction efficiency in reprocessed 2010 LHC proton–proton collision data recorded with the ATLAS detector. ATLAS-CONF-2011-063, 2011.

[102] ATLAS Collaboration. Search for long-lived neutral particles in pp collisions at $\sqrt{s} = 13\,\text{TeV}$ that decay into displaced hadronic jets in the ATLAS calorimeter. 2019.

[103] ATLAS Collaboration. Search for pair-produced long-lived neutral particles decaying to jets in the ATLAS hadronic calorimeter in pp collisions at $\sqrt{s} = 8\,\text{TeV}$. *Phys. Lett. B*, 743:15, 2015.

[104] A. L. Read. Presentation of search results: the CL_s technique. *J. Phys. G*, 28:2693–2704, 2002.

[105] G. Cowan et al. Asymptotic formulae for likelihood-based tests of new physics. *Eur. Phys. J.*, C71:1554, 2011. [Erratum: Eur. Phys. J.C73,2501(2013)].

[106] ATLAS Collaboration. A search for prompt lepton-jets in *pp* collisions at $\sqrt{s} = 8\,\text{TeV}$ with the ATLAS detector. *JHEP*, 02:062, 2016.

[107] ATLAS Collaboration. Search for long-lived particles in final states with displaced dimuon vertices in *pp* collisions at $\sqrt{s} = 13\,\text{TeV}$ with the ATLAS detector. *Phys. Rev. D*, 99:012001, 2019.

[108] CMS Collaboration. A search for pair production of new light bosons decaying into muons. *Phys. Lett. B*, 752:146, 2016.

[109] CMS Collaboration. A search for pair production of new light bosons decaying into muons in proton-proton collisions at 13 TeV. *Phys. Lett.*, B796:131–154, 2019.

[110] N. Arkani-Hamed et al. A Theory of Dark Matter. *Phys. Rev.*, D79:015014, 2009.

[111] LHCb Collaboration. Search for $A' \to \mu^+\mu^-$ decays. 2019.

[112] KLOE-2 Collaboration. Limit on the production of a new vector boson in $e^+e^- \to U\gamma$, $U \to \pi^+\pi^-$ with the KLOE experiment. *Phys. Lett.*, B757:356–361, 2016.

[113] ATLAS Collaboration. Search for dark matter and other new phenomena in events with an energetic jet and large missing transverse momentum using the ATLAS detector. *JHEP*, 01:126, 2018.

[114] LHC Higgs Cross Section Working Group. SM Higgs production cross sections at $\sqrt{s} = 13 - 14$ TeV (CERN Report 3). 2016.

[115] G. Apollinari et al. High-Luminosity Large Hadron Collider (HL-LHC). *CERN Yellow Rep. Monogr.*, 4:1–516, 2017.

[116] ATLAS Collaboration. ATLAS Phase-II Upgrade Scoping Document. Technical Report CERN-LHCC-2015-020. LHCC-G-166, CERN, Geneva, Sep 2015.

[117] ATLAS Collaboration. Technical Design Report for the Phase-II Upgrade of the ATLAS Muon Spectrometer. Technical Report CERN-LHCC-2017-017. ATLAS-TDR-026, CERN, Geneva, Sep 2017.

[118] ATLAS Collaboration. Technical Design Report for the Phase-II Upgrade of the ATLAS TDAQ System. Technical Report CERN-LHCC-2017-020. ATLAS-TDR-029, CERN, Geneva, Sep 2017.

[119] J. Anderson et al. FELIX: a High-Throughput Network Approach for Interfacing to Front End Electronics for ATLAS Upgrades. *J. Phys. Conf. Ser.*, 664(8):082050, 2015.

[120] P. Nason. A New method for combining NLO QCD with shower Monte Carlo algorithms. *JHEP*, 11:040, 2004.

[121] S. Frixione et al. Matching NLO QCD computations with Parton Shower simulations: the POWHEG method. *JHEP*, 11:070, 2007.

[122] H. Lai et al. New parton distributions for collider physics. *Phys. Rev.*, D82:074024, 2010.

[123] ATLAS Collaboration. Measurement of the Z/γ^* boson transverse momentum distribution in pp collisions at $\sqrt{s} = 7$ TeV with the ATLAS detector. *JHEP*, 09:145, 2014.

[124] ATLAS Collaboration. Expected performance of the ATLAS detector at the High-Luminosity LHC. ATL-PHYS-PUB-2019-005, 2019.